

Transcranial Ultrasound Stimulation:

Using Patient Specific Lenses to Focus on Deep Targets for Non-invasive Neuromodulation

A thesis submitted for the degree of Doctor of Philosophy

Xinghao Cheng

Institute of Biomedical Engineering

Department of Engineering

Magdalen College

University of Oxford

Hilary Term 2023

© 2023

Xinghao Cheng

All rights reserved.

Transcranial ultrasound stimulation: Using patient specific lenses to focus on deep targets for non-invasive neuromodulation

by Xinghao Cheng, Magdalen College,
supervised by Professor Robin Cleveland

ABSTRACT

Transcranial ultrasound stimulation offers a non-invasive and targeted option for neuromodulation of the brain. However, the clinical utility of transcranial ultrasound for brain function has been impeded by the highly variable attenuation and phase distortions of the human skull. A method to focus ultrasound using a target-specific acoustic lens at the temporal bone window is presented. Ultrasound frequency (500 kHz), transducer aperture size (d = 64 mm), and lens material (PDMS) were selected based on acoustic simulations (k-Wave). Through computational modeling, the utility of this concept was confirmed for deep brain targets such as the perirhinal cortex, anterior hippocampus, globus pallidus internus, and subthalamic nucleus. Experimental validation of the work on nine target-specific lenses for use through two cadaver skull samples confirmed reliable predictions by the acoustic model. To evaluate this method for clinical application for neuromodulation of Parkinson's disease, interference between ultrasound waveforms and implanted electrodes was studied. Two ways were found to best mitigate the observed mutual interference: (i) forming the acoustic focus away from the electrode tip and (ii) using ultrasound pulse repetition frequencies higher than those of brain signal bands. Taken together, this method of case-specific stimulation delivery with an acoustic lens guides the design and workflow of ultrasound-mediated deep brain stimulation at the temporal bone window for effective, safe, and reproducible transcranial ultrasound stimulation. Results from this project are being implemented in an upcoming clinical trial to demonstrate its efficacy.

STATEMENT OF ORIGINALITY

I hereby declare that this submission is my own work, and to the best of my knowledge, it contains no material previously published or written by another person or substantial proportions of material that have been accepted for the award of any other degree or diploma at the University of Oxford or any other educational institution, except where due acknowledgement is made in the thesis. Any contribution made to the research by others with whom I have worked at the University of Oxford or elsewhere is explicitly acknowledged in the thesis. I also declare that the intellectual content of this thesis is the product of my own work, except to the extent that assistance from others in the project's design and conception or in style, presentation, and linguistic expression is acknowledged.

Xinghao Cheng

February 28, 2023

ACKNOWLEDGEMENTS

I express my deepest gratitude to my supervisor, Professor Robin Cleveland, for his expert teaching, guidance, and advice during my DPhil. I'm incredibly lucky to have the opportunity to explore all aspects of scientific research as well as to work with such a diverse set of techniques, methods, and people. This is merely a testament to Robin's propensity as a mentor and willingness to allow me to engage in and help shape the development of the project. Thank you so much for everything.

I would also like to recognise all of the collaborators with whom I have had the pleasure of working: Dr. Chris Butler and Dr. Alex Green for all things neurological and medical; Prof. Tim Denison and Mr. Moaad Benjaber for all things electrical and knowledge on deep brain stimulation; Dr. Nima Khalighinejad, Dr. Alessandro Bongioanni, Dr. Miriam Klein-Flugge, and Prof. Matthew Rushworth for introducing me to the world of experimental psychology; and Dr. Joseph Blackmore for his contributions to ultrasound neuromodulation. Thank you all for expanding my horizons and constantly teaching me new things.

To all the members of the BUBBL group, thank you for all your help, advice, and contributions. There are too many people to thank individually, but a special mention goes to Romain, Luca, and Mike for their support. Furthermore, I'm indebted to Daphne and Mandy for all the help and to Jim, Kyle, and David in the workshop for the flawless creations.

To my family, thank you for always being there and supporting me. Thanks to all of my friends who have made Oxford such an enjoyable place to both work and live.

Finally, I'd like to thank Magdalen College and the Department of Engineering Science for supporting me through both degrees over the past 8 years.

DISSEMINATION

Peer Reviewed Journal Articles

C. R. Butler, E. Rhodes, J. Blackmore, **X. Cheng**, R. L. Peach, M. Veldsman, F. Sheerin and R. O. Cleveland, "Transcranial ultrasound stimulation to human middle temporal complex improves visual motion detection and modulates electrophysiological responses," *Brain Stimul.*, vol. 15, no. 5, pp. 1236-1245, 2022.

X. Cheng, C. R. Butler and R. O. Cleveland, "Simulation of bilateral transcranial focused ultrasound stimulation using dual sources with personalized lens" *Brain Stimul.*, 2023. [In preparation]

Conference Presentations

X. Cheng, C. R. Butler and R. O. Cleveland, "Simulation study of transcranial ultrasound delivery to the hippocampus to test the feasibility of non-invasive neuromodulation," *179th Meeting of the Acoustical Society of America*, online, 2020.

X. Cheng, C. R. Butler and R. O. Cleveland, "Transcranial ultrasound stimulation: a simulation study for non-invasive neuromodulation of the hippocampus," *7th International Symposium on Focused Ultrasound, online*, 2020.

X. Cheng, C. R. Butler and R. O. Cleveland, "Using lenses to focus ultrasound to the human hippocampus: modelling and validation," *2nd iTRUSST Focused Ultrasound Neuromodulation Symposium, online*, 2021.

CONTENTS

Abstract i

Statement of Originality ii

Acknowledgements iii

Dissemination iv

List of Acronyms & Symbols viii

1. Introduction & Literature Review 1

1.1 Motivation 2

1.2 Mechanisms 4

1.3 Hippocampus Studies 5

1.4 Safety 7

1.5 Ultrasound Pulsing Sequence 10

1.6 Human Head Tissues 12

1.7 Transcranial Ultrasound Challenges 15

1.8 Linear Acoustic Theory 20

1.9 Numerical Implementation 23

1.10 Acoustic Holography 28

1.11 Thermal Modelling 29

1.12 Acoustic Lens 31

1.13 Monitoring 38

1.14 Aim of Thesis 41

2. Modelling Method & Optimisation 42

2.1 Simulation Toolbox Testing 43

2.2 Acoustic Holography Testing 47

2.3 Improved Ultrasound Delivery Method 52

2.4 Lens Material Selection 54

2.5 Subject Imaging Data 57

2.6 Time Reversal Back Propagation 58

2.7 Forward Propagation 61

2.8 Thermal Simulations 67

2.9 Piston Transducer Size Selection 73

2.10 Piston Transducer Frequency Selection 77

2.11 Simulation Space Study — 80
2.12 Bilateral Stimulation Modelling — 82
2.13 Targeting GPi and STN — 85
2.14 Summary & Discussion — 87

3. Lens Method Validation on Skull Samples **90**
3.1 Transducer Calibration & Characterisation — 91
3.2 PDMS Lens Manufacturing Procedure — 94
3.3 PDMS Fresnel Focusing Lenses — 95
3.4 Skull Sample Segmentation — 99
3.5 Whole Skull Sample Simulations — 101
3.6 Smooth Lens Design — 104
3.7 Target Specific Lenses in Free Field — 106
3.8 Lenses on Whole Skull Sample — 108
3.9 BV Lenses on Whole Skull Sample — 113
3.10 BV Lenses on Half Skull Sample — 120
3.11 Transducer Position Sensitivity — 126
3.12 Measured Focal Peak Location Registration — 131
3.13 Paired Sources Measurement on Skull — 134
3.14 Summary & Discussion — 137

4. Ultrasound Interaction with DBS Electrode **142**
4.1 Electrode Geometry & Material Composition — 143
4.2 Impact on Acoustic Field: Validation — 145
4.3 Impact on Acoustic Field: Position — 148
4.4 Impact on Acoustic Field: Rotation — 151
4.5 Temperature Rise Due to Electrode: Modelling — 153
4.6 Temperature Rise Due to Electrode: Experiment — 158
4.7 Impact on Electrode Measurement in Water — 163
4.8 Impact on Electrode Measurement in Saline — 171
4.9 Impact on Electrode Measurement in Phantoms — 174
4.10 Impact on Electrode Measurement by Angling — 178
4.11 Summary & Discussion — 179

5. Conclusions & Future Work **185**

5.1 Summary & Discussion ——— 186

5.1.1 Feasibility Study of Acoustic Lens in Human Brain Stimulation ——— 186

5.1.2 Validation of PDMS Lens Method on Skull Samples ——— 188

5.1.3 TUS Feasibility on PD Patients with Implanted DBS Electrodes ——— 189

5.2 Future Work ——— 191

Appendix **195**

A. Dual Array Device ——— 196

B. Auditory Findings ——— 205

C. Transducer Coupling in Human Trial ——— 210

References **214**

LIST OF ACRONYMS & SYMBOLS

Acronyms

ABS	Acrylonitrile butadiene styrene
AH	Anterior hippocampus
ARF	Acoustic radiation force
ASM	Angular spectrum method
BD	Burst duration
BDC	Burst duty cycle
BoB	Binary lens acting on binary skull segmentation
BoP	Binary lens acting on porous skull segmentation
BS	Binary smooth lens
BV	Binary voxel lens
CA	Cornu ammonis
CFL	Courant-Friedrichs-Lewy number
CSF	Cerebrospinal fluid
CT	Computed tomography
CW	Continuous wave
DBS	Deep brain stimulation
DC	Duty cycle
DG	Dentate gyrus
EC	Entorhinal cortex
EEG	Electroencephalography
EMG	Electromyography
FDA	Food and drug administration

FFT	Fast Fourier transform
GPi	Internal globus pallidus
HHSS	Half head single source
HU	Hounsfield unit
ISI	Inter stimulus interval
LFP	Local field potential
MI	Mechanical index
MR	Magnetic resonance
MR-ARFI	Magnetic resonance acoustic radiation force imaging
NIBS	Non-invasive brain stimulation
PC	Perirhinal cortex
PDMS	Poly(dimethyl siloxane)
PL	Pulse length
PML	Perfectly matched layer
PMMA	Poly(methyl methacrylate)
PoP	Porous lens acting on porous skull segmentation
PPW	Point per wavelength
PRF	Pulse repetition frequency
PS	Porous smooth lens
PV	Porous voxel lens
PVA	Poly(vinyl alcohol)
PVDF	Polyvinylidene difluoride
PW	Pulsed wave
SPBA	Spatial-peak, burst-averaged
SPPA	Spatial-peak, pulse-averaged

SPTA	Spatial-peak, temporal-averaged
STN	Subthalamic nucleus
SWI	susceptibility-weighted imaging
TI	Thermal index
TUS	Transcranial ultrasound stimulation
US	Ultrasound
WHSS	Whole head single source
WHPS	Whole head paired sources

Symbols

f	Frequency	[Hz]
α	Attenuation, $\alpha = \alpha_0 f^n$	[dB/cm]
α_0	Attenuation coefficient	[dB/(cm·MHz^n)]
I	Intensity	[W/m^2]
c	Speed of sound	[m/s]
ρ	Density	[kg/m^3]
$\vec{v}$	Particle velocity	[m/s]
k	Wave number	[1/m]
s	Entropy	[J/K]
P	Pressure	[Pa]
Q	Volume rate of heat deposition	[W/m^3]
η	Dynamic viscosity	[Pa·s]
T	Temperature	[°C]

1

INTRODUCTION & LITERATURE REVIEW

This chapter introduces transcranial focused ultrasound as a form of non-invasive brain stimulation (NIBS) with potential. The mechanisms, safety, and delivery of transcranial ultrasound are discussed as challenges for its application. This chapter describes the fundamental governing equations for 3D acoustic wave propagation along with their numerical implementation to predict the generated pressure fields. The Pennes bioheat equation is also described, which is used to model the thermal distribution resulting from the acoustic simulation. The theory of acoustic lenses is then described, followed by an introduction to neuromodulation monitoring techniques and the aim of this thesis.

1.1 MOTIVATION

The alteration of nerve activity, or neuromodulation, is an evolving approach with wide-ranging potential applications, including as a technique for studying neural function, replacing impaired neural function, and as a novel form of treatment. Therefore, non-invasive techniques with sufficient spatial resolution are urgently required to broaden the utility of neuromodulation. Although invasive electrical and thermal neuromodulation methods have been in use since the 20th century, their use is restricted to specific applications in the clinical setting. Non-invasive techniques to bypass the skull and target regions with high accuracy and precision are therefore essential.

Focused ultrasound has been demonstrated to be a candidate to meet these criteria with the potential to outperform other existing non-invasive brain stimulation methods (Polanía et al., 2018) such as transcranial electric stimulation (Faria et al., 2012; Nitsche et al., 2008) and transcranial magnetic stimulation (Deng et al., 2013; Walsh and Cowey, 2000) in terms of precision and depth in the human brain. Whereas most methods are usually unable to target-specific regions of the brain due to the diffusive nature of their fields, ultrasound can be focused with a spatial resolution on the order of the wavelength of the driving frequency, i.e., approximately 3 mm at 0.5 MHz (Blackmore et al., 2019).

Transcranial ultrasound stimulation has been shown to improve mood and modulate network connectivity (Sanguinetti et al., 2020). Many primate studies have used transcranial ultrasound stimulation to induce behavioural changes (Bongioanni et al., 2021; Deffieux et al., 2013; Folloni et al., 2019; Fouragnan et al., 2019). The success in primates motivates the use of transcranial ultrasound in similar behavioural modulation studies in humans for neurological

and psychological scientific research (Blackmore et al., 2019; Braun et al., 2020; Butler et al., 2022; Fini and Tyler, 2020a; Fini and Tyler, 2020b; Legon et al., 2020).

Transcranial ultrasound stimulation also has many other potential areas of clinical utility, including: (i) treatment of neuropsychiatric disease (Tsai, 2015); (ii) suppression of epileptic activity (Min et al., 2011); (iii) inducing antinociceptive effects (Badran et al., 2020); and (iv) temporary blockade of peripheral nerves involved in pain signalling (Downs et al., 2018). In general, deep brain stimulation has been effective in clinically treating diseases such as Parkinson's disease, showing favourable outcomes in treating movement tremor. Ultrasound stimulation can also be developed into an effective and non-invasive tool for these applications. Transcranial ultrasound stimulation has even been claimed to awaken individuals from coma states (Monti et al., 2016).

Despite its potential, several aspects of transcranial focused ultrasound must be considered before clinical experimentation: (i) accurate modelling and prediction of the pressure distribution in the head from ultrasound wave propagation; (ii) safety analysis both in terms of pressure and temperature; (iii) monitoring during the experiments to ensure that the ultrasound focus is at the correct location; and (iv) evaluation of possible interference between ultrasound and other treatment modalities, such as electrode-based stimulation.

This project aims to demonstrate the feasibility of deep brain target stimulation in a high precision manner using focused ultrasound. As the desired targets are considerably deeper than in the majority of published work, sources other than single element transducers must be considered.

1.2 MECHANISMS

Most existing non-invasive brain stimulation methods have focused on inducing effects through electrochemical coupling, as described by the Hodgkin-Huxley model (Hodgkin and Huxley, 1952). However, mechanical forces within the brain have also been associated with modulation of cell functions such as proliferation, signalling, and differentiation (Mueller and Tyler, 2014; Tyler, 2012; Wang and Thampatty, 2006). As a non-invasive way of delivering mechanical forces deep into tissue in the form of acoustic pressure waves, focused ultrasound can induce both thermal and mechanical bioeffects, depending on the pulsing regime (ter Haar, 2010).

While the precise mechanism of ultrasound neuromodulation is still unknown, many hypotheses have been developed: (i) activation of mechanosensitive channels (Brohawn, 2015; Morris, 2012); (ii) sonoporation (Antonov et al., 1985; Yang and Kindt, 2015); (iii) generation of capacitive currents due to changes in membrane thickness (Heimburg, 2012), curvature (Petrov, 2002), and conformational state of lipids in membrane (Antonov et al., 1985; Taylor et al., 2017); and (iv) thermal effects (Lee et al., 2005; Thompson et al., 1985).

It is possible that the modulation is a result of a combination of all these above and potentially many others, but the acoustic radiation forces (ARF) were considered to be the most likely mechanism by which modulation occurs (Lovmo et al., 2021; Mihran et al., 1990; Prieto et al., 2018). Acoustic radiation force F_{ARF} is defined for a time-harmonic, progressive, plane wave (Nyborg, 1965) as:

$$F_{ARF} = \frac{2\alpha I}{c_0} \cong \frac{\alpha_0}{\rho_0 c_0^2} f P^2;$$

Where α is tissue attenuation, I is intensity, and c_0 is speed of sound in tissue. For tissue where $\alpha \approx \alpha_0 f$, this can be written as the second approximation term. Where ρ_0 is tissue density, f is frequency of the ultrasound, and P is pressure magnitude.

1.3 HIPPOCAMPUS STUDIES

The hippocampus is a C-shaped structure comprising a head, a body, and a tail (Destrieux et al., 2013). It is considered a memory indexer, important for converting short-term memories into long-term memories (Bailey, 2019). Anatomically, it is subdivided into the dentate gyrus (DG), subiculum (Sub), entorhinal cortex (EC), and cornu ammonis (CA) (Knierim, 2015). Fig. 1.1 shows these substructures. The posterior hippocampus is involved primarily in cognitive functions, and the anterior portion is attributed to stress, emotion, and affect (Fanselow and Dong, 2010; Rocca et al., 2018). The subiculum extending from the cornu ammonis is also part of the hippocampal formation (Duvernoy, 2005).

For deep brain targets such as the hippocampus, surgically implanted electrodes are typically required for electromagnetic-based methods of neuromodulation in a specific volume. While electromagnetic based methods have been developed to achieve non-invasive transcranial stimulation, their low spatial resolution often necessitates treatment of a large portion of the brain. Studies have therefore shifted to alternative methods such as ultrasound for non-invasive stimulation with improved spatial resolution. Lower frequencies (0.25 MHz) and spatial-peak, burst-averaged intensities (I_{SPBA}; 84 mW/cm^2) were found to give more robust electromyography (EMG) responses on the mouse hippocampus (Tufail et al., 2010). In an *in vitro* study on rat hippocampal neurons using an ultrasound frequency of 0.5 MHz, it was discovered that the neurons had the largest firing rate at 0.8 MPa and decreased at higher pressures up to 2 MPa (Choi et al., 2013). The ultrasound pulsing timings used in this study

were: 5 s of burst duration (BD) with a burst interval of 6 s, PL of 0.02 ms, PRF of 10 ~ 100 Hz, and 7 trials each of 5 minutes. The burst duty cycle (BDC) was as low as 0.002 ~ 0.2%. Spatial-peak, pulse-averaged intensity (I_{SPPA}) used was 19.6 ~ 122.4 W/cm^2, and spatial-peak, temporal-averaged intensity (I_{SPTA}) used was 16.1 ~ 92.8 mW/cm^2.

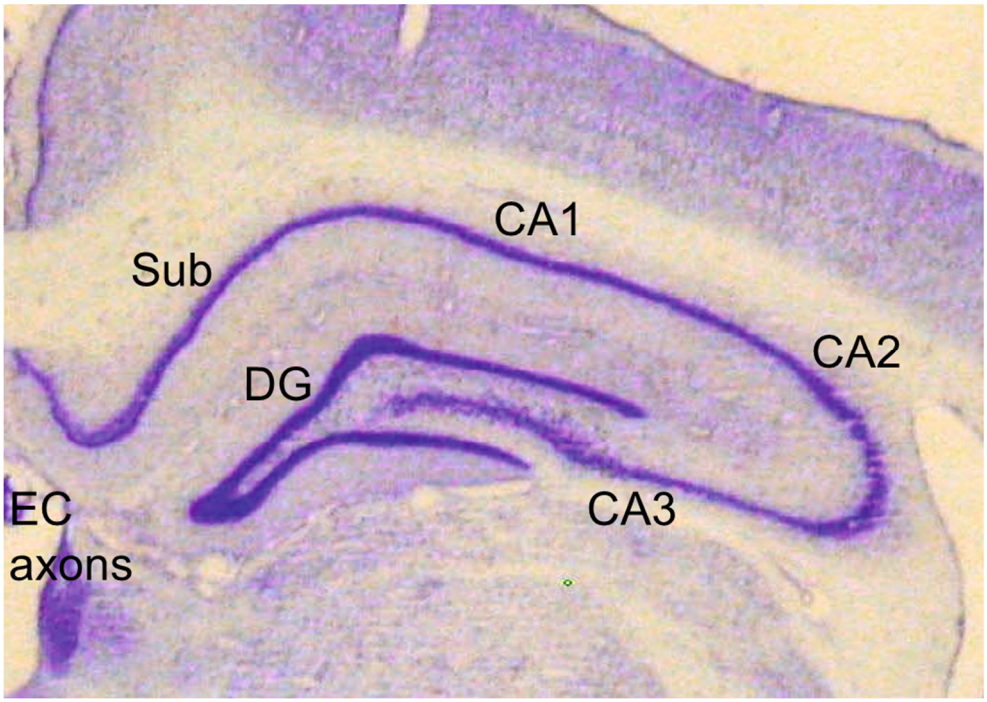

Fig. 1.1: Hippocampus anatomy. Coronal view through the transverse axis of the hippocampus. Image reproduced from Knierim (2015).

Low intensity, low frequency ultrasound was also found to induce action potentials, triggering voltage-gated Na^+ and Ca^{2+} channels, vesicle exocytosis, and synaptic transmission during whole-cell current clamp recordings in CA1 pyramidal neurons (Huang et al., 2019; Qiu et al., 2020; Tyler et al., 2008) *in vitro*. The ultrasound parameters employed were a pressure of 0.31 MPa, a frequency of 0.44 ~ 0.67 MHz, an I_{SPTA} of 0.023 mW/cm^2, and an I_{SPPA} of 2.9 W/cm^2. A study in single hippocampal neurons *in vitro* using ultrasound at 7.75 MHz and pressures between 1.28 and 2.21 MPa suggested that the increase in excitability is mainly achieved due to mechanical effects instead of thermal effects (Khraiche et al., 2008) after negligible temperature increases were observed. However, whether the induced stimulation

would cause excitatory or inhibitory behavioural outcomes depends on the connectivity of neurons at the network level. Indeed, previous *in vitro* studies evaluating rat hippocampal slices using 0.5 MHz ultrasound have shown both enhancement and depression of electrically evoked potentials (Bachtold et al., 1998). 0.75 MHz ultrasound has also been shown to successfully stimulate hippocampal tissue *in vitro* at a pressure of 1.62 MPa (Rinaldi et al., 1991). A first in-human pulsed low intensity focused ultrasound treatment of neurologic disorders was delivered using a device platform targeting the hippocampus (Brinker et al., 2020) showing successful targeting. The frequency of the ultrasound used was 548 kHz with a 500 Hz pulse repetition frequency. The pulsing parameters used were a pulse length of 0.5 s, a duty cycle of 36% to 50%, an inter stimulus interval of 7 s, an I_{SPTA} not exceeding 2.25 W/cm^2, and a free field equivalent peak negative pressure of 0.32 MPa.

1.4 SAFETY

For participant safety, several indices were adopted from the previous safety review conducted on transcranial focused ultrasound (Blackmore et al., 2019; Darmani et al., 2022). These indices include intensity, mechanical index (MI), and thermal index (TI). As these are only in place for diagnostic ultrasound imaging based on short pulse lengths, their relevance to this work is limited and thus will not be discussed in detail.

The thermal index is defined as the ratio between acoustic power, $W_{acoustic}$, and the power required to raise the tissue by 1°C, $W_{+1\,°C}$ (Duck, 2008):

$$TI = \frac{W_{acoustic}}{W_{+1\,°C}};$$

The TI is limited to 6, the maximum temperature in tissue is limited to 43 ℃ for both internal and external use, and the maximum temperature rise in tissue is limited to 10 ℃ for external use and 6 ℃ for internal use (Duck, 2007). The British Medical Ultrasound Society has a tighter restriction by limiting the thermal index to TI ≤ 0.7 for unlimited time or TI ≤ 3 if less than 1 minute (Safety Group of the British Medical Ultrasound Society, 2010). In the context of non-invasive neuromodulation, MR thermometry did not detect any temperature changes for frequencies between 220 kHz and 1.145 MHz up to a pressure of 1 MPa (Dallapiazza et al., 2018). To ensure the safety of the healthy human participants in the study, thermal simulations are performed. The predicted temperature rise is limited to within 1 °C anywhere in brain tissues, including the cerebrospinal fluid (CSF). The predicted temperature rise anywhere in the skull bone tissue is limited to within 3 °C. With simulated values within these parameters, both the TI and maximum temperature in humans are expected to be within the safety limit.

To assess the safety of therapeutic transcranial ultrasound beyond the thresholds used for short-pulse imaging, MR imaging in previous studies was used. Using ultrasound parameters discussed previously by Blackmore et al., 2019, post-sonication susceptibility-weighted imaging (SWI) on humans showed no clear signs of oedema or damage in the target site and surrounding brain tissue (Blackmore, 2018). Similar SWI results were observed in primates (Munoz et al., 2022), showing no obvious trauma, although only at I_{SPTA} = 156.7 mW/cm^2. When examining histology from treated human brain tissue following I_{SPTA} = 720 mW/cm^2 transcranial ultrasound, no tissue damage, apoptosis, or acute neuronal injury could be observed (Stern et al., 2021).

Based on previously explored acoustic properties for transcranial ultrasound, acoustic pressures and frequencies are expected to be smaller than 1.2 MPa and 1.2 MHz, respectively,

well within the range of safety assessed in previous studies (Blackmore et al., 2019). At these pressures and frequencies, the likelihood of endogenous cavitation is considered to be very low (Church et al., 2015; Gateau et al., 2011; Lee et al., 2016a). For transmission, low frequencies (200 ~ 500 kHz) are needed to avoid the high attenuation in the skull and other non-osseous tissue for delivery to deep-seated targets. Lower frequencies can also have the benefit of reduced aberration, but at the cost of larger focal volumes, reduced acoustic radiation force, and an increased risk of standing waves. At a frequency of 500 kHz, modulation of neural functions has previously been shown in both animals (King et al., 2013; Tufail et al., 2010) and humans (Butler et al., 2022; Legon et al., 2014; Legon et al., 2018a; Legon et al., 2018b). A qualitative safety study has also shown that 500 kHz ultrasound with various experimental protocols and energy levels results in similar side effect profiles to electromagnetic-based methods of neuromodulation (Legon et al., 2020). However, one reason to use the lower end of the feasible frequency range would be studies suggesting the possibility of higher thresholds for neuromodulation at higher frequencies in animal models (King et al., 2013; Tufail et al., 2010). Therefore, the ultrasound frequency to be used in this study's human experiments will be chosen from the range of 200 ~ 500 kHz.

The lower limit of the inter stimulus interval and the maximum number of trials (defined here as a burst duration with ultrasound stimulation and an inter stimulus interval without ultrasound input) for a target site are constrained based on the results of an ovine study (Lee et al., 2016b). The study showed that highly repetitive stimulation with a shorter inter stimulus interval could potentially lead to microhaemorrhages. The maximum intensity is based on the highest safe in situ intensity previously used in humans (Lee et al., 2016a). Although in that study the ultrasound frequency was 270 kHz, corresponding to a higher likelihood of cavitation at equal pressure, this nonetheless provides a safe upper limit.

For the single element focused transducer, the f-number is the ratio of the radius of curvature to the aperture size (source diameter). In the case of a single element transducer, an f-number of 1, i.e., radius of curvature equals aperture size, was found to be more suitable for applications in the human brain compared with lower or larger f-numbers within the subset tested (Pouliopoulos et al., 2020). Therefore, with increased target depth, larger sources should be used in anticipation of better performance. In the same study, the frequency used was 0.25 MHz, allowing for lower attenuation and aberration.

In summary, the existing literature for ultrasound stimulation of the central nervous system indicates that 200 ~ 500 kHz ultrasound delivered as 300 ~ 500 ms bursts consisting of 0.5 ms pulses at a pulse repetition frequency of around 1 kHz with pressure magnitudes in the range of 0.1 ~ 0.6 MPa in the brain and a total stimulation duration (including inter stimulus intervals) of less than 10 minutes are considered safe and effective parameters.

1.5 ULTRASOUND PULSING SEQUENCE

The three layers of the ultrasound pulsing sequence are shown in Fig. 1.2 (Blackmore et al., 2019). The first one in (a) is the outer level, representing the overall duration of ultrasound neuromodulation in one subject in the experiment. This total duration is made up of multiple trials. Each trial consists of a burst duration with ultrasound stimulation and an inter stimulus interval without ultrasound input. This is shown in the middle layer in Fig. 1.2 (b), denoted as the burst level. The settings of inter stimulus interval ensure that the safety limit on I_{SPTA} is not exceeded. The inner layer in (c) describes the pulse level. This level provides the detailed pulsing sequence inside each burst where ultrasound is present. Each burst is then characterised by the pulse length, pulse repetition frequency, and burst duty cycle.

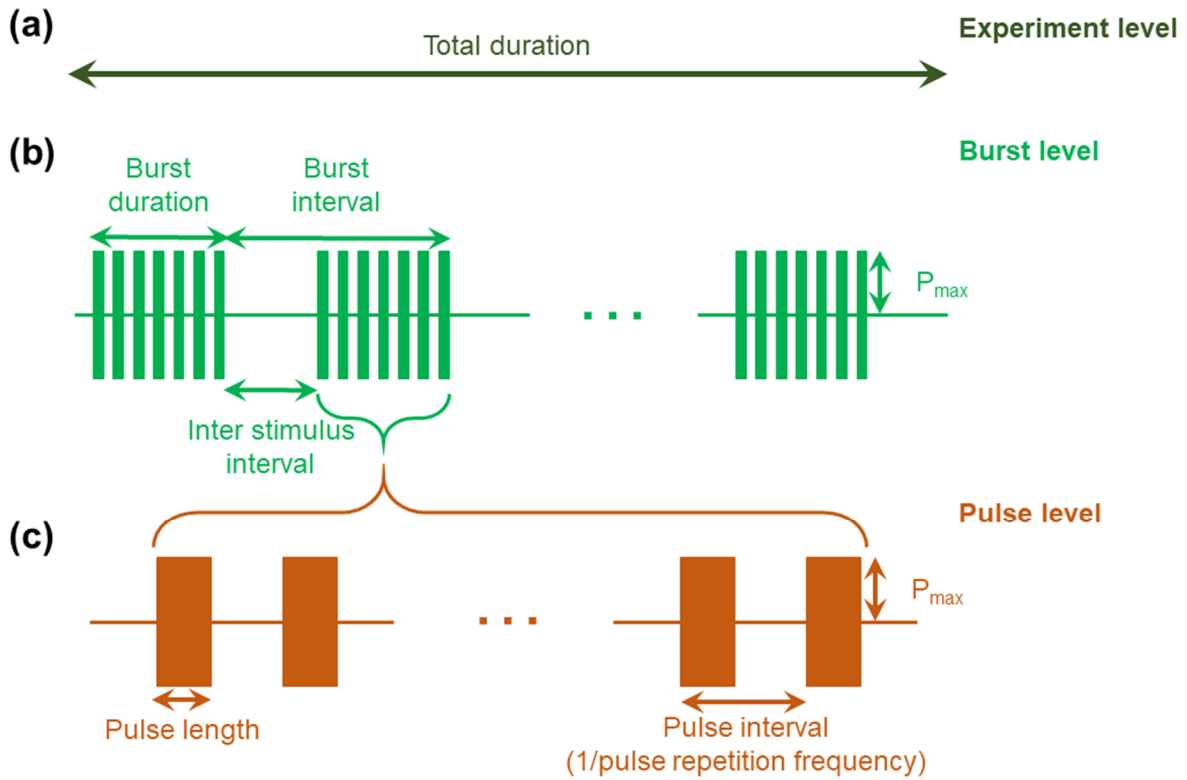

Fig. 1.2: Ultrasound pulsing sequence demonstration. The pulsing sequence in time can be separated into three layers. **(a)** The total duration of the experiment level. **(b)** The details of the sequence in the burst level. Bursts are separated by inter stimulus interval, ensuring the I_{SPTA} is below the FDA limit of 720 mW/cm^2. **(c)** Inside each burst, the details in pulse level are described by the pulse length, pulse repetition frequency, and burst duty cycle.

A burst duty cycle of 50% and a pulse repetition frequency of 1 kHz have been shown to effectively neuromodulate both at the neuronal level (Kubanek et al., 2018) in animals and in humans (Brinker et al., 2020), providing a good starting point for designing the pulsing sequence. As an example, the pulse length can be set to 0.5 ms. The burst duration can be set to 300 ms. The maximum pressure induced by ultrasound in cerebrospinal fluid and brain tissues is limited to 0.6 MPa or less. With these descriptions at pulse level inside a burst, the minimum of the inter stimulus interval is limited to 2.4 s to reduce the I_{SPTA} below 720 mW/cm^2. As a result, the minimum burst interval in Fig. 1.2 is 2.7 s. Finally, the maximum number of trials for each target site in the human head is limited to 250.

Specific ultrasound neuromodulation parameters such as burst duration and burst duty cycle can perform better than other parameters on the induced modulatory effects (Liao et al., 2021; Wang et al., 2020; Yoon et al., 2019). The details of the pulsing sequence are selected for each specific trial to optimise the modulation effect on a specific target in the brain. With the known pulsing sequence, thermal simulations can be used to predict the temperature rise during the stimulation period. This modelling process checks that the set maximum temperature rise in various tissues is not exceeded (1 °C in brain tissues and 3 °C in the skull). Tissue-mimicking thermochromic phantoms and fluorescent proteins (Dhar et al., 2011; Guo et al., 2012; Mikhail et al., 2016; Wu et al., 2009) are unlikely to be sensitive enough for the low temperature rise anticipated.

1.6 Human Head Tissues

Acoustic material properties must be well defined for the simulations to produce accurate results. However, this is challenging as there are large variations in values, especially for the skull. Sound speed has been shown to be the most influential acoustic property and must be defined with less than 4% error to obtain acceptable accuracy in the simulated focus pressure, position, and volume (Robertson et al., 2017). The material properties used for the ultrasound stimulations are stated in Table 1.1. For reference, the hippocampus has a density of 1044.5 kg/m^3 (Hasgall et al., 2018) and a speed of sound of 1562 m/s (Duck, 1990), which are close to the values for white matter.

Using T1-weighted MRI imaging, the different tissue types involved in the pathway for ultrasound neuromodulation can be segmented out using the MARS (Morphologically and Anatomically accuRate Segmentation) MATLAB toolbox (Huang and Parra, 2015). This is a

segmentation tool that can separate the head tissues into six homogeneous types given in Table 1.1.

		Acoustic		Thermal	
Material	Density ρ_0 [kg/m^3]	Speed of Sound c_0 [m/s]	Attenuation α [dB/cm]	Thermal Conductivity κ [W/(m K)]	Specific Heat Capacity C_p [J/(kg K)]
Water[1]	1000	1488	0	0.6	4178
Scalp[1,2,3,4]	1000	1500	0.15	0.528	3600
Skull[1,5]	1732	2820	3.28	0.32	1313
CSF[1,6,7]	1007	1504.5	0.004	0.57	4096
Grey Matter[1,4]	1045	1500	0.05	0.55	3696
White Matter[1, 4]	1041	1552.5	0.29	0.48	3583

Table 1.1: Acoustic and thermal properties of different tissues involved in the pathway for ultrasound neuromodulation. The values shown are the compressional properties. Attenuations are calculated for a frequency of 500 kHz using the corresponding power law $\alpha = \alpha_0 \cdot f^n$. [1]Hasgall et al. (2018), [2]Duck (2007), [3]Constans et al. (2018), [4]Barber et al. (1970), [5]Treeby and Cox (2014), [6]Goss et al. (1978), [7]Ortega et al. (2010).

Hair-induced losses of acoustic signal have been reported to be 17% at 710 kHz, although this type of attenuation becomes negligible at 220 kHz (Eames et al., 2014). In practice, experiments can be performed with the hair in the ultrasound pathway shaved off, both to mitigate the hair-induced attenuation and to reduce the likelihood of air cavities held within the air.

Anatomically, the scalp is made up of five layers. These are: the skin, the superficial fascia, the galea aponeurotica, the subaponeurotic areolar connective tissue, and the periosteum (Seidenberg and Beutler, 2008). As the MARS segmentation is a binary method, it is unable to distinguish these substructures from MRI images. However, as these tissues possess comparable acoustic properties (Barber et al., 1970), their impact on the simulations is likely low.

The attenuation values shown are calculated at a frequency of 500 kHz based on the corresponding power law relationship $\alpha = \alpha_0 \cdot f^n$. For example, the attenuation α [dB/cm] for the skull is $8.83f^{1.43}$ (frequency in MHz) for compressional waves and $19.5f^{1.43}$ (frequency in MHz) for shear waves (Treeby and Cox, 2014). The one for compressional waves is used here as the simulations in this study assume the skull to effectively be a fluid, neglecting the impact of shear waves. Compared to typical values of 0.3 dB/(cm MHz) for soft tissue in general (Szabo, 2004), the skull possesses an attenuation value that is more than an order of magnitude larger.

Computed tomography (CT) has the advantage of reporting the Hounsfield values at each voxel. The Hounsfield unit (HU) is defined as (Schneider et al., 1996):

$$HU = 1000\frac{\mu_x - \mu_{water}}{\mu_{water}};$$

Where μ is the radiotherapeutic attenuation coefficient that can be related to local density from which local acoustic properties can be estimated in the skull. Therefore, the skull inside simulation space can be represented as inhomogeneous tissue, showing the porous structure in cases where CT data are available. With the CT data, the skull can be treated as a composition of skull and water, assuming a linear mixture rule based on the porosity parameter at the voxel (Aubry et al., 2003; Rho et al., 1995). Due to porosity in the skull, the range of attenuation is defined by $\alpha_{0,min}$ = 0.72 dB/(cm·MHz^n) and $\alpha_{0,max}$ = 12.16 dB/(cm·MHz^n) where n = 1.16 from the power law skull bone attenuation fits from White et al. (2006) as detailed in Treeby and Cox (2014). For the lower limit, the density and the speed of sound are taken as the values of water in Table 1.1. This represents full porosity, consisting of only water. For the upper limit, the density and speed of sound take the values for cortical bone as $\rho_{max} = 1900$ kg/m^3 and

c_{max} = 3100 m/s, representing the skull without any porosity. Everything within the range represents the different extents of porosity variation in the skull. The skull acoustic properties in Table 1.1 are the average measurements representing the skull as a whole in the literature (Hasgall et al., 2018, Treeby and Cox, 2014).

1.7 TRANSCRANIAL ULTRASOUND CHALLENGES

Transcranial ultrasound stimulation requires the delivery of ultrasound through the skull, which is a significant acoustic barrier. The skull has a high density and speed of sound relative to soft tissue. In addition, it has variations in geometry and thickness as well as being a heterogeneous structure with multiple layers consisting of hard outer cortical shells and a blood- and fat-filled inner cancellous bone layer. The skull therefore possesses a significant impedance mismatch with respect to the surrounding soft tissues. But due to its complexity, acoustic propagation is hard to model exactly.

The cancellous bone, as a poroelastic medium, would also have two compressional waves: a fast wave where the solid and fluid move in phase with each other, and a slow wave where the solid and fluid move out of phase with each other. However, this additional condition of fast and slow waves has previously been shown to be almost unidentifiable in the time domain with only small differences in wave speeds when at perpendicular incidence (Hoffman et al., 2012; Hosokawa et al., 1998), which is the geometry relevant here as transducers will be placed on the temporal bone window on the human skull. The trabecular structure of this internal layer also results in strong scattering of the acoustic wave at frequencies above 1 MHz, effectively making the skull a low-pass frequency filter and thereby limiting the viable frequency range for transcranial ultrasound propagation (Pinton et al., 2010). Hence, besides the safety aspect,

the limit of frequency being lower than 1.2 MHz in Blackmore et al. (2019) is also a specific delivery requirement for transcranial ultrasound stimulation.

Challenges to high-resolution transcranial ultrasound imaging in humans have been caused by imaging degradation effects from aberration and reverberation. Studies of potential solutions were conducted on a human skull phantom (Soulioti et al., 2020). Transcranial ultrasound stimulation also faces the challenges of aberration and reverberation for accurate targeting and increasing the spatial precision of neuromodulation. Despite these intracranial effects causing high pressure magnitude spots, nonlinear acoustic simulations resulted in virtually identical intracranial pressure maps with linear acoustic simulations. Previous work conducting k-Wave transcranial simulations in humans has found the difference between linear and non-linear simulations to be less than 1%, as the pressure magnitude in neuromodulation is relatively low (Mueller et al., 2017).

The variation in skull thickness is also a challenge, as it results in wave front aberration that shifts the focusing site inside the brain (Fry and Barger, 1978; White et al., 1978). To overcome the delivery challenge through head tissue and focus accurately at the target site, a time reversal approach is used to correct for attenuation and aberration.

Time reversal methods allow for aberration correction using phase and amplitude compensation based on the information from back propagation simulations (Fink et al., 2003). In order to correct distortions or focus the wave at specific points, the time reversal method directly reverses the propagation direction of waves, whereas phase conjugation flips the phase of the wave. The second-order time derivative in the lossless wave equation has the reciprocal properties that make this method possible (see Section 1.8). Consequently, if a pressure field

propagating in the forward direction is a solution, then a pressure field reversed in time is also a solution. This temporally reversed solution is called ‘back propagation’. It is worth noting that frequency-dependent attenuation in tissue breaks the invariant nature of time reversal. But through the use of techniques such as amplitude compensation, the approach can still be applied to yield successful results (Tanter et al., 1998; Thomas and Fink, 1996). Arrays made out of ultrasound transducer elements sending out waves with required phases based on the information from back propagation can be a potential source to pinpoint target sites deep down inside the brain with high spatial precision for specific regions in the central nervous system (Pernot et al., 2003; Rosnitskiy et al., 2019). Based on the information from back propagation analysis, an acoustic lens possessing variable thickness can also be used to adjust the phase of the propagating wave based on the speed of sound inside the lens material to create constructive superposition at the desired site (Jang and Chang, 2016; Jiménez-Gambín et al., 2019; Maimbourg et al., 2018; Ferri et al., 2019). Since aberration correction through the use of lenses and array devices can be developed into a powerful tool for precise stimulation, both methods are considered in this study.

An available array device was analysed for its practicality for deep brain target stimulation. The analytical results of a baffled planar piston (Harris, 1981a; Harris, 1981b) can represent each of the elements in an array. Hence, a fast way to get the resulting ultrasound field, for both pressure magnitude and phase, of the array device is possible through the superposition of the analytical fields of each element in free field (ignoring the skull). This is compared to the results of simulations using the array arrangement and presented in Appendix A.

Acoustic lenses are attractive. Although a new lens is needed for every different target, they are still far less expensive than arrays. Furthermore, many studies that have access to array

devices only apply different phases to the elements for focusing and aberration correction, whereas the magnitude is commonly the same across all the elements (Rosnitskiy et al., 2019). This is effectively using the array as an ideal lens, where the acoustic loss through the imaginary lens material is zero.

The time reversal method can be performed in computational simulations to determine the required corrections for focusing at the target site. The simulation uses a virtual point source at the target site that propagates outward spherically in three-dimensional space using the tissue geometry from segmented imaging. To verify the reliability of the findings from back propagation simulations, *ex vivo* human skull samples are used in the validating experiments (Brinker et al., 2019; Sugino et al., 2021). In one study, a virtual point source at the target is propagating through the skull using a three-dimensional finite difference solver for the linear wave equation (Marquet et al., 2009). The waveforms outside the skull were simulated and used as the time reversal field for emitting back into the skull using an actual array with 300 elements. 90% of the pressure achieved by the implanted hydrophone was reached by the array non-invasively, and the position error was less than 0.7 mm. A study using non-invasive magnetic resonance thermometry was able to verify in a cadaver model that the accuracy of time reversal focusing was within a few millimetres (Chauvet et al., 2013). In terms of simpler and less computationally intensive methods other than solving the full wave equation, one study compared the results of four aberration correction methods, from semi-analytical ones to fully simulation-based ones (Kyriakou et al., 2015). The analysis suggested simulation-based methods generated tighter focal spots than analytical approaches. For specific applications such as neuromodulation, the largest numerical errors in time reversal simulations are likely due to the uncertainties in materials' acoustic properties based on the literature values (Robertson et al., 2017).

During the ultrasound stimulation, studies have shown the potential to directly activate the auditory cortex and higher order processes via ultrasound (Guo et al., 2018; Sato et al., 2018; Braun et al., 2020; Blackmore, 2018; Johnstone et al., 2021). Therefore, careful attention to sham and controlling measures must also be paid while designing the details and performing the trials so that the behavioural and electrophysiologic outcomes are genuine results of stimulation of the intended target sites in the human brain rather than additional auditory activations.

In summary, in order to deliver ultrasound to the brain, computational modelling is the most feasible technique to determine the source conditions. Ideally, a physical source should be placed directly in the brain tissue, but this is invasive and not applicable to healthy volunteers. Magnetic resonance acoustic radiation force imaging (MR-ARFI) is unlikely to work as the pressure amplitudes used in neuromodulation are too small for tissue displacement to be picked up. In terms of ultrasound sources, it is likely that lens or array methods are essential for targeting deep brain targets such as the hippocampus for improved precision of targeting. However, previous simulations done for rodents (Constans et al., 2017), rabbits (Yoo et al., 2011), primates (Constans et al., 2017), and human skull samples (Mueller et al., 2017; Robertson et al., 2017) have shown the practicality of simple sources in the form of a single element focused transducer for targeted brain neuromodulation. These analyses suggest a simple and inevitably more robust experimental source option for transcranial ultrasound stimulation. However, in the long run, the field requires even higher levels of spatial precision and control. The development of the field will be in the direction of lens or array approaches.

1.8 LINEAR ACOUSTIC THEORY

This section is a brief introduction to the underlying acoustic principles that are employed by the numerical solver (Blackstock, 2000; Hill et al., 2004; Pierce, 1990). When an ultrasound wave passes through a medium, it is assumed to affect the medium by inducing small perturbations in the field variables: density ρ, particle velocity $\vec{\boldsymbol{v}}$ and pressure P. In the assumption of a homogeneous medium at rest, using subscript 0 to represent the unperturbed properties of the medium, the values of ambient density and pressure are ρ_0 and P_0, respectively. Therefore, with the sound wave presenting in the medium, each of these variables can be written as a summation of the in rest, unperturbed quantity, and the perturbed acoustic quantity, denoted by a superscript ~. The changes in these three variables are expressed in equations using the small perturbations as:

$$\rho(\vec{\boldsymbol{x}}, t) = \rho_0 + \tilde{\rho}(\vec{\boldsymbol{x}}, t);$$

$$\vec{\boldsymbol{v}}(\vec{\boldsymbol{x}}, t) = \tilde{\vec{\boldsymbol{v}}}(\vec{\boldsymbol{x}}, t);$$

$$P(\vec{\boldsymbol{x}}, t) = P_0 + \tilde{P}(\vec{\boldsymbol{x}}, t);$$

Where $\vec{\boldsymbol{x}}$ is the location vector and t is time. For the medium at rest, there is no $\vec{\boldsymbol{v}}_{\boldsymbol{0}}$ term. The continuity equation is defined as:

$$\frac{\partial \rho}{\partial t} = -\nabla \cdot (\rho \vec{\boldsymbol{v}});$$

Substituting the equations above for varying medium density and particle velocity into this continuity equation and then ignoring the second-order terms gives the linearised continuity equation:

$$\frac{\partial \tilde{\rho}}{\partial t} = -\rho_0 \nabla \cdot \tilde{\vec{v}};$$

The Euler equation, describing the conservation of momentum in an inviscid fluid, is defined as:

$$\frac{\partial \vec{v}}{\partial t} + (\vec{v} \cdot \nabla)\vec{v} = -\frac{\nabla P}{\rho};$$

Substituting in the corresponding small perturbation forms and then neglecting the second-order terms, the Euler equation reduces to:

$$\frac{\partial \tilde{\vec{v}}}{\partial t} = -\frac{1}{\rho_0} \nabla \tilde{P};$$

There are three unknowns $\tilde{\rho}$, $\tilde{\vec{v}}$ and $\tilde{P}$ and only two equations. Therefore, a third equation is needed to solve these variables. The equation of state can be used to express any state variable as a function of any other two state variables. Therefore, in order to eliminate one of the unknowns, pressure can become a function of density and entropy, which is denoted as s, such that $P = P(\rho, s)$. Slight changes in pressure can be related to small changes in density and entropy. To leading order, this relationship is defined as:

$$\delta P = \left(\frac{\partial P}{\partial \rho}\right)_0 \delta\rho + \left(\frac{\partial P}{\partial s}\right)_0 \delta s;$$

Assuming the motion induced by the ultrasound wave is lossless and adiabatic, then $\delta s = 0$ and the linearised equation of state is reduced to:

$$\tilde{P} = {c_0}^2 \cdot \tilde{\rho};$$

Where the speed of sound in the fluid is defined as $c_0 = \sqrt{\left.\frac{\partial P}{\partial \rho}\right|_0}$. In order to derive the linearised continuity equation, it was assumed that $|\tilde{\rho}| \ll \rho_0$. Substituting this into the equation of state above, the magnitude of the pressure perturbation is $|\tilde{P}| \ll \rho_0 {c_0}^2$. In order to get the second-order lossless wave equation, the derivative in time of the linearised continuity equation is combined with the divergence of the linearised Euler equation. In addition, the linearised equation of state is used to eliminate density. The second-order lossless wave equation can then be obtained:

$$\nabla^2 P - \frac{1}{{c_0}^2}\frac{\partial^2 P}{\partial t^2} = 0;$$

In the wave equation, the acoustically perturbed pressure $\tilde{P}$ has been redefined as P. The assumption of being lossless for this wave equation can be dropped by incorporating the losses of thermoviscous fluids. However, for the body tissues for which the loss mechanisms are not fully understood, empirical loss behaviour can be added, when necessary, to the numerical modelling.

1.9 NUMERICAL IMPLEMENTATION

The analytical solutions provide the resulting ultrasound fields in a homogeneous medium from several typical ultrasound sources, such as an ideal bowl transducer for focusing at a certain depth (O'Neil, 1949; Chen et al., 1993) and an ideal piston of various cross-sectional sizes (Hutchins et al., 1986; Liauh and Lin, 1999). For more complicated inhomogeneous media that have spatially varying acoustic properties, the resulting wave propagation fields must be solved by numerical methods.

There exist a range of numerical methods that can be used for acoustic wave propagation modelling, such as boundary element, finite difference, finite element, finite volume, and particle based. As an example, the finite difference time-domain method allows for multi-resolution simulations using interaction equations to interconnect the grids of different resolutions (Kaufman et al., 2008; Taflove and Hagness, 2005; Top et al., 2016). Multi-resolution grids consisting of 0.5 mm and 1.0 mm resolutions would then speed up the simulation to an extent that it has a speed compatible with semi-real-time user feedback (within 30 s) with acceptable accuracy of under 3 mm in terms of focal position and dimension and less than 5% difference in peak pressure ratio (Yoon et al., 2018). Simulation can also be performed faster by using a lower frequency and an increased spatial grid size. In such a study, the faster simulations performed at 450 kHz can restore up to 85% of the optimal pressure at 900 kHz (Maimbourg et al., 2020a).

For this study, the open-source k-Wave MATLAB toolbox (Treeby and Cox, 2010) was selected due to its requirement for fewer points per wavelength (Tabei et al., 2002), down to only 2.56 grid points per wavelength for precise focusing (Jing et al., 2012), thus reducing the

memory requirements and computation cost for simulations. This section briefly outlines the numerical implementation of the fundamental equations.

The k-Wave solver is an open-source and MATLAB-based toolbox for simulating acoustic wave propagation in 1 to 3 dimensions (Treeby et al., 2018). Source terms and attenuation terms are implemented into the fluid solver using modified versions of the fundamental equations outlined previously. Nonlinearity can also be included as required. For an inhomogeneous medium with source terms and attenuation, the set of equations in the fluid solver are continuity:

$$\frac{\partial \rho}{\partial t} = -\rho_0 \nabla \cdot \vec{\boldsymbol{v}} - \vec{\boldsymbol{v}} \nabla \cdot \rho_0 + S_M;$$

Where S_M is mass source, conservation of momentum:

$$\frac{\partial \vec{\boldsymbol{v}}}{\partial t} = -\frac{1}{\rho_0} \nabla P + \vec{\boldsymbol{S}}_{\boldsymbol{F}};$$

Where $\vec{\boldsymbol{S}}_{\boldsymbol{F}}$ is force source, and the equation of state:

$$P = {c_0}^2 \left(\rho + \vec{\boldsymbol{d}} \cdot \nabla \rho_0 - L\rho\right);$$

Where $\vec{\boldsymbol{d}}$ is the acoustic particle displacement and L is a fractional Laplacian operator for accommodating the attenuation and dispersion. The other symbols in the above equations possess the same usual meanings as those in the fundamental equations.

Acoustic sources can be added to the k-Wave system as either a force source $\vec{\boldsymbol{S}}_{\boldsymbol{F}}$ or a mass source S_M. The mass source S_M is input of mass per unit volume and corresponds to a free space pressure source such that it acts as a monopole. The force source $\vec{\boldsymbol{S}}_{\boldsymbol{F}}$ is a body force per unit mass and corresponds to a free space velocity source such that it acts as a dipole.

Biological tissues have acoustic attenuation coefficients that can be well modelled by the power law relationship to the ultrasound frequency as:

$$\alpha = \alpha_0 f^n;$$

Where α represents the tissue acoustic attenuation coefficient in the unit of dB/cm, α_0 is a constant representing the attenuation coefficient in the unit of dB/cm MHz^n, f is the ultrasound frequency in MHz and n is the power exponent of the frequency. This power exponent n is typically close to 1 (Duck, 1990). A fractional Laplacian operator L is used to implement this power law dependence into the k-Wave system, which captures both the attenuation and dispersion. Due to the specific formulation used in the k-Wave toolbox, the valid values of the power exponent n is limited to $0 < n < 3, n \neq 1$ (Treeby and Cox, 2014).

A k-space corrected pseudospectral technique (Tabei et al., 2002) is used to discretise and calculate the numerical solutions for the set of equations in the k-Wave solver. This technique couples the calculation of the spatial gradients in the spectral domain with a finite difference procedure in the time domain. A conventional finite difference method estimates the gradient by fitting a polynomial of certain order to the surrounding nodes, from which the derivative is calculated. This is called the local approximation. To increase the accuracy of the approximation, either the order of the polynomial used or the number of nodes fitted needs to

be increased. In the pseudospectral method, instead of using a fixed order polynomial fitting to a fixed number of local points, a Fourier series is fitted to all the data in the given dimension. This is effectively taking the finite difference method to the limit and is thus a global method in contrast to the local approximation. By using the Fourier series, the elemental function is now sinusoidal. This means that, in theory, each wavelength can be represented with only two points. This is a significant spatial resolution relaxation compared to the finite difference method, which requires more than ten points per wavelength.

To ensure stability, constraints on the timestep size are needed to control the numerical errors added to the solution due to the finite difference approximations. The von Neumann stability criteria are used to determine the relationship between timestep and grid size. The k-space techniques come into place, correcting the dispersion error, which in turn relaxes this requirement so that bigger timesteps can be used. Increased stability for inhomogeneous media is also demonstrated, despite the fact that this modification should be strictly for homogeneous media only (Cox et al., 2007; Treeby and Cox, 2010).

The Courant-Friedrichs-Lewy (CFL) number is typically used to ensure stability and convergence of wave propagation algorithms. It is defined as the distance a wave can travel in one timestep:

$$CFL = c_0 \frac{\Delta t}{\Delta x};$$

Where c_0 is the speed of sound, Δt is the timestep, i.e., the temporal resolution of the numerical scheme, and Δx is the grid size, i.e., the spatial resolution of the simulating space. The CFL number is set to 0.3 by default for the k-Wave solver for stability in 3D. This value is used to

balance the solution's accuracy and the computation cost. This value is proven to be the appropriate choice both in the k-Wave toolbox manual and literature (Treeby and Cox, 2010; Treeby and Cox, 2011; Treeby et al., 2012). A few simple simulation cases were also tested to validate it. Therefore, for all fluid-based simulations used in this study, the timestep and grid size are chosen such that the CFL number is smaller than or equal to 0.3 for a fixed spatial resolution. As the spatial resolution is determined before the timestep, the timestep has to be chosen to be small enough to meet the stability requirement. For an inhomogeneous medium possessing different speeds of sound, the rule is to choose a small enough timestep such that the CFL number of the maximum speed of sound is still smaller than or equal to 0.3.

As a result, this k-space corrected pseudospectral solver uses fewer grid points to generate solutions with higher accuracy compared to the other numerical solvers. This is beneficial for large-scale three-dimensional simulations because the computation time and memory usage are reduced and limited to a generally acceptable range.

Since the fast Fourier transform (FFT) is used in the numerical solver, the field by definition must be periodic, which effectively gives multiple mirror sources in the domain. These artificial sources give rise to additional waves propagating into the simulation domain, distorting the field. The simulation space can be enlarged to mitigate this effect. But the space has to be expanded substantially so that this artificial effect is negligible. This defeats the desire to reduce the computational cost. Therefore, a special boundary called the 'perfectly matched layer' (PML) is added around the entire simulation domain and acts as an absorber with significant attenuation to the waves entering the simulation domain from this boundary. The default thickness of the PML in k-Wave is 10 grid points. At this thickness, the attenuation to the transmitted wave, i.e., the waves from the mirror sources, due to the periodicity of the fast

Fourier transform, is 84 dB, and the attenuation to the reflected wave is 65 dB. All the simulations conducted in this study use a perfectly matched layer of 10 grid points or larger. The perfectly matched layer's size was chosen such that the overall grid dimension yields a small prime factor, ideally as small as 2, minimising the computational cost. As the model makes heavy use of the fast Fourier transform, which is fastest for grid dimensions that are powers of two or have small prime factors (Wang et al., 2012).

1.10 ACOUSTIC HOLOGRAPHY

Acoustic holography is a method in which the measurement in a plane can be used to characterise the ultrasound sources (Sapozhnikov et al., 2003; Sapozhnikov et al., 2006; Zeng and McGough, 2008). This can be particularly helpful for representing certain sources used in a study, making the simulation results closer to reality in terms of the source conditions (Wang et al., 2012; Maynard et al., 1985). Backward propagation can thus derive the source plane from a measurable plane in front of the source. The assumption of level surfaces can be confirmed to be true by measurements taken in a plane parallel to the source.

Using acoustic holography by Rayleigh integral, the backward propagation is calculated by (Sapozhnikov et al., 2015):

$$P(\boldsymbol{r}_2) = \frac{1}{2\pi}\int_{\sum_1} P(\boldsymbol{r}_1)\frac{\partial}{\partial n_1}\left(\frac{e^{-ikR}}{R}\right)d\sum_1;$$

P is the complex pressure magnitude $P = A_p e^{i\phi_p}$ where A_p is the amplitude and the ϕ_p is the phase delay. $\boldsymbol{r}_1$ and $\boldsymbol{r}_2$ are position vectors of points in each plane $\sum$. Subscript 1 means the measurement or observation plane and subscript 2 means the plane to be determined by the

algorithm. $\partial/\partial n_1$ is the normal derivative ($\partial/\partial n_1 = \boldsymbol{n}_1 \cdot \nabla$), where $\boldsymbol{n}_1$ is the outward facing unit normal of the plane, k is wave number ($k = \frac{\omega}{c_0} = \frac{2\pi}{\lambda}$). $R = |\boldsymbol{r}_2 - \boldsymbol{r}_1|$.

The expression can be expressed for a discrete system, which is more useful in practise (Sapozhnikov et al., 2015):

$$P(x,y,z) \approx \frac{1}{2\pi} \sum_{u=-\infty}^{\infty} \sum_{v=-\infty}^{\infty} h^2 P_{uv} \frac{\partial}{\partial n} \left(\frac{e^{-ik|\boldsymbol{r}-\boldsymbol{r}_{uv}|}}{|\boldsymbol{r}-\boldsymbol{r}_{uv}|} \right);$$

h is step size, which is the spatial resolution in simulations or measurements, $P_{uv} = P(uh, vh, z_h)$ and $\boldsymbol{r}_{uv} = (uh, vh, z_h)$. z is defined as the wave propagation direction that is orthogonal to the source plane.

1.11 THERMAL MODELLING

The absorption of ultrasound in the body results in the deposition of heat into tissue. As a consequence, the temperature rise associated with it needs to be studied through thermal modelling to ensure the temperature rise is within the safety requirements. The thermal modelling is conducted on a case-by-case basis after the acoustic simulations have determined the pressure fields in the head. Particular attention is paid to the maximum elevation of temperature in the skull and brain tissues.

The temperature changes are modelled using the Pennes bioheat transfer equation (Pennes, 1948). This is a modified version of the heat diffusion equation, taking into account the heat deposition and the losses due to blood perfusion. It is stated below as:

$$\rho_t C_{p,t} \frac{\partial T}{\partial t} = \kappa \nabla^2 T + R_{bp} \rho_b C_{p,b} (T - T_a) + q;$$

Where ρ_t is the tissue density, $C_{p,t}$ is the specific heat capacity of tissue, T is the local temperature, κ is the thermal conductivity of the tissue, R_{bp} is the blood perfusion rate, ρ_b is the blood density, $C_{p,b}$ is the specific heat capacity of blood, T_a is the arterial temperature, and q is the volume rate of heat deposition in the Pennes bio-heat transfer equation. In the case where ultrasound is the dominant external heat input, $q = 2\alpha I$, where α is attenuation coefficient (absorption) and I is the acoustic intensity, which can be calculated using the plane wave assumption (Nyborg, 1981):

$$I = \frac{P^2}{2\rho_0 c_0};$$

Therefore, the volume rate of heat deposition becomes:

$$q = \frac{\alpha \cdot (P^2)}{\rho_0 c_0};$$

The k-Wave toolbox includes a numerical solver for the Pennes bioheat equation, which uses a k-space pseudospectral correction technique such that for homogeneous media, exact formulations are obtained. As a result, it is unconditionally stable for large time steps in homogeneous media. However, this does not hold true for inhomogeneous media. Therefore, simple tests of inhomogeneous cases revealing the largest timesteps that can be used while ensuring stability need to be performed before doing the thermal modelling on more

complicated actual cases. This was performed before running the thermal simulations and is presented in the next chapter.

1.12 ACOUSTIC LENS

An acoustic lens is an extra layer of material with a different speed of sound compared to the surrounding medium. By controlling the thickness at each position across the lens cross section, the phase of the ultrasound field once propagated through the lens layer can be altered as the pattern of the interaction of the waves is changed by the waves' arrival time. The development of acoustic lenses for transcranial therapies can also correct for focal distortions in a subject-specific manner, effectively turning a transducer into a high-resolution array at a reduced cost (Maimbourg et al., 2018; Maimbourg et al., 2020b).

Material	Density ρ [kg/m^3]	Speed of Sound c [m/s]	Acoustic Impedance Z [kg/(m^2 s)] × 10^6	Attenuation (at 0.5 MHz) α [dB/cm]
ABS[1]	1030	2230	2.31	1.11
PDMS[2,3,4,5]	1015	1035	1.05	1.05
PMMA[1,6]	1180	2740	3.23	0.7
PVA[7,8]	1100	1570	1.74	0.29

Table 1.2: Acoustic properties of different lens material candidates. These are the compressional properties. Attenuations calculated for a frequency of 500 kHz using the corresponding power law $\alpha = \alpha_0 \cdot f^n$. [1]Selfridge (1985), [2]Armani et al. (1999), [3]Cafarelli et al. (2017), [4]Guillermic et al. (2019), [5]Liu et al. (2018), [6]Bloomfield et al. (2000), [7]Kharine et al. (2003), [8]Zell et al. (2007).

In this work, lenses will be made by 3D printing, as it allows for relative ease in fabricating unique and complicated structures. Available materials for the 3D printers accessible to this project are ABS (Acrylonitrile Butadiene Styrene), PMMA (poly(methyl methacrylate)), and PVA (poly(vinyl alcohol)). It is noted that PVA has acoustic properties similar to those of general body tissues. Hence, it is not promising as an acoustic lens material but is kept for

comparison. Other available materials, such as acrylic rubber, which also possesses acoustic properties similar to tissues (Fujii et al., 1995), were neglected.

Due to concerns that directly printed lenses may have voids and other inhomogeneities that affect the lens' performance, PDMS (Poly(dimethyl siloxane)) was also added to the materials considered as candidates for the lens. PDMS is in a liquid state at room temperature and can be solidified at 60 °C in several hours. This property allows the finished product to be assumed to be a homogeneous material when the solidification process of PDMS is carefully controlled and degassed inside the 3D printed mould.

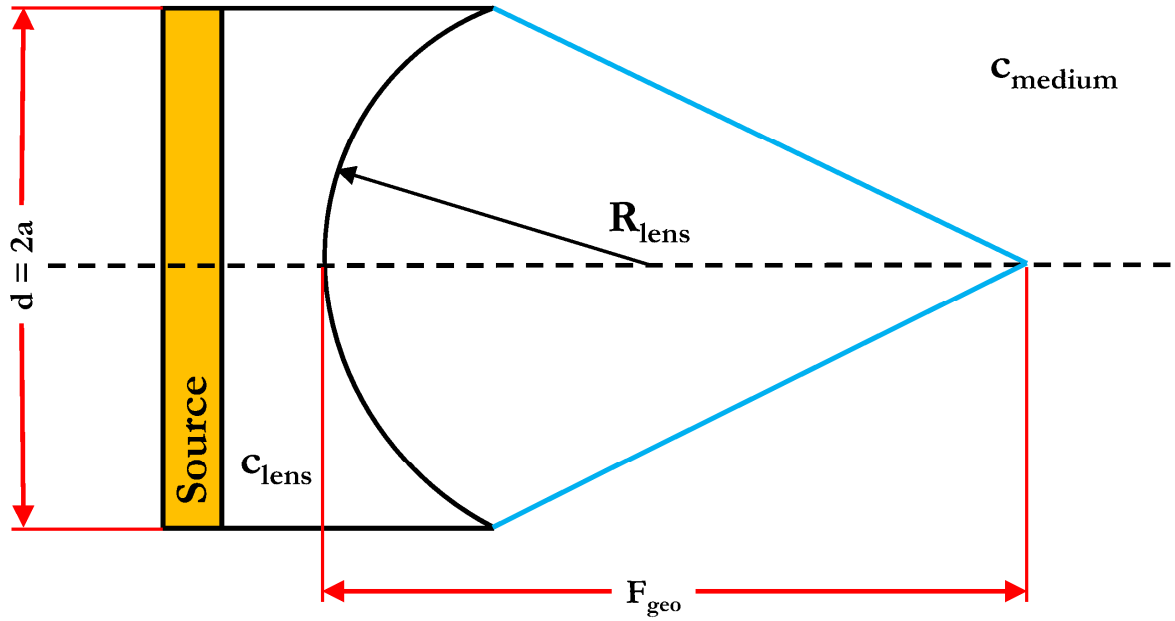

Fig. 1.3: Parameters for creating a focusing lens. The orange rectangle represents a piston source. F_{geo} represents the geometric focal length. d represents the aperture size. R_{lens} is the radius of curvature of the lens material layer. c is the speed of sound in the lens and medium, denoted with corresponding subscripts. The concave lens configuration shown is for the case where $c_{medium} < c_{lens}$.

The acoustic properties of the lens materials are summarised in Table 1.2. The best one will be chosen based on the pressure gain achievable at a certain depth, balancing between impedance mismatch effects and attenuation. The acoustic properties of the finished lens can be tested

using a previously proposed instrument setup (Choi et al., 2017). By comparing the resulting pressure fields of simulations to those in reality for the same lens geometry, the lens' acoustic properties that are hard to accurately acquire, such as the attenuation and speed of sound, can be updated from the literature values.

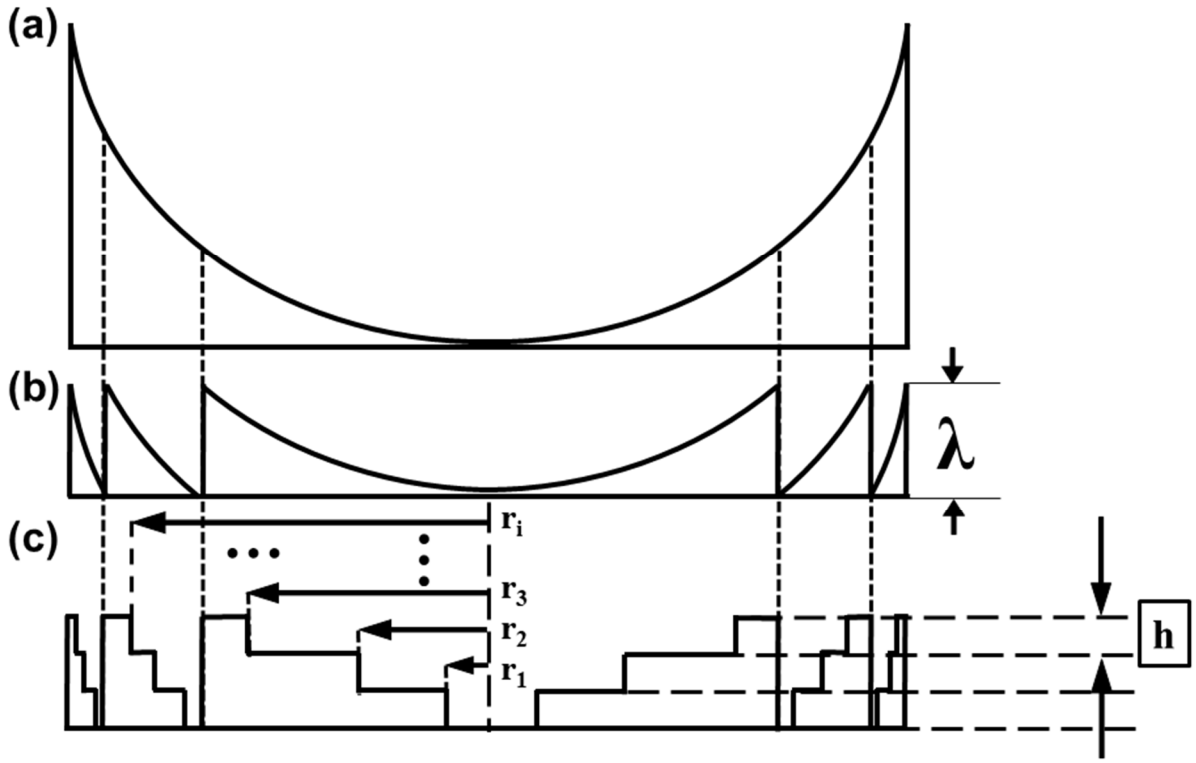

Fig. 1.4: 2D lens slices: structure illustration. For the same focusing, three different types of lenses are shown. **(a)** Standard bowl-shaped focusing lens, adopting thickness as needed. **(b)** Fresnel lens, constraining the lens thickness to be one wavelength. **(c)** Binary acoustic lens with 4 phase levels and a step height of h. Schematic redrawn based on Chan et al. (1995).

To create the lens needed, a way to address lens geometry based on focusing location, lens material acoustic properties, and medium acoustic properties is required. Such a method is presented above in Fig. 1.3 (Szabo, 2004), where, for the case shown, the concave geometry is appropriate for focusing when the speed of sound is higher in the lens than the medium. The flat ultrasound source is shown in orange with an aperture size of $d = 2a$ in diameter. The radius of curvature of the lens, R_{lens} shown by the black arrow, is related to the geometric focal length, F_{geo} (blue lines and range shown by the red arrow) by:

$$F_{geo} = \left|\frac{R_{lens}}{n-1}\right|; where\ n = \frac{c_{medium}}{c_{lens}};$$

Thus, $R_{lens} = F_{geo} \times |n-1|$ for both $c_{lens} > c_{medium}$ (concave lens) and $c_{lens} < c_{medium}$ (convex lens). The geometric focus can be calculated from the aperture radius of the source (a) and the depth into the medium as:

$$F_{geo} = \sqrt{a^2 + depth^2};$$

The lens in Fig. 1.3 with a thicker lens section for positions further away from the central axis has a disadvantage as the thicker lens material means more attenuation and hence reduced pressure amplitude at focus. A Fresnel lens (Fig. 1.4 (b)) can be used to reduce the lens thickness at each position by multiples of the wavelength of the ultrasound in the lens (Chan et al., 1995). The principle is that for constructive superposition at focus, for a signal with a length of more than a single period, the summation signal can be created not only using signals of the same period in time but also using the peaks in periods before and after to create the needed superposition. Fresnel lenses reduce the absorption in the lens and the room required for the lens. Both of these are desirable for this project.

In principle, the lens should have a continuous surface, as in Fig. 1.4 (b), only limited by the resolution of the specific 3D printer used. However, in order to apply the lens in the acoustic simulations, the lens needs to be digitised onto discrete simulation grids and was given the name ‘binary acoustic lens’ (Chan et al., 1995; Hadimioglu et al., 1993). The binary acoustic

lens derived from the same typical bowl-shaped focusing lens is shown in Fig. 1.4 (c), converting the continuous curvature into phase levels of fixed height.

In this study, the step height h will be fixed to be the same as the grid size used in the simulations. The number of phase levels N a lens needs can be calculated based on the determined step height h, ultrasound frequency f and the speeds of sound in the medium and lens:

$$N = \frac{1}{h \cdot f \cdot (\frac{1}{c_1} - \frac{1}{c_2})}; where\ c_1 < c_2$$

Assuming the frequency is 500 kHz and the grid size in simulations h = 0.5 mm, the phase levels for the materials considered can be calculated based on their acoustic properties in Table 1.2. Rounding to integer numbers, ABS lenses will have 18 phase levels, whereas PMMA and PDMS lenses will have 13 phase levels. This means the ABS lenses will be thicker than the other two. As ABS already has the highest attenuation among the three, its thicker binary acoustic lens nature further reduces expectations for it to be the suitable lens material. With the height of each phase level equal to 0.5 mm, the corresponding thickness of the lens is 9 mm for ABS and 6.5 mm for PMMA and PDMS. These values are larger than the wavelength of 500 kHz ultrasound in these materials, which is 4.46 mm for ABS, 5.48 mm for PMMA, and 2.07 mm for PDMS. This shows that in order to make a lens with discrete step changes to provide the required focusing ability, more thickness than the standard Fresnel lens is needed as compensation for the reduction in the curvature's smoothness.

The binary acoustic lens shown in Fig. 1.4 is a four-phase lens for simple demonstration purposes. It uses four phase levels to cover the whole thickness range. As one would expect, the higher the number of phase levels a lens has, the closer it represents the curved Fresnel lens, which therefore should possess better transmission and focusing efficiency. This is measured by diffraction efficiency. From the phase levels calculated above, all three materials will have first-order diffraction efficiencies over 98%. The first-order diffraction efficiency for N levels, η^N is given by (Chan et al., 1995):

$$\eta^N = \left[\frac{\sin\left(\frac{\pi}{N}\right)}{\left(\frac{\pi}{N}\right)}\right]^2 ;$$

The radius of the end of each phase level is measured from the centre axis, as shown in Fig. 1.4. This radius for the kth phase level is calculated by:

$$r_k = \left[(F + k \cdot \frac{\lambda}{N})^2 - F^2\right]^{0.5} ;$$

Where F is the focal length required from the lens, λ is the wavelength of the ultrasound, and N is the number of phase levels.

The required phases are converted into lens thickness L at particular locations on the cross-sectional area, which are given at the source plane from the time reversal simulations. Phase difference is defined as:

$$\Phi = 2\pi f \Delta t = 2\pi f \left(\frac{L}{c_1} - \frac{L}{c_2}\right);$$

Rearranging this equation converts the phase into lens thickness L:

$$L = \frac{\Phi}{2\pi f}\left(\frac{c_1 c_2}{c_1 - c_2}\right);$$

Where Φ is the phase in radians, f is frequency, and Δt is the time difference, which can be calculated as waves travelling through the distance L in two different materials with different speeds of sound c_1 and c_2. The symbols have the same meaning as before. As the thickness L cannot be negative, $c_1 > c_2$ is defined when using this conversion.

Further analysis is needed to select the best material for making the lens. The analysis was done in simulations to model the balance between impedance mismatch effects and attenuation and is presented in the next chapter. Both of these two factors influence the resultant focal gain, which should be the most important merit index when choosing the lens material.

The material properties in Table 1.2 are from the literature. Therefore, a method must be used to update the material properties of the chosen lens material. Standard experimental setups controlling positioning, orientations, and temperature with high precision were used to acquire the material properties for acoustic lenses (Choi et al., 2017). However, these experiments share a common assumption of plane wave propagation, which is unrealistic for a focused field. In addition, the attenuation is challenging to accurately determine. The reduction in magnitude when adding the lens material layer is not only due to the added attenuation by that layer but also due to the reflections. There are only partial transmissions at impedance mismatch boundaries between the lens material layer and the medium liquid where the layer is submerged. Therefore, the focused lens of the material chosen is manufactured in the same

geometry as that in the simulation. This lens creates focused pressure distributions in the free field that can be compared to the simulation results.

The density of the material can be measured with high accuracy by standard engineering procedures (scale for mass and water displacement for volume). The speed of sound of the lens material is then adjusted from the literature value when needed until the focus spot is the same between the experiment results and the simulation results. Finally, the attenuation values can be adjusted to match the amplitude measurements in the experiment. The attenuation values shown in Table 1.2 are extrapolated from literature values, as reported data rarely go below 1 MHz for these materials. Therefore, it is necessary for the ultrasound frequency in the range considered in this study to update the lens attenuation from the literature values. In this way, the lens materials will be represented more accurately in the simulations, producing predictions closer to reality. The possibility of showing successful ultrasound stimulation at target sites by a lens while ensuring safety is also maximised.

In contrast to the literature (Jang and Chang, 2016; Jiménez-Gambín et al., 2019; Maimbourg et al., 2018; Ferri et al., 2019), the lens in this work is applied to a flat transducer, where the lens is in charge of both the skull aberration correction and focusing. In this way, a target-specific lens can be used on a variety of brain sites without working against the built-in transducer's focusing curvature. Additionally, the improvement in cost-effectiveness by using a flat transducer can make the lens technique more accessible in the field of brain stimulation.

1.13 MONITORING

Although computational simulations are used to determine the required source conditions for transcranial ultrasound stimulation, it is still desirable to have the ability to monitor the location

where the ultrasound is being delivered in real time and confirm that the intended brain target is being stimulated. In addition, the data resulting from the experiments on human participants needs to be recorded and analysed to show the induced neuromodulation effects.

Functional ultrasound imaging has been shown to be effective at imaging microvascular dynamics in the brain in small animals with high temporal resolution (Macé et al., 2011). However, it would not be feasible to scale this modality up and use it in humans for neuromodulation monitoring in this study. Scaled-up transcranial ultrasound imaging with high resolution for human use is still under development (Soulioti et al., 2020) and will require detailed investigation before being used as a reliable and non-invasive method for monitoring and recording in real time. Non-invasive magnetic resonance thermometry was used to verify in a cadaver model that the accuracy of time reversal focusing was within a few millimetres (Chauvet et al., 2013). However, for neuromodulation, where the temperature rise is a fraction of a degree, this non-invasive approach is likely not applicable for monitoring neuromodulation, despite the fact that it is used to determine the focus for more intensive scenarios such as thermal ablation (Rieke and Pauly, 2008). Indeed, for the pressure and frequency range relevant to neuromodulation, magnetic thermometry failed to detect any temperature change, let alone serve as a monitoring tool (Dallapiazza et al., 2018). Magnetic resonance acoustic radiation force imaging (MR-ARFI) can provide a non-thermal monitoring method with tissue displacements encoded as phase shifts (Kaye and Pauly, 2013; Nightingale et al., 2002). However, this method typically requires higher pressures than those needed for neuromodulation to image the tissue displacement induced. For example, 1.9 MPa at 850 kHz generated less than 2 µm of tissue displacement in MR-ARFI (Ozenne et al., 2020). It was also found that the brain tissue pulsation due to cardiac cycles has a comparable or larger amplitude

(Turner et al., 2020). In summary, neuromodulation by ultrasound lacks a method for stimulation targeting that can be monitored non-invasively in real time.

In terms of brain activities, non-invasive monitoring is typically done by electroencephalogram (EEG) and functional magnetic resonance imaging (fMRI). EEG uses multiple electrodes on the scalp to measure the evoked potentials. This superficial nature makes it challenging to monitor deep brain sites. One study, however, has extended the use of EEG to deep brain targets by tagging a small volume of brain with a unique EEG signal induced by ultrasound (Darvas et al., 2016). fMRI is a powerful 3D mapping tool for measuring brain activities deep inside the brain and discovering linkages between brain areas. It uses the blood oxygen level in the brain to quantify neural activity. It is a more applicable tool for monitoring not only the real-time ultrasound-induced brain activity but also the induced long-term effects on brain connectivity (Verhagen et al., 2019). Its outstanding monitoring capabilities in the anterior hippocampus were demonstrated in previous neurological studies (Zeidman and Maguire, 2016). In order to use fMRI during the experiments, the ultrasound sources must be MR-compatible so that they can operate inside the MRI scanner. Other than these physiological-based monitoring modalities, overall network-level brain activities can be revealed through the recorded performance of the tasks during the experiments. This task-based method is commonly used in psychological studies on the perirhinal cortex (Kreher et al., 2019) and anterior hippocampus (Zeidman et al., 2015) to study their functionalities.

The best invasive method for monitoring brain functions is implanted electrodes, which capture the local field potentials (LFPs) of meaningful brain activities (Yang et al., 2020). This would be possible to scale up to human subjects that have implanted electrodes for other purposes, such as deep brain stimulation for Parkinson's disease.

1.14 AIM OF THESIS

This thesis intends to develop and validate a lens method to stimulate deep brain targets in humans with improved spatial specificity non-invasively and cost-effectively. Through computational modelling techniques, Chapter 2 aims to: (i) demonstrate the viability of using PDMS lenses on the temporal bone window to target various deep brain targets in humans unilaterally and even bilaterally; and (ii) provide a stimulation planning method based on modelling such that the target pressure gain can be maximised and focal volume can be confined in size and orientation based on the need in each case. With the human brain stimulation trials in mind, experiments in Chapter 3 aim to: (i) validate the lens method modelling findings in Chapter 2 on *ex vivo* human skull samples; (ii) prove that the modelling technique is adequate for stimulation planning; and (iii) demonstrate that adequate binary skull segmentation is applicable for making accurate lenses for targeting. By considering the human trial on Parkinson's disease patients with implanted DBS electrodes, Chapter 4 aims to demonstrate the feasibility of applying focused ultrasound to the human brain while mitigating the risks of ultrasound-electrode interactions. In summary, this thesis aims to provide a thorough study progressing towards the human trial where local brain signals recorded by the DBS electrode can act as more robust evidence of ultrasound stimulation effects in the human brain than behavioural responses.

2

MODELLING METHOD & OPTIMISATION

This chapter presents the numerical modelling studies. Validation of the numerical tools was done through testing against analytical cases using an ideal focused transducer and comparing them with experimental measurements employing acoustic holography. The lens material was selected based on simulation results. Patient-specific modelling was implemented by segmenting MRI imaging data into the simulation space. Thermal modelling was then tested in simple cases before being applied to the actual simulation space. The optimal transducer size and frequency were then chosen based on the modelling results of the relevant left or right half head single source (HHSS) simulations. Simulations for HHSS, whole head single source (WHSS), and whole head paired sources (WHPS) are also compared.

2.1 SIMULATION TOOLBOX TESTING

All simulations were done with the open-source k-Wave MATLAB toolbox (Treeby and Cox, 2010) due to its reduced computational cost and the fewer points per wavelength needed. The k-Wave toolbox was tested using an ideal focused single-element transducer in free field and compared to the analytical solution (O'Neil, 1949). An ideal transducer has three characteristics: (i) a wave pattern that is identical across the transducer surface; (ii) acoustic properties that are compatible with the nearby medium next to the transducer surface; and (iii) only one frequency content in the frequency spectrum, which is at the driving frequency. The idealised transducer used here has the following physical properties: a radius of curvature of 63.2 mm, an aperture diameter of 64 mm, a frequency of 500 kHz, and a wavelength of about 3 mm in water. These values were adapted from a real transducer (H-107, Sonic Concepts Inc., Bothell, WA, USA).

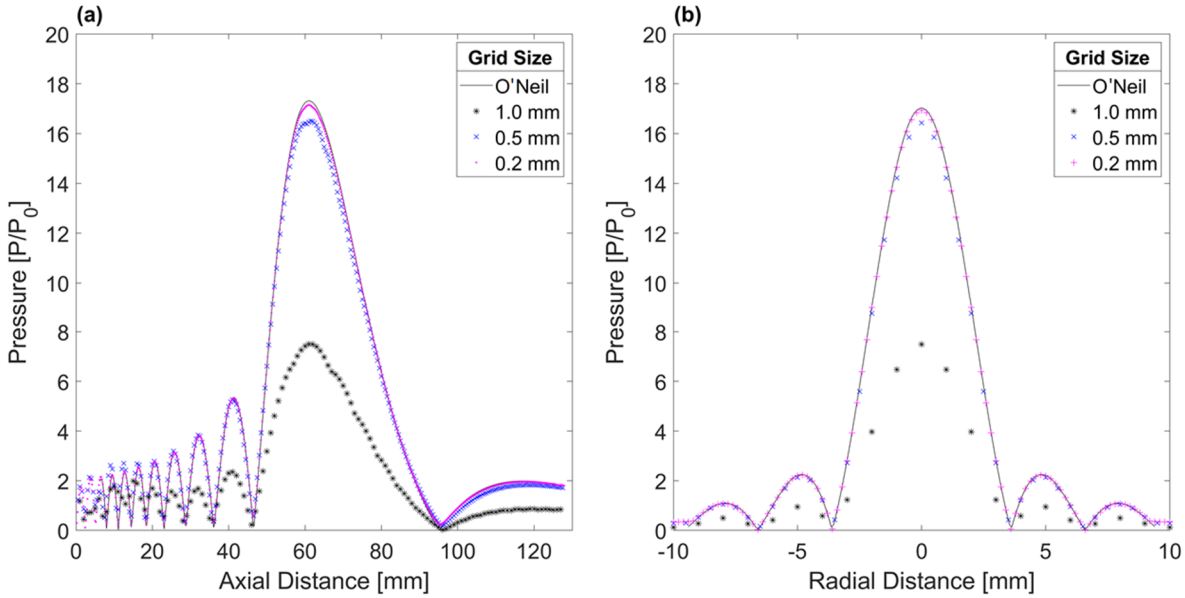

Fig. 2.1: Ideal focused transducer's axial and radial pressure distribution. Analytical O'Neil solutions are compared to pressure distributions from k-Wave 3D simulations using grid size of 0.2 mm, 0.5 mm, and 1.0 mm. **(a)** Axial pressure distribution comparison. **(b)** Radial pressure distribution comparison.

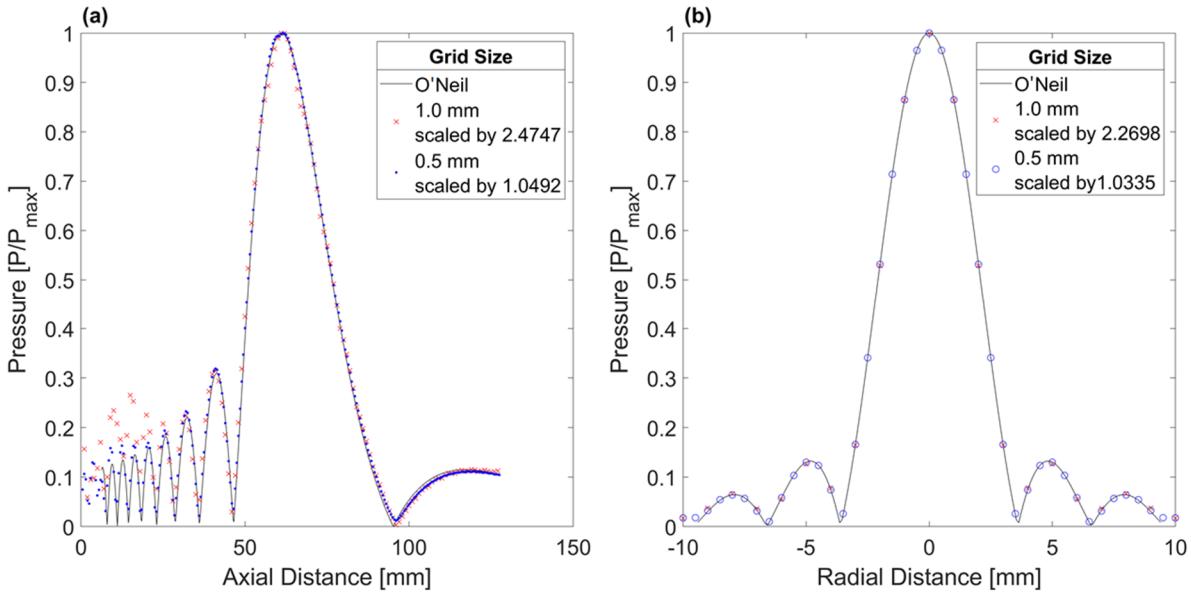

Fig. 2.2: Magnitude correction for simulation results of an ideal focused transducer. The vertical axis shows pressure in a normalised range between 0 and 1. Normalisation is done by the maximum pressure P_{max}. **(a)** Magnitude corrected axial pressure distribution. **(b)** Magnitude-corrected radial pressure distribution.

With the CFL number set at 0.3, the spatial resolution reliability in 3D was tested using this focused transducer propagating ultrasound into water at 1500 m/s, 1000 kg/m^3, and zero attenuation. Fig. 2.1 shows the axial and radial results of the analytical solution and simulations using different grid sizes: 15 PPW (0.2 mm), 6 PPW (0.5 mm), and 3 PPW (1.0 mm). Pressure magnitude is expressed in terms of pressure gain P/P_0 where P_0 is the effective source pressure. In the axial view, all three cases correctly show the location of the maximum pressure at 61 mm, the same as the analytical solution. Note that this is slightly closer to the source than the geometric focus of 63.2 mm. The pressure magnitude is shown to vary with grid spacing. For a grid spacing of 1.0 mm, despite correctly predicting the location of peaks and troughs, the pressure gain at the focus is less than 50% of the expected value. In addition, the main lobe is not as smooth as the analytical solution between 60 ~ 100 mm axially. A grid spacing of 0.5 mm captures the location of peaks and troughs correctly and gives a 5% magnitude reduction axially and 3% radially at focus. For a grid spacing of 0.2 mm, the pressure

distribution tracks the O'Neil solution with less than 1% difference axially and less than 0.5% difference radially at the focus.

The computation time for a grid size of 1.0 mm was about 8 minutes, for 0.5 mm, about 30 minutes, and for 0.2 mm, over 6 hours. Therefore, a grid size of 0.5 mm (6 PPW) was chosen to be used for all simulations at this wavelength or higher, as it has been shown to provide sufficient accuracy (less than 5% difference in pressure magnitude) with an acceptable computation cost (Aubry et al., 2022). The 5% difference is sufficient, as this is most likely better than the accuracy of measurements that can be done in experiments.

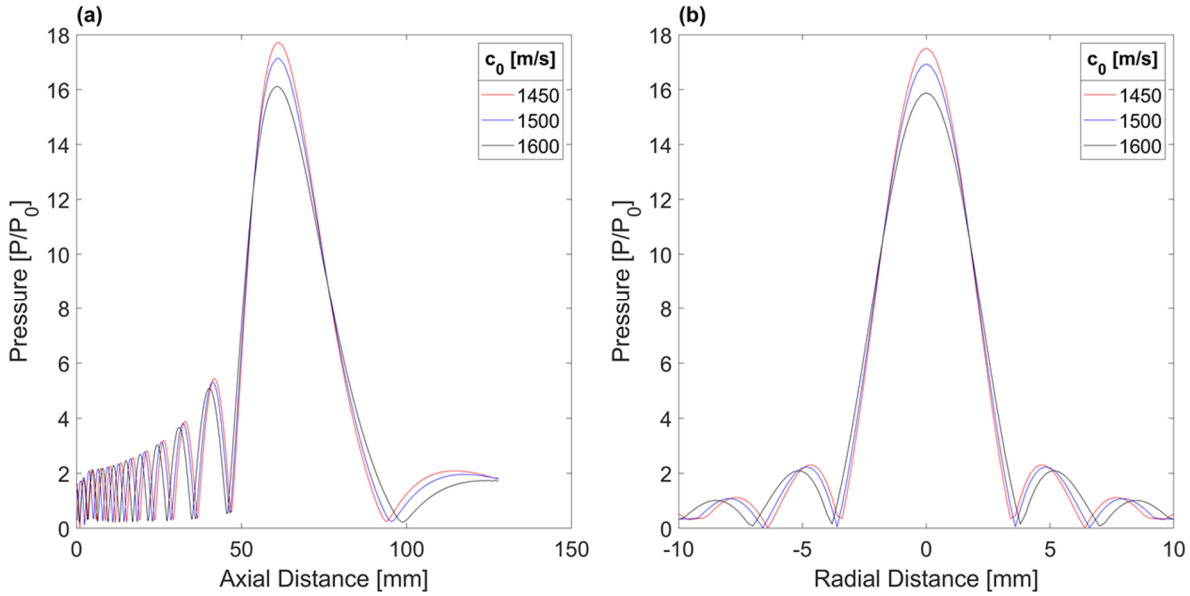

Fig. 2.3: Comparison of simulated pressure distributions with different medium speeds of sound. Pressure is normalised by source pressure P_0. **(a)** Axial distribution. **(b)** Radial distribution.

A magnitude correction factor can be applied to simulations where an ideal focused transducer is used to generate fields without underestimating the pressure gain (Martin et al., 2016). Fig. 2.2 shows the results of magnitude-corrected pressure distributions for grid sizes 0.5 mm and 1.0 mm, axially and radially. The pressure shown is normalised by the maximum pressure P_{max}. Note that axially, the near field distribution significantly overestimates the pressure

magnitude when using a grid size of 1.0 mm, suggesting that even with magnitude correction, a grid size larger than 0.5 mm is not reliable as the near field pressure does not match.

With density kept the same ($\rho = 1000$ kg/m^3 for water as before) for the homogeneous medium, analysis of speed of sound variation was simulated using the described ideal focused transducer at a grid size of 0.5 mm and a CFL number of 0.3. The speed of sound c_0 used were 1450 m/s, 1500 m/s, and 1600 m/s, covering the speed of sound ranges in soft tissue. Fig. 2.3 shows the resulting axial and radial pressure distribution using the described ideal focused transducer.

As the speed of sound increases, the focal gain can be seen to decrease due to the reciprocal relationship between focal gain and speed of sound:

$$G = \frac{\frac{1}{2}ka^2}{R_c};$$

Where G is the focal gain, $k = \frac{2\pi f}{c}$ is the wave number, a is the radius of aperture of the focused ultrasound source, and R_c is the radius of curvature of the focused ultrasound source. The numerator is the Rayleigh distance.

As a lower focal gain is observed with increased speed of sound, the distribution of the pressure field is widened due to the diffusion of acoustic energy. This is shown by the main lobe and side lobes covering a larger range as the whole distribution is widened from the focus.

In conclusion, a variation of 10% in the speed of sound resulted in the focal pressure also varying by about 10% and the focal spot changing in size. This shows the significance of the accuracy of the speed of sound in varying the simulated pressure field, even in an ideal, homogeneous case. For future inhomogeneous simulations using subjects' MRI data, in order to be accurate to within 10%, reliable values for the speed of sound in tissues are needed (Robertson et al., 2017).

2.2 ACOUSTIC HOLOGRAPHY TESTING

To capture and include the specific characteristics of the real pressure field created by the transducer in the simulation, acoustic holography was used. The theory is described in Chapter 1. The method was tested using a focused source (H-107, Sonic Concepts Inc., Bothell, WA, USA).

Pressure measurements were taken in a plane parallel to the source. The measurements can be used to reconstruct a source plane representing the non-ideal perspectives of this actual transducer. The parallel plane for the holography measurement was chosen to be 35 mm in front of the focus. The holography measurement plane was decided to have a dimension of 70 mm by 70 mm, with the transducer's centre axis in the wave propagating direction placed at the centre. Measurements were taken at a step size of 0.5 mm to match the grid size decided for the simulations in the previous section.

The numerical tools for acoustic holography were first validated by using the fluid-based linear k-Wave simulation results of an ideal focused transducer with the same geometric parameters as the H-107 transducer. Forward simulations were done, and measurements were taken at the holography plane. Based on this measurement, acoustic holography using forward and

backward propagation was used to conduct planes at the focus and source, respectively. The magnitude and phase at each of these three planes are shown in Fig. 2.4. The source plane was reconstructed at the transducer's exiting plane.

A focal spot is observed as expected in the reconstructed focal plane in Fig. 2.4 (c). For the reconstructed source plane in Fig. 2.4 (a), the inner cut-out can be seen as a region of low pressure in the middle of the plane. In all plots, for both phase and magnitude, axial symmetry can be seen, as these are the simulated results using an ideal circular source. This is an artefact created by mapping the arcs of the curvature and circular shape of the ideal focusing source onto the finite 0.5 mm grid size in the simulation. The overall result proves that the algorithm is working as intended.

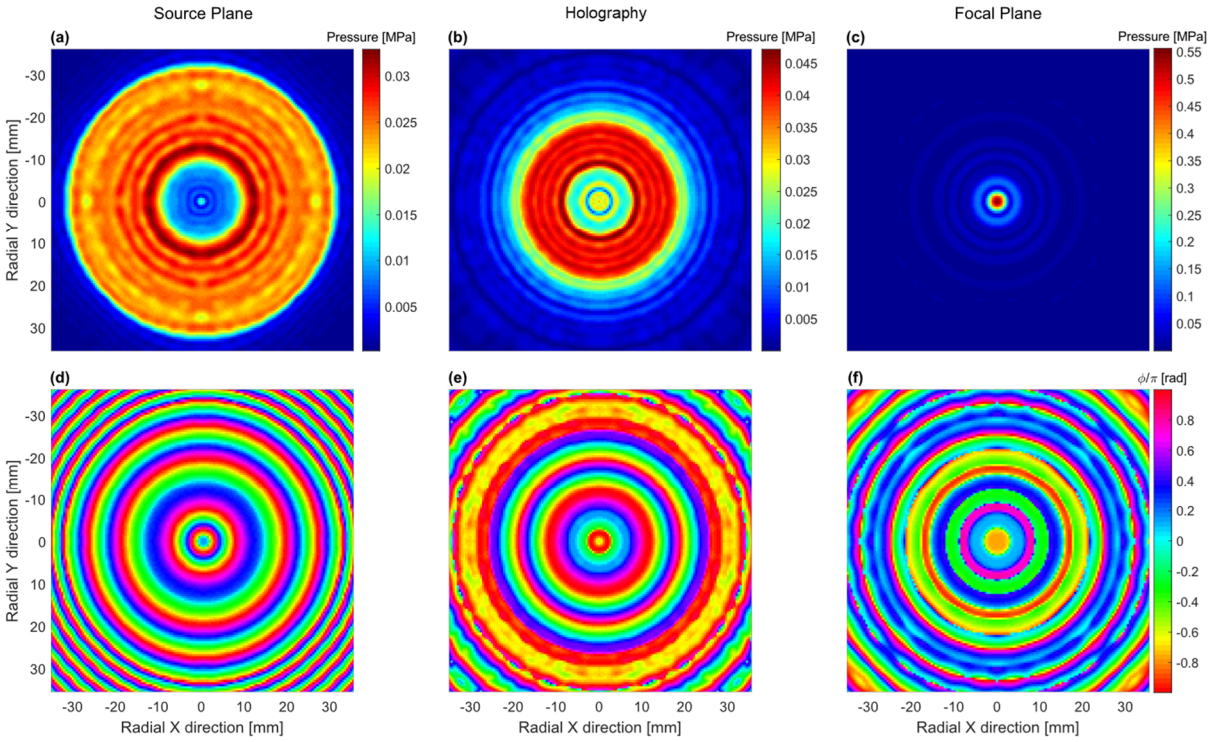

Fig. 2.4: Source reconstruction by acoustic holography. Ideal H-107 transducer. **(b), (e)** Magnitude and phase in the holography plane resulted from a k-Wave fluid-based linear simulation of the transducer in free field (an ideal transducer of the type). **(c), (f)** Forward propagation to the focal plane. **(a), (d)** Back propagation to the source plane.

The same reconstructions were then performed using the experimentally measured near-field plane. The real pressure field created by a calibrated H-107 transducer was measured by a hydrophone (HNA-0400, ONDA, Sunnyvale, CA, USA) in a water tank filled with deionised and degassed water, as shown in Fig. 2.5. A signal generator (33250A, Agilent, Santa Clara, USA) sending the output of a 40 µs (20 cycles) 500 kHz sinusoidal signal was amplified by a 55 dB broadband amplifier (1140LA, E&I, Rochester, NY, USA) and then applied to a matching box connected to the transducer. A needle hydrophone was fitted to a 3D positioning system so that it could be moved to do the scan in the water tank. An oscilloscope (HDO4024, Teledyne LeCroy, Chestnut Ridge, NY, USA) was used to take measurements from the hydrophone and the output of the amplifier. It was synchronised with the signal generator. The oscilloscope also recorded the output of the amplifier.

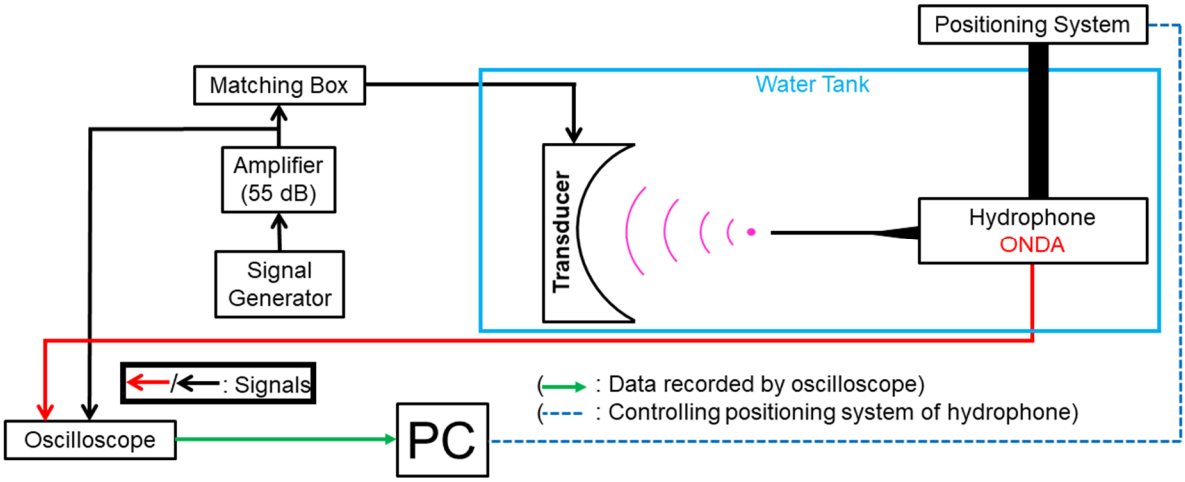

Fig. 2.5: Schematic of the experimental setup for transducer calibration and characterisation. The transducer was placed in a water tank filled with deionised and degassed water. A matching box for the transducer was in place after the amplifier. A needle hydrophone was used to take the measurements. Hydrophone positioning was controlled by a computer through a 3D positioning system. Hydrophone signals were recorded by the oscilloscope and then saved on the computer.

The same reconstructions are performed using the experimentally measured near-field plane. The scan result and the reconstructed planes are presented in Fig. 2.6. In the measured near-field plane in Fig. 2.6 (b) and (e), asymmetric perspectives are observed. When the focal plane

is reconstructed using acoustic holography in the forward direction, the asymmetric aspect is hard to observe in the magnitude map in Fig. 2.6 (c), as significant pressure magnitude exists in a tight region at the focus. The asymmetry was, however, visible in the phase map in Fig. 2.6 (f). For the reconstructed source plane in Fig. 2.6 (a), despite the non-ideal asymmetric aspects, the inner cut-out is shown with a region of low pressure magnitude in the middle of the map. In Fig. 2.6 (b), in the measured magnitude field, a region of high pressure is observed as a region of red. Despite the difference in colour scale, the simulated results in Fig. 2.4 (b) suggest that there should still be low pressure for the ideal case, indicating further non-ideal aspects of the actual transducer along the propagation direction.

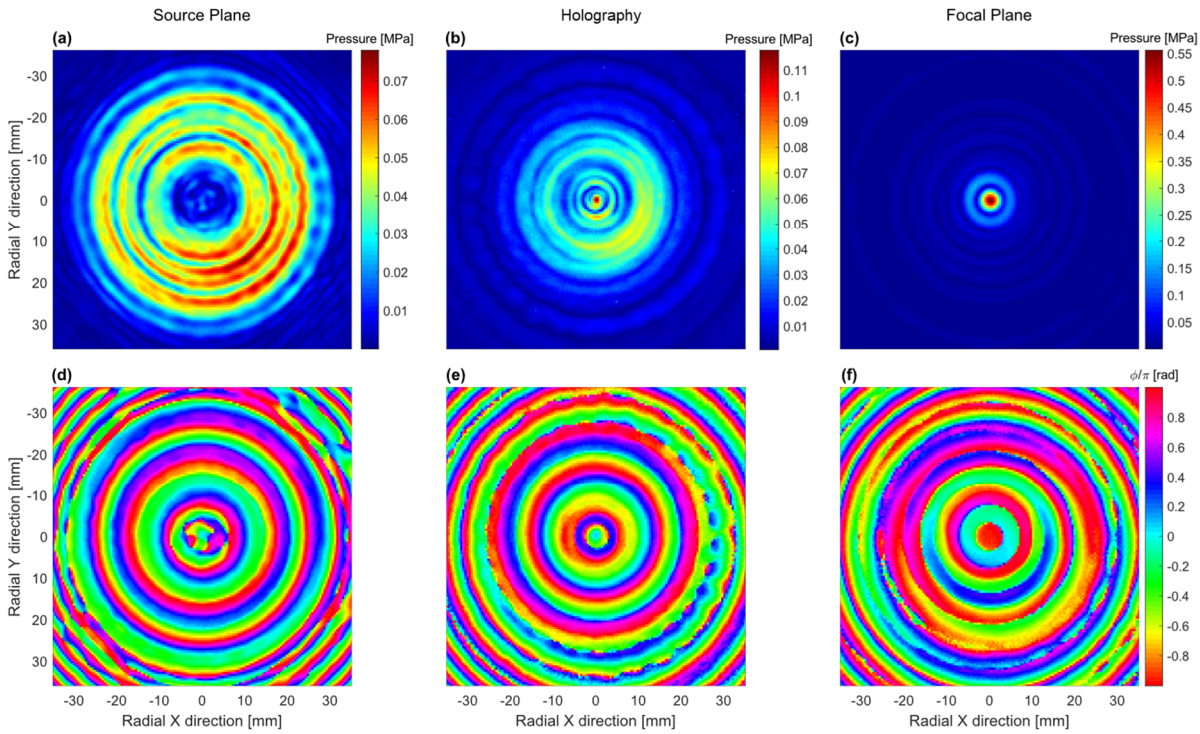

Fig. 2.6: Source reconstruction by acoustic holography. Real H-107 transducer. **(b), (e)** Magnitude and phase in the holography plane from experimental measurements done by a hydrophone. **(c), (f)** Forward propagation to the focal plane. **(a), (d)** Back propagation to the source plane.

Forward propagation simulation was then done using the reconstructed source to better reflect transducer characteristics. The axial and radial views of the resulting pressure distribution compared to the analytical results and experimental measurements are shown in Fig. 2.7.

The O'Neil analytical solution (O'Neil, 1949) is used for the axial view in Fig. 2.7 (a). The simulated pressure distribution using the reconstructed source agrees more than the ideal when compared to the experimentally measured pressure distribution. This is demonstrated by a wider main lobe axially than that of the analytical solution. The importance of the reconstructed source can be illustrated by the differences in locations and amplitudes of pre-focal lobes between the ideal case and the measured pressure distribution.

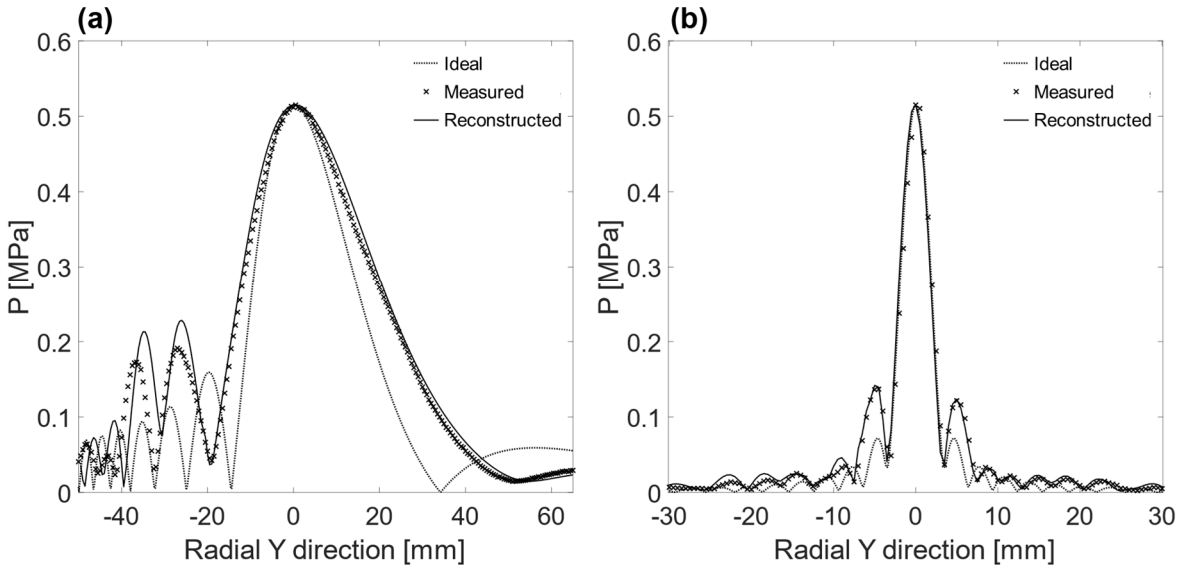

Fig. 2.7: Reconstructed source in comparison to analytical results and experimental measurements. The forward propagation k-Wave results using the reconstructed source (solid lines) are compared with the analytical solutions (dotted lines) and the experimental measurements (cross markers). **(a)** Axial pressure distribution. The O'Neil analytical solution is used. **(b)** Radial pressure distribution at the pressure peak location instead of at the geometric focus. The Chen analytical solution is used.

Although O'Neil does give a solution for radial field at the geometric focus, the experimental data is at the focal peak, which is about 2.2 mm in front of the geometric focus. Chen et al.

(1993) gives a quasi-analytical pressure distribution for all locations, which was thus used to create the radial field at the pressure peak location used in Fig. 2.7 (b). In the radial view, all three results: analytical, experimentally measured, and reconstructed source simulation agree on the main lobe pressure distribution. However, for the side lobes, the analytical solutions failed to capture the location and amplitude of the side lobes, whereas the reconstructed source gives good agreement with the measured data. With side lobes further off axis, the disagreement between experimental measurements and the result of the reconstructed source starts to appear on the left side (Y negative). However, this disagreement remains smaller than that of the analytical result, with correctly located troughs and peaks, with disagreement only on the magnitude. As the pressure magnitude is low at this far off axis, this difference in magnitude is likely beyond the accuracy of the pressure that can be measured.

Based on the positive validation from the reconstructed source, simulations can now include the characteristics of a real transducer. The experiments and methods described in this section can be extended to apply to any single-element source, e.g., a flat single-element transducer. With adequate modifications, these methods can also be applied to elements of array devices, representing their non-ideal aspects in the simulations.

2.3 Improved Ultrasound Delivery Method

The single-element focused transducer H-107 was checked to see if it could focus on deep brain targets. Fig. 2.8 shows four possible target locations in one subject, each representing a desired target sphere of 5 mm diameter. One pair (Target 1 and 2) represents the bilateral perirhinal cortex target sites. The other pair (Target 3 and 4) represents the bilateral anterior hippocampus target sites. The deepest target is 60 mm from the nearest outside body location in the MRI. For a transducer with a diameter of 64 mm, the same as the H-107, the minimum radius of

curvature required to reach this target (68 mm) is larger than the radius of curvature of the H-107 (63.2 mm).

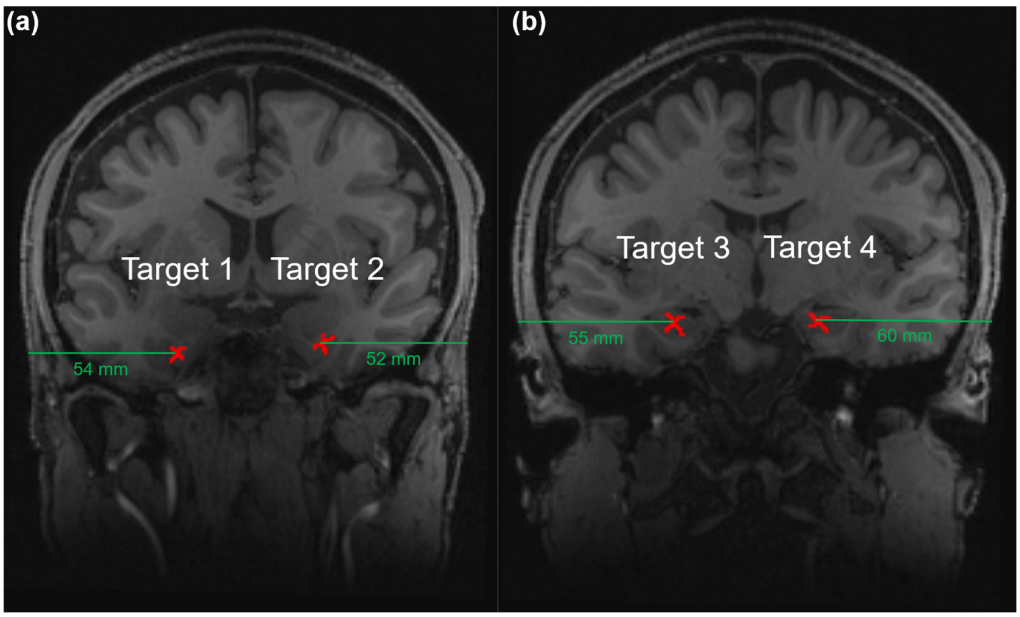

Fig. 2.8: Marked targets in the subject's MRI. Coronal views of MRI are shown, with the target sites marked by red crosses. The images used are T1-weighted MRIs. The green lines indicate the shallowest depth from the outside of the head to reach each of the targets. **(a)** Bilateral target sites of the perirhinal cortex. **(b)** Bilateral target sites of the anterior hippocampus.

Other than the increased depth, there are also significant target depth variations up to 20 mm in the three subjects so far examined. Alternative ultrasound sources were therefore required. This could be: (i) a new single-element geometrically focused transducer with an increased radius of curvature above 68 mm; (ii) an array device; or (iii) acoustic lenses produced for each target site mounted in front of flat ultrasound sources for focused stimulation. The use of an array or an acoustic lens may improve the focused pressure field in the brain as they can take into account the aberration correction used in human transcranial ultrasound delivery (Jang and Chang, 2016; Maimbourg et al., 2018; Pernot et al., 2003; Rosnitskiy et al., 2019). However, as the array system available for this study was found to have too small a total active surface area to provide sufficient focal gain at 60 mm or further (the depth of deep brain targets; summarised in Appendix A), acoustic lenses were chosen for this project.

Ultrasound propagation in each subject's head needs to be studied in a case-by-case manner due to variations in skull morphology. Therefore, lenses for focusing on particular target sites can be created such that one transducer may be used for all targets for all subjects while still achieving the required degree of focusing, correcting the skull aberration effects, and coping with the variations in target depth shown in Fig. 2.8.

A flat transducer was chosen for the lens method for three reasons. Firstly, the built-in curvature of a focused source adds difficulty to a firm and tight contact between the whole source surface and the lens. Secondly, manufacturing a lens structure that accounts for aberrations on the curved transducer surface causes difficulties in controlling the quality of the finished product compared to the designed structure. Thirdly, a flat transducer is less expensive than a focused transducer, even with typical manufacturer configurations. By using a flat transducer, all focusing and aberration corrections can be modified by adjusting the lens structure.

In the rest of this chapter, the details of the methods for using an acoustic lens with a flat piston transducer are addressed, along with simulation results showing its feasibility. MRI data from three human heads is used as the propagation medium in the simulations to demonstrate the capability of the lens to deal with the inhomogeneity of the propagation medium.

2.4 LENS MATERIAL SELECTION

The available materials that can be used as lenses are discussed in Chapter 1, with their acoustic material properties listed from the literature. Some of them, such as PVA, possess a speed of sound too similar to that of water to be effective as lenses. This material selection analysis focuses on three materials: ABS, PDMS, and PMMA. Each of the three materials was used to construct a binary acoustic lens (digitised Fresnel lens as described in Section 1.12, Chapter 1)

from the phase that different locations on the transducer surface require to focus to a certain depth on axis. For comparison purposes, all three lenses were assumed to be driven by an ideal piston transducer with an aperture diameter of 64 mm and a frequency of 500 kHz. Fresnel lenses were used in the comparison because they possess a comparable thickness despite the difference in material properties, and the thinner nature of Fresnel lenses means lower losses than those in standard concave or convex lenses, which is unconditionally desirable for this project. The goal of this analysis is to find the material that provides the maximum focal pressure gain and minimum focal volume at the same source condition and same focal depth in the medium.

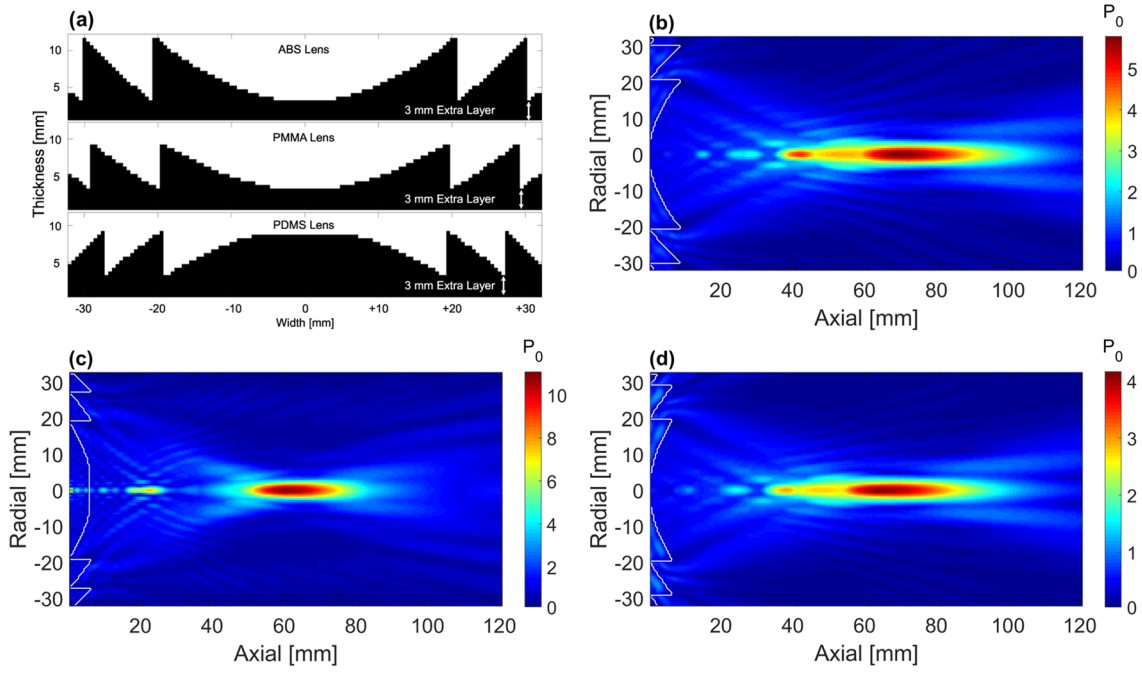

Fig. 2.9: Simulated pressure distributions created by ABS, PDMS, and PMMA lenses. All three lenses are created to have a focal volume about 60 mm deep into the medium after the lens thickness. **(a)** Slices through the cross-section diameter reveal the thickness and geometry of the lenses. **(b)** The pressure distribution by the ABS lens. **(c)** The pressure distribution by the PDMS lens. **(d)** The pressure distribution by the PMMA lens.

Fig. 2.9 shows the resultant pressure distributions following simulations performed in the free field. Notice that the ABS and PMMA lenses have a concave shape, whereas the PDMS lens

has a convex shape, as the speed of sound in ABS and PMMA is faster than water, whereas the speed of sound in PDMS is slower than water.

The lenses were produced based on the frequency, speed of sound differences, and desired focal depth as described in Chapter 1. To accommodate the full 2π phase variation, each lens was produced with a slightly different thickness. The ABS lens has a thickness of 9 mm, whereas both the PMMA and PDMS lenses have a thickness of 6.5 mm. Therefore, the ABS lens focuses to 70 mm, 1.5 mm further behind than that of PDMS and PMMA (68.5 mm). These foci are set so that the depth into the medium by these lenses is the same for comparison purposes. The lenses' slices in Fig. 2.9 (a) reveal the geometry of the structure through the diameter of the cross sections. The lenses were constructed using 0.5 mm quantisation, matching the grids used in the k-Wave simulations.

The simulations predicted that all three lenses produced their foci at the desired locations, as shown in Fig. 2.9 (b) to (d). The PDMS lens showed the best performance, with a focal pressure gain of 11.1 compared to 5.8 and 4.2 for ABS and PMMA, respectively, and a tighter focal volume compared to the other two. In the case of ABS and PMMA, the main lobes are so large that they are in contact with a pre-focal lobe that also has a significant pressure magnitude.

While the PDMS lens did result in one pre-focal lobe with a significant pressure magnitude, its magnitude relative to the focal region was much smaller than similar pre-focal lobes created by the ABS and PMMA lenses. More importantly, the pre-focal region generated by the PDMS lens occurs far away from the target, making it less likely to induce unwanted neuromodulation effects beyond the region of interest. In fact, the pre-focal region is so close to the lens that its location anatomically is most likely in the skull rather than anywhere inside the brain tissue.

To conclude, PDMS outperforms both ABS and PMMA as the lens material, showing a higher focal pressure gain with a tighter focal volume. Practically speaking, the mild temperature and slow speeds for PDMS solidification allow 3D printed moulds of the complicated lens structure to be used for a well-controlled manufacturing process to reduce inhomogeneities during the curing process and ensure lens performance.

2.5 SUBJECT IMAGING DATA

Using the available head T1-weighted MRI imaging data, the MARS (Morphologically and Anatomically accuRate Segmentation) MATLAB binary segmentation toolbox (Huang and Parra, 2015) was used to segment the head into six different materials: air (outside head), skin and scalp, skull bone, cerebrospinal fluid (CSF), grey matter, and white matter (Fig. 2.10).

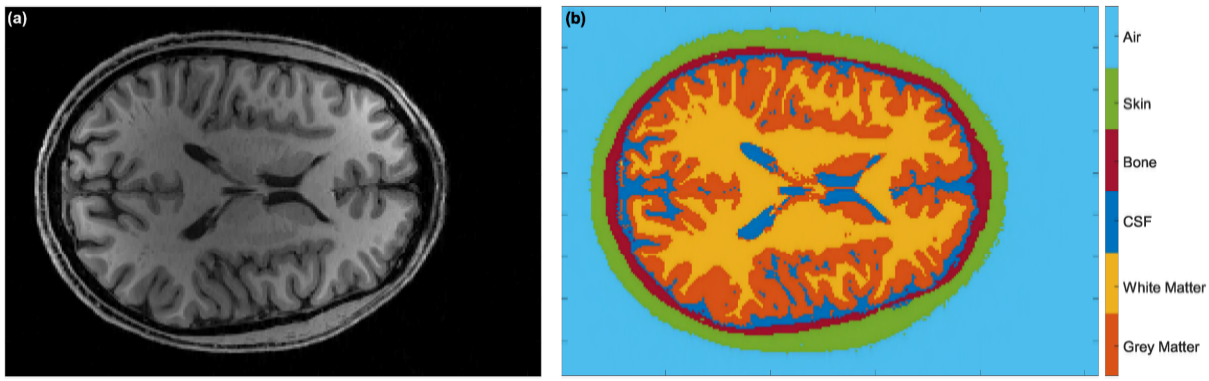

Fig. 2.10: Example of MARS toolbox segmented MRI. (a) T1-weighted MRI data slice in grey scale. **(b)** Segmented results of the same slice. The space is divided into six different tissue types.

As the spatial resolution of the MRI was limited to 1 mm^3 voxels, whereas the simulations used 0.5 mm grids, each MRI voxel was mapped to 8 simulation voxels (2 by 2 by 2). It is noted that the simulation space can also be constructed from segmentations of CT data. CT can reveal the porous bone structure inside the skull, but it comes at the cost of X-ray radiation to the subject. The detailed description of CT segmentation methods is presented in Chapter 3, where the skull samples' CT data are used in simulations for comparison with the validation

experiments. However, obtaining ethics approval for CT scans is uncommon due to the radiation risks, whereas approval for MRI is usually straightforward.

2.6 TIME REVERSAL BACK PROPAGATION

The temporal bone acoustic window was evaluated, as the skull in this region is generally thinner and flatter. In addition, the temporal bone window represents the shallowest path to reach many deep brain targets. Sensor planes in back propagation simulations were fixed in the YZ plane (Fig. 2.11) such that the head was slightly rotated to get as close to the sensor plane as possible without touching the plane in each case. In this way, digitisation-induced numerical errors were mitigated. In order to save computation time, only the relevant sagittal half of the head containing the target was included in the simulation space.

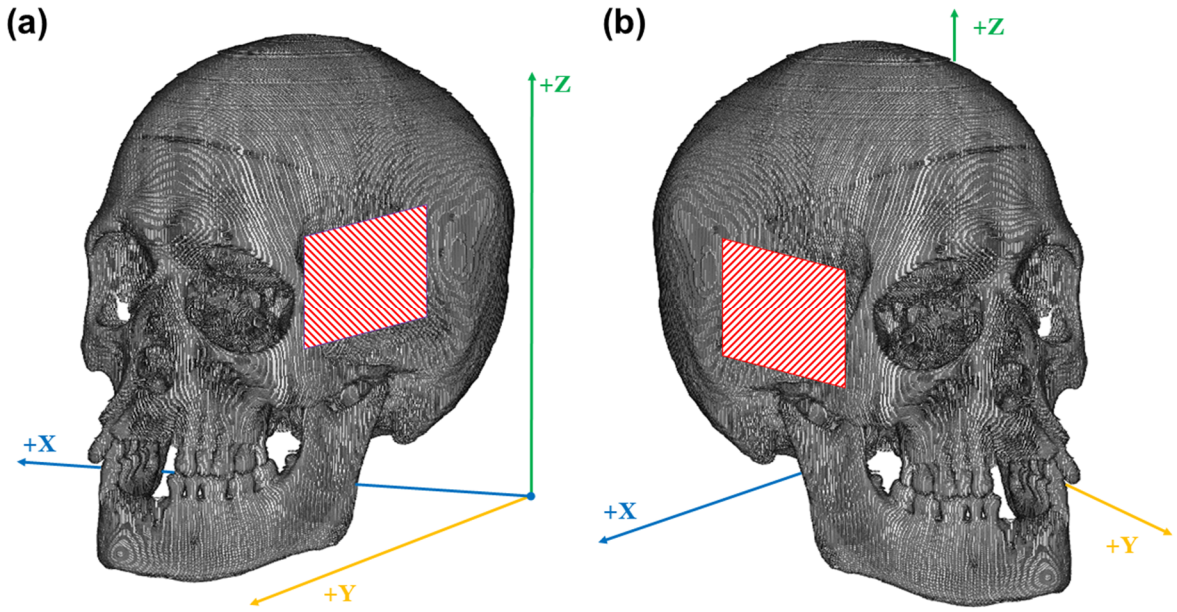

Fig. 2.11: Back propagation sensor placement demonstration. The 3D coordinate system starts from the bottom left rear corner of the 3D imaging data matrix, which is the same as the matrix indexing used in simulations. The red rectangles show the positioning of the sensor planes in back propagation simulations. These sensor planes are kept in the YZ plane for consistency. Their sizes are smaller than the actual sensor planes for demonstration purposes. A CT skull sample outline is used to illustrate the orientation. **(a)** Sensor plane placement on the left side. **(b)** Sensor plane placement on the right side.

Back propagation simulations were performed for each of the targets separately at an ultrasound frequency of 500 kHz. An example of a resultant magnitude and phase map of the received signals at the sensor plane obtained by a fast Fourier transform is shown in Fig. 2.12. The phase map is shown using a periodic colourmap from – π to π to account for phase wrapping. The projection of the target (left perirhinal cortex) onto the sensor plane is at Y = 113 mm and Z = 44 mm, where the target is X = 58.5 mm in terms of depth from the plane. A relatively homogeneous region of phases is observed near the target projection on the phase map. In regions beyond the target projection, heavily distorted circular patterns can be seen in the phase variation, caused by the aberration of the inhomogeneous medium, namely, the skull on the acoustic pathway.

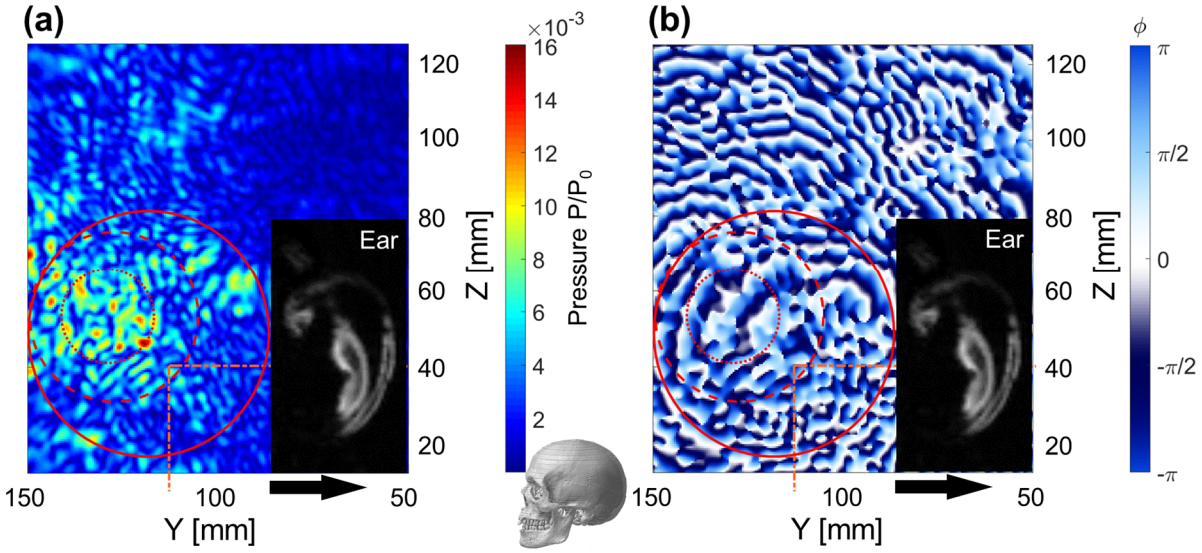

Fig. 2.12: Examples of back propagation measurements. The orientation of the view relative to the head is shown by the skull. The position of the ear occupies the region with a Y value of 85 mm or smaller. The dashed lines marked out the target location at (Y, Z) of (113, 44) [mm] in the plane and a depth of X = 58.5 mm into the page. The three circles of diameters 25 mm, 45 mm, and 65 mm are at optimal placements in terms of maximised average pressure magnitude in the areas encircled. **(a)** The pressure magnitude distribution by back propagation simulation. **(b)** The pressure phase distribution by back propagation simulation. The phase map uses a colourmap that can demonstrate the periodic nature of the phase in the 2π range, clearly showing the phase variation.

In this instance, the size of the sensor plane is limited by the curvature of the head anatomy from the MRI in the superior (increasing in Z), anterior (increasing in Y), and posterior (decreasing in Y) directions. The sensor plane stops on each of these three edges when the distance perpendicular to the plane between the nearest head tissue and the plane exceeds 10 mm. For distances beyond this, firm contact with the head is unlikely, even with the help of a flexible membrane coupling cone filled with degassed water. This is done so that only regions with the potential to be used as transducer locations were recorded in the simulations. The fourth edge of the sensor plane, the inferior direction (decreasing in Z), is limited by the quality of MRI and its corresponding segmentation. In regions lower than the nose, the MRI becomes darker (see Fig. 2.8), and its segmentation fails to separate the anatomical structures. Most of that region is classified as homogeneous skin-type soft tissue, with a small partition classified as air because of the mouth cavity. As the air-filled mouth cavity likely proves an insurmountable barrier for ultrasound delivery, it is unlikely this region will be considered for effective positioning, prompting its exclusion from the sensor map.

To optimise source position for transmission, the maximal average magnitude covered by the area of three different sized sources was chosen (Fig. 2.12). As can be seen in the magnitude map, smaller sources are encircling regions with higher average magnitude inside the larger sources. These positions were replicated in the phase map, showing the phases needed to be extracted for each source's forward propagation. The optimal transducer size study is presented in detail later in this chapter.

The three red dotted, dashed, and solid circles in both the magnitude and phase maps in Fig. 2.12 of diameters 25 mm, 45 mm, and 65 mm, respectively, represent the optimal placements of the three aperture-size transducers transmitting ultrasound into the page. The

largest diameter of 65 mm is chosen to avoid interference from the ear anatomically, as denoted by the rectangular MR image overlaid on Fig. 2.12.

2.7 FORWARD PROPAGATION

The lens design was first tested by applying the recorded phase from back propagation over the source plane, neglecting reflection and refraction in the lens. One example of such forward propagation is shown in Fig. 2.13 for a 65 mm diameter source when targeting the left perirhinal cortex. Three orthogonal views taken through the target point are shown. The -6 dB focal volume is roughly spherical with a volume of 30 mm^3 and has a peak pressure gain of 7.3. Despite the attenuation values of the medium materials, the simulated gain in peak pressure when using the recorded phases from the back propagation is promising for the use of lens-focused piston transducers as the source for transcranial ultrasound neuromodulation.

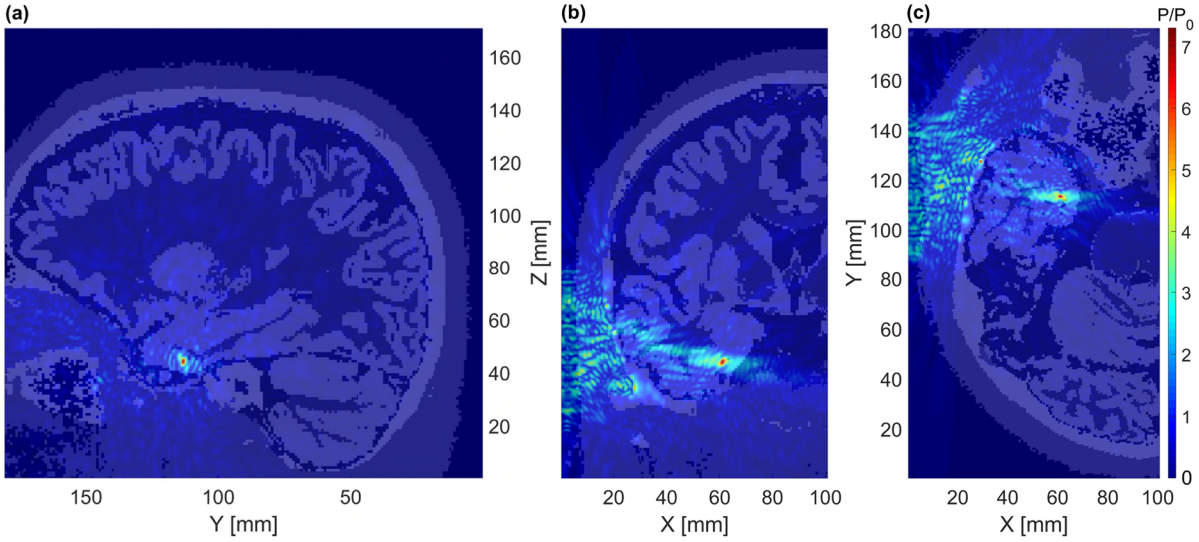

Fig. 2.13: Views of forward propagation 3D pressure distribution through the target site using phase from back propagation. The three views are orthogonal to each other. The piston source used has a diameter of 65 mm. Only the left side, where the target is located, is included in the simulation. Hence, only about half of the head is shown in both the axial and coronal views. **(a)** Sagittal view of pressure distribution through the target. **(b)** Coronal view of pressure distribution through the target. **(c)** Axial view of pressure distribution through the target.

One issue of concern is that the global maximum pressure gain of 8.9 is not at the target but rather in the skull. This is a common challenge for transcranial focused ultrasound studies due to the inhomogeneity in head tissue and the impedance mismatch introduced by the skull, causing near-field diffraction and reverberations in the skull.

At the anterior hippocampus, the simulation predicts a pressure gain of 0.34, less than 5% of the pressure at the left perirhinal cortex target site. The pressure difference between the target site and nearby areas was considered sufficient for this lens-focused piston source method to be used further in the study.

Before further analysis to determine optimal piston source size and frequency, forward propagation simulations using PDMS lenses were performed to check their performance compared to back propagation phase simulations. In order to prove the feasibility of using a PDMS lens, the formed focus should cover the target and not be multiple times larger than what would be obtained by applying the recorded phase directly. Firstly, the conversion from the measured phases to the geometry of the lens was conducted. The phase difference Φ in radians can be written as:

$$\Phi = 2\pi f \Delta t = 2\pi f \left(\frac{L}{c_1} - \frac{L}{c_2}\right);$$

Where f is frequency and Δt is time difference, which can be calculated as waves travelling through distance L in two different materials with different speeds of sound c_1 and c_2. Rearranging this equation converts the phase into lens thickness L:

$$L = \frac{\Phi}{2\pi f}\left(\frac{c_1 c_2}{c_1 - c_2}\right);$$

Where $c_1 > c_2$ and $\Phi \in [0, 2\pi]$ are defined for non-negative L.

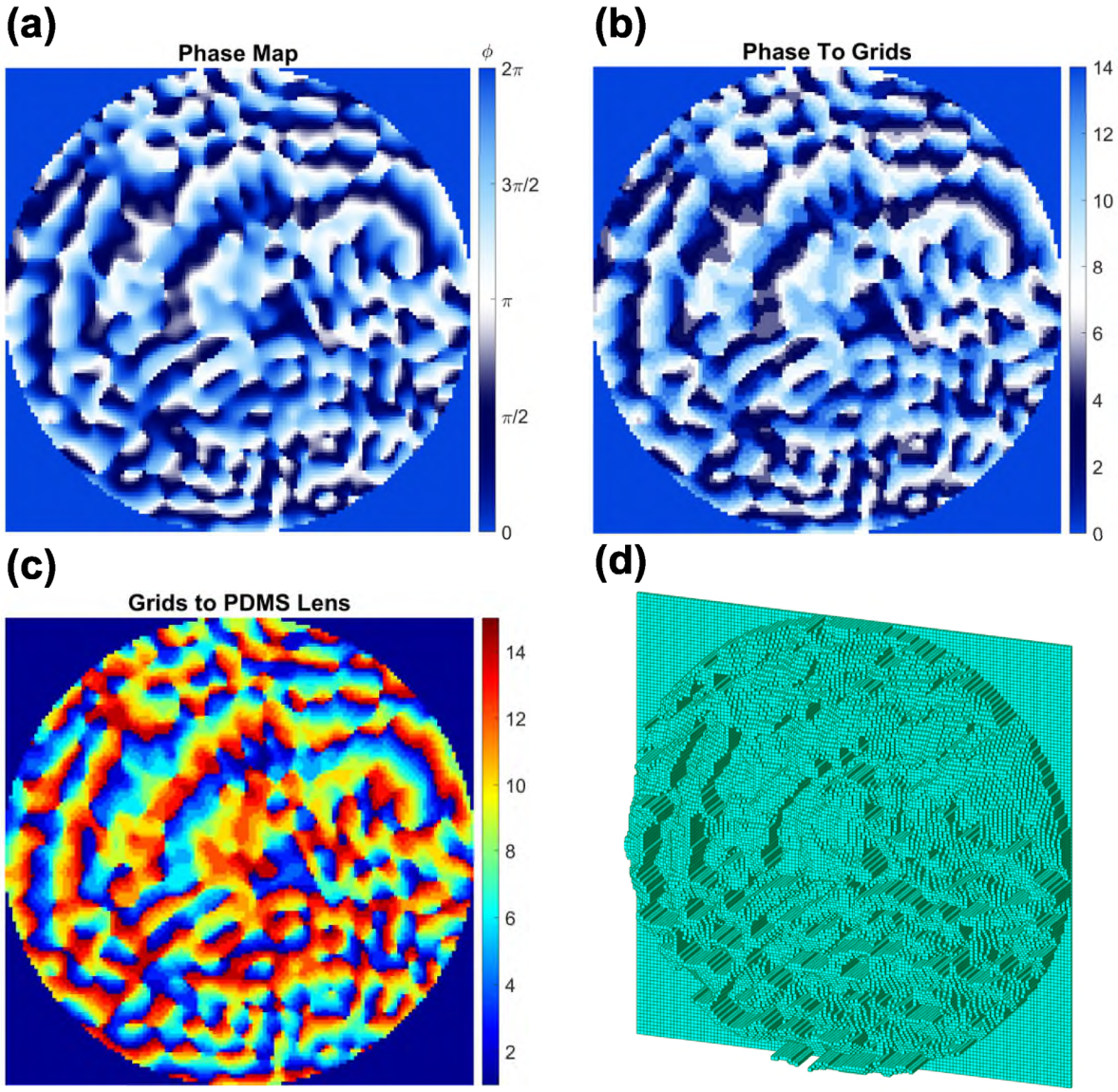

Fig. 2.14: Example of PDMS lens construction from the back propagation phases. This is a lens for a circular piston of 65 mm diameter. **(a)** The phase from back propagation employed by the lens. **(b)** Lens thickness representing the phase at each grid is digitised on to the computational grid with a uniform base layer added to the final lens design in **(c)** a 2D colour map view of the lens and **(d) a** 3D lens structure visualisation.

In back propagation simulations, the simulations have a step size of 50 ns. At a frequency of 500 kHz, this represents 40 samples per cycle, providing a resolution of 40 levels. This was directly used for the forward propagation described above to apply the required phase to the source plane. However, in order to implement the phases using an acoustic lens, this information has to be converted into the spatial domain, which in the simulations has a 0.5 mm grid size. At 500 kHz, with the properties of PDMS material, this 0.5 mm step size provides only 14 levels for the lens to accommodate the phases. This is shown by Fig. 2.14 (b) having clearer step changes than Fig. 2.14 (a), despite the overall pattern agreement. The final lens design shown in Fig. 2.14 (c) and (d) therefore required an additional layer of 0.5 mm at all positions to provide a support for the lens such that the regions surrounded by zero phases were connected. This base layer was also used to mount the lens to the transducer in experiments.

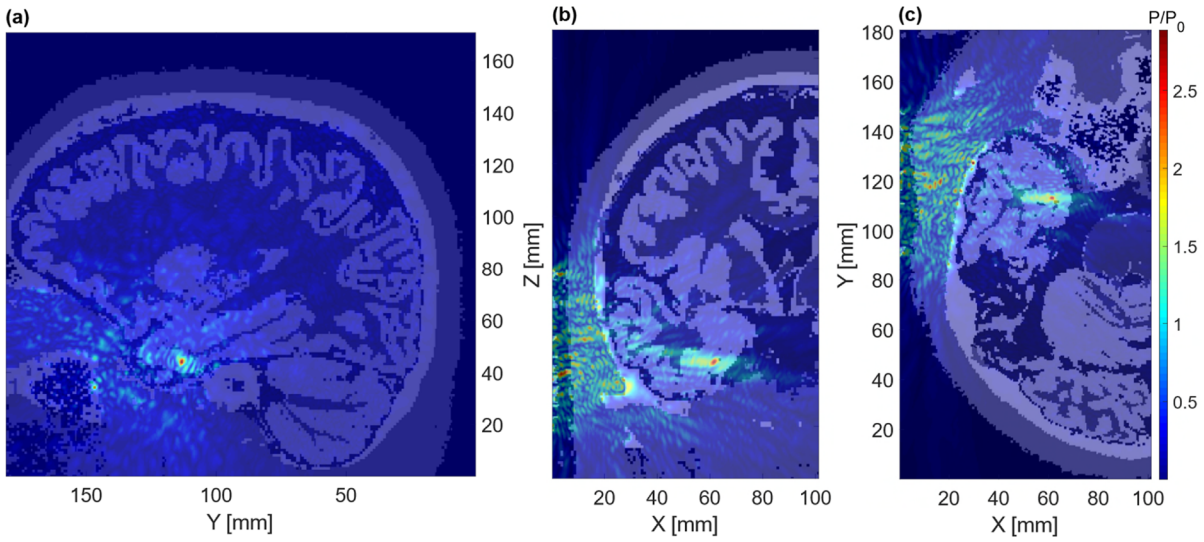

Fig. 2.15: Predicted 3D pressure distributions through the target site with a 14-level PDMS lens. The three views are orthogonal to each other. The piston source used has a diameter of 65 mm. Only the left side of the head, where the target is located, is included in the simulation. Hence, only about half of the head is shown in both the axial and coronal views. **(a)** Sagittal view of pressure distribution through the target. **(b)** Coronal view of pressure distribution through the target. **(c)** Axial view of pressure distribution through the target.

The pressure distribution predicted by k-Wave simulation for the discretised lens is shown in Fig. 2.15. The focusing was seen to occur at exactly the targeted location, showing the practical

power of the lens in correcting the skull aberration. Compared to the case of a smooth phase source shown in Fig. 2.13, the pressure distributions in the brain are similar. However, the pressure gain at the target site with the lens was reduced by 60%, from 7.3 to 2.9. Therefore, by introducing the lens materials into the simulation, there is a significant reduction in the magnitude of the focal pressure. The global maximum still resides in the skull, now having a pressure gain of 4.6, 58% higher than the target pressure, giving a significant increase in the magnitude difference between the target pressure and the global maximum. Three main causes of focal pressure gain reduction are: (i) the reduction of lens focusing ability caused by the resolution of phase dropping to 14 levels from the 40 levels in the recorded phase in back propagation; (ii) the reverberation in the lens due to reflections at surfaces; and (iii) the attenuation of the lens material.

Qualitatively, in Fig. 2.15, other than the reduction in magnitude, the pressure distribution is not considerably different from that in the benchmark case shown in Fig. 2.13 using phase from back propagation. This shows that the effect of reducing the levels used in the lens to represent the phases is a minor reason among the three. In terms of target pressure gain, when the perirhinal cortex is targeted, the anterior hippocampus shows a minimal pressure gain of 0.37 in the lens case, similar to the benchmark case. With the drop in the target pressure gain, the percentage difference in pressure between the targets was seen to reduce by about 8% compared to the benchmark case, indicating a wider spread of the ultrasound energy inside the head. It can therefore be concluded that about 8 percentage points out of the total 60% pressure gain reduction can be attributed to the reduced focusing ability when using a lens with fewer phase levels.

The significance of the reflection on the boundary of the wave leaving the source and entering the lens was then studied in simulations. The source was placed inside a water medium next to the lens materials to better reflect the built-in water matching layer present for most biomedical ultrasound transducers. To reveal the effect of the first reflection at the source-lens boundary, the source material was changed from water to PDMS. In doing so, the pressure gain at the target increased by 50.7% compared to the case with the source in water, to 3.7. This gives about a 10% increase in the pressure gain relative to the benchmark case, showing the reflection's role in the pressure reduction. Therefore, while reflection at the source-lens boundary may not be the most significant cause among the three, it does appear to be more important than the reduction in lens focusing ability caused by the lower phase resolution.

Based on the analysis of the above two causes, the loss in lens material is considered to be the most significant reason for the reduction in pressure gain, responsible for about 40 percentage points out of the total focal pressure reduction of 60%. This agrees with the plane wave transmission coefficient and loss estimated for ultrasound propagating through PDMS with the average thickness of the lens in water.

While there may be other causes of the pressure reduction, such as the reflection in the lens-water boundary when ultrasound leaves the lens and also reverberation in the lens, their existence is inseparable as long as the lens is in use. Consequently, the insertion loss of the lens method was considered to be the cause of the majority of the target pressure reduction compared to the benchmark case.

To conclude, when simulating using a lens, the pressure distribution inside the skull was similar to the benchmark case, yielding a tight focal volume at the target. This shows the promising

potential for using lenses for specific brain target stimulation. However, these simulations also show some potential risks for using lenses, as they were observed to introduce additional losses in target pressure gain compared to the benchmark case using phase from back propagation.

2.8 THERMAL SIMULATIONS

Based on the pressure distributions, the temperature rise caused by the ultrasound can be modelled by thermal simulations using the Pennes bioheat transfer equation (Pennes, 1948) described in Chapter 1. The simulated pressure distributions are given as pressure gains relative to the source pressure at each location. In order to conduct the thermal simulations in this section, the pressure is set to 0.6 MPa at the focus peak, which is the target pressure. The pulsing sequence follows that described in Chapter 1.

Before performing the thermal simulations in the complicated field of the head, simple testing cases were used to check the thermal simulation toolbox and justify the simplification of the pulsing sequence such that the computation time could be reduced. The PDMS Fresnel lens shown in Fig. 2.9 (d) was used. To test the reliability in a heterogeneous medium, a uniform skull layer of 5 mm thickness was added 5 mm in front of the lens to mimic the scalp-skull layer of the subject. The pulsing simplification was conducted in one burst of 0.3 s, comparing a half-intensity continuous wave throughout the burst length against the exact pulsing of 50% duty cycle with a pulse repetition frequency of 1000 Hz.

Firstly, the new pressure field with the added 5 mm skull layer was generated. There are only three types of material in this simulation: the PDMS lens, the soft tissue, and the skull. The thermal properties of PDMS are from the literature (Mark, 1999; Livermore and Voldman, 2016): 0.15 W/(m·K) for thermal conductivity and 1.46 kJ/(kg·K) for specific heat capacity.

The thermal properties of the skull and soft tissue are listed in Table 1.1. The new pressure field in Fig. 2.16 (a) shows locations with significant pressure magnitudes other than the focus. Therefore, based on the pressure fields, three locations were chosen to take measurements of temperature variation over time: a global pressure maximum in tissue between the lens and the skull, the maximum pressure location in the skull, and the maximum pressure in the focal volume. These three points are marked in Fig. 2.16 (b) by red, black, and blue points, respectively. In the pressure field, between the lens and the skull layer, standing waves are also present. The standing waves are created by reflection off the tissue-skull boundary, contributing to the magnitude of the global maximum.

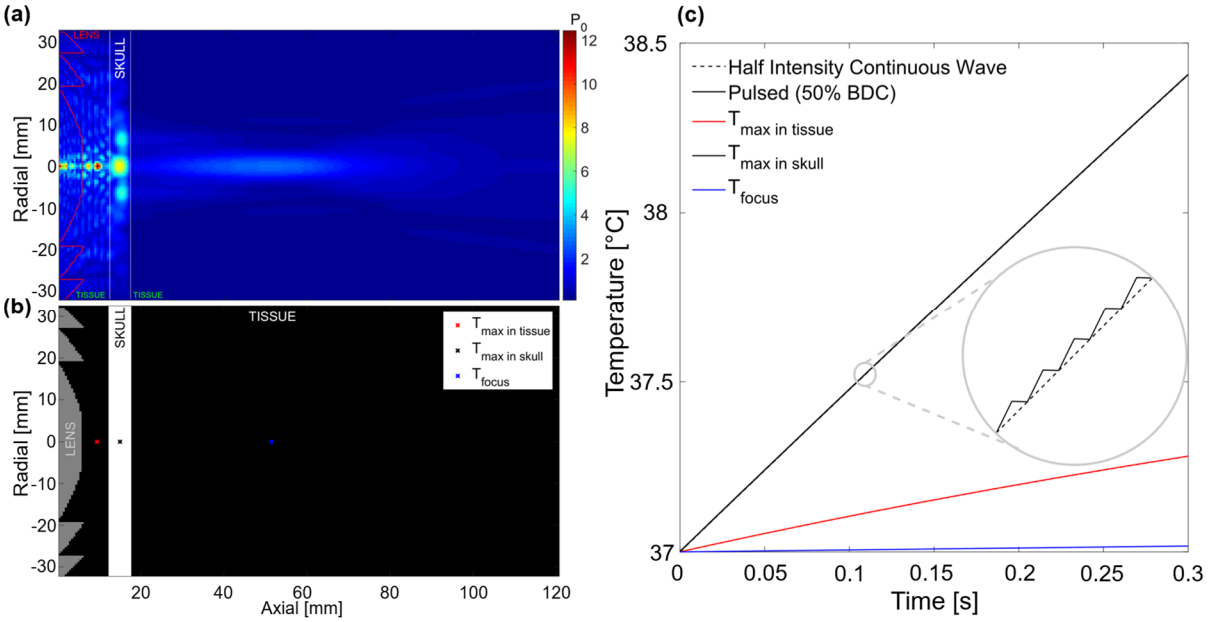

Fig. 2.16: k-Wave thermal solver: PDMS lens test case. Fresnel PDMS lens focusing through a uniform layer of skull. **(a)** A cross-sectional view of the test case pressure field with the skull layer. This is the input for the thermal simulations. **(b)** A cross-sectional view of the simulation space showing the materials. The crosses show significant locations in tissue (maximum pressure in tissue, skull, and focal region) at which the temperature was measured over time. **(c)** Pulsed (50% BDC) vs. half-intensity continuous wave. A continuous wave heating pulse at half the intensity and the 50% duty cycle pulsed waveform were compared to determine whether the individual pulses must be captured to accurately estimate the overall temperature rise.

The temperature field was calculated using the thermal solver in k-Wave. Periodic boundary conditions were used. The spatial grid was kept at 0.5 mm, and the time step was set to 0.1 ms in order to accurately represent the burst pattern. The initial condition was set to 37 °C everywhere in the simulation space.

In this test case with simple heterogeneous medium geometry, the three marker locations in Fig. 2.16 (b) representing the local pressure maxima in the regions correspond to the locations of the local highest temperature rise. The marker in the skull has the global maximum temperature rise despite not possessing the highest pressure gain. This is because the skull has lower thermal conductivity and specific heat capacity, resulting in easier heat accumulation and temperature rise. For the two markers in tissue, the red one with higher pressure gives a higher temperature rise, as expected.

The pulsed case, where the pulsing sequence is represented accurately, is compared to the half-intensity, continuous wave case. The difference, as shown in zoomed-in view in Fig. 2.16 (c), is overall insignificant, as the largest difference between the two is less than 0.01 °C, with the pulsed case above or equal to the continuous case as expected. Therefore, for the thermal simulations, the exact modelling of the pulsing within each burst is not necessary to yield accurate temperature rise results. Based on this, the timestep can be relaxed to use larger values, such that the computation cost can be greatly reduced.

Four time steps were tested using one burst of 0.3 s and its subsequent cooling period of 2.4 s. The timesteps tested are: 1 ms, 10 ms, 100 ms, and 300 ms. The results are shown in Fig. 2.17 (a). In these simulations, the global maximum temperature rise occurred in the skull bone, reaching 1.41 °C, which reduced to 0.95 °C at the end of the cooling period. In the tissue,

the maximal temperature elevation was only 0.28 °C. It can be seen that the predicted temperature profiles are within 0.2% over time in the range of time steps considered for all three marked locations. The temperature maps at the end of heating (t_1) at 0.3 s and cooling (t_2) at 2.7 s are shown in Fig. 2.17 (b). The temperature map in the skull clearly follows the pressure distribution pattern, with the side lobes in temperature corresponding to the side lobes in the pressure field. The thermal simulation can use a half-intensity continuous wave to represent the burst scheme of 50% duty cycle at a pulse repetition frequency of 1000 Hz with a timestep of 300 ms.

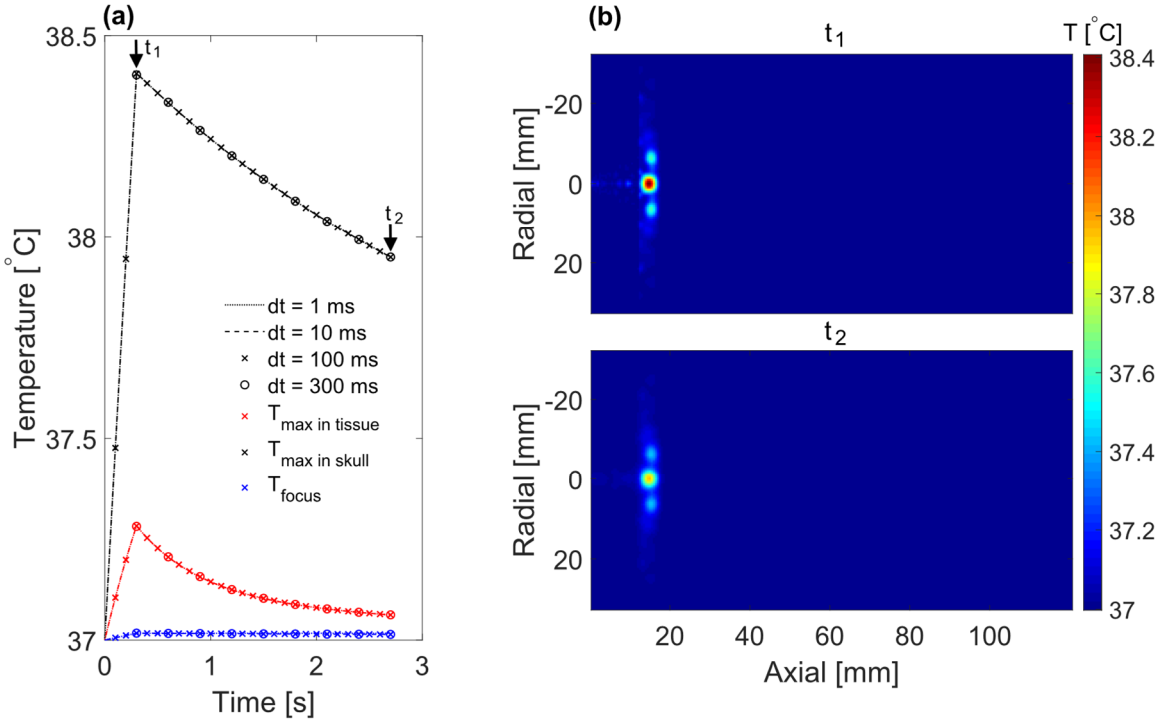

Fig. 2.17: k-Wave thermal solver: effect of timestep. (a) Temperature curves for three points in the simulated domain: maximum pressure in tissue, skull, and focal region, as indicated by the crosses in Fig. 2.30. Four different timesteps: 1 ms, 3 ms, 100 ms, and 300 ms were considered. **(b)** Spatial temperature maps at the end of the heating phase (t_1) and cooling phase (t_2).

In thermal simulations, an ultrasound pulsing sequence is set to 200 trials, each consisting of one 0.3 s burst and a subsequent 2.4 s cooling period, the inter stimulus interval. For now, the pulsing assumes ultrasound presents at every other trial, and in the trials, half of the pulses will

be control, i.e., no ultrasound stimulation. This effectively extends the inter stimulus interval from 2.4 s to 5.1 s, which consists of two 2.4 s designed inter stimulus intervals and one 0.3 s burst duration without ultrasound. For tasks with the desire to have grouped trials with ultrasound followed by grouped trials without ultrasound, heat simulations can be performed to reveal the maximum number of grouped trials available with ultrasound while ensuring safety constraints. Heat simulations will also be used to control the ultrasound pressure in order to fulfil the safety requirements.

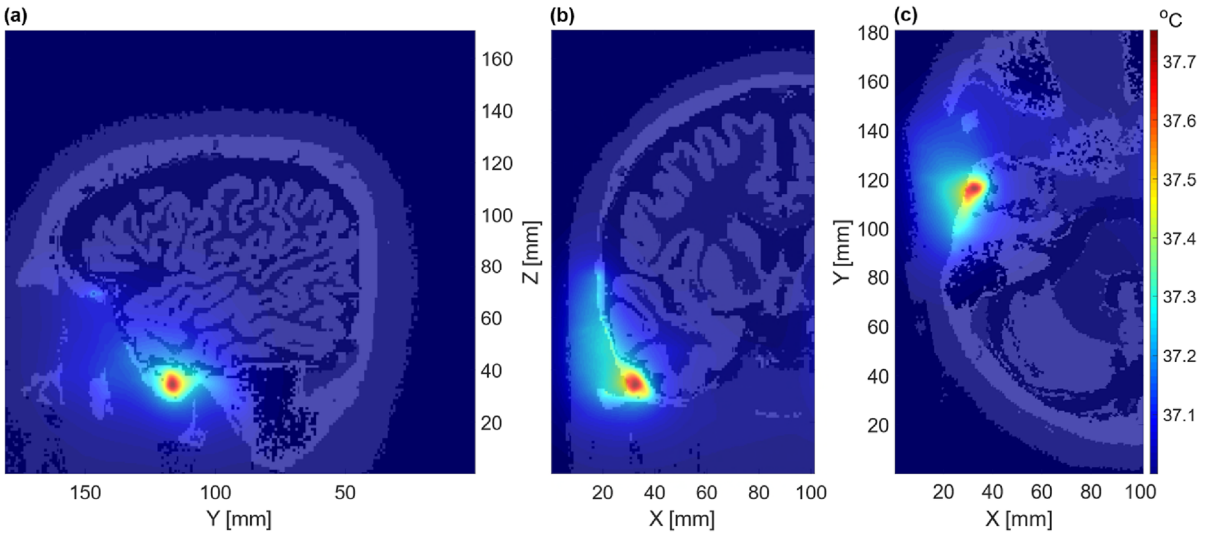

Fig. 2.18: Temperature distribution in the head due to the pressure distribution using the PDMS lens to target the left perirhinal cortex, as shown in Fig. 2.15. The three orthogonal views are through the point of global maximum temperature. This point is at a location where a bulk volume of skull is present. Only the left side, where the target is located, is included in the simulation. Hence, only about half of the head is shown in both the axial and coronal views. **(a)** Sagittal view of temperature distribution. **(b)** Coronal view of temperature distribution. **(c)** Axial view of temperature distribution.

As an example, the temperature rise map resulting from the pressure distribution by the PDMS lens acoustic simulation (Fig. 2.15) is shown in Fig. 2.18. The temperature rise mainly occurs where a bulk volume of skull material exists. The temperature at the target and in the majority of the brain tissue is small compared to this global maximum temperature. This is as expected, as the soft brain tissue has higher thermal conductivity and specific heat capacity than the skull. The maximum temperature rise in soft tissue occurs right next to the skull, near the global

maximum temperature. Clearly, this is caused not directly by an ultrasound-induced pressure field but by heating in the skull that conducts into the soft tissue. This maximum temperature rise in tissue was 0.55 °C. The temperature rise at the global maximum in the skull was 0.75 °C. The temperature rise at the target was 0.03 °C, which is considered negligible.

For the same target, i.e., the left perirhinal cortex of the same volunteer, the heat simulations for the benchmark case pressure distribution (Fig. 2.13) are also performed. Since the focal peak pressure is set to 0.6 MPa and the benchmark case has a higher target pressure gain, the temperature rise in the benchmark case is simply lower overall than the case with a PDMS lens. In the ideal case, the maximum temperature rise anywhere in brain tissue was 0.22 °C. The temperature rise at the global maximum in the skull was 0.32 °C. The temperature rise at the target was 0.02 °C.

For extra detail in the temperature map shown in the coronal view in Fig. 2.18 (b), relative high temperatures can be seen along the skull, illustrated by a long cyan shape extending far away from the global maximum up to about 80 mm in the Z direction. This is revealing the rough range of the skull covered by the pathway of ultrasound in the Z direction through the skull's absorption of the ultrasound energy. In addition, in the axial view in Fig. 2.18 (c), the diffusive pattern of heat is not uniform but more towards the outside of the skull. This is not solely caused by diffusion from the global temperature maximum but also caused by the reflecting ultrasound waves meeting the incoming waves, thereby creating a high pressure profile on the outside of the skull, resulting in a slightly higher temperature rise in this direction.

To summarise, when delivering 0.6 MPa to a deep target with 500 kHz ultrasound and a pulsing sequence of 0.3 s bursts followed by a 2.4 s inter stimulus interval with ultrasound every other

trial for 200 trials, the temperature rise in the head is well within the safety limit when using a PDMS lens. The result is also the worst-case scenario because: (i) the surrounding temperature in simulation is 37 °C higher than the room temperature; and (ii) CSF perfusion and blood circulation perfusion are not included in the model to take away the heat energy in the system. Even under these conditions, the temperature rise in brain tissue, especially at the target, is small. The temperature rise in brain tissue can be considered negligible except at that point next to the global temperature maximum in the skull.

2.9 PISTON TRANSDUCER SIZE SELECTION

Based on the acoustic and thermal modelling tools above, the desired aperture size of the ultrasound source was studied. The upper limit of the size was found to be 65 mm, representing the largest transducer that could be placed at the temporal window without interference with the auditory canal. While an ultrasound source with a larger aperture size can give a higher focal gain in free field, results in Fig. 2.12 indicate that the 65 mm diameter source had limited freedom in choosing the optimal position, defined here as the maximal average pressure magnitude in the overall region when analysed using back propagation. Indeed, there is the possibility that larger sources may be unable to irradiate the full region of interest, causing little to no transcranial ultrasound delivery and unwanted high pressure regions outside of the skull due to reflections. This section assesses the size of the source when dealing with this complicated, heterogenous case.

Three source aperture diameters were tested: 25 mm, 45 mm, and 65 mm. The ultrasound frequency was chosen to be fixed at 500 kHz. Three subjects' MRI data were randomly chosen for this analysis, each with 4 target sites, giving 12 targets in total. The four targets are the left and right perirhinal cortex and the left and right anterior hippocampus. Each location was

targeted with all three different-sized sources, giving a total of 36 sets of simulations. The details of each set of simulations are described in the flowchart shown in Fig. 2.19.

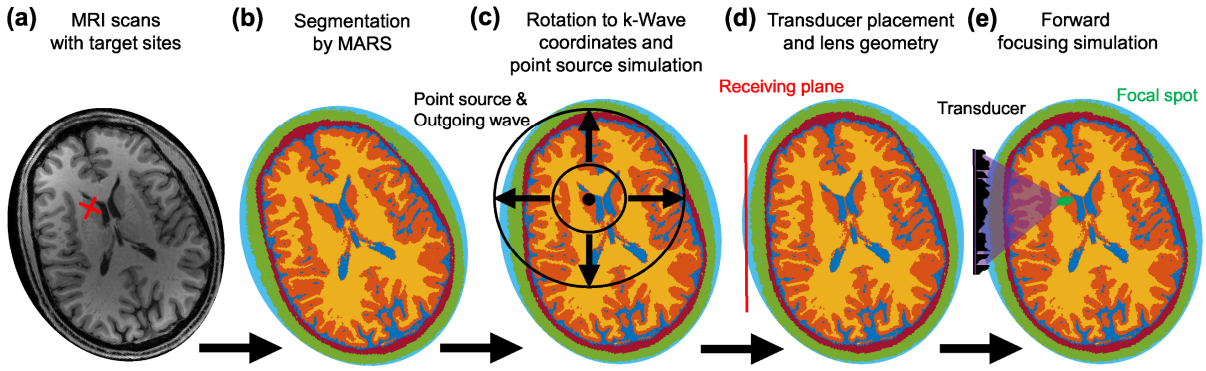

Fig. 2.19: Flowchart in the source selection analysis. Summary of the modelling procedure for optimal source conditions. **(a)** T1-weighted MRI provides the head anatomy and markers of target sites. **(b)** Segmentation of MRI into tissue types and target marker positions calculated in preparation for simulations. **(c)** An acoustic point source is placed at the target, and the wave propagates outwards through the skull to a receiving plane placed as close to the head as possible without contact, corresponding to the set of all possible transducer positions for focusing on the target site. **(d)** The steady-state magnitude and phase distribution are extracted on this receiving surface, giving the selection of transducer placement. For the same target, different-sized sources possess different optimal positions. **(e)** The forward simulations. Both the pressure and temperature distributions are generated for comparison purposes.

Based on the MRI segmented data and the target locations, the point source simulations described previously were utilised to reveal the optimal location for placing the source in each case. In addition, the required phases to focus on the target were extracted, as shown in Fig. 2.12. Benchmark case forward acoustic simulations, which directly apply the back propagated phases to the source elements, were used. In this case, the phases have the same quality, such that differences in results for a target could be isolated primarily to the size of the aperture.

When comparing the pressure distributions produced by the different-sized sources, it becomes clear that the largest source of 65 mm in diameter still yields the highest target pressure gain

and the smallest focal volume across all 12 targets, despite the complicated heterogenous medium (Fig. 2.20 (b) and (c)). Based on these results, a 65 mm diameter source is preferred.

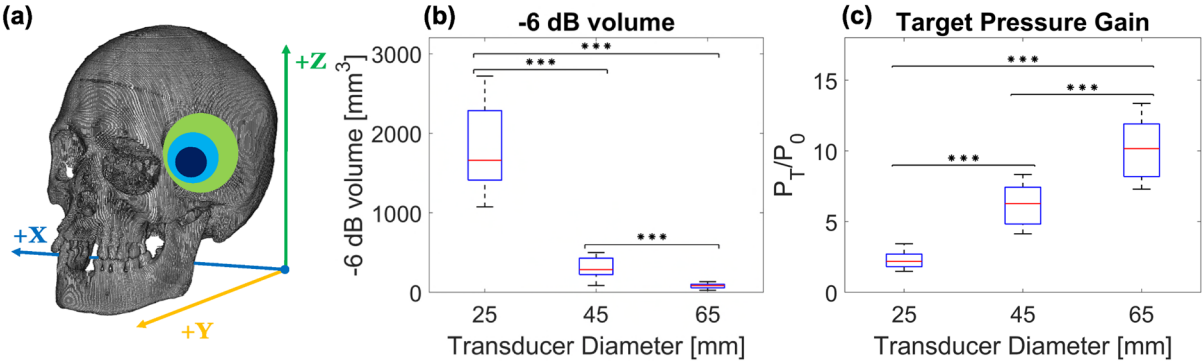

Fig. 2.20: Piston size analysis comparison. One-tailed Welch's t-test (unknown variance, assuming normal distribution) and Hommel methods with adjusted p-values for multiple comparisons are used. ***: $p \leqslant 0.001$, N = 12. **(a)** Illustration of transducer size analysis: 25 mm (navy blue), 45 mm (cyan), and 65 mm (green). **(b)** -6 dB focal volume. **(c)** Target pressure (P_T) gain.

To verify this, comparisons were also carried out on the brain as a whole (global pressure maxima) and the other region of interest to assess off-target effects, e.g., left anterior hippocampus when the left perirhinal cortex is targeted and vice versa.

In all twelve cases, the global pressure maxima increased with increasing source size. However, in three cases, global maximum gains were found to be insignificantly different between source sizes of 45 and 65 mm diameter, suggesting that the ultrasound energy wasted transmitting through the skull was not significantly reduced between the two. However, the target pressure gain was still reduced significantly when using the 45 mm source. Sources with a diameter of 25 mm always gave the lowest global pressure maximum in each case.

When comparing the percentage difference between the target pressure and the global maximum pressure, the source of size 25 mm has the highest difference in most cases, showing the lowest effectiveness in transcranial ultrasound delivery. These results suggest that smaller

sources have little to no improvement in improving delivery, supporting the use of the largest source in the range available, i.e., the 65 mm diameter source, for effective transcranial focused ultrasound delivery.

In evaluating the off-target site, the 45 mm diameter source was found to have a higher pressure gain compared to the 65 mm diameter source, likely due to the reduced focusing ability of smaller sources. In terms of the percentage difference between the pressure gain at the target and the other target, it is universally the case that larger sources provided larger differences as desired.

Thermal modelling was also performed. As the target pressure for all cases was set to 0.6 MPa, it is expected that smaller sources will have a higher temperature rise given their lower target pressure gain, as shown in Fig. 2.20 (c). This trend was seen to be universally true for both the temperature rise at target, at the global temperature maximum, and in brain tissues.

The global maximum temperature rise always occurs in the skull. While all sources were found to be within the 3 °C safety limit in the skull, the 65 mm diameter source showed less than a 0.35 °C increase compared to the 1.6 °C increase simulated with the 25 mm diameter source.

At the target, the temperature rise for the 65 mm diameter source in all cases was less than 0.14 °C. The temperature rise in brain tissue closer to the skull was higher due to conduction from the skull, but within 0.22 °C. For the 25 mm diameter sources, the values of brain tissue maximum temperature rise exceed 1 °C for three cases, exceeding the set safety limit of 1 °C in brain tissue, suggesting that a 25 mm diameter source is not appropriate.

To conclude, a 65 mm diameter source focused better than the 45 mm and 25 mm sources, as it provided: (i) higher target pressure gain; (ii) smaller -6 dB focal volume; (iii) lower difference between target pressure and global maximum pressure; (iv) larger difference between target pressure and the pressure at the other target on the same side at the time; and (v) lower temperature rises in tissue. Therefore, based on the pressure and temperature modelling results presented, this analysis of the desired size of piston transducer supports a piston transducer of size 65 mm.

2.10 Piston Transducer Frequency Selection

The effect of ultrasound frequency on the pressure and temperature fields was considered using the 65 mm diameter source. The same three randomly chosen subjects' MRI data from the size analysis were used, each with 4 target sites, giving 12 targets in total. The four targets are the left and right perirhinal cortex and the left and right anterior hippocampus. Each location was targeted with three sources of different frequencies and the individual case's optimal source position and corresponding phase information.

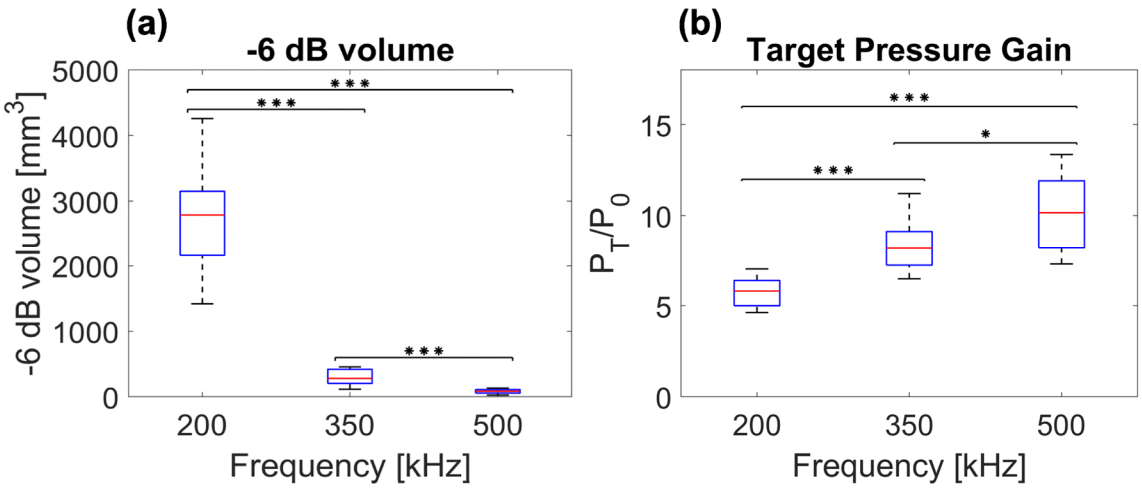

Fig. 2.21: Piston frequency analysis comparison. Three frequencies were tested: 200 kHz, 350 kHz, and 500 kHz. One tailed Welch's t-test (unknown variance, assuming normal distribution) and Hommel methods adjusted p-values for multiple comparisons are used. *: $p \leqslant 0.05$, ***: $p \leqslant 0.001$, N = 12. **(a)** -6 dB focal volume. **(b)** Target pressure (P_T) gain.

Three frequencies within the range of 200 ~ 500 kHz used in ultrasound neuromodulation (Blackmore et al., 2019) were chosen for analysis: 200 kHz, 350 kHz, and 500 kHz. Frequencies lower than 500 kHz, which have lower medium attenuation, have the potential to provide higher focal gain by transmitting more ultrasound energy through the skull with constant source power. However, the lower frequency also means a more dispersed focal region, even in free field, leading to lower focal gain and a higher risk of developing standing waves, which raises more safety concerns. The preferred frequency balances between these two effects when propagating through the subject's head.

The -6 dB volume and target pressure gain using different frequencies are summarised in Fig. 2.21 (a) and (b), respectively. The results show that 500 kHz generated the smallest -6 dB focal volume and highest target pressure. It also had a smaller variation in predicted focal volume. Therefore, 500 kHz was preferred for this work. Higher frequencies are shown to increase brain stimulation threshold (King et al., 2013; Tufail et al., 2010) and increase reflections on ultrasound reaching the skull (Chen et al., 2023).

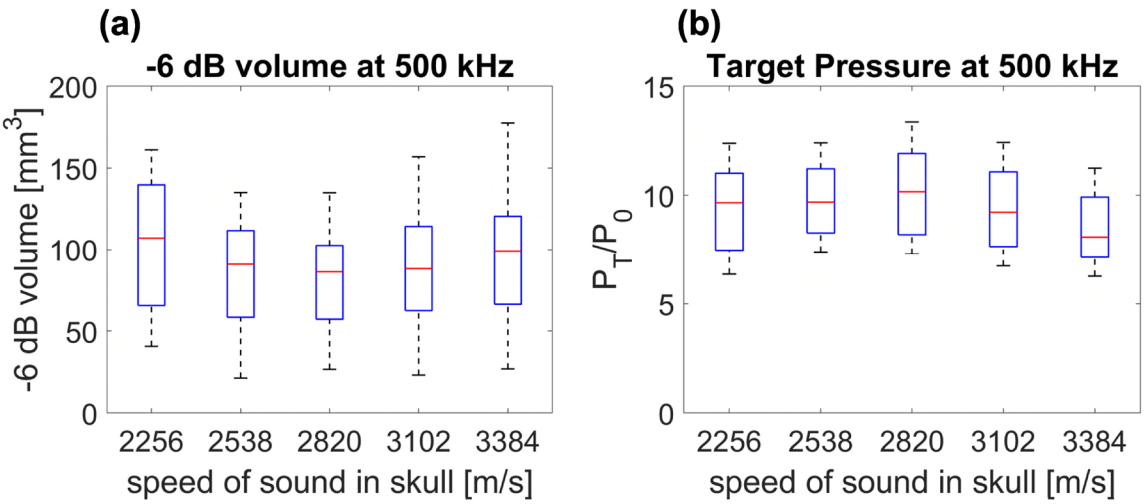

Fig. 2.22: Impact on the 500 kHz ultrasound field due to variation in the speed of sound in the skull. Five speeds of sound in the skull were tested: 2256 m/s (–20%), 2538 m/s (–10%), 2820 m/s, 3102 m/s (+10%), and 3384 m/s (+20%). One-tailed Welch's t-test (unknown variance, assuming normal distribution) and Hommel methods with adjusted p-values for multiple comparisons are used. N = 12. **(a)** -6 dB focal volume. **(b)** Target pressure (P_T) gain.

Thermal modelling was also performed with the same pulsing sequence and target pressure of 0.6 MPa as in the source size analysis previously. The highest target temperature rise is 0.12 °C from a 200 kHz source. All global maximum temperature rises occur in the skull. The highest is 1.5 °C from a 200 kHz source. Lower frequency gives lower tissue attenuation, hence lower heat generation from the absorption of the delivered acoustic energy. Despite this, the lower frequency resulted in a higher temperature rise at the target, global maximum, and brain tissue maximum. Across all cases, the 500 kHz source gives the lowest temperature rise in the head.

The robustness of 500 kHz to variations in the speed of sound in the skull was also tested. A speed of sound of 2820 m/s was used in the acoustic simulations based on the data in the literature (see Table 1.1). Due to the cortical bone and trabecular bone in the inhomogeneous skull, there are significant variations in the skull's presence at different locations on one skull and across different subjects. The focusing phases for all cases were from the point source simulations using 2820 m/s for the skull. But the forward propagation was carried out using a speed of sound of ±10% and ±20%. That is from 2256 m/s to 3384 m/s, covering the reported range of sound speed in the skull. The -6 dB volume and target pressure gain using different speeds of sound in the skull are summarised in Fig. 2.22 (a) and (b), respectively. The data suggest that as the speed of sound varies away from the designed speed of sound (2820 m/s), the target pressure decreases and the -6 dB volume increases, although the differences were not statistically significant.

To conclude, compared to the lower frequencies, 500 kHz can reliably provide: (i) higher target pressure gain; (ii) smaller -6 dB focal volume; (iii) lower variation in the -6 dB focal volume; (iv) lower temperature rise in the subject; and (v) sufficient robustness against ±20% variation

in the speed of sound of the skull, the most significant acoustic barrier in the human head. Therefore, based on the pressure and temperature modelling results presented, the desired frequency of the piston transducer is 500 kHz.

2.11 SIMULATION SPACE STUDY

The acoustic simulations shown so far only used the relevant half of the subject's head as the ultrasound propagation space for the single ultrasound source. This type of simulation is given the name 'half head single source' (HHSS). HHSS simulation is fast to compute due to the smaller simulation space used, and it captures the main features of the acoustic field on the relevant side of the head. It is important to compare HHSS results to whole head single source (WHSS) simulations to see if it is necessary to include the whole head in the modelling space.

Axial and coronal views of pressure distribution from the WHSS simulation are shown in Fig. 2.23 (a) and (b), respectively. The focus is formed by a target-specific PDMS lens made for this subject's right anterior hippocampus. The focal peak is formed within the 5 mm diameter sphere target spot. The WHSS predicts standing waves on the left side of the head, which are outside the simulation space of the HHSS simulation for the right anterior hippocampus. The standing waves are formed by the interaction of the incident ultrasound and the reflection from the left side of the skull. Although the magnitude of the standing waves was only 40% of the pressure at the target, they could potentially stimulate other off-target brain locations, demonstrating that a WHSS simulation is necessary to consider assessing its impact and safety within the brain.

The yellow arrow in Fig. 2.23 (b) also shows other high-pressure spots with comparable magnitude to the standing waves far off the main ultrasound pathway. Although this is on the

right side of the head within the simulation space of HHSS simulation, it is not observed in HHSS simulation, as shown in Fig. 2.24 (c). These pressure spots show the complicated ultrasound pathway inside the skull, consisting of multiple reflections off the skull.

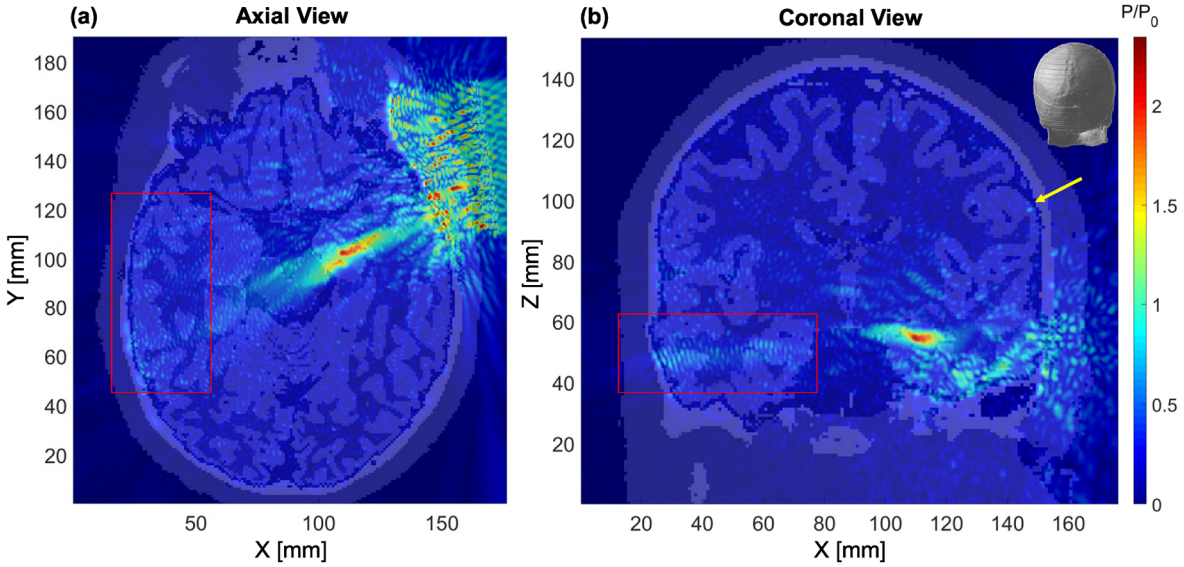

Fig. 2.23: Example of whole head single source (WHSS) simulation. A PDMS lens is used to target the right anterior hippocampus in this case. Red rectangles show standing waves on the left side of the head that are not captured by HHSS. **(a)** Axial view of pressure distribution through the target. **(b)** Coronal view of pressure distribution through the target. The yellow arrow shows an example of high-pressure spots that were not observed in the HHSS simulation.

Quantitatively, the pressure gain at the target in the WHSS simulation for the right anterior hippocampus is 2.34, only 2.5% higher than the calculated 2.29 in the HHSS simulation. This small increase is likely due to the reflection of ultrasound waves against the skull and their propagation back to the target, forming a constructive interference wave pattern. When targeting the right anterior hippocampus, HHSS simulation predicts a pressure gain of 0.44 at the right perirhinal cortex, only 19% of the target pressure. However, WHSS simulation predicts 0.53 at the right perirhinal cortex, corresponding to 23% of the target pressure at the right anterior hippocampus. The WHSS simulation also reveals the pressure gain at the left perirhinal cortex (0.38) and left anterior hippocampus (0.72) when targeting the right anterior hippocampus, when these locations were otherwise not included in the HHSS simulation space.

The above results show that the simulation including the whole head space is necessary to reveal a more complete picture of the ultrasound field created inside a subject's brain. The differences of -6 dB focal volume between the results of the corresponding HHSS simulations and WHSS simulations were less than 0.5%. Thermal simulations were also performed for the WHSS simulations. Despite the differences in the pressure distribution, the temperature rise is negligibly lower due to the small increase in target pressure gain for the WHSS simulations.

2.12 Bilateral Stimulation Modelling

To expand clinical application to bilateral brain targets, simultaneous paired source stimulation interference was examined. Bilateral structures in the brain, such as the anterior hippocampus and perirhinal cortex, are expected to be stimulated simultaneously, necessitating whole head paired sources (WHPS) simulations.

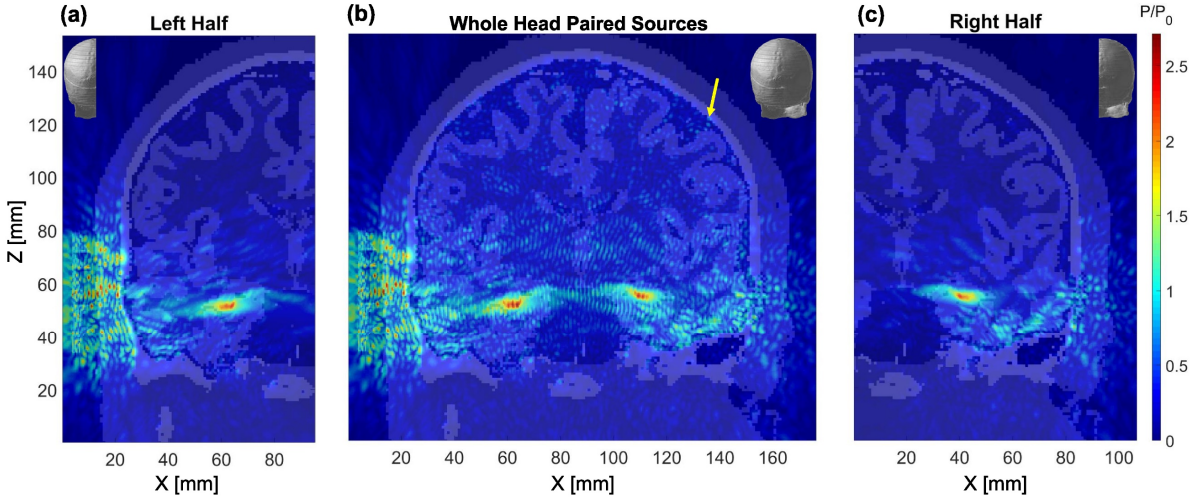

Fig. 2.24: Comparison of whole head paired sources (WHPS) simulation to HHSS simulations. PDMS lenses are used to target the left and right anterior hippocampus. **(a)** Coronal view of pressure distribution by HHSS simulation for the left anterior hippocampus. **(b)** Coronal view of pressure distribution by WHPS simulation for the anterior hippocampus pair. The yellow arrow shows an example of high-pressure spots that were not observed in HHSS. **(c)** Coronal view of pressure distribution by HHSS simulation for the right anterior hippocampus.

Fig. 2.24 compares the coronal views of the WHPS simulation to the corresponding HHSS simulations when targeting the anterior hippocampus pair. In Fig. 2.24 (b), the WHPS predicts a standing wave pattern across the entire pressure distribution inside the skull. Strong standing waves are expected as two transducers transmit ultrasound to each other. In Fig. 2.24 (b), the peak focal positions are formed within the 5 mm diameter sphere target spots with a 0.50 mm shift and a 0.71 mm shift compared to the corresponding left and right HHSS simulations. Similar to the WHSS simulation in Fig. 2.23, the yellow arrow in Fig. 2.24 (b) shows pressure spots that are not observed in the HHSS simulation, as shown in Fig. 2.24 (c). A lot more of these pressure spots are observed in WHPS simulation results compared to HHSS or WHSS simulations.

In WHPS simulations targeting the anterior hippocampus pair, the pressure gain at the left anterior hippocampus is 2.71, 13% higher than the 2.36 in the HHSS simulation, and the pressure gain at the right anterior hippocampus is 2.48, 7.8% higher than the 2.29 in the HHSS simulation. The pressure gain at the left perirhinal cortex is 0.98, 36% of the target gain at the left anterior hippocampus, and the pressure gain at the right perirhinal cortex is 0.93, 37% of the target gain at the right anterior hippocampus. Overall, with two sources sending ultrasound into the head in WHPS simulations, energy is sent into the head and passes through the midline. The percentage increase in the non-targeted region (perirhinal cortex pair in the example here) is therefore higher than that in the target region (anterior hippocampus pair in the example here).

Due to the presence of standing waves, the -6 dB focal volume is changed in the WHPS simulation. For the left anterior hippocampus, the -6 dB focal volume is reduced by 5% from 372 mm^3 in the HHSS simulation to 355 mm^3 in the WHPS simulation. For the right anterior

hippocampus, the -6 dB focal volume is increased by 32% from 486.5 mm^3 in the HHSS simulation to 713 mm^3 in the WHPS simulation. The variability in the focal volume change reveals that the contribution of reflections and the ultrasound from the source on the other side depends on the particular travelling path in each case, which impacts the travelling time, hence the nature of whether the ultrasound waves have constructive or destructive interference at the focus.

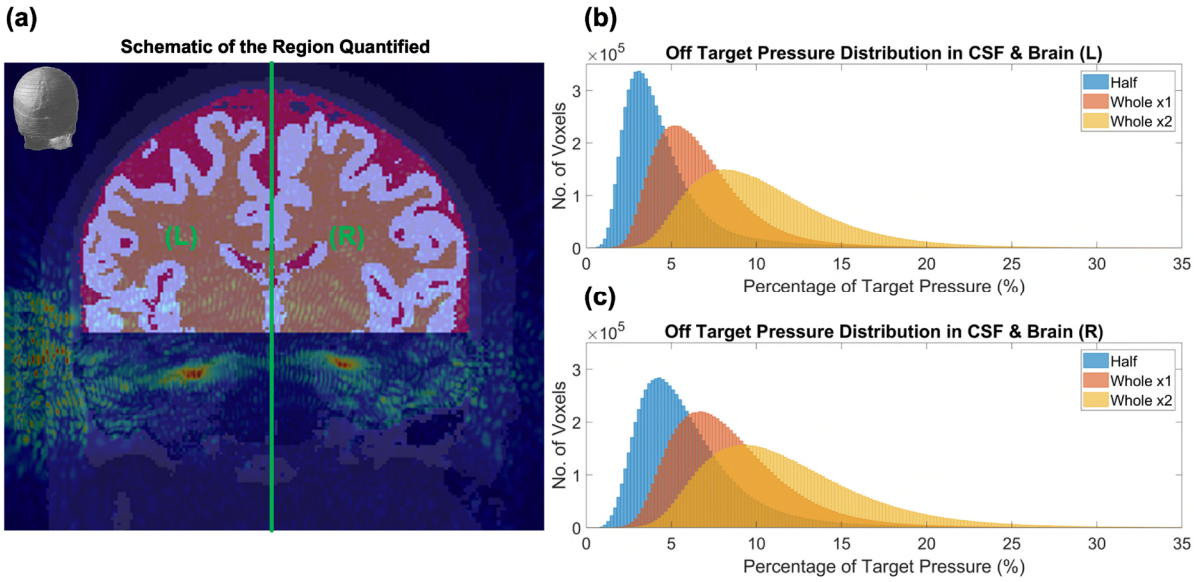

Fig. 2.25: Pressure distribution comparison in the brain region far away from the target. Half head single source simulation (Half), whole head single source simulation (Whole ×1), and whole head paired sources simulations (Whole ×2) for targeting the anterior hippocampus pair in the same subject are compared. **(a)** Coronal view schematic indicating the region used in this comparison. **(b)** Histogram of pressure distribution for the left side of the head. **(c)** Histogram of pressure distribution for the right side of the head.

So far, high pressure spots have formed in WHSS and WHPS simulations far away from the target locations, as seen in Fig. 2.23 and Fig. 2.24. The pressure distribution far away from the targets was quantified and compared in Fig. 2.25 for HHSS, WHSS, and WHPS simulations in the same subject. The region used in this comparison is highlighted in the illustration in Fig. 2.25 (a). Only voxels representing CSF and brain are included in the comparison, excluding the main acoustic pathway and target focal regions. In order to compare the HHSS simulations, the left and right sides of the head were compared separately. The results shown

in Fig. 2.25 (b) and (c) are for the left and right sides of the head, respectively. The histograms are plotted as the number of voxels against normalised pressure magnitude in the form of a percentage of target pressure.

The HHSS distributions (blue) have the lowest mean percentage of target pressure among the three types of simulations. The WHSS distributions (orange) start to increase in mean and spread out. The WHPS distributions have the highest mean and the greatest spread of pressure. The results show that: (i) by including the whole head into simulation space, more high pressure spots are formed far away from the main ultrasound path and targets due to the ultrasound reflections off the skull boundary; and (ii) by using two sources, even more high pressure spots are formed far away from the main ultrasound path and targets due to an increase in ultrasound energy sent into the skull.

To conclude, the simulations using the whole head space reveal more useful information about the pressure distribution inside the subject's head. As long as the computation power and time permit, whole head simulations should be performed as the adequate simulation standard for human trial planning. WHPS simulations show standing wave patterns across the formed pressure distribution. As a result, certain aspects of the focal region have changed significantly from the HHSS simulation results. Therefore, when two transducers are used to stimulate two locations in the brain simultaneously, the WHPS simulation must be performed to check the changes from the corresponding HHSS simulations.

2.13 TARGETING GPi AND STN

Utilising the temporal bone window on the human skull and target-specific acoustic lenses, deep brain targets in humans can be targeted by transcranial focused ultrasound with high

spatial resolution. In the sections presented so far, PDMS lenses were demonstrated to successfully target the anterior hippocampus and perirhinal cortex in simulations. Here, it is demonstrated that the PDMS lens can also be used to target the internal globus pallidus (GPi) and subthalamic nucleus (STN) using the 500 kHz, 65 mm diameter transducer.

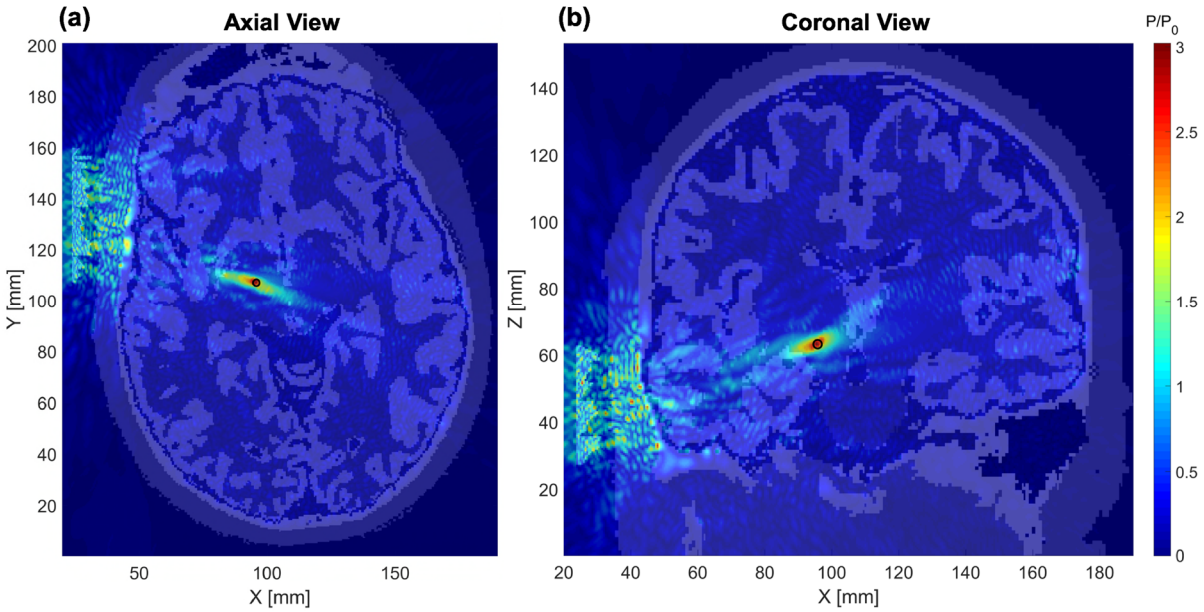

Fig. 2.26: Stimulating the left STN. A PDMS lens is used in WHSS simulation. The black circles of 5 mm diameter demonstrate the desired stimulation location. **(a)** Axial view of pressure distribution through the target. **(b)** Coronal view of pressure distribution through the target.

The pressure distribution when stimulating the left STN is shown in Fig. 2.26. The desired stimulation location (volume of a 5 mm diameter sphere) is shown by black circles. This volume is fully covered by the created ultrasound focus. The focal pressure gain at the target is 3.12, and the created -6 dB focal volume is 219 mm^3. In this particular case, the lens is not only responsible for focusing and skull aberration correction but also for steering the ultrasound towards the top of the head to reach the target from the selected transducer position.

Bilateral targeting of the GPi pair is shown in Fig. 2.27. The focal pressure gain is 2.37 at the left GPi and 2.12 at the right GPi. The -6 dB focal volume is 400 mm^3 at the left GPi and

611 mm^3 at the right GPi. As the WHPS simulations conducted before for the anterior hippocampus and perirhinal cortex showed, standing waves are affecting the focal region.

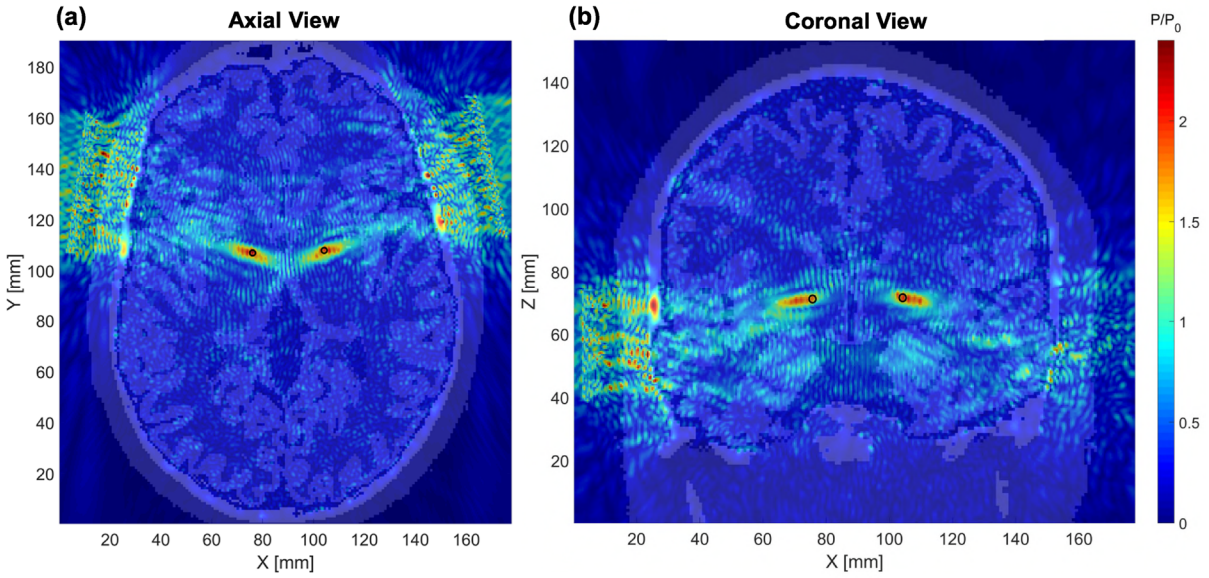

Fig. 2.27: Stimulating the GPi pair. PDMS lenses are used in WHTS simulation. The black circles of 5 mm diameter demonstrate the desired stimulation location. **(a)** Axial view of pressure distribution through the target. **(b)** Coronal view of pressure distribution through the target.

2.14 SUMMARY & DISCUSSION

The method of using acoustic lenses together with a piston ultrasound transducer for transcranial ultrasound stimulation has been investigated here. Target-specific lenses can cope with the variation across targets and subjects, such that the same transducer can be used for a number of targets. PDMS is chosen as the lens material through simulation analysis comparing the 3D printable materials: ABS, PDMS, and PMMA.

Patient-specific lenses were then designed by importing MRI data into simulation. A point source at the target was used to determine the phase and amplitude outside the head, from which the lens was designed. Forward simulations were then performed to create the focus using the lens with a sufficient amount of target pressure gain. The pressure field by lens

generally agreed with a benchmark case using the recorded phase only but with a substantially lower focal gain due to the losses related to the lens material layer. For better performance, array systems similar to those used for brain surgery (Exablate Neuro, Insightec, Tirat Carmel, Israel) are options for neuromodulation in the long run, despite the high cost of a similar device.

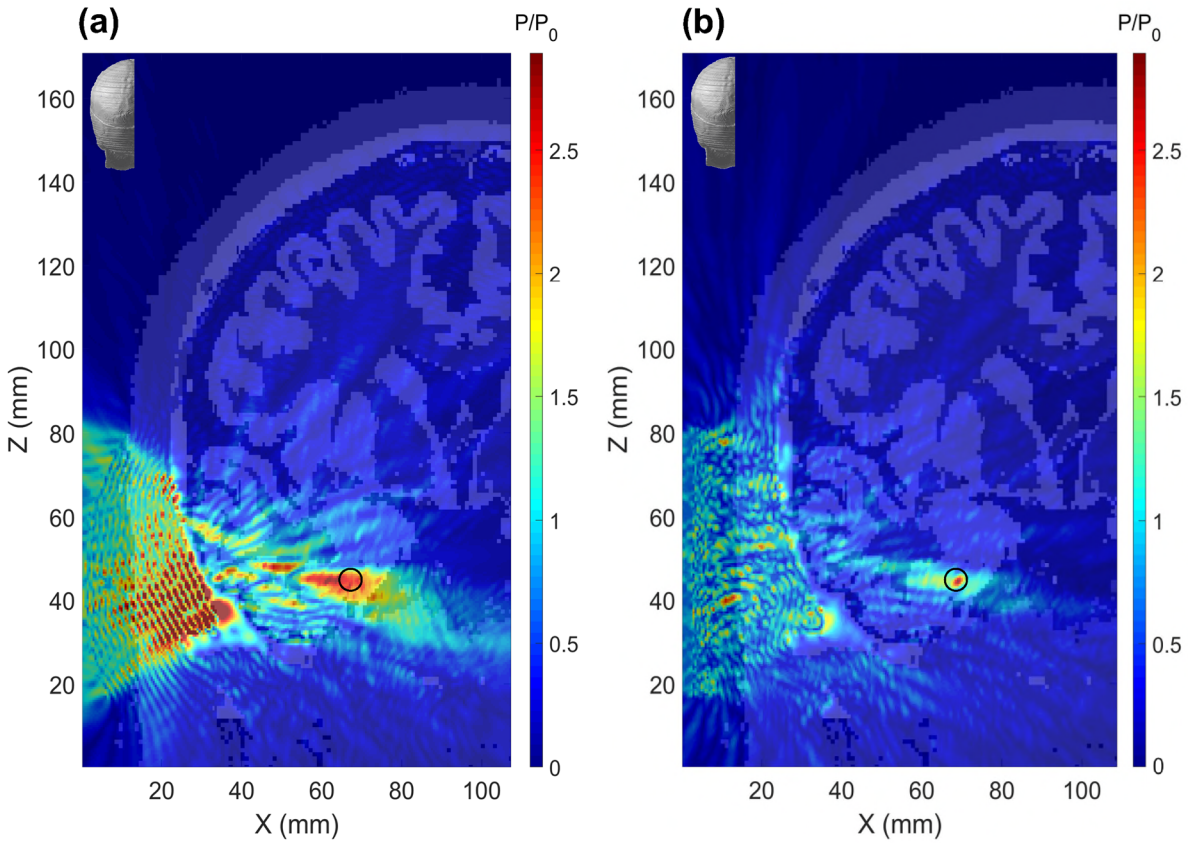

Fig. 2.28: Focusing capability comparison: target-specific lens versus single-element focused transducer. The single element transducers have the same frequency of 500 kHz and an aperture diameter of 64 mm. The left anterior hippocampus is targeted in HHSS simulations. **(a)** Coronal view of the pressure field by a single-element focused transducer. **(b)** Coronal views of the pressure field by the PDMS lens.

The simulations have shown that a target-specific lens with a piston transducer can generate a smaller focus than a single-element focused transducer inside the head. An example comparison for the left anterior hippocampus using 64 mm diameter, 500 kHz transducers is shown in Fig. 2.28. The radius of curvature of the single-element focused transducer is set to be 68 mm in order to reach the target, resulting in a target pressure gain of 2.72 and a -6 dB volume of 1461 mm^3, as in Fig. 2.28 (a). In comparison, the PDMS lens shown in Fig. 2.28 (b)

has a higher target pressure gain of 2.91 and a tighter -6 dB focal volume of 194 mm^3. This comparison shows the necessity of the lens for creating a more spatially specific and reliable focal volume inside the human head.

Simulations using a range of transducer diameters and frequencies were performed. The best results were obtained with a 65 mm diameter transducer with a frequency of 500 kHz. 65 mm is the largest size that can be fitted to the temporal bone window of the human skull without covering the ear. This provides the best target pressure gain and the lowest side effects, such as the pressure gain inside the skull on the ultrasound path and the temperature rise in the head. The robustness of focus formation against variation in the speed of sound in the skull was also demonstrated.

Simulations using the whole head space have revealed more useful information about the pressure distribution inside the head as they capture the new and vital nature of the sound field inside the skull. Due to the existence of the additional standing wave pattern, modelling is still necessary for the whole head space despite the increased computation cost. Temperature rises in the brain tissue caused by the additional standing waves in the WHSS and the WHPS simulations were found to be negligible.

3

LENS METHOD VALIDATION ON SKULL SAMPLES

Validation studies of the lens method for TUS in humans described in Chapter 2 are presented in this chapter. Firstly, three Fresnel PDMS lenses based on different simulated focal depths (65 mm, 75 mm, and 85 mm) were created and evaluated in the free field. Secondly, 9 target-specific lenses were made for focusing on regions that represented the anterior hippocampus and perirhinal cortex in 2 cadaver skull samples. The structure of each lens was designed by phase conjugation based on simulations utilising CT scans of the cadaver skull samples. A comparison was then made between the pressure fields generated by the lenses in the free field and the simulation's predictions. Finally, samples of skulls were used to evaluate the 9 lenses, and the measured pressure fields within the skull were compared to the simulations. Beyond the nine target-specific lenses mentioned, several other alternative lens designs were also examined with the aim of improving focusing and matching better with the simulations. In addition, transducer position sensitivity was also experimentally investigated. Together, the experimental validation suggests that the simulation can reliably predict the pressure field produced by the lens through the skull, providing feasibility for a subject-specific lens to target deep locations in the human brain.

3.1 TRANSDUCER CALIBRATION & CHARACTERISATION

Calibration and characterisation of the free field of a 500 kHz, 64 mm diameter unfocused transducer (Fig. 3.2 (a); H-294, Sonic Concepts Inc., Bothell, WA, USA) were carried out using the experimental setup in Fig. 3.1. A signal generator (33250A, Agilent, Santa Clara, CA, USA) with an output of a 500 kHz sinusoidal signal of 40 µs (20 cycles) was amplified by a 55 dB broadband amplifier (1140LA, E&I, Rochester, NY, USA) and applied to a matching box connected to the transducer. The transducer was mounted in a water tank filled with deionised and degassed water. A needle hydrophone (HNA-0400, ONDA, Sunnyvale, CA, USA) mounted to a 3D positioning system was attached to an oscilloscope (HDO4024, Teledyne LeCroy, Chestnut Ridge, NY, USA) to allow evaluation of the pressure field in the water tank. The oscilloscope was also synchronised with the signal generator and recorded the output of the amplifier.

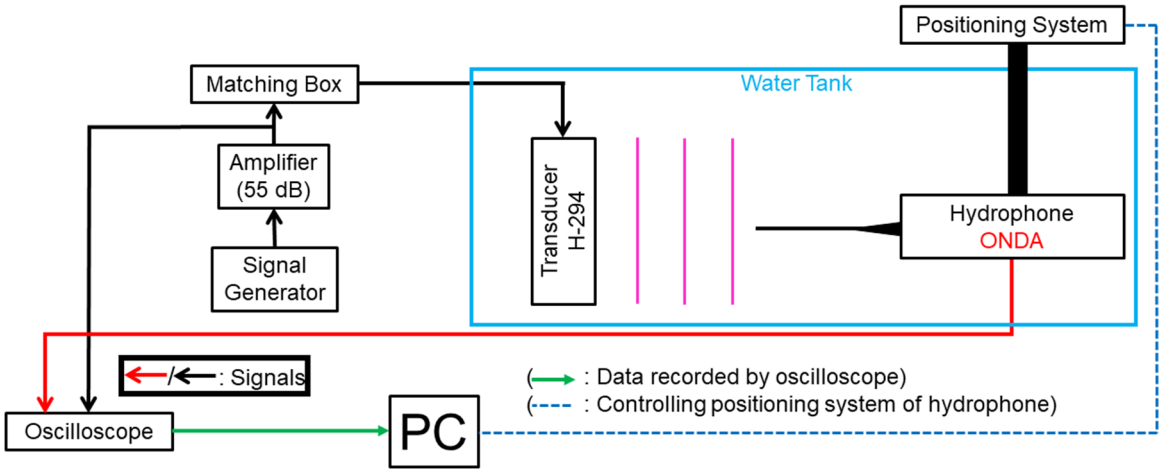

Fig. 3.1: Schematic of the experimental setup for transducer calibration and characterisation. The transducer was placed in a water tank filled with deionised and degassed water. A matching box for the transducer was placed after the amplifier. A needle hydrophone was used to take the measurements. Hydrophone positioning was controlled by a computer through a 3D positioning system. Hydrophone signals were recorded by the oscilloscope and then saved on the computer.

Transducer calibration results are shown in Fig. 3.2 (b) where the peak positive transducer surface pressure (P_0) is plotted against the peak-to-peak amplifier output voltage. In an ideal free field generated by a flat transducer (Hutchins et al., 1986; Liauh and Lin, 1999), the peak focal gain is 2 for all on-axis lobes. Measurements were taken at a location corresponding to a focal gain of 2 to characterise the pressure-voltage relationship of the transducer. Ten readings were taken at each voltage step. Error bars (< 0.5%) are not shown in Fig. 3.2 (b) for clarity.

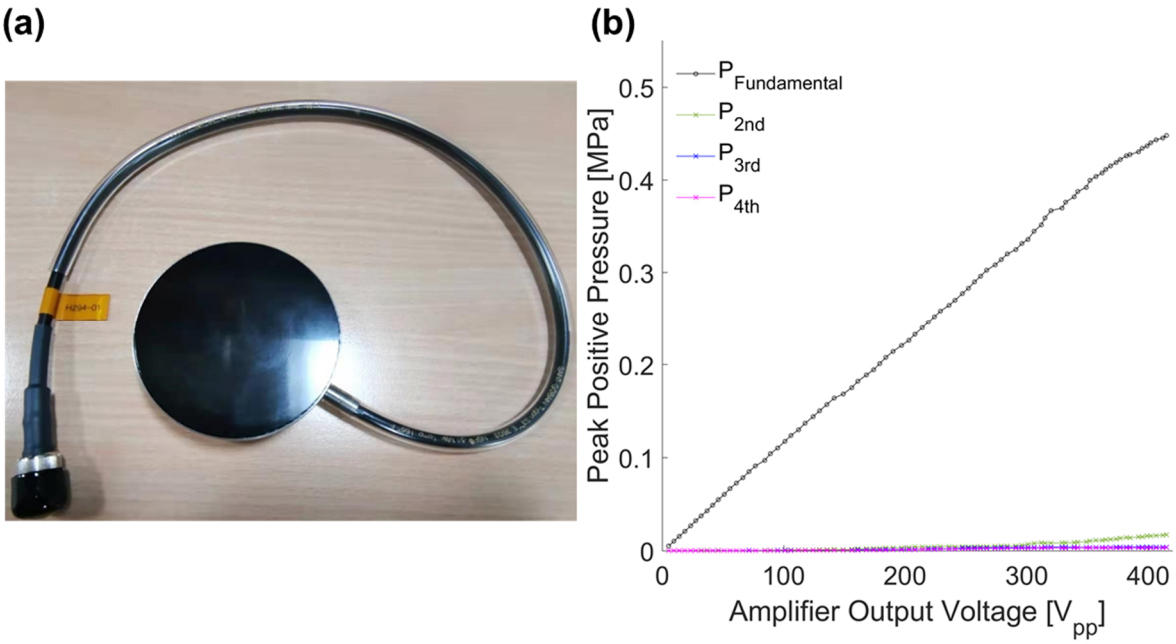

Fig. 3.2: The unfocused transducer H-294 and its calibration. (a) The 500 kHz customised single-element unfocused transducer. **(b)** Transducer surface pressure calibration for the H-294 transducer.

The ideal acoustic field formed by a flat circular single-element transducer can be predicted analytically in free field for various diameters and frequencies (Hutchins et al., 1986; Liauh and Lin, 1999). Fig. 3.3 (a) shows the calculated field for a 500 kHz ideal source with a diameter of 64 mm. However, the generated pressure field from a real ultrasound transducer is expected to differ from the ideal situation due to its non-ideal characteristics, such as non-uniform excitation and finite electrical impedance. Indeed, in the measured field from the H-294, it can be seen that the near fields are qualitatively different from the ideal, with the on-

axis lobe structure of the analytical expression not present in the measured real field (Fig. 3.3 (b)).

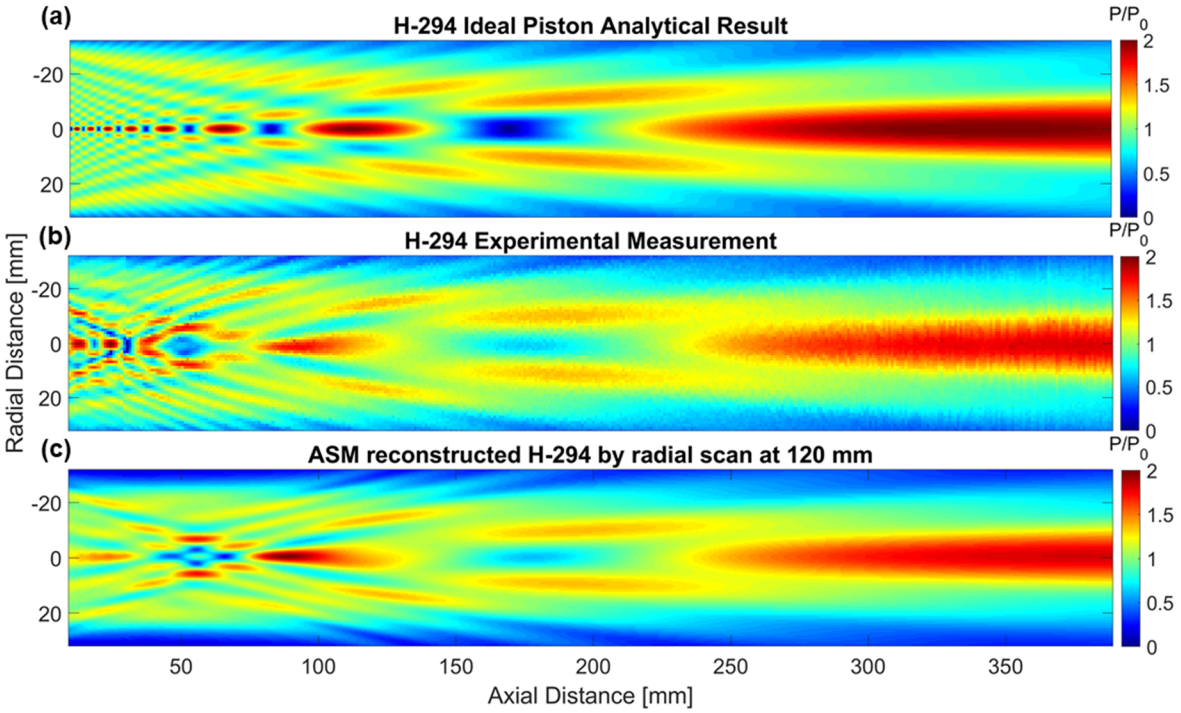

Fig. 3.3: Transducer H-294 characterisation. (a) Analytical field calculated for an ideal H-294 transducer. **(b)** Measured field of the real H-294 transducer by hydrophone. **(c)** Simulated field using the reconstructed source created by the radial scan at 120 mm.

A 2D planar scan (parallel to the transducer surface) 120 mm away from the transducer surface was measured by the hydrophone. This planar scan was used to reconstruct the source using the acoustic holography application of the angular spectrum method (Sapozhnikov et al., 2015). The reconstructed source was then used as an input in simulations to generate the pressure field shown in Fig. 3.3 (c). Using this reconstructed source, near-field effects at a distance of around 50 mm from the source surface can be captured, as seen in the experimental validation. In testing planar scans at 90 mm and 150 mm from the source surface, pressure fields with poorer agreement to the measured field were observed compared to scans at 120 mm. The reconstructed source at 120 mm from the source surface was therefore used in all subsequent simulations for this transducer.

3.2 PDMS LENS MANUFACTURING PROCEDURE

The PDMS lenses made for this project were manufactured with the following procedure:

Firstly, the lens structure designed from the simulation was made by a 3D printer (Form 2 printer, Formlabs, Somerville, MA, USA). The printed part was washed in an isopropanol bath for 20 minutes and then dried in a vacuum oven at 45 °C for 48 hours. Once dried, the part was used to make the negative lens mould. The negative mould was made of silicone (Dragon Skin^{TM} 10 Slow, Smooth-On, Macungie, PA, USA) with a Shore A hardness of 10 on a scale of 0 to 100. This level of hardness means the mould can be deformed and separated from the lens while the lens product is still in one piece.

The silicone was prepared according to the manufacturer's instructions. Briefly, the two parts, part A and part B, were mixed at a 1:1 ratio and stirred for 3 minutes. The mixture was degassed (< -0.95 bar for 3 ~ 5 minutes) to get rid of the large bubbles created during stirring before pouring onto the printed lens structure. This step reduced the amount of foam in the next degassing stage. The liquid state silicone mixture was degassed for another 30 minutes (< -0.95 bar) to get rid of the bubbles trapped on the lens structure surface. After degassing, the mould was left at room temperature on a level surface to cure overnight (> 7 hours).

As this negative mould material is silicone-based, it will adhere to the PDMS that will be used for the lens. A PVA coating treatment protocol was used to ensure separation of the cured PDMS lens from the mould (Trantidou et al., 2017). Firstly, the surface of the cured negative mould was O_2 plasma treated for 3 minutes at 80% power in a plasma surface treatment system (HPT-200, Henniker Plasma, Runcorn, UK). This process added hydroxyl bonds to the mould surface to improve the adhesion of the PVA coating. A PVA solution of 1% w/v was made

from deionised water, degassed, and stored at 4 °C. Before using the solution, it was filtered through 5 µm nylon filters. The negative mould was submerged in the PVA solution for 10 minutes. Bubbles trapped on the surface structure of the negative mould were removed by jetting PVA solution through a syringe with a needle. The negative mould was then dried at 115 °C for 15 minutes. This process of applying PVA solution and drying was repeated three times. In the final drying process, the mould was removed from the hot plate once it was completely dry from the PVA solution. The negative silicone mould could then be used to make the PDMS lens.

PDMS (SYLGARD^{TM} 184 Silicone Elastomer, Dow, Midland, MI, USA) was mixed with a base to curing agent ratio of 10:1 and stirred for at least 5 minutes. The mixed PDMS was degassed (< -0.95 bar) for 30 minutes to eliminate bubbles introduced during the stirring, which reduced the amount of foam formed during the next degassing stage. The PDMS was poured onto the PVA-treated negative silicone mould and degassed for another 3 ~ 4 hours to remove all bubbles in the PDMS. Specifically, the bubbles trapped on the lens structure surface of the negative mould necessitated an extended degassing period. The PDMS-filled mould was then put on a level surface in a 60 °C oven to cure overnight (15 ~ 20 hours).

3.3 PDMS Fresnel Focusing Lenses

To examine PDMS material properties, Fresnel focusing lenses were designed for the simple case of focusing in the free field. The density of PDMS was confirmed by casting a cuboid of 91 ml (85.5 mm × 85.5 mm × 12.5 mm) and found to be 1011.29 kg/m^3, within 0.4% of the 1015 kg/m^3 reported in the literature (Armani et al., 1999; Cafarelli et al., 2017; Guillermic et al., 2019; Liu et al., 2018). Using the literature values, PDMS Fresnel lenses were designed, focusing to 65 mm, 75 mm, and 85 mm from the transducer surface in simulations. The speed

of sound and attenuation of PDMS were then checked by comparing the measured acoustic fields using the below setup to the simulations of the three Fresnel lenses.

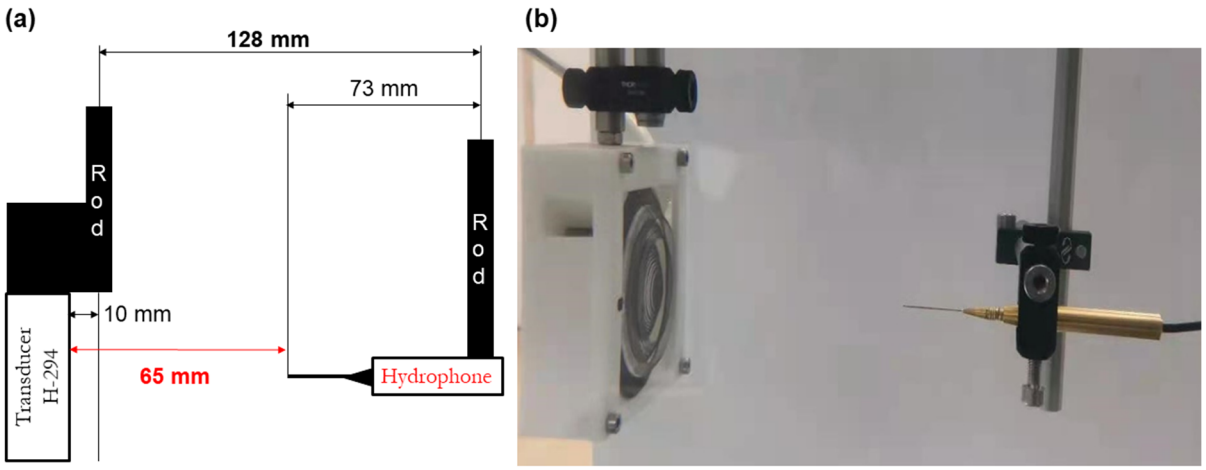

Fig. 3.4: The setup using the H-294 transducer with the Fresnel lens. (a) Schematic of distance measurement when the hydrophone was at the focal peak for the 65 mm lens. **(b)** Image of the transducer mounted with the lens and the hydrophone.

Fig. 3.4 (a) shows the setup used with positions registered beforehand, as shown, with an estimated error of less than 0.5 mm. The transducer was held by a Delrin® block on the left in Fig. 3.4 (b), which was also responsible for clipping the lens on to the transducer. The lens was mounted directly in contact with the transducer surface in deionised and degassed water. Bubbles between the lens and transducer surface were removed during the assembly process, and bubbles on the lens structure were also removed before the start of the experiment. A 3D positioning system was used to move the hydrophone in Fig. 3.4 (b) to measure the generated acoustic field. When the hydrophone was at the actual focal peak in the created acoustic field, the distance between the hydrophone tip and transducer surface was calculated again through the measured distance between the rods holding the transducer and the hydrophone.

When testing the three PDMS Fresnel lenses, foci were formed at 65 mm, 75 mm, and 85 mm, for the 65 mm, 75 mm, and 85 mm focused lenses, respectively, as predicted in simulations. The central slices of the lens structure for the 65 mm, 75 mm, and 85 mm lenses, respectively,

can be seen in Fig. 3.5 (a ~ c). The actual lens flat base layer was larger than that shown in the slices so that it could be easily fixed to the transducer. The measured axial pressure distributions of the three lenses are plotted in Fig. 3.5 (d). As the focal peaks occur at the locations predicted for all three lenses, the literature speed of sound value (1035 m/s) was verified for PDMS (Armani et al., 1999; Cafarelli et al., 2017; Guillermic et al., 2019; Liu et al., 2018).

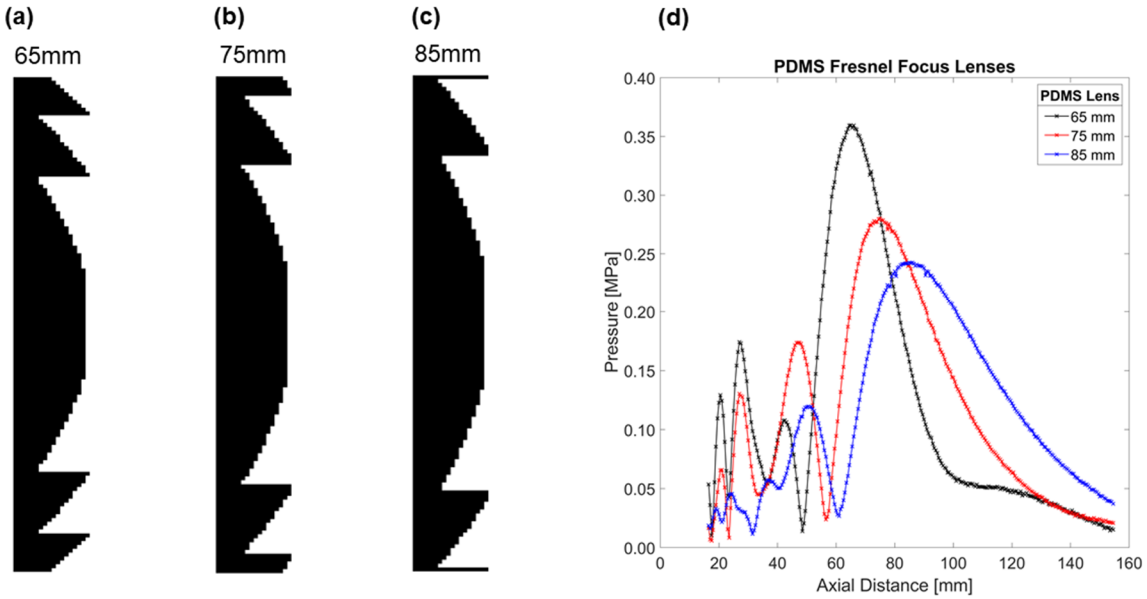

Fig. 3.5: The Fresnel lenses. (a) A central slice showing the structure of the 65 mm lens. **(b)** A central slice showing the structure of the 75 mm lens. **(c)** A central slice showing the structure of the 85 mm lens. **(d)** Measured axial pressure distribution of the three lenses where 0 mm axial distance marks the transducer surface. Measurements did not go closer than 17 mm to avoid the hydrophone tip crushing into the lens.

In evaluating acoustic attenuation at 500 kHz, the focal peak pressure gain values for the three lenses were compared to their corresponding simulations. To match the measured focal gain, the acoustic attenuation in simulation was updated to 1.28 dB/cm at 500 kHz, a 22% increase from the literature value of 1.05 dB/cm. The change in attenuation was not surprising, as the literature values were measured at or above 1 MHz and then extrapolated down to 500 kHz.

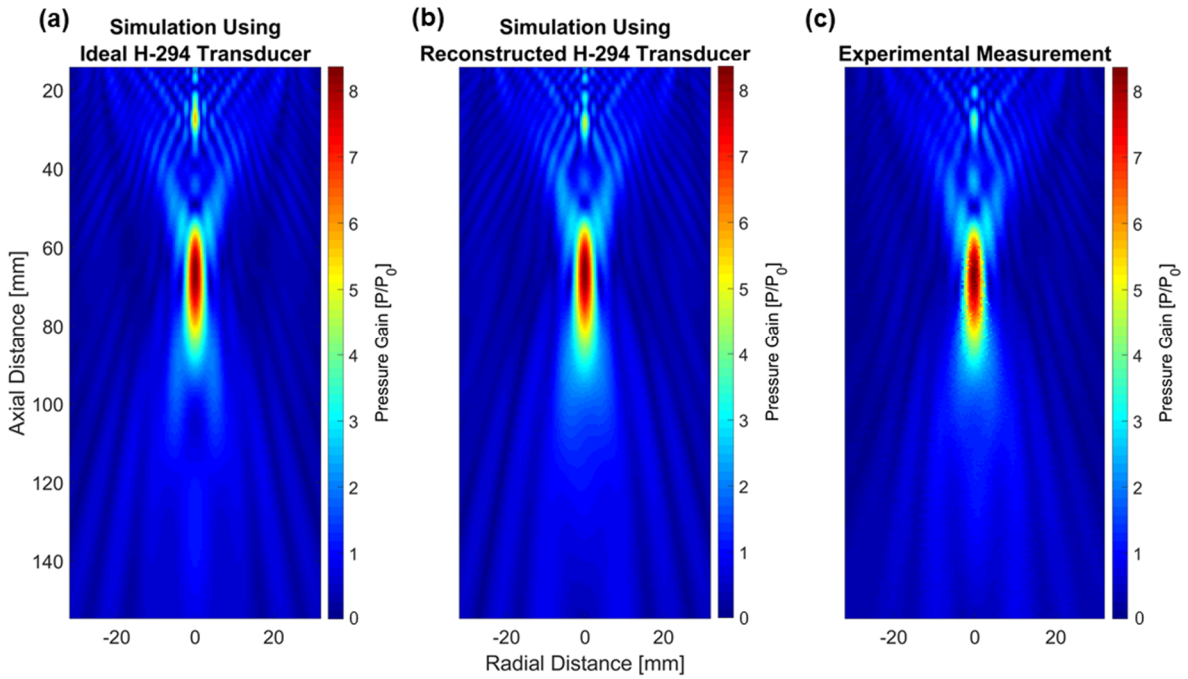

Fig. 3.6: Comparison of the simulations with the experimental measurement. The results for a 65 mm lens are shown here. P_0: transducer surface pressure. **(a)** The k-Wave fluid-based linear acoustic simulation using an ideal source. **(b)** The k-Wave fluid-based linear acoustic simulation using the reconstructed source. **(c)** Experimental measurement field by hydrophone.

The use of an ideal source versus the reconstructed source (recall Section 3.1) was investigated by comparing the two simulated fields to the measured field. The comparison for the 65 mm lens is shown in Fig. 3.6 as an example. Fig. 3.6 (a) used an ideal source sending out a sinusoidal wave in linear acoustic simulation, hence giving pressure gain values (P/P_0) relative to source surface pressure P_0. Fig. 3.6 (b) shows the simulated acoustic field generated by the reconstructed source. The measured acoustic field is shown in Fig. 3.6 (c). Raw pressure measurements were normalised by the source pressure in each case. Overall, both simulated pressure distributions agreed with the measurement in the 2D range covered in Fig. 3.6. Relative to the magnitude of the main focus, the ideal source simulation in Fig. 3.6 (a) overestimated the magnitude of the pre-focal lobes 35 mm or closer from the source. The simulation using the reconstructed source in Fig. 3.6 (b) was in closer agreement with the measured field in Fig. 3.6 (c). The reconstructed source is useful for providing computational predictions that match better with the experimental measurements.

3.4 SKULL SAMPLE SEGMENTATION

To validate the lens method for delivering transcranial focused ultrasound, experiments and simulations on *ex vivo* skulls were done. CT skull scans were segmented prior to use in the simulation. Two different approaches to segmentation were considered. First, a binary threshold segmentation for the skull samples could be used, separating the skull from the air. This gave a homogeneous skull with the same material properties. The second option assigned material properties to the skull based on the Hounsfield unit measured by CT. By doing this, the inhomogeneous, porous nature of the skull could be represented in the simulation. Axial views of the two options are compared in Fig. 3.7 using the same slice in the scan data.

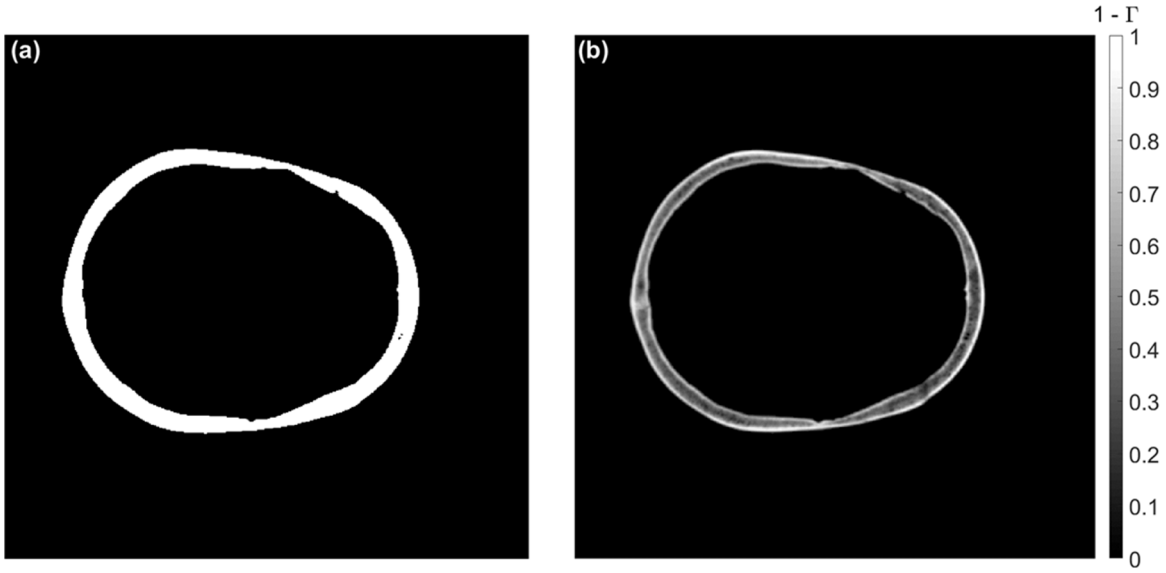

Fig. 3.7: CT segmentation comparison. (a) Binary threshold segmentation, where skull bone = 1 and air (during the CT scan) = 0. **(b)** Inhomogeneous material property assignment based on the CT signal attenuation and application of the mixture rules. Here, the plotted map is 1−Γ, where Γ is the porosity.

Hounsfield units (that is, a measure of radiodensity), can vary from ~300 for cancellous bone up to ~1900 for cortical bone in the skull, with a value of –1000 for air. For the binary segmentation, the threshold was set to 0, making voxels with positive Hounsfield values skulls and voxels with negative Hounsfield values non-skulls, as shown in Fig. 3.7 (a). Only a few

large porosities were observed. These are shown as cavities surrounded by skull material. The homogeneous skull took the average skull acoustic properties (Hasgall et al., 2018): c_{bone} = 2820 m/s, ρ_{bone} = 1732 kg/m^3 and α_{bone} = 3.28 dB/(cm MHz^n) where n = 1.

For the inhomogeneous skull segmentation result in Fig. 3.7 (b), brighter voxels occurred at skull-air boundaries, and the inner structures are darker. This is as expected, as cortical bone forms the outer shells of the skull, and the porous cancellous bone is between the cortical shells. The conversion from Hounsfield unit (HU) to porosity was calculated by (Aubry et al., 2003; Blackmore, 2018):

$$\Gamma = 1 - \frac{HU}{\tau};$$

Where Γ is porosity, HU is Hounsfield Unit, and τ is the threshold. The threshold τ is chosen to be the highest Hounsfield value in the CT data for the skull cortical bone, which is 1750. The threshold was chosen so that the porosity could be converted accurately. Γ is between 0 and 1, representing skull (no porosity) and no skull (full porosity), respectively. Metal parts on the whole skull sample gave a Hounsfield value significantly higher than 1900 (> 3000). Because of this, negative Γ values were observed in the mouth region due to higher-than-threshold Hounsfield values. Therefore, all negative Γ values were set to 0, representing solid bone. Similarly, as air has a negative Hounsfield value (−1000), it gives an Γ value larger than 1. Therefore, results larger than 1 were all set to be 1, representing the absence of bone.

For practical implementation of the inhomogeneous skull segmentation, each voxel took on acoustic material properties based on these mixture rules calculated from Γ:

$$c = c_{pore} + (c_{bone} - c_{pore})(1 - \Gamma);$$

$$\rho = \rho_{pore} + (\rho_{bone} - \rho_{pore})(1 - \Gamma);$$

$$\alpha = \alpha_{pore} + (\alpha_{bone} - \alpha_{pore})(1 - \Gamma);$$

The subscripts $bone$ and $pore$ stand for the largest and lowest variations of each acoustic material property. The $bone$ values were taken as the properties of the densest skull cortical bone measured (Hasgall et al., 2018; Maimbourg et al., 2018; White et al., 2006; Marsac et al., 2017): c_{bone} = 3100 m/s, ρ_{bone} = 1900 kg/m^3, and α_{bone} = 12.16 dB/(cm MHz^n) where n = 1.16. The $pore$ values were taken as the properties of water: c_{pore} = 1488 m/s, ρ_{pore} = 1000 kg/m^3, and α_{pore} = 0.003 dB/(cm MHz). In the experiments, the skull samples were submerged in water with pores filled with water.

3.5 WHOLE SKULL SAMPLE SIMULATIONS

Using the binary and porous skull segmentations, three types of simulation were performed. A virtual point source was placed at the target, as shown in the left column of Fig. 3.8. Simulation signals were recorded in a plane covering the potential positions of the transducer outside the skull, and the magnitude and phase at 500 kHz were determined. As described in Chapter 2, the magnitude field was used to select the optimal transducer location by maximising the average magnitude in the area covered by the transducer surface. The phase of the selected area covered by the transducer was then used to derive the lens structure shown in the middle column of Fig. 3.8. The created lens, together with the transducer, was placed at the selected

location to focus ultrasound energy on the target in the forward simulation, as illustrated in the right column of Fig. 3.8.

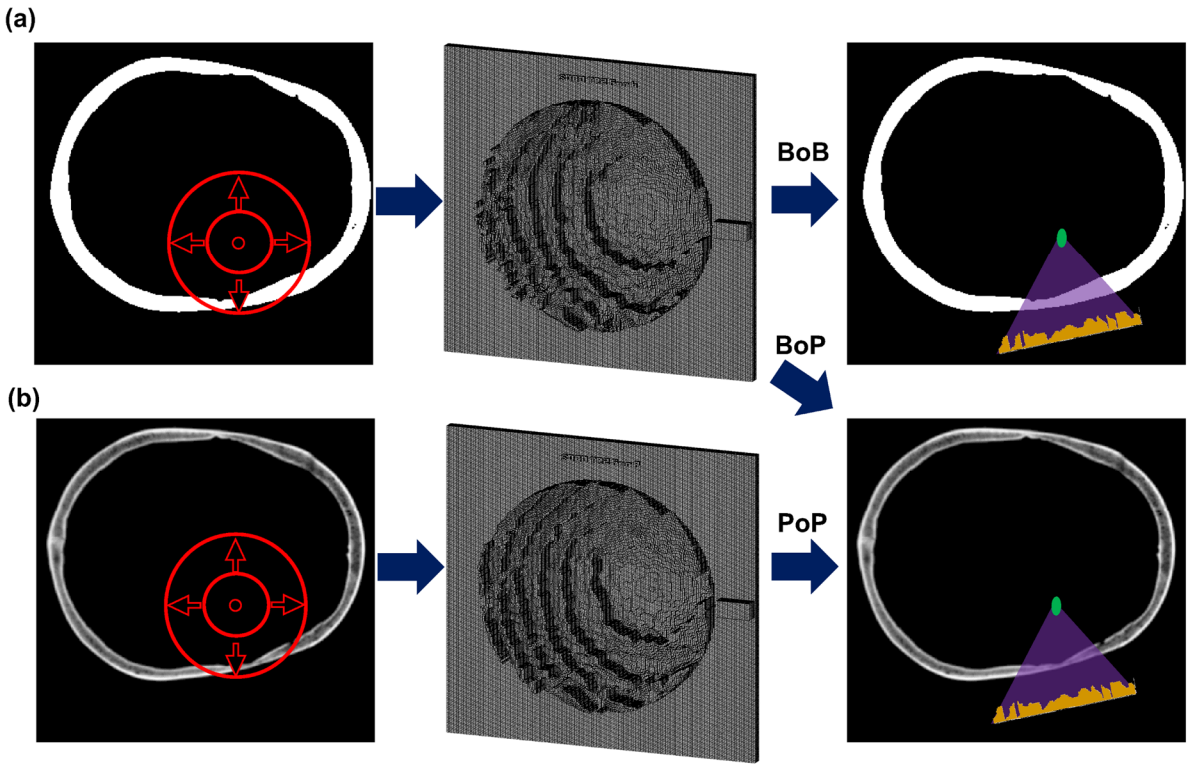

Fig. 3.8: Skull sample simulation types. Data from point source simulations (left column) were used to create the lenses (middle column). They were then used in the forward simulations (right column), focusing on the target locations. **(a)** The 'BoB' type: lens designed using binary skull segmentation and then tested on the binary skull. **(b)** The 'PoP' type: lens designed using porous skull segmentation and then tested on the porous skull. In addition, the 'BoP' type: lens designed using binary skull segmentation and then tested on the porous skull.

Fig. 3.8 (a) shows the simulation process using only the binary segmented skull. This type is called 'BoB': binary lens acts on the binary skull. Fig. 3.8 (b) shows the simulation process using only the porous skull segmentation. This type is called 'PoP': porous lens acts on the porous skull. Fig. 3.8 also shows the simulation process using the binary skull segmentation to create the binary lens but using it on the porous skull segmentation in the forward simulation. This type is called 'BoP': binary lens acts on the porous skull. This represents the case where only binary lenses can be created from MRI-based modelling and then used on human participants.

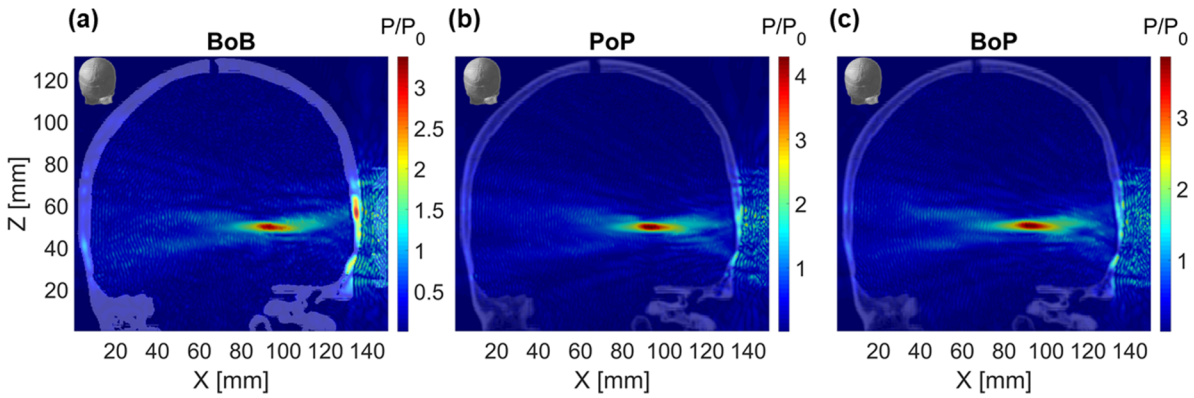

Fig. 3.9: Comparison of different types of simulation. The target location represents the right anterior hippocampus on the whole skull sample. Coronal views are shown for all three simulation cases. **(a)** The BoB simulation, where a lens created from the binary skull is used on the binary skull. **(b)** The PoP simulation, where a lens created from the porous skull is used on the porous skull. **(c)** The BoP simulation, where a lens created from the binary skull is used on the porous skull.

Using the described three simulation processes, four target locations on the whole skull sample were evaluated: the left and right perirhinal cortex and the left and right anterior hippocampus. These target locations were estimated by a neurologist based on the skull morphology in the imaging data. The coronal views of the simulations for the right anterior hippocampus are shown as an example in Fig. 3.9. In all cases, the lens successfully focused on the target with the focal peak inside the spherical target volume of 5 mm diameter. For all target sites, the relationship of the simulated target focal gain was PoP > BoP > BoB. This was caused by the overall lower skull presence in the cases where the porous skull was used, as shown in Fig. 3.9 (b) and (c). In addition, the pressure inside the skull material on the ultrasound pathway shown in Fig. 3.9 (a) was more significant than that in Fig. 3.9 (b) and (c) due to the stronger reverberation effect in the solid skull. The BoB simulation gave the worst-case scenario in terms of the standing waves inside the skull. These standing waves were caused by ultrasound reflected off the other side of the skull, which could be artificially higher due to the stronger reflections from the sharper water-skull interface.

3.6 SMOOTH LENS DESIGN

Due to the smaller spatial resolution of the CT scan (0.468 mm) compared to the 0.5 mm grid size determined for the 500 kHz ultrasound simulation, further simulations directly used the CT resolution. In the case of a lens, the phase conjugated structure was rounded to the same spatial resolution, yielding staircase lens structures as shown in Fig. 3.10 (a) and (b).

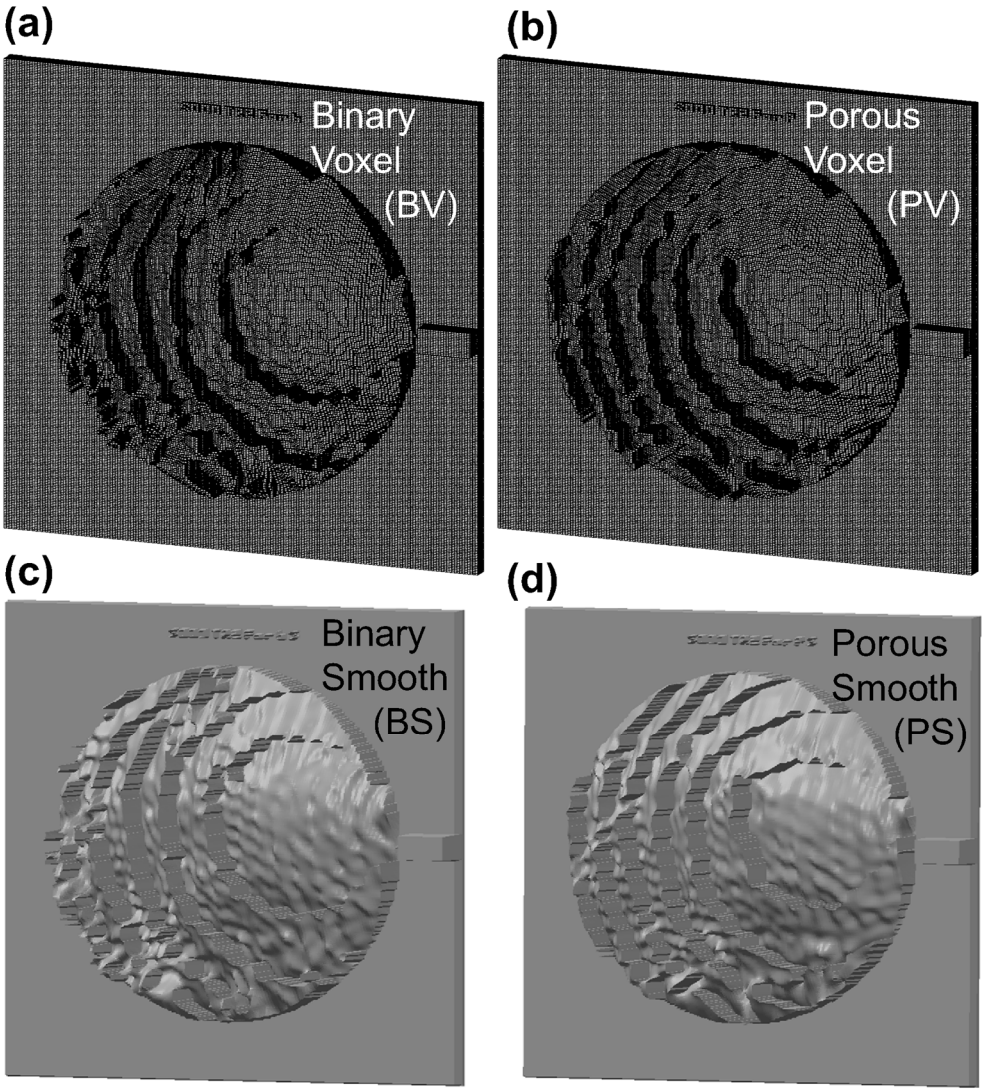

Fig. 3.10 Different lens types tested. All four lenses target the right anterior hippocampus of the whole skull sample. Binary (B) lenses were constructed using binary skull segmentation. Porous (P) lenses were constructed using porous skull segmentation. Voxel (V) lenses had the same shapes as those used in simulations. Smooth (S) lenses were potential lens improvements in reality, with more phase levels. **(a)** Binary Voxel (BV) lens. **(b)** Porous Voxel (PV) lens. **(c)** Binary Smooth (BS) lens. **(d)** Porous Smooth (PS) lens.

However, the lenses to be manufactured are not limited by this spatial resolution but rather by the manufacturing process. Hence, a finer resolution can be determined by utilising more of the available temporal phase information. In the k-Wave simulation, a temporal resolution of 25 ns was used to ensure stability, corresponding to a spatial resolution of 37.5 µm in lens thickness. In this case, the 3D printer employed has a layer thickness of 50 µm which is thus the true spatial resolution limit when making the real lenses. Despite this, it was anticipated that the smooth lens would provide better focusing through the skull as its structure possesses more phase information.

As the lens structures no longer possess circular symmetry around the centre, as shown in Fig. 3.10, an additional block was needed to ensure correct lens orientation. This block was added to the flat part of the lens, outside the 64 mm diameter circular effective lens area, as shown on the right side of each lens.

Lens Type Designation

Skull / Structure	Binary Segmentation	Porous Segmentation
Following Simulation Grid Size	Binary Voxel (BV)	Porous Voxel (PV)
Following 3D Printer Resolution	Binary Smooth (BS)	Porous Smooth (PS)

Table 3.1: Summary of four lens types designed and tested. Lens structure can be derived from simulations using binary or porous skull segmentation. Lens structure can also be limited by simulation grid size or 3D printer resolution.

Four types of lenses were compared using the right anterior hippocampus of a whole skull as a sample target location, as shown in Fig. 3.10 and Table 3.1: (a) a binary voxel (BV) lens constructed using skull binary segmentation based on the structure used in simulations; (b) a porous voxel (PV) lens constructed using skull porous segmentation based on the structure used in simulations; (c) a binary smooth (BS) lens constructed using skull binary segmentation based on the resolution limit of the 3D printer; and (d) a porous smooth (PS) lens constructed using skull porous segmentation based on the resolution limit of the 3D printer. In the lens manufacturing process, the resolution limit of the 3D printer was 50 μm (printing layer thickness) in the lens thickness direction and 140 μm (printer laser spot size) in the other two directions.

3.7 TARGET-SPECIFIC LENSES IN FREE FIELD

The different types of lenses targeting the right anterior hippocampus of the whole skull sample were first tested in the free field in deionised and degassed water to confirm their effect in simulations. The goal is to find out if a specific lens type can provide better performance on a skull sample, i.e., higher focal pressure gain at the target and tighter focal volume.

The axial and coronal views of the pressure fields created by the four types of lenses were compared to simulations (Fig. 3.11). Qualitatively, the measured focal lobes created by the lenses had comparable spatial distributions to their corresponding simulations. To compare the measurements to the simulations quantitatively, three values were used: (i) the pressure gain at the focal peak; (ii) the -6 dB focal length; and (iii) the -6 dB focal width.

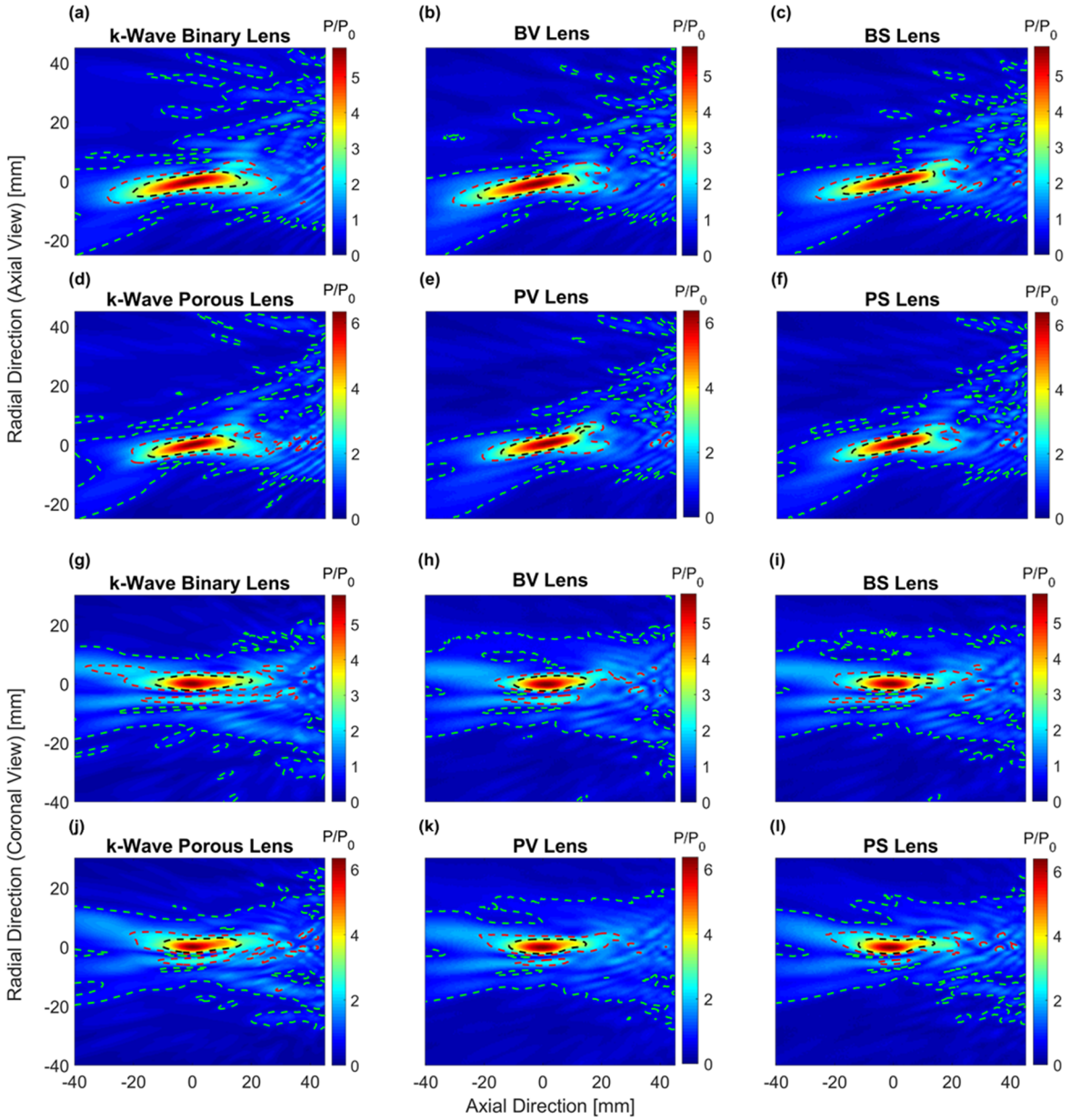

Fig. 3.11 Lens measurements in free field in comparison with simulations. Four types of lenses, all targeting the right anterior hippocampus of the whole skull sample, were tested in the free field. Axial and coronal views are shown in **(a)~(f)** and **(g)~(l)**, respectively. Contours of -6 dB (black), -10 dB (red), and -20 dB (green) are shown. In all views, the transducer and the lens are on the right outside the measured field. **(a), (g)** Views of binary lens simulated in the free field. **(b), (h)** Views of measured BV lens in the free field. **(c), (i)** Views of measured BS lens in the free field. **(d), (j)** Views of porous lens simulated in the free field. **(e), (k)** Views of measured PV lens in the free field. **(f), (l)** Views of measured PS lens in the free field.

The measured peak focal gain values for the BV and BS lenses were both 5.80, agreeing with the simulated binary lens free field focal gain of 5.82 within 1%. Similarly, the measured focal gains for the PV and PS lenses were 6.36 and 6.39, again agreeing with the simulated field

focal gain of 6.34 within 1%. Comparing between the simulation resolution-limited (voxel) and 3D resolution-limited lenses (smooth), the difference in focal gain was 0.02% for lenses constructed using binary segmentation (BV/BS) and 0.43% for lenses constructed using skull porous segmentation (PV/PS). Therefore, the smooth lenses did not result in the expected performance improvement in the free field despite having more phase levels incorporated into their geometry.

The length and width of the -6 dB focal lobe were quantified in both the axial and coronal views. For each parameter, the larger value was used when the values were different across the two views. All four lenses showed identical measured -6 dB focal widths of 5 mm, 2.7% smaller than the simulated 5.14 mm for binary lenses (BV and BS) and 1.9% smaller than the simulated 5.10 mm for porous lenses (PV and PS). In evaluating the -6 dB focal length, both the binary voxel (BV; 36.86 mm) and binary smooth (BS; 33.98 mm) lenses showed shorter focal lengths compared to the simulated value (37.34 mm; -1.3% and -9% for BV and BS, respectively). For the porous lenses (PV and PS), the voxel lens (PV) generated from simulation resolution limits showed a 0.42% higher -6 dB focal length compared to simulation (29.61 mm compared to 29.49 mm; +0.42%), while the smooth lens (PS0) generated from manufacturing resolution limits showed a -6.2% shorter focal length compared to simulation (27.66 mm compared to 29.49 mm). In the pressure spatial distribution, the smooth lenses were measured to have a -6 dB focal length, 6% to 9% shorter than that in the simulations created by their voxelated counterparts.

3.8 LENSES ON WHOLE SKULL SAMPLE

The four lenses of different types were tested in the whole skull sample. For the target location representing the right anterior hippocampus, the optimal source location in the porous skull

simulation was identical to that in the binary skull simulation. Therefore, all four lenses took the same position relative to the skull. Only one skull holder was needed in order to test all four types of lenses. The skull holder was 3D printed, assembling the lens and transducer to the skull with the same spatial arrangement as that in the simulations, with accuracy limited by the printer's dimensional error of 140 µm.

To take acoustic measurements inside the skull cavity, a fibre-optic hydrophone (FOH, Precision Acoustics, Dorset, UK) was used in place of the piezoelectric PVDF (polyvinylidene difluoride) hydrophone due to its smaller size. The setup used in this experiment is shown in Fig. 3.12.

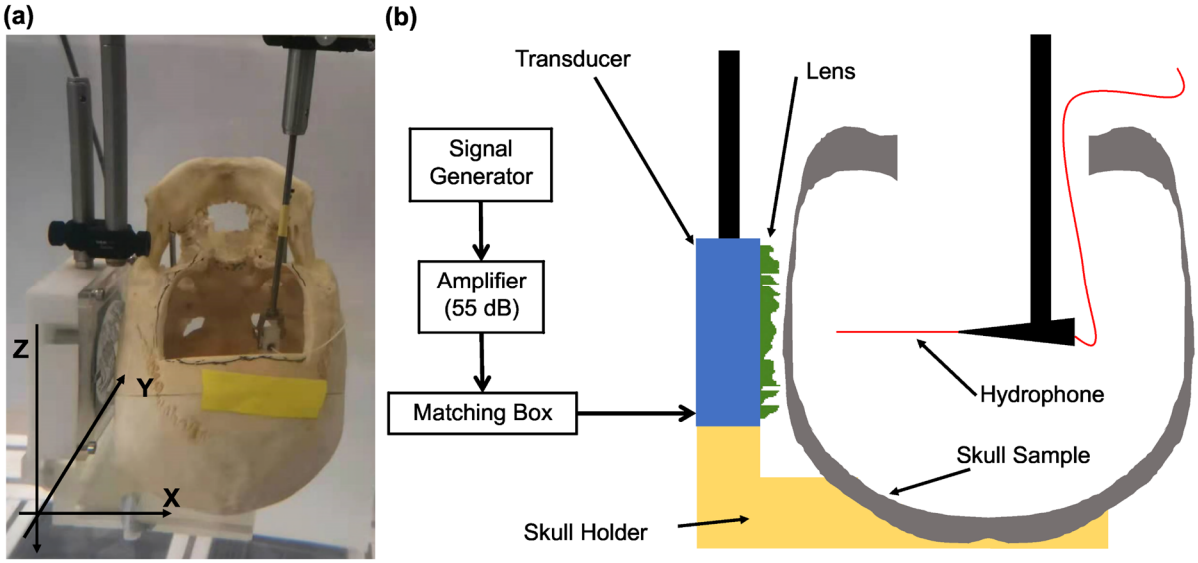

Fig. 3.12 Setup for lens testing on the whole skull sample. The transducer holder fixed the transducer to the lens. The skull holder assembled the transducer and lens to the skull with the same orientation as in the simulations. FOH entered the skull cavity to take pressure measurements. It was moved around by the 3D positioning system with orientation defined by XYZ, as shown in **(a)**, where the YZ plane is parallel to the transducer surface plane and the X direction is orthogonal to it. In each experiment, the orientation of the hydrophone was chosen to avoid as much interaction as possible between its holder and the ultrasound. **(a)** Photo of the setup. **(b)** Schematic of the setup. The orientation of the hydrophone here is for illustration purposes only.

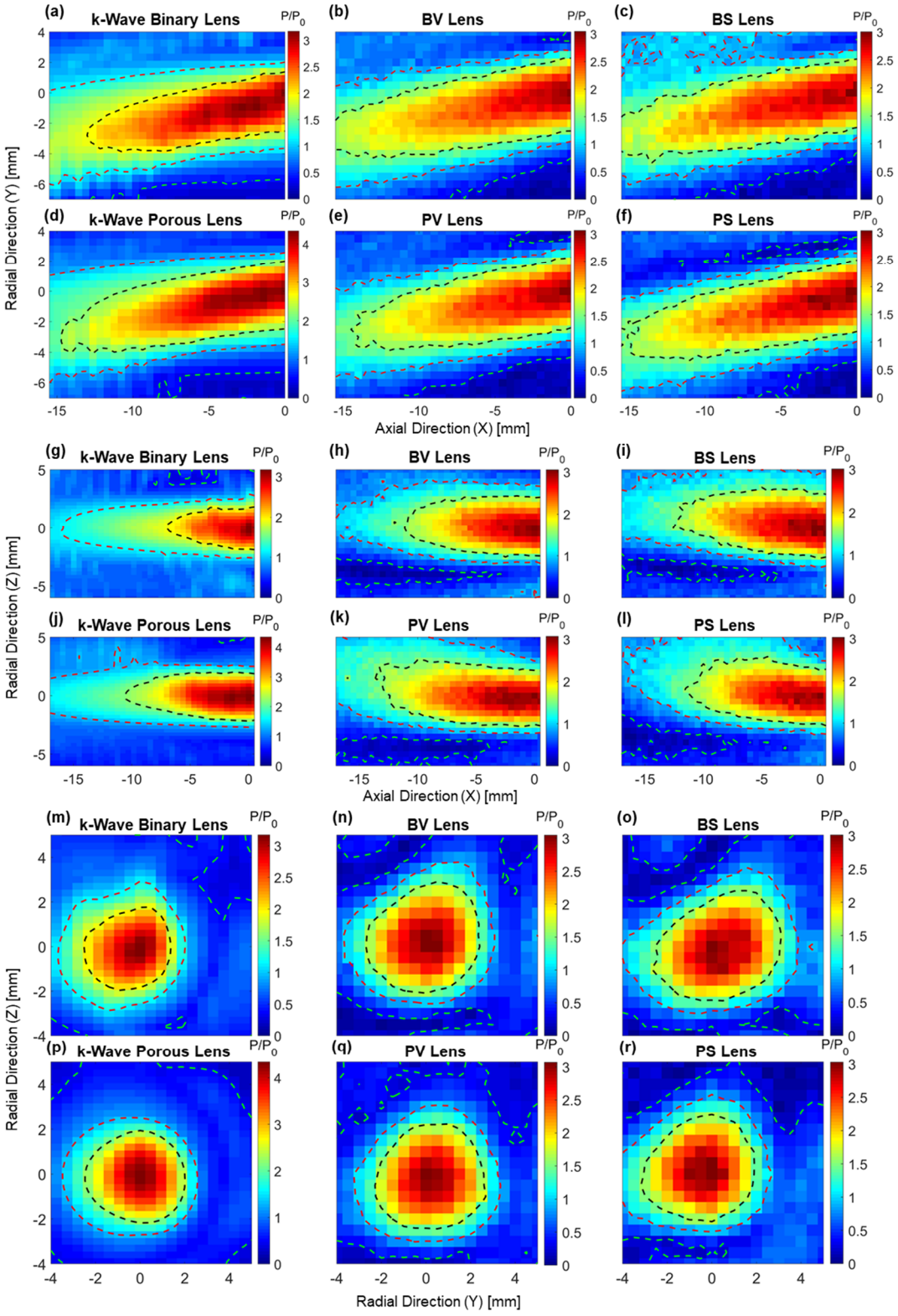

Fig. 3.13 Measurements on the whole skull sample in comparison with simulations. Axial (XY), coronal (XZ), and sagittal (YZ) views of the pressure field are shown in **(a)~(f)**, **(g)~(l)** and **(m)~(r)**, respectively. Contours of -6 dB (black), -10 dB (red), and -20 dB (green) are shown. **(a), (g)**, **(m)** Views of the simulated binary lens field in the skull (BoB simulation). **(b), (h), (n)** Views of the measured BV lens field. **(c), (i), (o)** Views of the measured BS lens field. **(d), (j), (p)** Views of the simulated porous lens field in the skull (PoP simulation). **(e), (k), (q)** Views of the measured PV lens field. **(f), (l), (r)** Views of the measured PS lens field.

Axial, coronal, and sagittal pressure field scans were taken for the four lenses on the skull sample (Fig. 3.13). In each subplot of Fig. 3.13, the origin was at the focus peak of each case, although due to limited access in varying areas of the skull, scans could not cover the entire focal volume. All four lenses formed foci near the target location on the skull sample. Qualitatively, the measured pressure distributions were comparable to the corresponding computational predictions, especially for the axial views in Fig. 3.13 (a)~(f) and sagittal views in Fig. 3.13 (g)~(l).

Fig. 3.13 (a), (d), (g), and (j) show the axial and coronal views of the BoB and PoP simulations for binary lenses and porous lenses, respectively. The focal peak pressure gain was calculated for all cases based on the hydrophone measurements. The measured peak focal pressure gain was 3.05 for the BV lens, 3.01 for the BS lens, 3.07 for the PV lens, and 3.03 for the PS lens. The gain of the BV lens was 0.54% smaller than that of the PV lens, and the gain of the BS lens was 0.67% smaller than that of the PS lens. The improvement in the porous lenses was negligible. The gain of the BV lens was 1.5% larger than that of the BS lens, and the gain of the PV lens was 1.4% larger than that of the PS lens. Therefore, regarding the peak focal gain, the extra process to obtain the smooth lenses was not justified by their performance. While this contradicts the expectation of a better focus in the smooth lens due to an increase in phase levels within the structure, it is possible that the dimensional rounding errors of the 3D printer affected its manufacture. Specifically, the phase level of the smooth lens was artificially limited by the printer layer thickness of 50 μm rather than the ideal 37.5 μm based on simulation. This rounding error could potentially mitigate the improvement that the smooth lens offers by providing more phase levels, each with rounding errors.

Comparing standing wave formation between simulation and validation, standing waves with a magnitude of -10 dB or lower could not be observed experimentally at pressure fields corresponding to simulation. This low-magnitude predicted phenomenon is likely to be the result of the insufficient signal-to-noise ratio of the fibre-optic hydrophone system used. Alternatively, it is possible that the standing wave may be buried in the swelled focal volume inside the limited scan range, as indicated by the larger measured focal lobes in the coronal views.

All four lenses provided peak focal gain values comparable to those predicted by the BoB simulation, confirming its ability to make representative predictions. As the simulations using the porous skull (PoP and BoP) gave peak focal gain values significantly larger than the measurements (41% lower in PV; 43% lower in PS lenses), it is likely that the porous skull segmentation exaggerated the porosity of the skull and underestimated the overall skull presence. Taken together, this shows that the PoP simulation did not have enough absorption in the model. On the contrary, the focal gain was only 3.8% lower for the BV lens and 5.4% lower for the BS lens compared to a peak focal gain of 3.17 in BoB simulations. In terms of pressure distribution, the PoP simulation did not capture some characteristics of the focus in the skull. For example, the measured coronal views of the foci created by the PV and PS lenses in Fig. 3.13 (k) and (l) ‘bend’ to the top left, whereas the PoP simulation result shown in Fig. 3.13 (j) predicts a straight focus. The BV and BS lenses in Fig. 3.13 (n) and (o) show similar deformations away from a circular cross section for a regular focal lobe in free field. Therefore, the current porous skull segmentation does not appear to provide a better simulation prediction than the binary skull simulation.

Inside the skull cavity, hydrophone movement was restricted due to spatial limitations, constraining the size of 2D scans that could be taken inside the skull. Therefore, for this target, the axial and coronal scans in Fig. 3.13 did not manage to cover the entire focal lobe to allow the -6 dB focal length to be quantified. Although multiple readings of the -6 dB focal width were available in the three views for each lens (Fig. 3.13), the largest width reading was used because the focus was not aligned with the XYZ coordinate in the scan. Compared with the 4.68 mm -6 dB focal width shown in PoP simulations, both the PV and PS lenses showed a 6.8% increase in -6dB focal width (5 mm). Similarly, the BV (5 mm) and BS (5.5 mm) lenses showed a 19% and 31% increase, respectively, compared to the BoB simulated -6 dB focal width of 4.21 mm, suggesting that the binary lenses provided worse agreement than the porous lenses to their corresponding simulations. The smooth lenses also did not show evidence of improvement in focal width compared to their voxel counterparts.

In summary, with regard to the peak focal gain, the BoB simulation provided the closest prediction to the experimental measurements for all lens types. Among the four lens types, the BV lens had the closest measured peak focal gain value compared to the BoB simulation. With regards to the -6 dB focal width, the measured focal width for all four lenses on the skull was about 5 mm, agreeing with measurements in free field. The data collectively suggests that neither the smooth lenses nor the porous lenses provide an improvement in performance over the BV lens. Therefore, for simplicity, the binary skull simulation BoB and the BV lens were chosen to be used for the experiments in the rest of this thesis.

3.9 BV LENSES ON WHOLE SKULL SAMPLE

In the previous study, different types of lenses were tested using the right anterior hippocampus as a model target, yielding the binary voxel lens as the lens of choice. In this section, the BV

lens was tested on three more target locations: the left anterior hippocampus and the left and right perirhinal cortex. Three more target-specific BV lenses were made, one for each of the targets. The lenses were tested in the free field first and then on the whole skull sample.

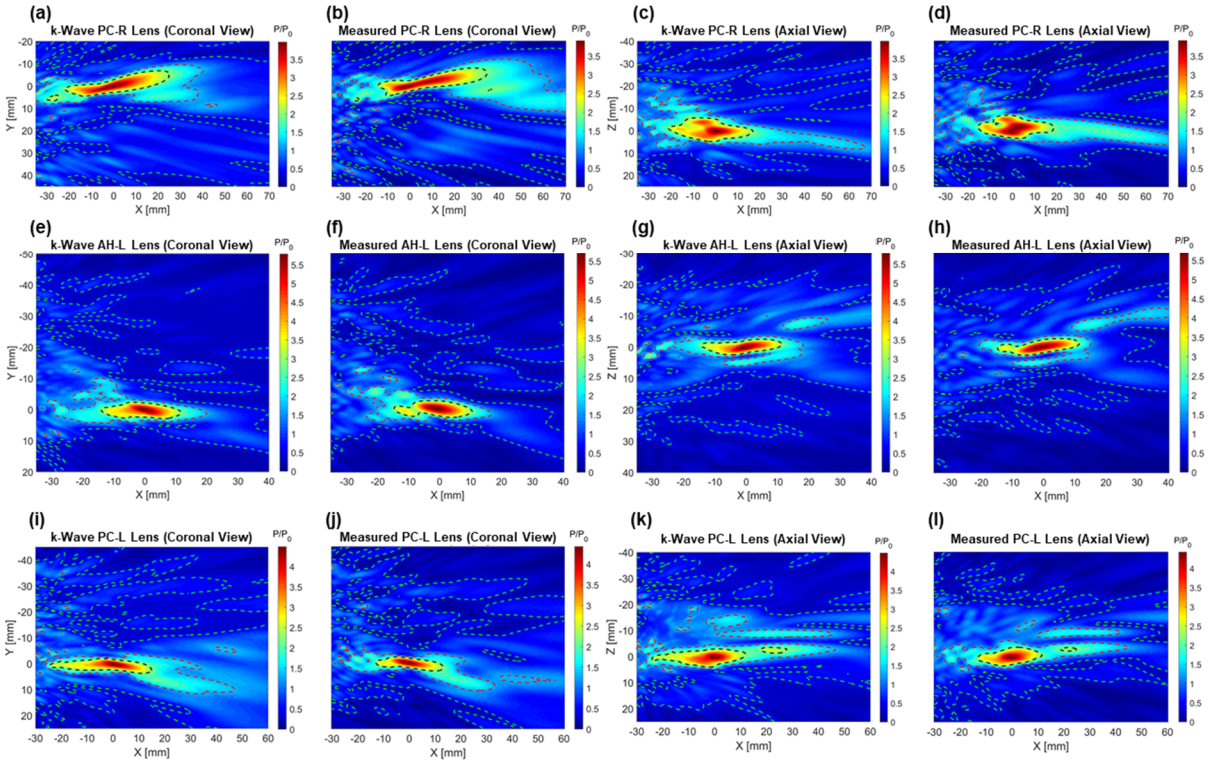

Fig. 3.14 Acoustic measurements in the free field in comparison with simulations for the BV lenses. Target-specific lenses were tested for: the right perirhinal cortex (PC-R) in **(a)~(d)**, the left anterior hippocampus (AH-L) in **(e)~(h)**, and the left perirhinal cortex (PC-L) in **(i)~(l)**. Contours of -6 dB (black), -10 dB (red), and -20 dB (green) are shown. In all views, the transducer and the lens are on the left outside the measured field. **(a), (e), (i)** Coronal views of the free field simulations using the three BV lenses. **(b), (f), (j)** Coronal views of the free field measurements of the three BV lenses. **(c), (g), (k)** Axial views of the free field simulations using the three BV lenses. **(d), (h), (l)** Coronal views of the free field measurements of the three BV lenses.

The free field measurements of each lens were first compared to their corresponding simulations in Fig. 3.14. In each subplot, the origin is at the focus peak. Note that the 'focus' mentioned here is not the designed focus but the focus that appears in water with the skull absent. The transducer is on the left, outside the measured field in all cases. The peak focal pressure gain, -6 dB focal length, and width were then quantified for each lens.

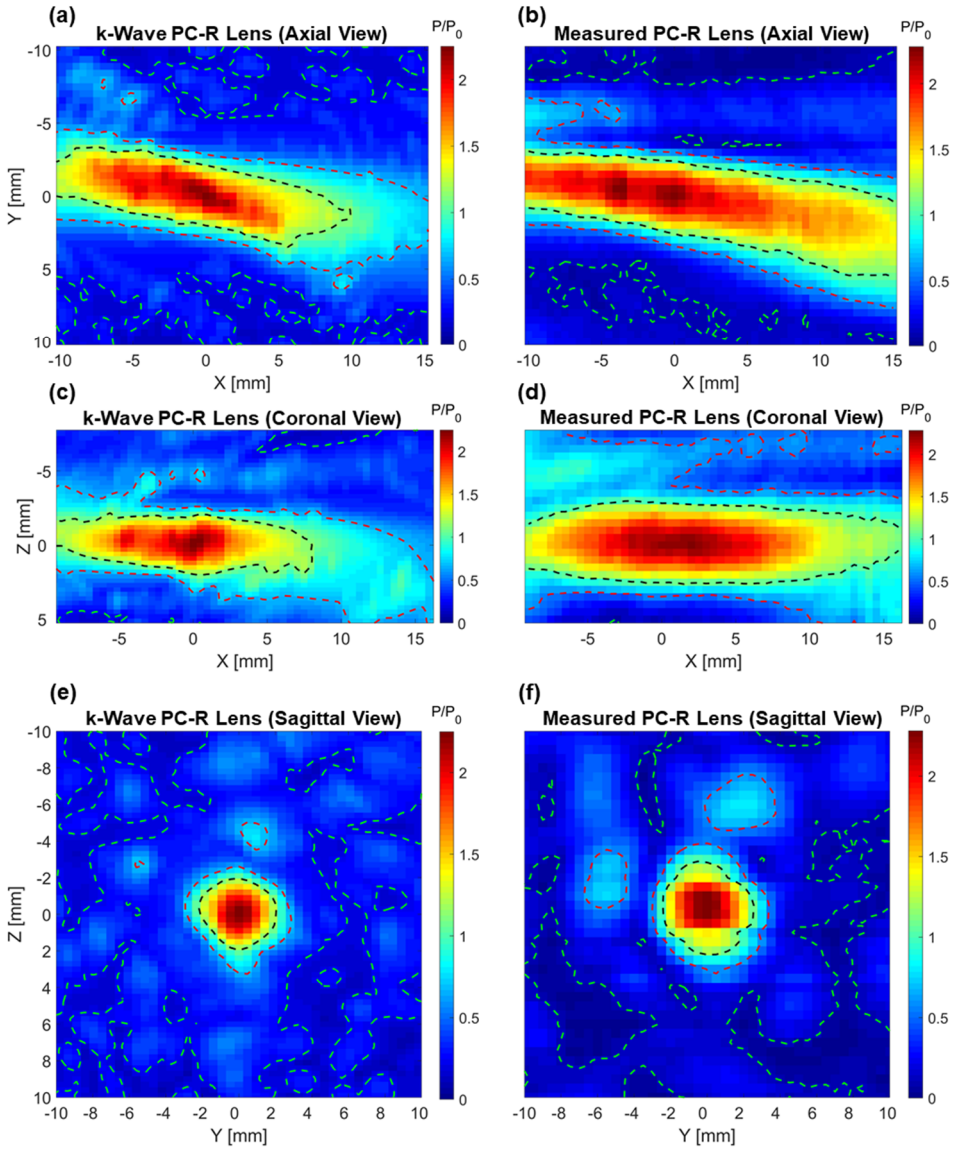

Fig. 3.15 Measurements of the BV lens targeting PC-R on the whole skull sample in comparison with the simulation. Axial (XY), coronal (XZ), and sagittal (YZ) views of the pressure field in the skull cavity are shown in **(a)~(b)**, **(c)~(d)**, and **(e)~(f)**, respectively. The transducer is on the left for axial and coronal views. Contours of -6 dB (black), -10 dB (red), and -20 dB (green) are shown. **(a), (c)**, **(e)** Views of the simulated BV PC-R lens field in the skull. **(b), (d), (f)** Views of the measured BV PC-R lens field in the skull.

The lens targeting the right perirhinal cortex (PC-R) generated a peak focal gain of 3.92 compared to 3.97 in the simulation; the lens targeting the left anterior hippocampus (AH-L) generated a peak focal gain of 5.71 compared to 5.79 in the simulation; and the BV lens targeting the left perirhinal cortex (PC-L) generated a peak focal gain of 4.43 compared to 4.49 in the simulation. Therefore, for all targets on the whole skull sample, free field focal gain had

less than or equal to a 1.5% difference from the corresponding simulation result when a BV lens was employed.

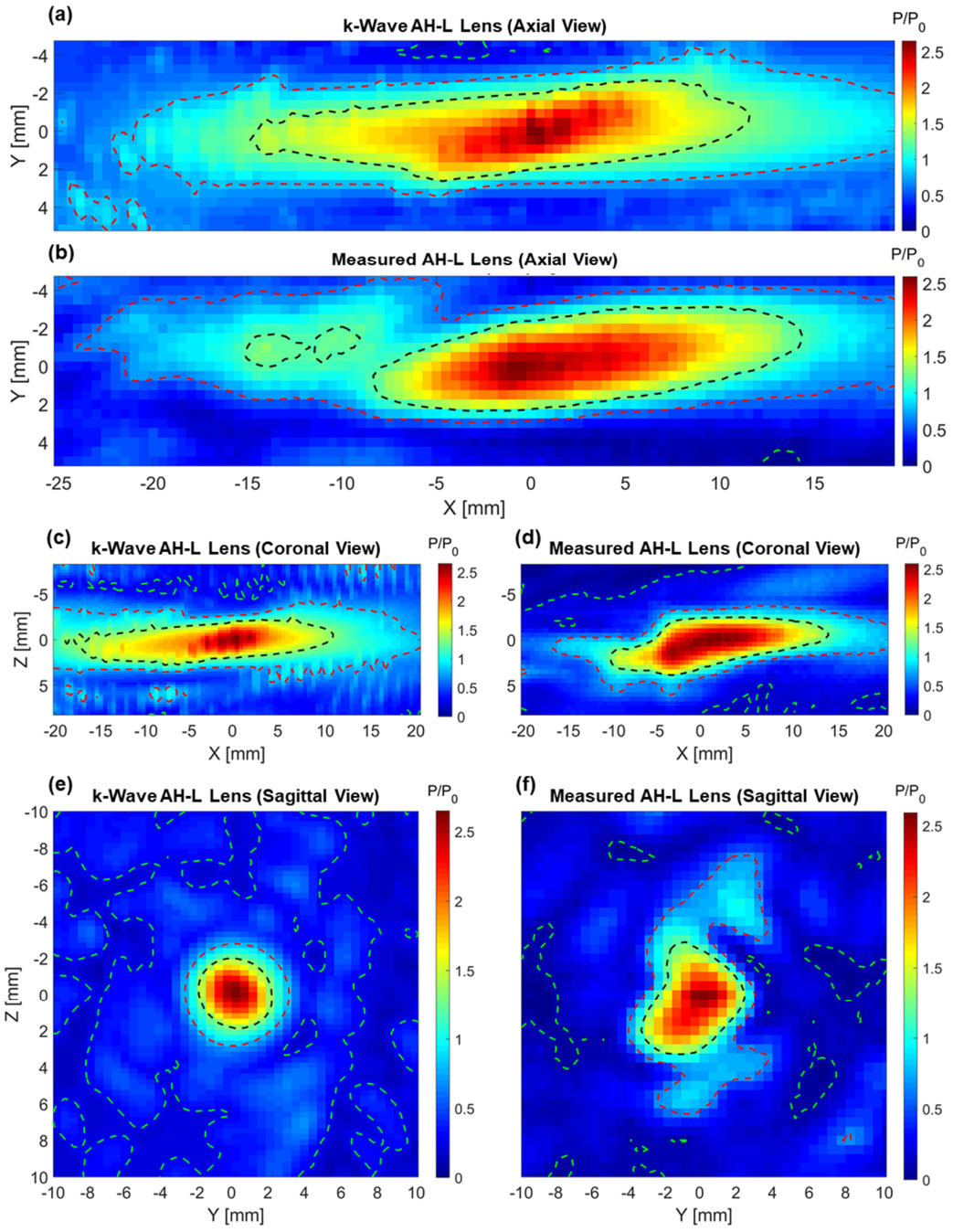

Fig. 3.16 Measurements of the BV lens targeting AH-L on the whole skull sample in comparison with the simulation. Axial (XY), coronal (XZ), and sagittal (YZ) views of the pressure field in the skull cavity are shown in **(a)~(b)**, **(c)~(d)**, and **(e)~(f)**, respectively. The transducer is on the left for axial and coronal views. Contours of -6 dB (black), -10 dB (red), and -20 dB (green) are shown. **(a), (c)**, **(e)** Views of the simulated BV AH-L lens field in the skull. **(b), (d), (f)** Views of the measured BV AH-L lens field in the skull.

In evaluating the -6dB focal length in free field, large differences were only observed when targeting the PC-L, showing a 33% shorter focal length experimentally, particularly in the region distal to the highest pressure, compared to simulation (PC-R: 49.36 mm measured vs. 47.32 mm simulated; AH-L: 26.00 mm measured vs. 25.27 mm simulated; PC-L: 26.00 mm measured vs. 38.85 mm simulated).

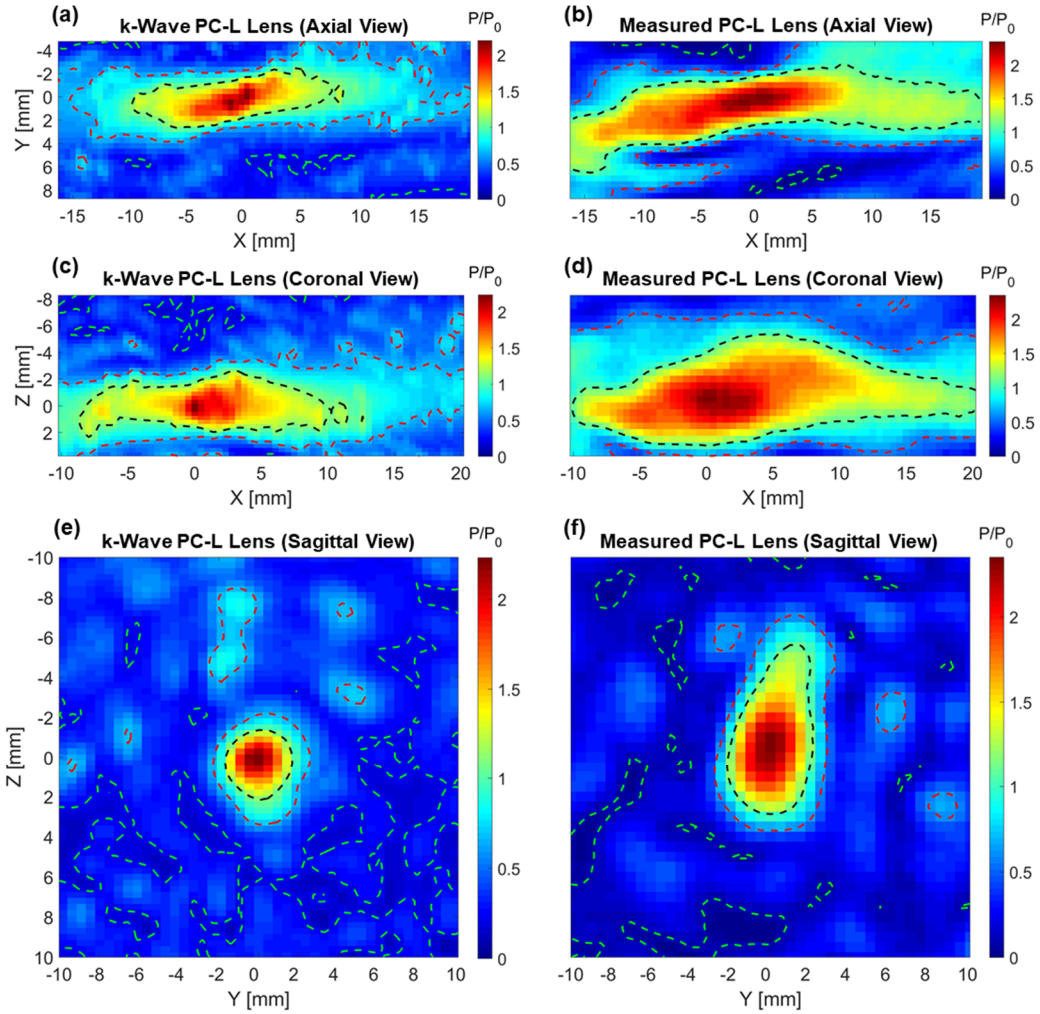

Fig. 3.17 Measurements of the BV lens targeting PC-L on the whole skull sample in comparison with the simulation. Axial (XY), coronal (XZ), and sagittal (YZ) views of the pressure field in the skull cavity are shown in **(a)~(b)**, **(c)~(d)**, and **(e)~(f)**, respectively. The transducer is on the left for axial and coronal views. Contours of -6 dB (black), -10 dB (red), and -20 dB (green) are shown. **(a), (c)**, **(e)** Views of the simulated BV PC-L lens field in the skull. **(b), (d), (f)** Views of the measured BV PC-L lens field in the skull.

In evaluating the -6 dB focal width in free field, the differences between measured values and simulation values were less than 3% (PC-R: 10.00 mm measured vs. 10.20 mm simulated;

AH-L: 5.00 mm measured vs. 5.15 mm simulated; PC-L: 6.50 mm measured vs. 6.60 mm simulated).

Apart from the focal length of the PC-L lens, the functions of beam forming of these three BV lenses were well predicted by the free field simulations with respect to focal peak gain, -6 dB focal width, and -6dB focal length, suggesting that free field measurements could be used to assess the lens performance and the lens structure's quality.

These lenses were then tested on the whole skull sample using measurement techniques as described previously. Briefly, each lens (for a different target) used its own 3D printed skull holder, assembling the transducer and lens to the skull with the same arrangement as that in the simulation.

The simulated and measured pressure fields when targeting the right perirhinal cortex (PC-R) on the skull sample are shown in Fig. 3.15. The available room in the skull was again not sufficient to cover the whole -6 dB focal lobe for this target, preventing the -6 dB focal length from being quantified. However, from the available views in Fig. 3.15 (a)~(d), it could be estimated that the measured focus was at least 30% longer than that in the simulation. The measured -6 dB focal width was 5.50 mm, 18% larger than the 4.68 mm in the simulation. The measured peak focal pressure gain was 2.28, 1.4% higher than the 2.25 in the simulation.

The simulated and measured pressure fields when targeting the left anterior hippocampus (AH-L) are shown in Fig. 3.16. The measured peak focal pressure gain is 2.59, 2.6% lower than the 2.65 observed in the simulation. Here, the 2D scans managed to capture the entire -6 dB main focal lobe. The measured -6 dB focal length is 24.00 mm, 18% shorter than that of

29.48 mm in the simulation. The measured -6 dB focal width is 6.00 mm, 28% wider than that of 4.68 mm in the simulation. The measured focus was distorted to be shorter and wider than the simulation prediction. Standing waves with a magnitude higher than -10 dB were observed in the coronal view of the simulated pressure field in Fig. 3.16 (c). However, in the coronal view of the measurement in Fig. 3.16 (d), these standing waves were not observed.

The resultant pressure fields when targeting the left perirhinal cortex (PC-L) are shown in Fig. 3.17. The measured peak focal pressure gain is 2.35, 5.2% higher than the 2.23 in the simulation. The available room in the skull was again not sufficient to cover the whole -6 dB focal lobe for this target, preventing the -6 dB focal length from being quantified. However, from the available views in Fig. 3.17 (a)~(d), it could be estimated that the measured focus was about 50% longer than that in the simulation. The measured -6 dB focal width was 8.50 mm, 82% larger than the 4.68 mm in the simulation.

In summary, focused ultrasound fields were formed by the BV lenses for these four targets on the whole skull sample. The peak focal pressure gain values measured for BV lenses were comparable to their corresponding BoB simulations. Both the left and right anterior hippocampus had comparable measured focal lobe sizes to the BoB simulation results. However, the measured focal lobes for both the left and right perirhinal cortex had significantly larger focal lobes compared to simulations. As the lenses were performing as predicted in free field, it is suspected that these differences were caused by an inaccurate representation of the skull on the ultrasound pathway.

3.10 BV LENSES ON HALF SKULL SAMPLE

Due to the insufficient room for the hydrophone in the cavity of the whole skull sample, only one out of the four target site scans covered the whole -6 dB focal lobe. Therefore, a second skull sample was used, for which only the left half of the skull was used to allow for larger scans, but at the expense of limiting targets to one hemisphere (left) and neglecting reflections from the far side of the skull.

The half skull sample's CT scan has a spatial resolution of 0.9766 mm × 0.9766 mm × 1.25 mm (X × Y × Z), over two times coarser than the whole skull sample's CT scan resolution (0.468 mm × 0.468 mm × 0.30 mm). However, this coarser resolution was closer to the T1-MRI scan resolution (1.00 mm × 1.00 mm × 1.00 mm) employed in human trials. To maintain reliable simulation predictions, the BoB simulations were done with a spatial resolution of 0.4883 mm × 0.4883 mm × 0.5 mm. This was done by expanding one imaging voxel into 12 voxels (2 × 2 × 3) in simulation space. The success of the half skull sample using BoB simulation with comparable resolution to the T1-MRI scans supports the use of T1-MRI when manufacturing lenses in human trials where direct validation measurements are unavailable.

Two target locations were estimated based on skull geometry, and a single lens was designed for each. Each lens was tested in free field, checking that the structure of the lenses was as intended and that the generated acoustic field was comparable to the field predicted by the simulation (Fig. 3.18).

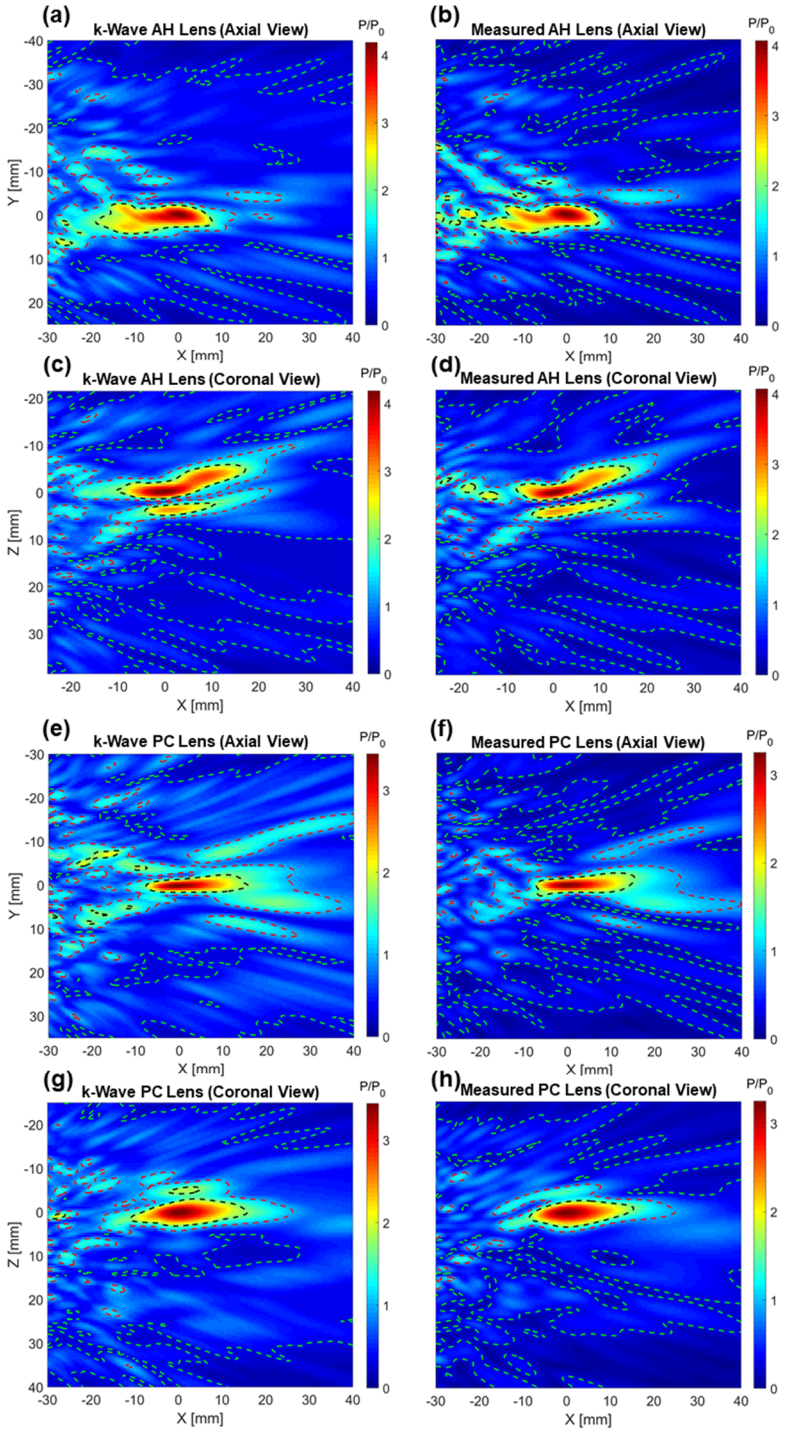

Fig. 3.18 Free field measurements of the BV lenses in comparison with simulations. Target-specific BV lenses for two sites on the left half skull sample were tested in free field: the left anterior hippocampus (AH) in **(a)~(d)** and the left perirhinal cortex (PC) in **(e)~(h)**. Contours of -6 dB (black), -10 dB (red), and -20 dB (green) are shown. In all views, the transducer and the lens are on the left outside the measured field. The left column shows the simulations, and the right column shows the measurements. **(a), (b)** Axial views using the BV AH lens. **(c), (d)** Coronal views using the BV AH lens. **(e), (f)** Axial views using the BV PC lens. **(g), (h)** Coronal views using the BV PC lens.

The free field measurement of the BV lens for the left anterior hippocampus (AH) generated a peak focal gain of 4.07, 2.8% lower than the 4.19 calculated in the simulation. The free field measurement of the BV lens for the left perirhinal cortex (PC) generated a peak focal gain of 3.25, 5.5% lower than the 3.44 calculated in the simulation. The measured -6 dB focal length of the AH lens was 27.50 mm, 2.4% longer than the 26.86 mm calculated in the simulation. The measured -6 dB focal length of the PC lens was 24.00 mm, 11% shorter than the 26.86 mm calculated in the simulation. The measured -6 dB focal width in free field was 7.50 mm for the AH lens, 19% shorter than the 9.28 mm calculated in the simulation. The free-field focal width of the PC lens was the same as that in simulation (6.00 mm).

Overall, there was good agreement between the measurements and simulations for the effective foci formed by these lenses in the free field. There were, however, a few discrepancies. For example, the measurements revealed several -6 dB pre-focal lobes in the AH lens, whereas the simulation predicted fewer and smaller -6 dB lobes at different locations in the axial view (Fig. 3.18 (a)). For the PC lens, this was reversed. Where the simulation predicted several -6 dB pre-focal lobes, none were detected experimentally. Moreover, for the PC lens, the simulation predicted a -6 dB pressure magnitude side lobe on the negative Z side of the main focal lobe in the coronal view shown in Fig. 3.18 (g). However, in the corresponding measurement shown in Fig. 3.18 (h), this side lobe was below -6 dB in magnitude. As these discrepancies between simulation and measurements occur in the free field, this may suggest errors and uncertainty in the simulation procedure and lens manufacture rather than skull-related modelling.

The AH and PC lenses were then tested on the left-half skull sample and compared with the simulations in Fig. 3.19 and Fig. 3.20 for AH and PC, respectively. The measured peak focal pressure gain, -6 dB focal length, and width were quantified for both lenses.

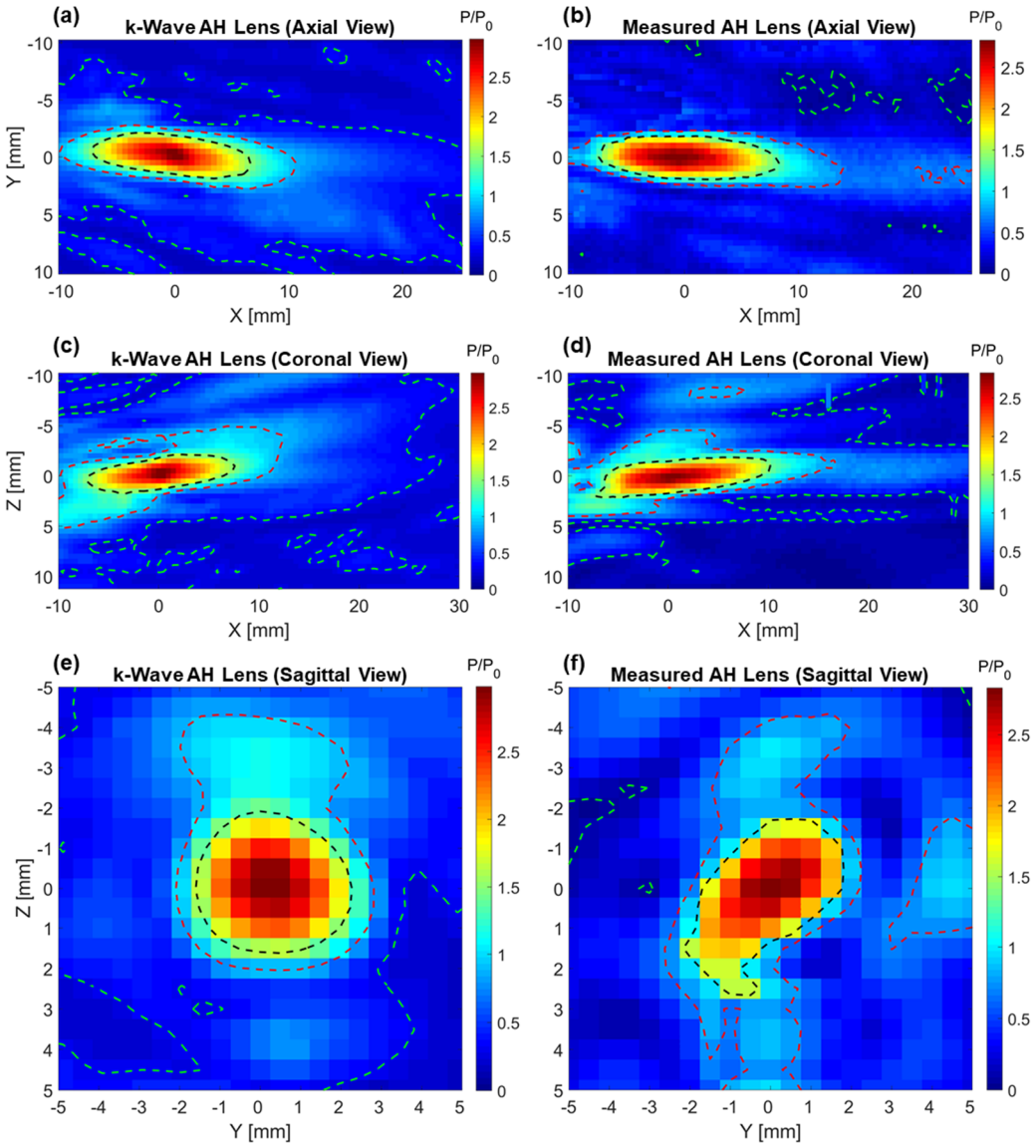

Fig. 3.19 Measurements of the BV lens targeting AH on the left of the half skull sample in comparison with the simulation. Axial (XY), coronal (XZ), and sagittal (YZ) views of the pressure field in the skull cavity are shown in **(a)~(b)**, **(c)~(d)**, and **(e)~(f)**, respectively. The transducer is on the left for axial and coronal views. Contours of -6 dB (black), -10 dB (red), and -20 dB (green) are added. **(a), (c)**, **(e)** Views of the simulated BV AH lens field in the skull. **(b), (d), (f)** Views of the measured BV AH lens field in the skull.

The measured peak focal pressure gain was 2.83 for the BV AH lens, 5.1% lower than the predicted value of 2.98 in simulation. The measured -6 dB focal length was 15.50 mm for the

BV AH lens, 5.8% longer than that of 14.65 mm in simulation. The measured focal width was 4.25 mm for the BV AH lens, 6.3% wider than that of 4.00 mm in the simulation.

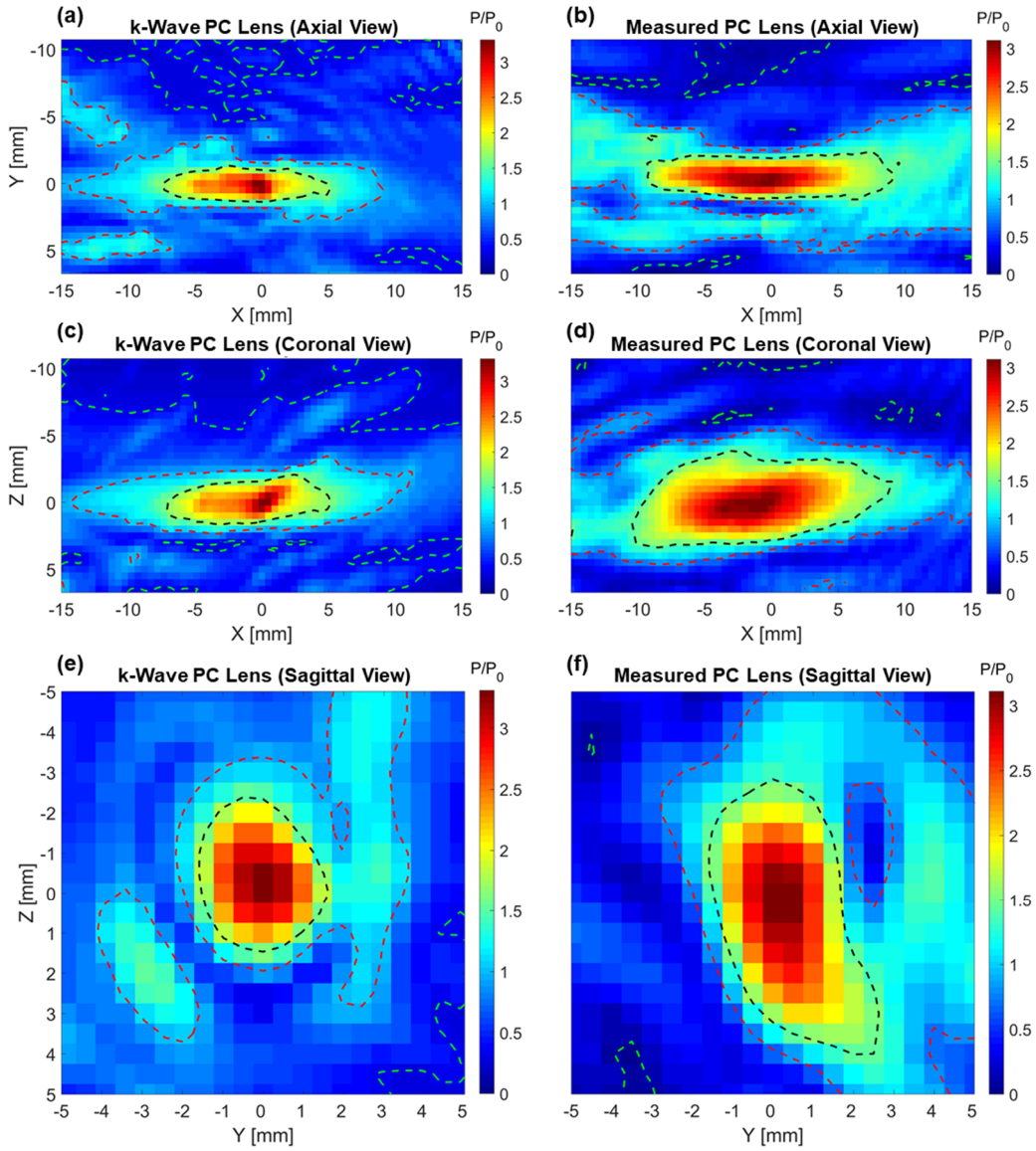

Fig. 3.20 Measurements of the BV lens targeting PC on the left of the half skull sample in comparison with the simulation. Axial (XY), coronal (XZ), and sagittal (YZ) views of the pressure field in the skull cavity are shown in **(a)~(b)**, **(c)~(d)**, and **(e)~(f)**, respectively. The transducer is on the left for axial and coronal views. Contours of -6 dB (black), -10 dB (red), and -20 dB (green) are added. **(a), (c)**, **(e)** Views of the simulated BV PC lens field in the skull. **(b), (d), (f)** Views of the measured BV PC lens field in the skull.

The measured peak focal pressure gain was 3.11 for the BV PC lens, 6.1% lower than the predicted value of 3.31 in simulation. The measured -6 dB focal length was 19.00 mm for the BV PC lens, 56% longer than that of 12.21 mm in simulation. The measured focal width was

6.75 mm for the BV PC lens, 80% wider than the 3.75 mm in the simulation. The measured focal size of AH was comparable to the simulation, as shown in Fig. 3.19. However, the measured focal size of the PC was noticeably larger than the simulation, as shown in Fig. 3.20.

In summary, the results for the half skull sample were consistent with the findings for the whole skull sample. Focused ultrasound fields were successfully formed by the BV lenses for these two targets on the left of the half skull sample. The peak focal pressure gain values measured for BV lenses were comparable to their corresponding simulations. The anterior hippocampus had a measured focal lobe size comparable to the simulation results. However, for the perirhinal cortex on this left half of the skull, the measured focal volume was significantly larger than the simulations, which was consistent with the findings on the whole skull sample.

The measured focal lobes were significantly larger than those in simulations for all three perirhinal cortex sites tested over two different skull samples. This consistent observation suggests that the perirhinal cortex, despite being shallower to the head surface than the anterior hippocampus, is harder to focus on with ultrasound stimulation. As the perirhinal cortex is a shallower target, it is likely that more of the acoustic signals will be at an oblique incidence angle, creating shear waves in the skull. However, as the simulations employed a fluid-based acoustic approach, shear waves were not captured, potentially explaining some of the discrepancies between measurement and simulation. In addition, the ultrasound pathway to the perirhinal cortex is closer to the edge of the temporal bone, an area with complicated skull geometry. Within the region, significant variations in skull thickness and porosity can result from: (i) the gap between sphenoid and temporal bone; (ii) the pterion; and (iii) the zygomatic process of temporal bone. These microscale variations are challenging for imaging techniques to pick up and represent accurately in acoustic field modelling.

3.11 TRANSDUCER POSITION SENSITIVITY

In the previous transcranial ultrasound neuromodulation human trial (Blackmore, 2018; Braun et al., 2020; Butler et al., 2022), the transducer position was recorded for 9 participants using a neuronavigational system (Brainsight, Rogue Resolutions, Montreal, Canada) while stimulating the middle temporal area (MT) and fusiform face area (FFA).

Two values were recorded for each stimulation: (i) the transducer's angling error in degrees compared to the designed transducer orientation; and (ii) the transducer's target distance error in millimetres between the selected target location in the brain (MT and FFA) and the relative focal point created by the transducer within the brain. The measured data is summarised in Fig. 3.21, categorised based on stimulation subject and target.

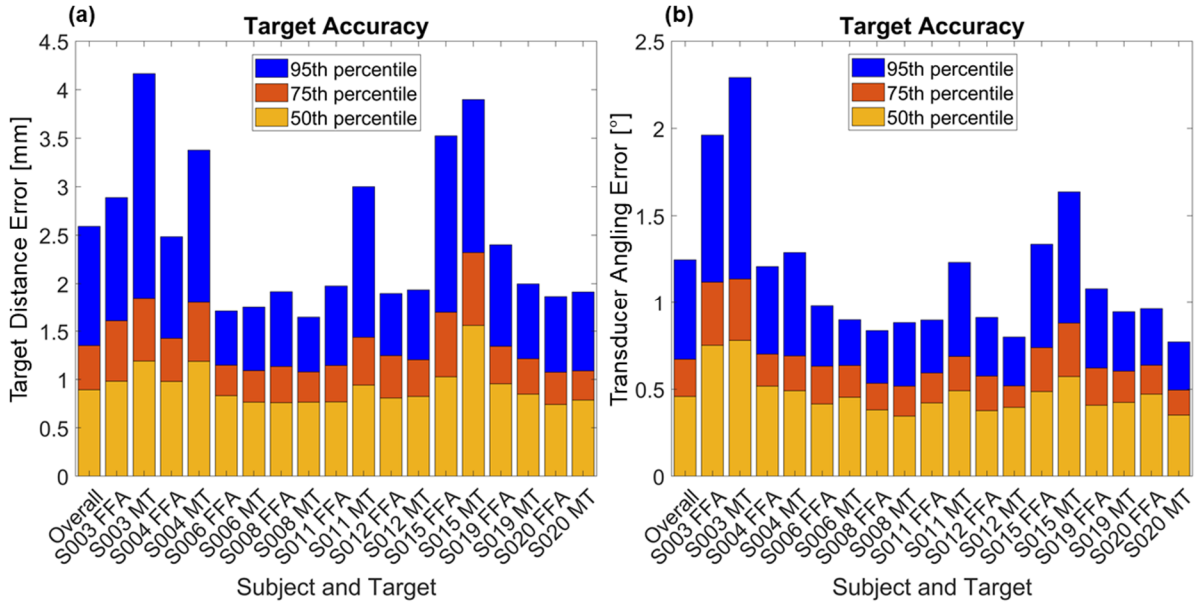

Fig. 3.21 Transducer position recordings in the previous human trial. The transducer position error readings were recorded for each stimulation. The data were summarised by 50th percentiles, 75th percentiles, and 95th percentiles for each subject and target case. **(a)** The target distance error in millimetres between the designed target location and the ultrasound focus. **(b)** The transducer angling error in degrees compared to the designed transducer orientation.

Across all the ultrasound firings, the 95th percentile of the overall target distance error was 2.59 mm. The largest target distance error occurred for the MT of subject S003, with a value of 4.16 mm. In all cases, the 95th percentile of the overall transducer angling error was 1.25°. The largest transducer angling error occurred for the MT of subject S003, with a value of 2.29°. These transducer position datasets from the previous human trial revealed the range that the transducer position sensitivity study needed to cover.

In this transducer position sensitivity study, the sensitivity of the 4 lens types (BV, BS, PV, and PS) to the error in transducer position was tested to determine if any one of the lenses was most robust to transducer positioning error. This study was also used to determine what accuracy was needed to ensure stimulation of the desired target location. The acceptable pressure drop due to the transducer position error was set to be within 10%. Six degrees of freedom were identified and tested based on the XYZ coordinates shown in Fig. 3.12. X is in the lateral to medial direction, Y is in the posterior to anterior direction, and Z is in the cephalic to caudal direction. Translation and rotation were tested for each of the three directions. The rotations have directions following the right-hand rule. To study the lens type, four lenses (one for each type) made for the right anterior hippocampus were used on the whole skull sample. The 3D printed skull holder shown in Fig. 3.12 was cut into two parts to separate the transducer side from the skull side and held together using two additional customised parts. When in place, the added parts retained the previous transducer-skull relative position by firmly holding the skull holder in one piece. When the added parts were removed, the transducer could be moved relative to the skull.

Firstly, the transducer (mounted with a lens) and the skull were placed together in deionised and degassed water. The skull holder retained the relative transducer-skull position. The fibre-

optic hydrophone was used as before in the skull cavity to locate the focus peak created by each lens. The hydrophone was then fixed at this location relative to the skull, such that the hydrophone is always measuring relative to the designed peak focal pressure at the target. The skull side of the skull holder was then demounted from the transducer side, allowing the transducer to move around. Based on the ranges utilised in the previous human trial, a translation of ±5 mm and a rotation of ±5° were tested in each direction, with a step size of 0.5 mm for translation and 1° for rotation. Ten readings were taken at each position of translation and rotation. Four lenses for the right anterior hippocampus of the whole skull sample were tested for all six degrees of freedom.

In Fig. 3.22 (a), target pressure measurements as a function of transducer translation in the X direction are shown, representing the axial direction of the ultrasound focus. For all translations in Fig. 3.22 (a), the loss in pressure amplitude rarely exceeded 25% compared to the 80% to 90% measured in the other two translation directions (Fig. 3.22 (c) and (e)). Using the target error range in the previous human trial, the BV, BS, and PS lenses were within a 10% and 13% target pressure reduction on the -2.59 mm and +2.59 mm sides, respectively. The PV lens was more sensitive to the transducer position than the other three lenses in this direction.

In Fig. 3.22 (c), the target pressure measurements as a function of transducer translation in the Y direction are shown, representing the radial direction of the cigar-shaped ultrasound focus. A smooth and symmetric distribution was measured here for all lenses, with no lens showing lower sensitivity in this direction. In order to control the target pressure reduction to be within 10%, the transducer translation needed to be within ±1 mm.

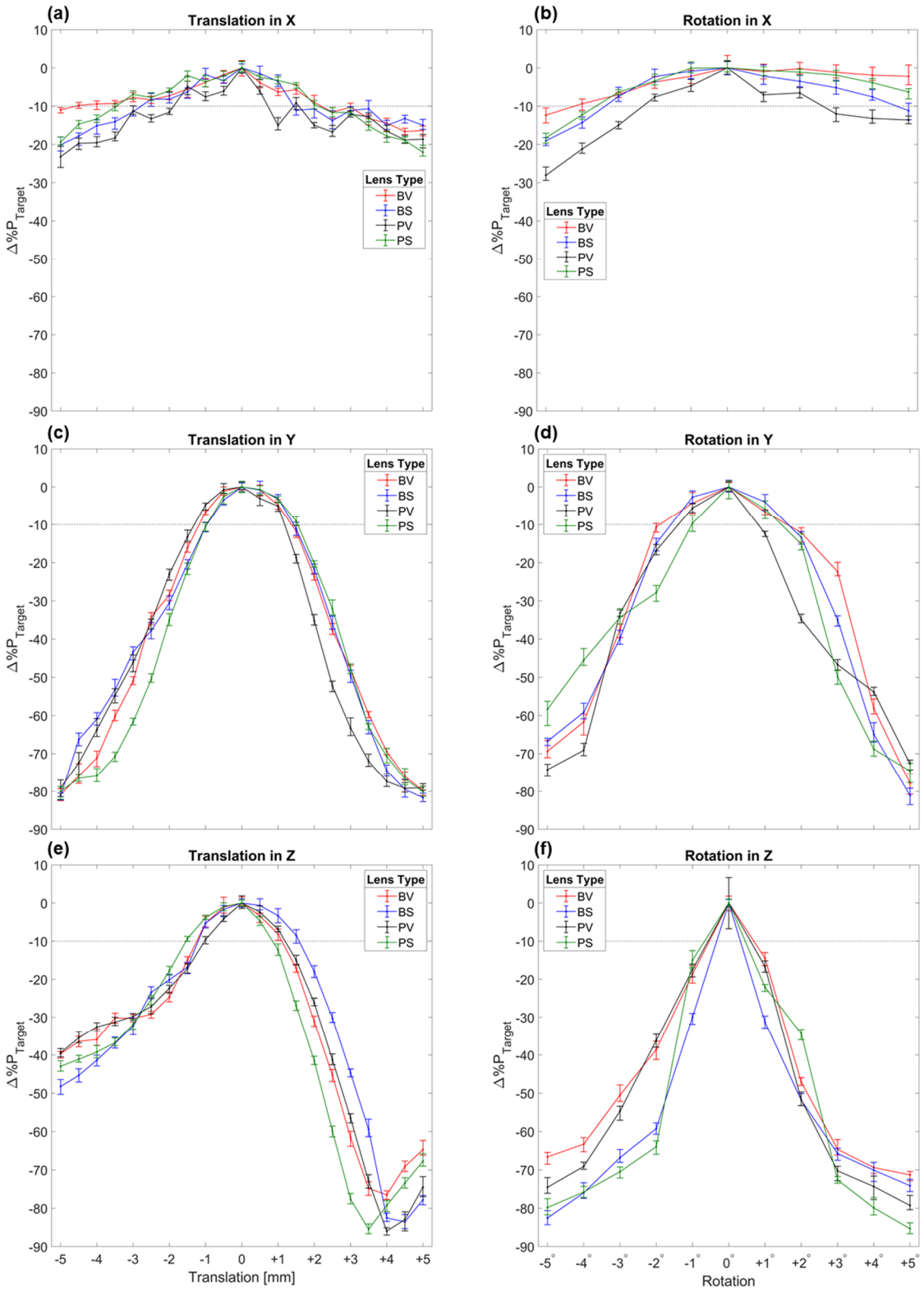

Fig. 3.22 Transducer position sensitivity study: target pressure change measurement. The right anterior hippocampus of the whole skull sample was the target. Four lens types from before were tested on six degrees of freedom. A horizontal line of -10% is added to each subplot showing the threshold. **(a), (b)** Transducer translation and rotation in the X direction. **(c), (d)** Transducer translation and rotation in the Y direction. **(e), (f)** Transducer translation and rotation in the Z direction.

In Fig. 3.22 (e), target pressure measurements as a function of transducer translation in the Z direction are shown, representing the other radial direction of the cigar-shaped ultrasound focus. In the free field, the distribution is expected to be symmetric (Fig. 3.22 (c)). However, the non-symmetric distribution measured here for all four lenses demonstrated the impact of the presence of the skull on the acoustic pathway. In order to control the target pressure reduction to be within 10%, the transducer translation needed to be within ±1 mm. The BS lens was slightly less sensitive than all other lenses in the +Z direction. The PS lens was slightly less sensitive than all other lenses in the -Z direction.

In Fig. 3.22 (b), target pressure measurements as a function of transducer rotation in the X direction are shown. The PV lens was noticeably more sensitive than the other lenses. For all four lenses, the target pressure drop was controlled to be within 10% in ±2.29° range, covering the extreme 95th percentile of angling error recorded in the previous human trial.

In Fig. 3.22 (d), target pressure measurements as a function of transducer rotation in the Y direction are shown. A symmetric distribution centred on 0° was observed, with comparable distributions across all lenses. To keep the target pressure reduction within 10%, the transducer rotation in this direction had to be controlled to be within ±1°. The PS lens was more sensitive to angling error in the -Y rotation direction for small angles less than -3° but was interestingly less sensitive than the other three lenses for larger angles in the same rotation direction. The PV lens was more sensitive to angling errors in the +Y rotation direction.

In Fig. 3.22 (f), target pressure measurements as a function of transducer rotation in the Z direction are shown. It was discovered that the distribution was symmetric and centred at 0°.

With this degree of freedom, all of the lenses were sensitive to angling errors. The transducer rotation must be within ±0.5° to control the target pressure reduction to within 10%.

To summarise, when using the PDMS lens, the transducer's position error needs to be restrained within 1 mm or 0.5° such that the target pressure drop can be within 10%. This relationship agrees with the findings in the literature (Maimbourg et al., 2020b). As the data recorded in the previous human trial did not specify the direction, the tightest measured error limit is used for all directions. Over half of the stimulations in the previous human trial were within the 10% tolerance, as the overall 50th percentiles for the error distance and angle were within the corresponding measured error limits. Based on these results, an improved transducer-head holder needs to be designed to use the lens method in the upcoming human trial.

Overall, none of the four lenses had noticeably lower sensitivity to translation or rotation. As a result, the BV lens remains the first option for continuing this project. However, the similar results in transducer motion sensitivity suggest that it would be possible to switch to a different lens type if needed.

3.12 Measured Focal Peak Location Registration

For all the simulated pressure maps shown in this chapter, the location of the peak focus was known in the simulation space and within the 2.5 mm radius spherical target volume. However, in all the measurements, the location of the peak focus was experimentally found, and field scans were done around the focus. The distance between the target site and the measured peak focus could only be estimated with an accuracy of about 5 mm.

In order to have accurate spatial error registration, the Brainsight neuronavigational system was added to the validation experiment, as shown in Fig. 3.23. The system uses an optical tracking camera to track the movement of reflective trackers in the field of view. Each tracker has three reflective spheres to allow the recording of translation and rotation. The first tracker (Tracker 1) was fixed to the transducer, which itself was fixed to the skull by a 3D printed skull holder, as discussed earlier. Using four distinct locations on the skull chosen based on the neuronavigational sample and imaging data, the skull position was linked to its imaging data via Tracker 1. On the half skull sample, the error varied from 0.3 mm to 1.8 mm across the four registration points. On the whole skull sample, the error varied from 0.4 mm to 1.5 mm across the four registration points.

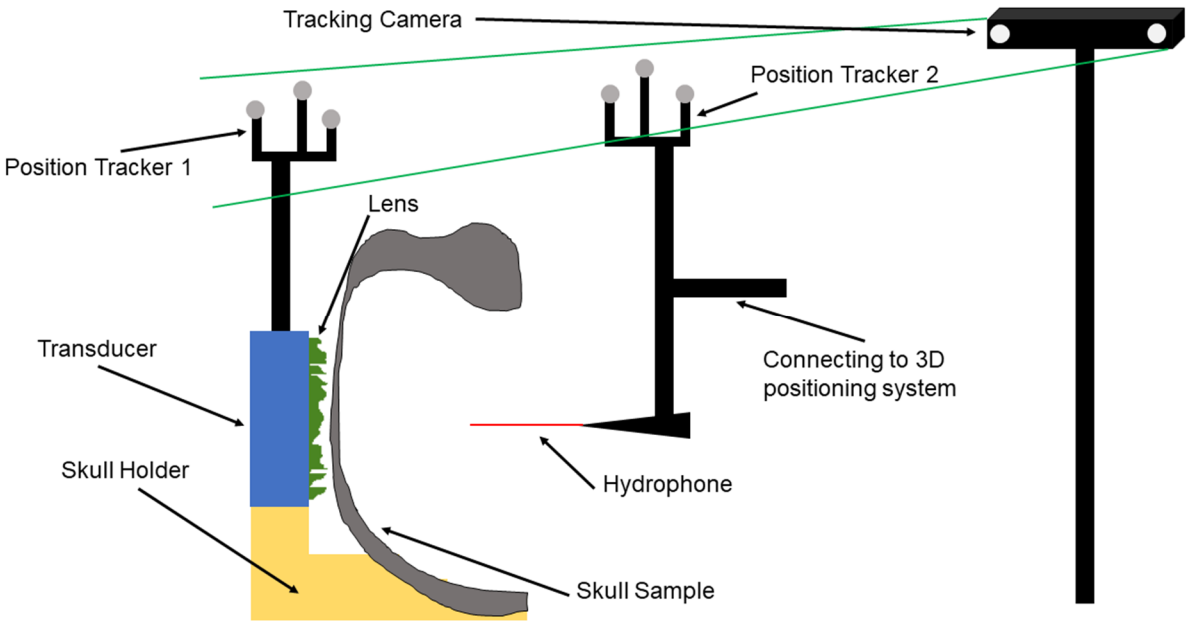

Fig. 3.23 Schematic of the experimental setup for Brainsight position registration. The example shows the half skull case. Tracker 1 was added to the transducer, which was fixed to the skull sample by the target-specific, 3D printed skull holder. The relative position of Tracker 1 to the skull was registered at four selected locations on the skull sample. Tracker 1 linked the position of the skull sample to its imaging data. Tracker 2 was registered to the tip of the hydrophone and moved together by the 3D positioning system. The trackers were monitored by the tracking camera.

To prevent damage to the hydrophone, Tracker 2 in Fig. 3.23 was fixed to within 1 mm of the hydrophone tip rather than directly, potentially adding another systematic error to the distance measurement.

To validate its positioning, the focus peak was first found, where the target distance error and pressure magnitude were recorded. Then, the hydrophone was moved to a target location where the target error in Brainsight became negligible and the pressure magnitude was recorded. This was repeated for the BV lenses on the 6 targets, across both the whole and half-skull samples, as summarised in Table 3.2.

		Δ%Pressure Focus Peak vs Target	Overall Distance Error [mm]	Axial Distance Error [mm]	Lateral Distance Error [mm]
Half Skull	AH-L	4.82%	3.17	2.35	2.13
	PC-L	1.81%	2.75	2.03	1.85
Whole Skull	AH-L	3.66%	2.73	2.38	1.34
	AH-R	4.64%	2.97	2.29	1.90
	PC-L	2.94%	2.90	2.15	1.95
	PC-R	2.80%	3.10	2.25	2.13
Mean		**3.45%**	**2.94**	**2.24**	**1.88**

Table 3.2: Summary of Brainsight position registration results on skull samples. Error is defined as the offset of the measured pressure peak from the registered target location. BV lenses were used in this study on the 6 target sites across the 2 skull samples. **AH-R**: right anterior hippocampus. **AH-L**: left anterior hippocampus. **PC-R**: right perirhinal cortex. **PC-L**: left perirhinal cortex.

For all target sites, the pressure magnitude drop at the target was less than 5% when compared to the focus peak pressure. The pressure differences for the perirhinal cortices were lower than the pressure differences for the anterior hippocampi, likely due to the smaller reduction in pressure magnitude from the larger foci volume within the perirhinal cortices compared to that of the anterior hippocampi.

In this case, ‘distance error’ was defined as the offset of the measured pressure peak location from the registered target location. For all the target sites, the mean overall distance error was less than 3 mm, and the largest overall distance error was less than 3.2 mm. The ~3 mm overall distance error can likely be attributed to: (i) the set-up errors introduced when the skull and hydrophone were registered to the tracking system; and (ii) imperfections in targeting by the lens. The distance error was available in 3-dimensional coordinates, from which the axial and lateral errors can be calculated, as listed in Table 3.2. The axial error was found to always be larger than the lateral error for all target sites.

3.13 PAIRED SOURCES MEASUREMENT ON SKULL

The WHPS BoB simulations were also computed. Two transducers focused on the left and right anterior hippocampus or the left and right perirhinal cortex of the whole skull sample were sent at the same time. The simulation results were compared with measurements made by a hydrophone inside the skull. In these experiments, the BV lenses for the four targets on a whole skull sample were used in pairs. New skull holders were 3D printed and used here such that the positions of the two transducers on the whole skull sample were identical to those used in simulations. As an example, the axial views of the anterior hippocampus pair are shown in Fig. 3.24.

Fig. 3.24 (a) shows the axial pressure distribution of the entire simulation space. The BV AH-L lens and BV AH-R lens can be seen on the sides of the skull in this slice. Three rectangles are overlaid on this colormap to show the regions of the scans in Fig. 3.24 (c), (f), and (g). The red rectangle shows the middle scan, which can capture both foci but only partially. In order to capture more of the focal regions on each side, the white and brown rectangles represent the

scans that were done with the hydrophone pointing to the left and right sides of the whole skull sample to access regions closer to the skull.

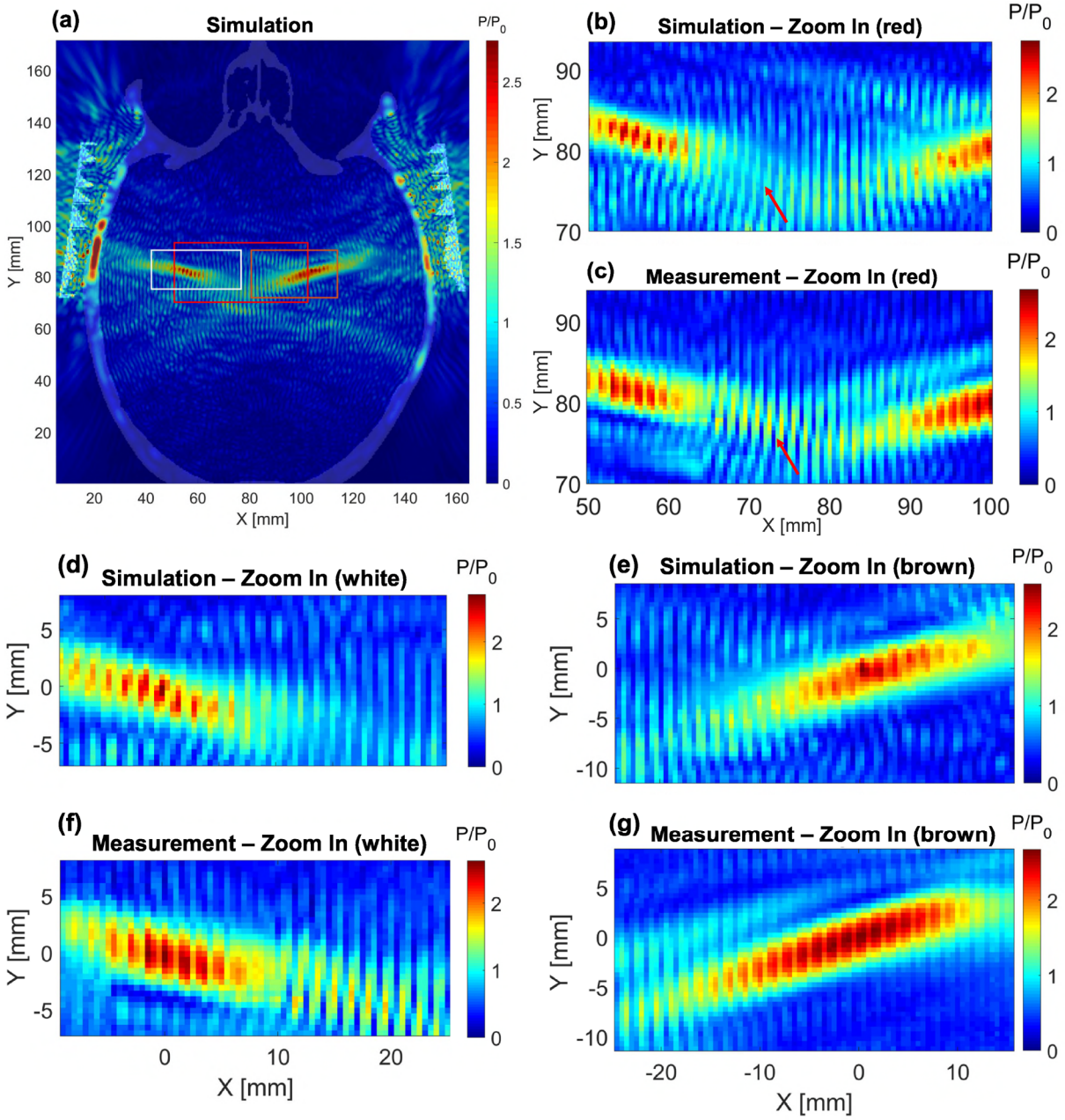

Fig. 3.24 Measurements of BV lenses targeting the AH pair on the whole skull sample in comparison with the simulation. The WHPS BoB simulation results are shown here. All subplots are axial views. **(a)** An axial view of the whole simulation space. The red, white, and brown rectangles show the middle, left, and right regions of the scans. **(b), (c)** simulation and measurement in the middle scan (red rectangle). **(d), (f)** simulation and measurement in the left scan (white rectangle). **(e), (g)** simulation and measurement in the left scan (brown rectangle).

For the middle scan region, the simulated pressure distribution is shown in Fig. 3.24 (b) and the measured acoustic field is shown in Fig. 3.24 (c). The standing waves that were predicted in simulation to be present in the whole field of view were confirmed in the measurement. Between the foci, the magnitude of the measured standing waves is higher than that modelled. At the position shown by the red arrows, the measured standing wave pressure gain of 1.74 is higher than 50% of the peak focal gain (2.65).

At the left anterior hippocampus, the measured peak focal gain is 2.63, 4.4% lower than the 2.75 calculated in the simulation. The measured -6 dB focal width is 5.03 mm, 14% larger than the 4.42 mm calculated in the simulation. The measured -6 dB focal length is 19.78 mm, 13% larger than the 17.56 mm calculated in the simulation. This value of measured focal length excludes standing waves of sufficient magnitude. If these are included, the focal length is easily twice as long as that in simulation. Comparing to the measurements where only one transducer is used on the skull sample, 1.5% higher focal gain is achieved with about 20% smaller -6 dB focal length and width.

At the right anterior hippocampus, the measured peak focal gain is 2.67, 3.0% lower than the 2.76 calculated in the simulation. The measured -6 dB focal width is 6.02 mm, 5.6% larger than the 5.70 mm calculated in the simulation. The measured -6 dB focal length is 30.56 mm, 31% larger than the 23.27 mm calculated in the simulation. Comparing the measurements when only one transducer is used on the skull sample, the focal gain is 13% lower with a -6 dB focal width that is about 20% larger.

This comparison was also done for the perirhinal cortex pair on the whole skull sample. At the left perirhinal cortex, the measured peak focal gain is 1.67, 2.6% higher than the 1.62 calculated

in the simulation. The measured -6 dB focal width is 4.50 mm, 44% larger than the 3.11 mm calculated in the simulation. Despite the larger focal width in measurements compared to simulation, this does follow the trend observed previously when evaluating single-source measurements. Compared to measurements performed with a single source, the focal width is 47% smaller and the peak focal gain is 29% lower, even with a narrower focal volume.

At the right perirhinal cortex, the measured peak focal gain is 1.70, 2.9% smaller than the 1.75 calculated in the simulation. The measured -6 dB focal width is 7.25 mm, 15% larger than the 6.30 mm calculated in the simulation. Compared to the single source case, the measured peak focal gain is 25% lower with a 32% wider -6 dB focal volume.

In the paired source measurements, the standing wave patterns are more significant than in the single source case. This is because the two transducers are sending ultrasound waves towards each other, and this agrees with the simulations. The standing wave patterns occurring in the main focal lobes affect the focal pressure distribution significantly. In addition, the magnitude of standing waves between the formed foci is significantly larger than predicted in simulations. In one case, at the left anterior hippocampus, the interference of left- and right-travelling waves can help increase the focal gain and reduce the focal volume. However, this effect is insignificant, and in all three other cases, this interference works against the focusing with a significant reduction of peak focal gain at the target.

3.14 SUMMARY & DISCUSSION

The validation of using PDMS lenses for the purpose of focusing ultrasound through the skull to target locations for neuromodulation was described in this chapter. Overall, this novel method of using a PDMS lens and flat transducer via the temporal bone window on the human

skull to target deep brain targets has been validated on two human skull samples. The modelling pipeline described in Chapter 2 was shown in experiments in this chapter to be a feasible stimulation planning method, along with providing the information needed for making the target-specific lenses.

Firstly, the transducer was calibrated and characterised to allow it to be used in the simulations. PDMS with a base to curing agent ratio of 10:1 was found to have acoustic properties consistent with literature values. Using a regular cuboid of PDMS and three PDMS Fresnel lenses focusing to 65 mm, 75 mm, and 85 mm in front of the transducer surface, density, attenuation, and speed of sound were measured using a different method than the traditional (Xia et al., 2013) to better match the focal gain in free field water. Although sufficient for the existing purpose, the PDMS lens manufacturing procedure could be optimised further by, for example, centrifuging PDMS in the liquid state to reduce the length of the degassing process (LaFratta et al., 2004).

Validation of the lenses was done on two CT-scan mapped cadaver skull samples. Each skull was segmented either using a binary or a porous segmentation, and three types of simulations were carried out: BoB, using only binary skull segmentation; PoP, using only porous skull segmentation; and BoP simulations, using binary skull segmentation generated lenses on the porous skull segmentation. Simulations were then compared to the corresponding lens measurements.

The lenses were then tested on specific deep brain targets within the skull. Using the right anterior hippocampus target on the whole skull, all 4 types of lenses were tested. After selecting the BV lens to move forward with, three additional targets were tested: the left and right

anterior hippocampus and the left and right perirhinal cortex. However, as the experimentally measured scans were not able to capture the entire -6 dB focal length for 6 out of the 7 cases due to space limitations within the skull cavity, a half-skull sample was needed. For the half skull sample, 2 targets were tested: the left anterior hippocampus and the left perirhinal cortex. All measurements and simulation results are summarised in Table 3.3.

			1	2	3	4	5	6	7	8	9
		Skull Sample	Whole Skull	Whole Skull	Whole Skull	Whole Skull	Whole Skull	Whole Skull	Whole Skull	Half Skull	Half Skull
		Target	AH-R	AH-R	AH-R	AH-R	PC-R	AH-L	PC-L	AH-L	PC-L
		Lens Type	BV	BS	PV	PS	BV	BV	BV	BV	BV
Lens in Free Field	k-Wave Simulation Results	Focal Peak Gain [P/P_0]	5.82		6.34		3.97	5.79	4.49	4.19	3.44
		-6 dB Focal Length [mm]	37.34		29.49		47.32	25.27	38.85	26.86	26.86
		-6 dB Focal Width [mm]	5.14		5.10		10.20	5.15	6.60	9.28	6.00
	Experimental Measurement	Focal Peak Gain [P/P_0]	5.80	5.80	6.36	6.39	3.92	5.71	4.43	4.07	3.25
		-6 dB Focal Length [mm]	36.86	33.98	29.61	27.66	49.36	26.00	26.00	27.50	24.00
		-6 dB Focal Width [mm]	5.00	5.00	5.00	5.00	10.00	5.00	6.50	7.50	6.00
	Measurement vs Simulation	Δ% Focal Peak Gain	-0.38	-0.38	+0.29	+0.73	-1.30	-1.50	-1.50	-2.80	-5.53
		Δ% -6 dB Focal Length	-1.29	-9.00	+0.42	-6.21	+4.32	+2.89	-33.08	+2.40	-10.65
		Δ% -6 dB Focal Width	-2.72	-2.72	-1.96	-1.96	-1.96	-2.87	1.52	-19.16	0.00
Lens on Skull	k-Wave Simulation Results	Focal Peak Gain [P/P_0]	3.17		4.34		2.25	2.65	2.23	2.98	3.31
		-6 dB Focal Length [mm]	27.70		27.14		16.88	29.48	21.06	14.65	12.21
		-6 dB Focal Width [mm]	4.21		4.68		4.68	4.68	4.68	4.00	3.75
	Experimental Measurement	Focal Peak Gain [P/P_0]	3.05	3.01	3.07	3.03	2.28	2.59	2.35	2.83	3.11
		-6 dB Focal Length [mm]						24.00		15.50	19.00
		-6 dB Focal Width [mm]	5.00	5.50	5.00	5.00	5.50	6.00	8.50	4.25	6.75
	Measurement vs Simulation	Δ% Focal Peak Gain	-3.83	-5.40	-41.38	-43.33	+1.40	-2.55	+5.22	-5.05	-6.06
		Δ% -6 dB Focal Length						-18.59		+5.80	+55.64
		Δ% -6 dB Focal Width	+18.71	+30.58	+6.84	+6.84	+17.52	+28.21	+81.62	+6.25	+80.00

Table 3.3: Comparison of all lens cases in the validation experiment. BoB simulation results are used for cases with BV and BS lenses. PoP simulation results are used for cases with PV and PS lenses. 6 out of 7 cases on the whole skull sample were not able to acquire the -6 dB focal length. **P_0**: transducer surface pressure. **AH-R**: right anterior hippocampus. **AH-L**: left anterior hippocampus. **PC-R**: right perirhinal cortex. **PC-L**: left perirhinal cortex. **BV**: Binary Voxel lens, structure derived from homogeneous skull segmentation rounded to simulation grid size. **PV**: Porous Voxel lens, structure derived from porous skull segmentation rounded to simulation grid size. **BS**: Binary Smooth lens, structure derived from homogeneous skull segmentation rounded to the 3D printer's layer thickness. **PS**: Porous Smooth lens (structure derived from porous skull segmentation rounded to the 3D printer's layer thickness).

In the free field, the lenses had comparable measured performance to simulations, demonstrating that the target-specific PDMS lenses were manufactured to an acceptable standard. However, when evaluating the overall percentage differences between the measurements and simulations in free field, it was evident that there are lens structural errors introduced in the manufacturing process, inaccuracies in material properties, and aspects of acoustics not represented in the linear, fluid-based k-Wave acoustic simulation.

For comparison inside the skull, BoB simulation results were shown to provide the best agreement with the measured peak focal gain. Across all four different types of lenses, the measured peak focal gain values for AH-R on the whole skull sample agreed with those in the BoB simulation. Both simulation types using porous skull segmentation (BoP and PoP) significantly overestimated the actual peak focal gain, indicating that the current approach of porous segmentation was not able to capture the complex mixture of solid skull bone and fluid in the real skull. Simulations assume that the pores in the skull are filled with water, i.e., skull is a bone-water mixture. However, the *ex vivo* skull samples have been outside the body for a long time. It is reasonable to say that a lot of the pores are filled with air and are impractical to be fully filled with water again, i.e., skull is more likely to be a bone-air mixture. This mismatch between simulation and experiment may help explain the poor performance of simulations using porous skull segmentation.

All four lenses generated comparable results for AH-R in the whole skull, as shown in Table 3.3. Compared to the corresponding voxel lenses (BV and PV), the smooth lenses (BS and PS) provided insignificant improvements for focusing. Similarly, the porous lenses (PV and PS) provided insignificant improvements compared to the binary focusing lenses. BV lenses were then tested further on the remaining 5 targets across the two skull samples, showing satisfactory ultrasound focusing results through the skulls on all targets tested.

The transducer position sensitivity was studied for the four lens types. Although a tighter position limit than the limit utilised in the previous human trial was needed, none of the four lens types were significantly less sensitive to changes in transducer position (translation and rotation) away from the designed location. Therefore, for the simplicity of the lens method in human trials, the BV lens was decided to be the type to use. By using the BV lens and BoB

simulation, porous information about the skull is no longer required, allowing T1-MRI to be used in place of CT imaging for homogenous skull segmentation in future human trials.

When evaluating the three perirhinal cortex target sites, it was found that the BV lenses generated foci significantly larger in volume than predicted in simulations. This observation suggests that the perirhinal cortex, despite being shallower than the anterior hippocampus, is more difficult to target by focused ultrasound. One reason for this is that the ultrasound focusing on the perirhinal cortex, a shallower target, would be further away from the normal incidence at the boundary of the skull, creating shear waves that can no longer be neglected. In addition, the ultrasound pathway to the perirhinal cortex is closer to the edge of the temporal bone, a region with more complicated skull geometry.

WHPS BoB simulations were compared to the experimental measurements on the whole skull sample. The measurements confirmed the findings in simulations that the standing waves start to change the pressure distribution in the main focal lobe. However, the measurements also found that the magnitude of the standing waves between the two foci was significantly larger than that in the simulation. In cases using a single source, the focus on each side in reality is already larger in volume than that predicted in simulations. This causes a larger-magnitude ultrasound to be able to reach the other side. As a result, the standing waves between the foci acquire a larger magnitude than those in simulations. With these findings on standing waves when using paired sources, the standing wave effect must be carefully examined and mitigated when possible, including potentially utilising offset ultrasound pulses between transducers.

4

ULTRASOUND INTERACTION WITH DBS ELECTRODE

In order to measure how ultrasound might change local brain wave patterns, it would be useful to measure the local electrical field potential in the brain. One patient cohort in which this could be carried out is Parkinson's disease patients with deep brain stimulation (DBS) electrodes. Before applying ultrasound to the patients, the interaction between the ultrasound field and the DBS electrode was studied and presented in this chapter. The impact on the acoustic field of the presence of the DBS electrode at various positions in the acoustic field was studied in simulations and experiments. Based on the changes to the acoustic field, the DBS electrode's thermal influence was measured by a thermocouple of similar geometry. Lastly, the impact on the DBS electrode recording from the presence of an acoustic field was investigated in water, saline, and agar phantoms.

4.1 ELECTRODE GEOMETRY & MATERIAL COMPOSITION

Deep brain stimulation (DBS) through implanted electrodes can be used to treat movement disorders associated with Parkinson's disease, a long-term degenerative disorder primarily affecting the motor system. While its cause is still under great debate, motor symptoms are thought to be due to the loss of dopamine-secreting neurons in the substantia nigra pars compacta, depleting overall dopamine levels and producing an overall reduction in motor output (hypokinesia). By using an electrode-based neurostimulator, high-frequency electrical impulses can be sent to specific parts of the brain, usually the STN or GPi, to regulate faulty neural signals and reduce motor symptoms. It can also be used in recording mode to measure the local field potential of brain activities introduced by external treatment, such as transcranial ultrasound stimulation. Before applying transcranial ultrasound stimulation clinically, the interaction between the electrode and the acoustic field must therefore be investigated. In order to model the electrode in acoustic simulations, its geometry and material composition were determined and described here.

The electrode lead (Picostim-DyNeuMo, Bioinduction, Bristol, UK) utilised in this study consists of four contacts at the electrode tip, four wires for each contact, and two types of thermoplastic polyurethane elastomers, one with the wires in the lead body (Pellethane® 2363 55D, Lubrizol, Wickliffe, OH, USA), and the other as the contact spacer (Pellethane® 2363 75D, Lubrizol, Wickliffe, OH, USA). Among these components, the biggest acoustic impedance mismatch with tissue, and therefore the most likely cause of changes in the acoustic field, is the metal alloy base material. The contacts are made of 90% platinum and 10% iridium, giving an overall acoustic impedance of about 74 MPa·s/m (overall speed of sound: 3417 m/s, overall density: 21606 kg/m^3). The wires are made of 28% platinum and 72% high-performance alloy (35N LT, Fort Wayne, IN, USA). In the finished wire, there is 37% nickel,

21% chromium, 13% molybdenum, and 1% iron. As a result, the wire's overall acoustic impedance is about 64 MPa·s/m (overall speed of sound: 5303 m/s, overall density: 12016 kg/m^3).

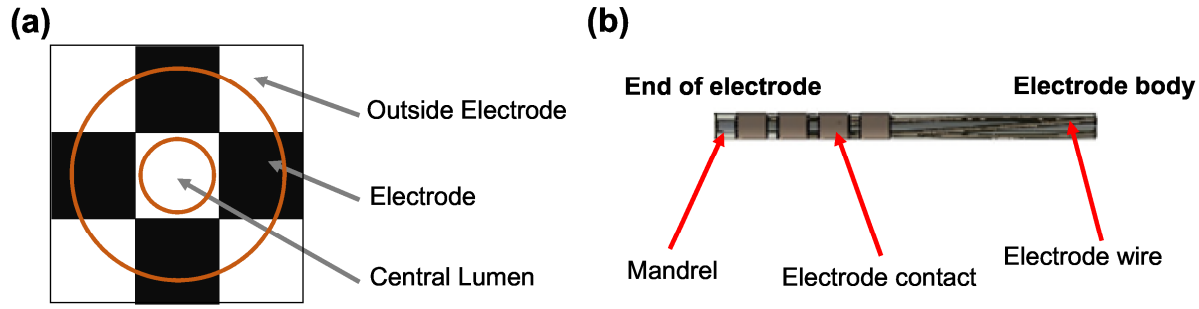

Fig. 4.1 Electrode geometry details. The real electrode has a diameter of 1.27 mm. **(a)** Cross-section of the modelling arrangement of the electrode. Each pixel is 0.5 mm wide. Four wires are represented by black pixels, with the central lumen in the middle. **(b)** Schematic of electrode geometry. Four contacts are at the end of the electrode on the left. The four wires from them are arranged in a helical shape (6°) in the electrode body. The stainless-steel mandrel is moved during implantation.

The electrode's diameter is 1.27 mm, with a central lumen of 0.445 mm diameter inserted in a stainless-steel mandrel for transportation, which is removed during implantation surgery. On the 0.5 mm simulation grids, in order to represent the central lumen and four wires, the electrode was designed as a cross section of 3 pixels by 3 pixels, as shown in Fig. 4.1 (a), giving an overall diameter of 1.5 mm. The four wires each occupy a black pixel in the cross-section. The four surrounding white pixels outside the electrode and the central lumen are represented by the medium surrounding the electrode. A schematic of the electrode tip geometry is shown in Fig. 4.1 (b). The four wires are arranged in a helical shape of 6° in the electrode lead body. This is a geometry that the modelling arrangement of the implanted electrode in Fig 4.1 (a) does not represent. Another aspect of the electrode that could not be represented here are the polyurethane materials on the electrode.

In order to represent the worst-case scenario of ultrasound-electrode interference and compensate for the absence of helical wire arrangement and polyurethane materials, the entire electrode in the simulation takes the material acoustic properties of a 90% platinum and 10% iridium electrode contact to represent the highest possible acoustic impedance that could be made with the electrode.

4.2 IMPACT ON ACOUSTIC FIELD: VALIDATION

To investigate the impact on the acoustic field due to the presence of the electrode, the Fresnel PDMS lens of 85 mm focal depth in Chapter 3 was used in water. The simulation was set to generate 0.6 MPa at the focal peak when the electrode is absent. At the same source conditions, the electrode was added to the simulation. To start, the tip of the electrode was placed at the free field focal peak, i.e., 85 mm axially, and normal to the axis of ultrasound propagation to represent the worst-case scenario where the ultrasound is directly focused on the electrode. Two axial views of the simulated pressure field with the electrode present are shown in Fig. 4.2 (a) and (b).

The colour bar range in Fig. 4.2 (a) and (b) is limited to 0.6 MPa to reveal the features of the pressure distribution. Due to the ultrasound interaction with the electrode, standing waves were formed between the electrode and the transducer in the axial range. The focus was disrupted due to waves bouncing off the electrode. When evaluating the electrode oriented into the page, incoming ultrasound waves were split symmetrically to the sides, creating noticeable standing wave patterns on both sides of the formed focus. When evaluating the electrode oriented vertically coming from the top of the focus, noticeable standing wave patterns could be observed to the edge of the simulation space on the side with the electrode (negative radial direction) but could barely be spotted once outside the focus in the positive radial direction.

With the electrode in the acoustic field as shown, the peak focal pressure became 0.86 MPa, a 43.3% increase from 0.6 MPa when the electrode was absent. In total, 30 mm^3 of the focal volume has a pressure higher than 0.6 MPa.

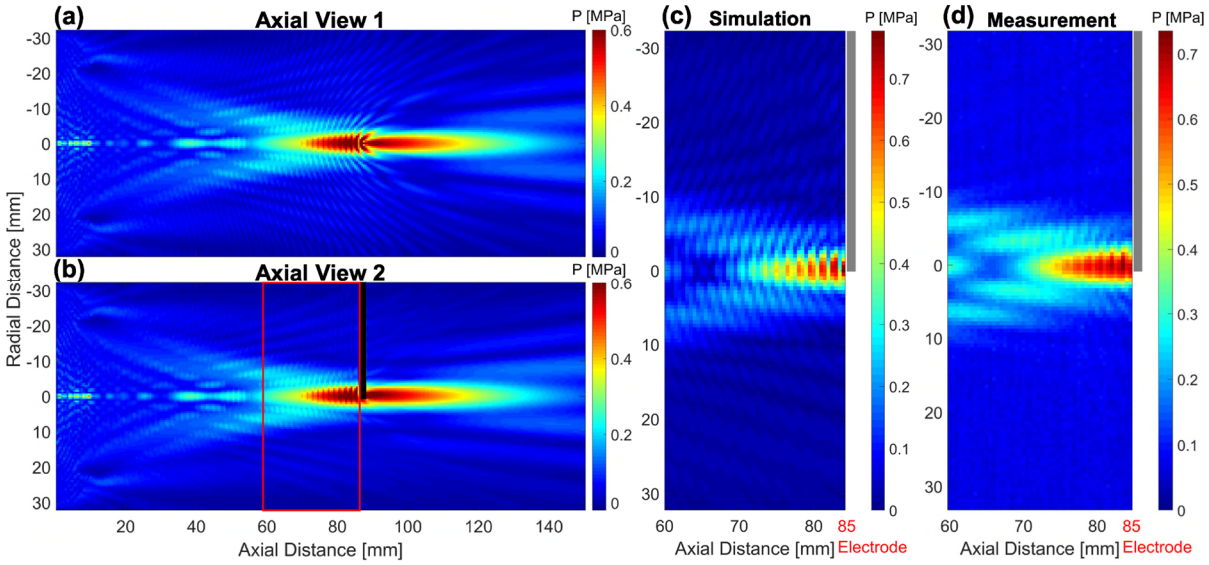

Fig. 4.2 Electrode impact on the acoustic field. A Fresnel PDMS lens focusing to 85 mm was used here. The tip of the electrode is placed at the free-field focal peak. In all views, the piston transducer and the lens are on the left side of the pressure field. **(a)** Axial view 1 of the simulated pressure field. The electrode is going into the page. **(b)** Axial view 2 of the simulated pressure field. The electrode is vertical, as shown by the black line. The red rectangle reveals the zoomed-in view shown in (c). **(c)** Zoomed in view of the simulated pressure field between the electrode and the transducer in the axial range. The electrode is the grey line just outside the pressure field on the right. **(d)** Measured pressure field between the electrode and the transducer in the axial range. The electrode is the grey line just outside the measured field on the right.

In order to validate the simulation results, a fibre-optic hydrophone (FOH, Precision Acoustics, Dorset, UK) was used to measure the acoustic field when the electrode tip was at the free field focal peak. Due to the existence of the electrode, measurements were conducted both (i) between the source and electrode; and (ii) behind the electrode. An example measured pressure field between the source and electrode is shown in Fig. 4.2 (d). The corresponding simulation zoomed in view is shown in Fig. 4.2 (c) which is the range shown by the red rectangle in

Fig. 4.2 (b). In Fig. 4.2 (c) and (d), the electrode is just outside the range on the right side, as shown by a grey line.

In Fig. 4.2 (c), this simulated pressure field shows standing wave patterns throughout. However, due to the poor signal-to-noise ratio of the hydrophone used, the regions far from the focus in the measured field in Fig. 4.2 (d) were close to uniform, with only small perturbations showing the noise floor in the measurement system. Nevertheless, the expected asymmetric standing waves in this view were observed in the focus region, accompanied by less obvious standing wave patterns in the side lobes. Quantitatively, in the measured range, the maximum pressure between the source and electrode was 0.73 MPa, closely matching the simulated maximum pressure of 0.77 MPa. This was considered reasonable given that the circular electrode cross section was modelled as four elements in the simulation. In this way, the simulation should always give a slight overestimate of the electrode impact on the acoustic field.

Symmetric standing wave patterns were also observed as expected when scanning between the source and electrode in the axial view (Fig. 4.2 (a)). The expected patterns in axial scans behind the electrode were found to be mainly in the low pressure magnitude regions far away from the focus in simulations. As a result, they could not be easily observed experimentally due to the high noise floor in this region. Low-magnitude patterns may have become visible by increasing the number of averaging sweeps on the oscilloscope when measuring.

Together, these experimental results validated the modelled disruptions to the acoustic field caused by the presence of the electrode. With the electrode at the free field focal peak, standing waves were formed in the focal region, and the pressure formed at the focus increased as a

result. This model can reliably predict the electrode impact on the acoustic field with a slight overestimate. Using these simulations, methods to mitigate the electrode impact on the acoustic field were investigated.

4.3 IMPACT ON ACOUSTIC FIELD: POSITION

In the above section, the electrode was placed at the free-field focal peak. In the analysis presented in this section, the electrode was placed at various locations in the simulation space to study its impact on the acoustic field. The GPi is potentially large enough (cm-level dimension) that it might be possible to use TUS on a GPi that also has an electrode in place where direct LFP can be taken without interfering with the ultrasound. The axial direction and two radial directions orthogonal to each other were studied. As shown in Fig. 4.2, when the electrode was introduced into the system, the cylindrical symmetry condition was no longer valid. As a result, the radial directions parallel and normal to the electrode were investigated. A Fresnel PDMS lens focusing at 85 mm was used. In this study, only the location of the electrode relative to the focused ultrasound field was changed. The electrode was oriented orthogonally to the ultrasound propagation direction as before.

The movement of the electrode along the axial direction was studied first. The electrode was moved on the symmetry axis of the transducer at 5 mm steps and with 1 mm steps around the focus. The pressure recorded at the target was set as the free-field focal peak when the electrode was absent. The simulated target pressure is presented in Fig. 4.3 (a). The transducer is on the left at -85 mm of the horizontal axis. The highest target pressure occurs when the electrode is at the target (0 mm). The pressure distribution in this case is shown in Fig. 4.2. The flat dashed line at 0.6 MPa marks the target pressure when the electrode is absent. When the electrode is

outside the range of -25 mm to +40 mm, the target pressure returns to 0.6 MPa. The -6 dB focal region is between -20 mm and +40 mm in the axial direction when the electrode is absent. This means that as long as the electrode is outside the -6 dB focal region in the axial direction, either closer to the transducer or further behind the focus, the target pressure is not affected.

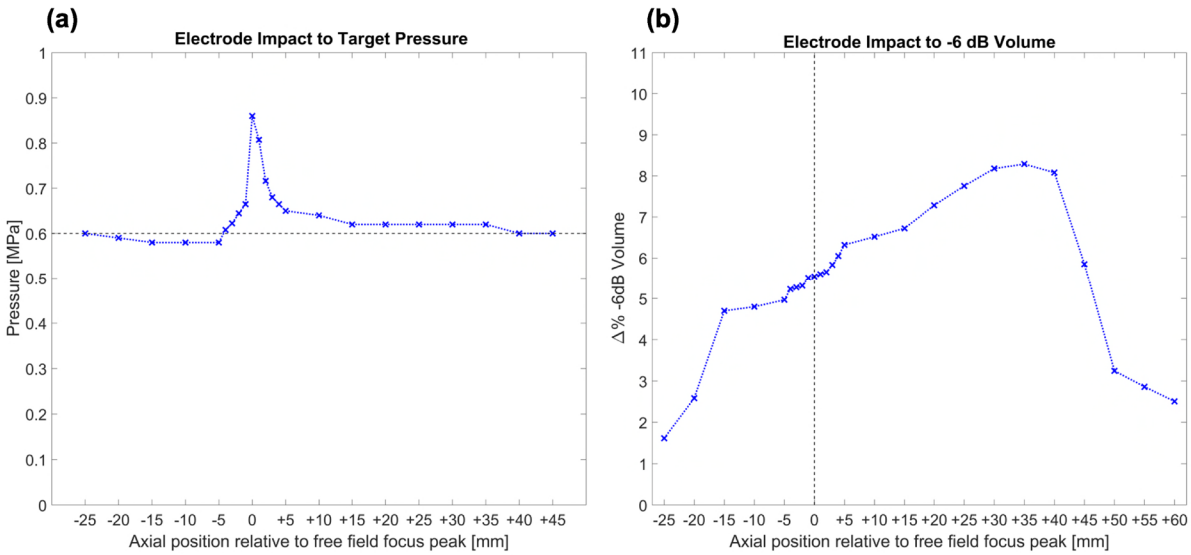

Fig. 4.3 Electrode impact on the acoustic field at various axial locations. The electrode was moved axially on the centre axis of the transducer. The electrode was kept orthogonal to the ultrasound propagation direction. The transducer was at -85 mm on the left for both plots' horizontal axes. **(a)** Target pressure against the electrode's axial position. The target was the free-field focal peak when the electrode was absent. The flat dashed line at 0.6 MPa marks the free field target pressure. **(b)** Change of -6 dB volume against electrode axial position. The vertical dashed line marks when the electrode is at the free-field focal peak.

When the electrode was closer to the transducer, i.e., from -5 mm to -25 mm in Fig. 4.3 (a), the target pressure was slightly lower than 0.6 MPa. The electrode was between the transducer and the target, splitting the incoming ultrasound wave, as shown in Fig. 4.2 (a), and creating an acoustic shadow covering the target. This causes fewer ultrasound waves to arrive at the target, giving a lower target pressure than when the electrode is absent. On the contrary, when the electrode was distal to the free-field focus, the target pressure was higher than 0.6 MPa until the electrode was at +35 mm. In this case, the electrode scatters the incident ultrasound, and

the backscattered signal propagates along the axis, giving a higher target pressure than when the electrode is absent.

The free field -6 dB focal volume created by the 85 mm Fresnel PDMS lens is 1271.5 mm^3 in simulation without the electrode. The changes in focal volume using -6 dB of the free field target pressure ($\geq$ 0.3 MPa) with the electrode at different axial positions are quantified in Fig. 4.3 (b). The biggest increase in focal volume occurred where the electrode was 35 mm behind the target (+35 mm). This is an 8.3% increase in volume (105.4 mm^3). This occurs because the electrode backscatters energy into the beam, resulting in enhanced pressure in front of it. The volume increases as the electrode moves back until it is far enough away from the focus that the backscattering effect is too small to result in a significant pressure increase compared to the free field. This is because a larger portion of the focus is affected by the backscattered waves when the electrode is further back. However, even at electrode positions where the target pressure is no longer affected, the -6 dB focal volume still does not return to its value when the electrode is absent. This shows that the ultrasound focus is still disturbed by the electrode's presence.

In the radial direction shown in Fig. 4.2 (a), the electrode needs to be 6 mm away from the target such that the target pressure is not disturbed. However, in the radial directions, the electrode only needs to be moved by 3 mm to be outside the free field -6 dB focal volume. This is again due to the fact that the electrode is scattering the incoming ultrasound wave in the radial direction orthogonal to the electrode. As a result, the electrode has a wider range of impact in this radial direction. On the other hand, in the radial direction shown in Fig. 4.2 (b), the electrode only needs to be moved 2 mm away from the target such that the target pressure is not disturbed.

4.4 IMPACT ON ACOUSTIC FIELD: ROTATION

The electrode implanted in the body can also take angles other than orthogonal to the ultrasound propagation direction. The impact of the angle of the electrode relative to the ultrasound propagation direction was investigated in simulations between 30° and 165° at 15° steps, as this covered the realistic range of angling in practice. For all these angles, the tip of the electrode was always kept at the free field focal peak (when the electrode was absent). In order to prevent artefacts from angling the electrode on the simulation grids, the ultrasound source was rotated relative to the electrode while the electrode was fixed in the simulation space. In order to do this with as few artefacts as possible, a bowl-shaped transducer was used in simulation instead of the piston transducer and Fresnel lens used in previous analyses. The transducer has an aperture diameter of 64 mm, the same as that for the piston transducer. The transducer's radius of curvature was set to be 85 mm, the same focal depth as that achieved by the piston transducer and Fresnel lens.

Fig. 4.4 (a) shows the schematic of the simulation setup used in this analysis. The focus is denoted as a green cigar shape with the blue electrode's tip at the focal peak. The incoming ultrasound is shown by the black arrow denoting the ultrasound propagation direction. The angles of the electrode are defined in a clockwise direction, as shown by the red arrow. Two examples of electrode angling are shown, one with an angle smaller than 90° where energy is expected to be reflected into the focal zone and the other with an angle larger than 90° where energy will be scattered away.

The target pressure variation relative to the electrode angling is shown in Fig. 4.4 (b) with the dashed line at 0.6 MPa representing the free field target pressure. The maximum target pressure of 1.29 MPa is achieved at 45°, which is more than double the free field target pressure of

0.6 MPa. The lowest target pressure of 0.72 MPa is achieved at 105°, which is still 19% higher than that in the free field. In general, for cases with angles smaller than 90°, the target pressure values are higher than those for cases with angles larger than 90°. This is consistent with the expectation that waves reflected off the electrode with an angle smaller than 90° interact with the incoming waves from the source at the focal region before leaving, whereas waves reflected off the electrode with an angle larger than 90° are predominantly scattered away from the focal region immediately.

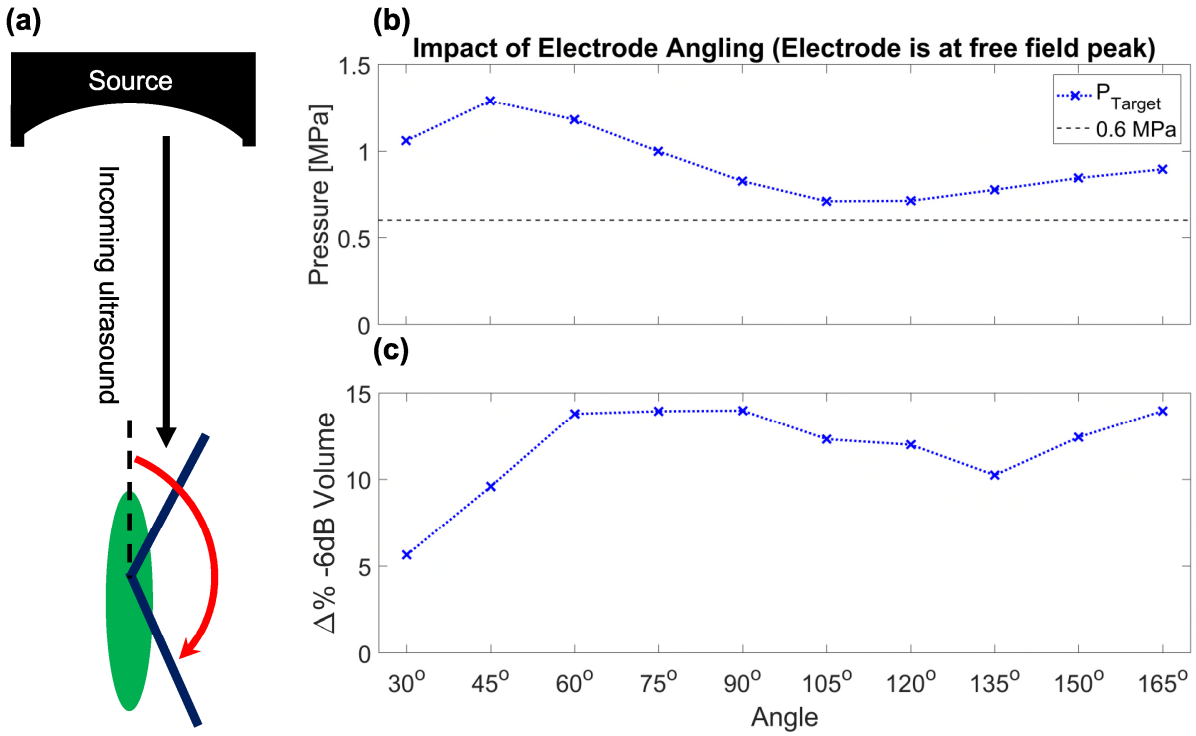

Fig. 4.4 Electrode impact on the acoustic field at various angles. The electrode tip is at the free field focal peak when the electrode is absent. A bowl transducer with an aperture diameter of 64 mm and a radius of curvature of 85 mm was used. The transducer was rotated in the simulation space instead of the electrode to avoid digitisation artefacts. **(a)** Schematic of the simulation setup with the electrode in blue. The red arrow indicates the definition of angle value and direction. **(b)** Target pressure against electrode angling. The flat dashed line at 0.6 MPa marks the free-field target pressure. **(c)** Change of -6 dB volume against electrode angling.

Fig. 4.4 (c) plots the change in -6 dB volume (relative to the free field case, which is volume with pressure ≥ 0.3 MPa) as a function of electrode angling. All angles tested caused over a

5% increase in the -6 dB focal volume. For all angles larger than 60°, the increase in -6 dB volume is between 10% and 15%, with the highest of 14% at 90°. Between 60° and 90°, the size of the newly formed -6 dB volumes is not significantly affected by the change in angle. From 90° to 135°, the percentage increase of the newly formed -6 dB volumes reduces and then starts to increase again after passing 135°.

In order to mitigate the impact on the acoustic field from an angled electrode, an angle of around 120° produced the least impact but still produced a 19% increase in target pressure and an over 10% increase in focal volume. This is an electrode entering the acoustic field from the side opposite the transducer at an angle. Therefore, the creation of the acoustic field away from the electrode tip is more important and effective than the angling of the electrode relative to the ultrasound propagation direction.

4.5 Temperature Rise Due to Electrode: Modelling

It has been shown that the acoustic field is affected by the presence of the electrode. Based on the changes in the acoustic field, i.e., increased pressure magnitude, thermal modelling was conducted to check the temperature rise against the safety limit when the electrode is in the acoustic field.

In order to match typical stimulation frequencies used in DBS, a PRF of 130 Hz was used in the pulsing sequence of ultrasound in the thermal modelling here (Chen and Chen, 2019; Merola et al., 2013; Nie et al., 2021; Romagnolo et al., 2021). The pulsing sequence is illustrated in Fig. 4.5 (a). As in Chapter 2, the pulsing sequence was set with these parameters: 50% duty cycle, a burst of 0.3 s T_{ON} and 5.1 s T_{OFF} before the next burst. At a PRF of 130 Hz and 50% DC, the on- and off-pulsing periods inside a burst are both 3.85 ms. The total duration

is 540 s, formed by 100 bursts. The initial temperature of the entire simulation space is set at 37 °C with a floating periodic boundary as described in Chapter 2, such that no heat energy leaves the simulation space. In this way, the worst-case scenario of a temperature rise is presented and studied.

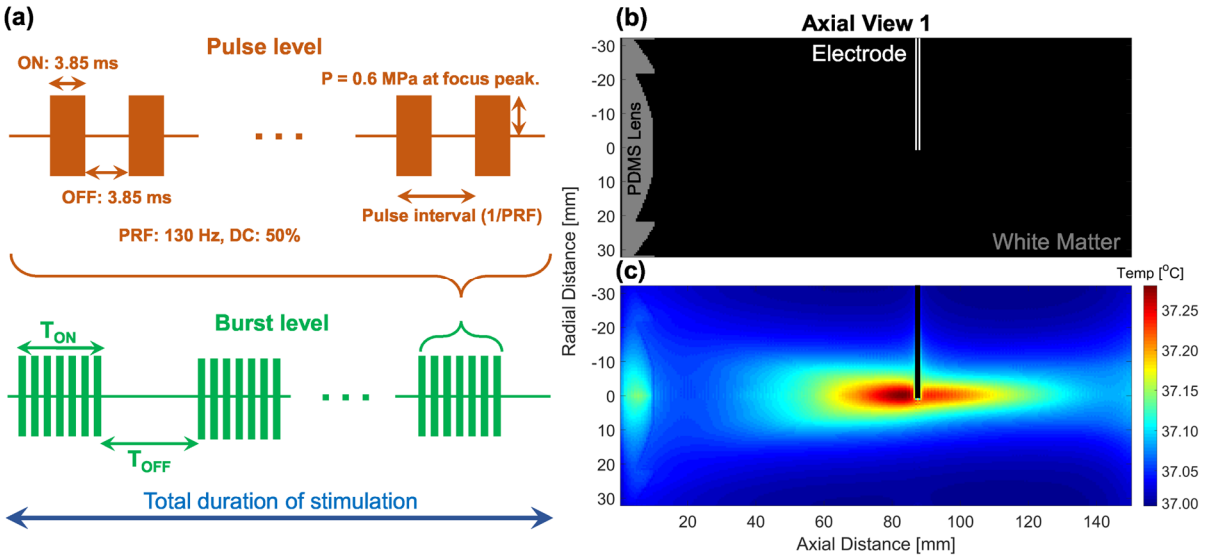

Fig. 4.5 Thermal modelling with the electrode. A Fresnel PDMS lens focusing at 85 mm is used. **(a)** Schematic of the ultrasound pulsing sequence. PRF: pulse repetition frequency. DC: duty cycle. **(b)** The material layout in the simulation space. The lens and transducer are on the left end. The electrode is white, with its central lumen shown in black, the colour of the medium. White matter is used as the homogeneous medium because it has the most heat-accumulative material properties compared to CSF and grey matter. **(c)** The modelled temperature rise field. The electrode is shown as a black line.

As in previous sections, a Fresnel PDMS lens focusing to 85 mm was used. The electrode was placed at the free field focal peak where 0.6 MPa was created by the ultrasound source when the electrode was absent, i.e., the pressure distribution in Fig. 4.2 (a) and (b) was used in the thermal simulation. In the thermal simulation, the medium was set to take the material thermal properties of white matter as in Table 1.1. The white matter has the highest acoustic attenuation, the lowest thermal conductivity, and the lowest specific heat among the CSF, white matter, and grey matter. As a result, white matter is the material among the three in the human brain that

generates the highest local temperature rise. It is therefore used here to show the worst-case scenario of the surrounding medium's temperature rise.

As in the thermal simulations in Chapter 2, the thermal conductivity and specific heat of PDMS are 0.15 W/m·K and 1460 J/kg·K, respectively (Mark, 1999; Livermore and Voldman, 2016). As before, the electrode is made of 90% platinum and 10% iridium, giving an overall thermal conductivity of 79 W/m·K, and a specific heat of 1328 J/kg·K. The simulation space is shown in Fig. 4.5 (b). The PDMS lens is grey, and the transducer is on the left of the lens. The electrode is white. In the axial slice shown here, the central lumen of the electrode is also revealed.

The map of maximum temperature at the end of the ultrasound sequence is shown in Fig. 4.5 (c). The maximum temperature reached is 37.28 °C, giving a 0.28 °C rise at 4.5 mm closer to the ultrasound source than the target. On the electrode-tissue boundary, lower temperature values are recorded. This is because the high thermal conductivity of the alloy in the electrode removes heat from the focus region in the simulation space. However, these lower temperature values on the electrode-tissue boundary are not realistic. The thermocouple artefacts exist on the electrode-tissue boundary, where the temperature rise measured by the thermocouple is higher than the real temperature rise due to the viscous heating effect (Huang et al., 2004; Zohdi and Krone, 2018). As a result, the temperature should be higher on the electrode-tissue boundary instead of lower.

In order to make the model more realistic, the thermal simulation of the electrode needs to also consider the viscous heating effect. In the configuration used, the electrode is transverse to ultrasound propagation. The second heat source Q_{VH} is added to model the viscous heating

effect for the transverse configuration (Fry and Fry, 1954a; Fry and Fry, 1954b; Tiennot et al., 2019):

$$Q_{VH} = \frac{P^2 \pi f M' \cdot \left[\frac{2\eta^{\frac{1}{2}}}{r_0(\pi f \rho)^{\frac{1}{2}}} + \frac{{r_0}^2 \pi f \rho}{4\eta}\right] \cdot \left\{1 - \left[\frac{2 + \frac{2\eta^{\frac{1}{2}}}{r_0(\pi f \rho)^{\frac{1}{2}}}}{\frac{M}{M'} + 1 + \frac{2\eta^{\frac{1}{2}}}{r_0(\pi f \rho)^{\frac{1}{2}}}}\right]\right\}^2}{\rho^2 {c_0}^2 \cdot \left\{1 + \left[\frac{\frac{2\eta^{\frac{1}{2}}}{r_0(\pi f \rho)^{\frac{1}{2}}} + \frac{{r_0}^2 \pi f \rho}{4\eta}}{\frac{M}{M'} + 1 + \frac{2\eta^{\frac{1}{2}}}{r_0(\pi f \rho)^{\frac{1}{2}}}}\right]^2\right\}};$$

This Q_{VH} is the heat generated rate per unit length of electrode by the viscous force, where P is pressure, f is ultrasound frequency, M' is the mass of tissue displaced per unit length of the electrode, r_0 is the radius of wire, ρ is tissue density, η is tissue dynamic viscosity with a value of 0.5 Pa·s, c_0 is tissue speed of sound, and M is mass per unit length of the electrode. This viscous heating source was applied to voxels representing the electrode in the thermal simulation space.

As before, the focal peak pressure was set to be 0.6 MPa with the electrode absent, and the same pulsing sequence was used. The resulting temperature field, including the viscous heating effect, is shown in Fig. 4.6. The simulation space and the modelled temperature field in the axial view in which the electrode is included are shown in Fig. 4.6 (a) and (c), respectively. Fig. 4.6 (b) and (d) are the other axial views where the electrode is extending into the page. In the map of maximum temperature at the end of the ultrasound sequence in Fig. 4.6 (c) and (d), it can be seen that high temperature occurs next to the electrode and the highest temperature

rise occurs at the tip of the electrode. The maximum temperature reached is 44.25 °C, giving a 7.25 °C rise from the initial temperature of 37 °C. This global maximum temperature occurs 1 mm closer to the ultrasound source than the target lying in tissue on the left of the tip of the electrode. This modelled maximum temperature exceeds the 43 °C safety limit in tissue by 1.25 °C. If the pressure is reduced such that the maximum pressure when an electrode is present is controlled to be 0.6 MPa (see Section 4.2), the maximum temperature reached is then 38.82 °C, giving only a 1.82 °C rise.

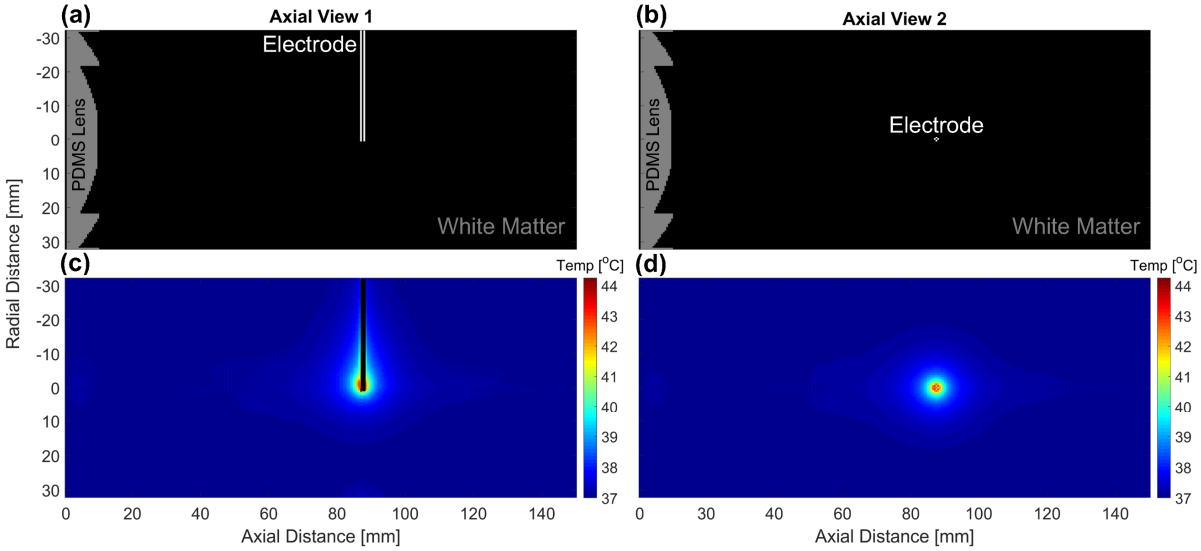

Fig. 4.6 Electrode thermal modelling with viscous heating. A Fresnel PDMS lens focusing at 85 mm is used. **(a), (b)** The material layout in the simulation space for two axial views. The lens and transducer are on the left end. The electrode is white, with its central lumen shown in black, the colour of the medium. White matter is used as the homogeneous medium because it has the most heat-accumulative material properties compared to CSF and grey matter. **(c)** The modelled temperature rise field in axial view 1. The electrode is shown as a black line. **(d)** The modelled temperature rise field in axial view 2. The electrode is extending into the page.

The thermal modelling results in Fig. 4.5 (c) exclude the viscous heating effect. It is clearly an underestimate of the real temperature rise, as it only includes the heating effect from the focused ultrasound. With the viscous heating effect from the electrode-tissue boundary, the temperature exceeds 43 °C for the same ultrasound input. This modelling result needs to be validated by experiment.

4.6 TEMPERATURE RISE DUE TO ELECTRODE: EXPERIMENT

To experimentally validate the temperature rise calculated in simulations, a thermocouple was used to mimic the electrode. To best match its physical properties, a Type K thermocouple (TJ1-CASS-IM15U-300, Omega, CT, USA) with a diameter of 1.5 mm was selected. The thermocouple was connected to a data logger (TC-08, Pico, Cambridgeshire, UK), where the temperature measurements were saved. An agar phantom of 3% was used with additives to represent the body's soft tissue (Collin, 2009; Burlew et al., 1980; Ramnarine et al., 2001): 11.21% glycerol, 0.53% SiC powder, 0.94% Al_2O_3 powder (3.0 µm diameter), and 0.88% Al_2O_3 powder (0.3 µm diameter). As the phantom was not transparent, the positions in which the thermocouple was inserted were marked on the surface of the phantom beforehand. The depth of the thermocouple was controlled by a second set of markers on the thermocouple lead.

Acoustic simulations were first done to check the new focus formed in the phantom with and without the electrode at the free field focal peak. The focal peak was 3 mm closer to the transducer in the phantom, and the location used in the experiment was corrected by this distance. The peak pressure was reduced by 23.9%, and this too was corrected to reach 0.6 MPa at the focal peak in the phantom when the electrode is absent. In the experiment, the thermocouple with the same diameter took the position of the electrode in previous simulations, i.e., the tip at the free field focal peak.

Using this acoustic simulation, new thermal modelling was performed for the thermocouple in order to compare it to the experiment. This is because the viscous heating relation in the previous section involves mass per unit length term M, i.e., density with modified units. The thermocouple used here consists of 95% nickel, 2% aluminum, 2% manganese, and 1% silicon, giving an overall density of 8678 kg/m^3, which is only 40% of that of the electrode tip

(21606 kg/m^3). The thermal modelling result is shown in Fig. 4.7. The ultrasound pulsing sequence was the same as the simulations in the previous section. The resulting temperature rise due to viscous heating of the thermocouple was 1.24 °C, only 17% of the 7.25 °C modelled for the electrode. It can be seen that the modelled viscous heating temperature rise is very sensitive to the density values used.

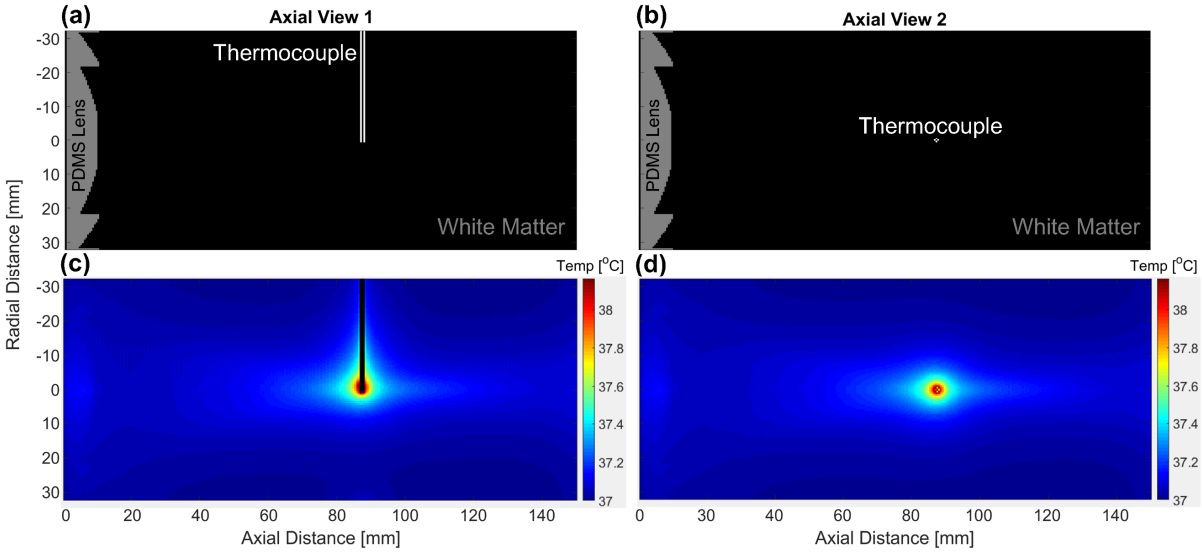

Fig. 4.7 Thermocouple thermal modelling with viscous heating. A Fresnel PDMS lens focusing at 85 mm is used. **(a), (b)** The material layout in the simulation space for two axial views. The lens and transducer are on the left end. The thermocouple is white, taking the same geometric arrangement as the electrode, with the central lumen shown in black, the colour of the medium. White matter is used as the homogeneous medium because it has the most heat accumulative material properties compared to CSF and grey matter. **(c)** The modelled temperature rise field in axial view 1. The thermocouple is shown as a black line. **(d)** The modelled temperature rise field in axial view 2. The thermocouple is extending into the page.

The temperature rise using the same ultrasound pulsing sequence as in thermal modellings was tested first at the focal peak. That is, 9 minutes of stimulation are formed by 100 trials of 0.3 s T_{ON}, 50% duty cycle burst, followed by 5.1 s T_{OFF}. The recorded temperature in time is shown in Fig. 4.8. Temperature recordings of the first five trials are shown in Fig. 4.8 (a). The pulsing sequence was revealed as oscillations in temperature could be seen with the same timing. This oscillation effect existed until the end of the ultrasound sequence at about 600 s in Fig. 4.8 (b).

The measured temperature rise at the end of the ultrasound sequence is 0.47 °C, larger than the 0.28 °C simulated when excluding the viscous heating effect. It is therefore likely that the additional 0.19 °C increase was caused by viscous heating, which accounted for 40.4% of the measured temperature rise. This contribution agrees with previous literature values (Kamimura et al., 2020; Morris et al., 2008) and also confirms that the modelling result where the viscous heating was included in Fig. 4.7 still significantly overestimated the temperature rise by 2.62 times. Alternatively, based on the measurements here, a more accurate temperature rise estimate can be derived by adding 70% to the temperature rise value given by the thermal modelling without the viscous heating.

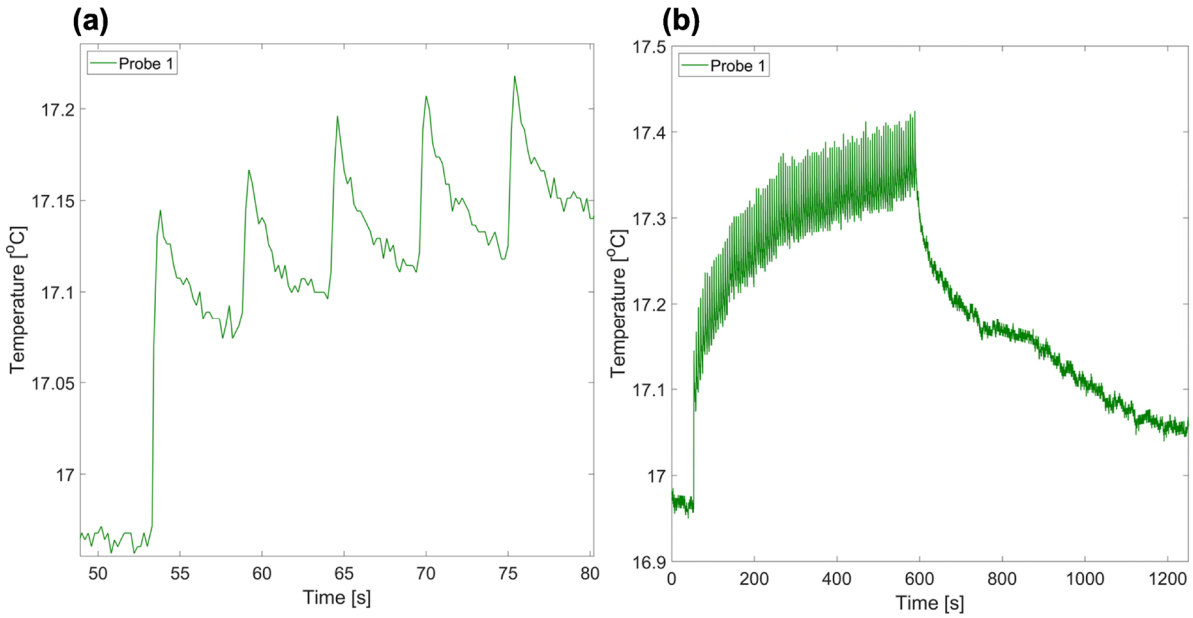

Fig. 4.8 Temperature measurement by thermocouple in tissue phantom. The thermocouple took the position of the electrode, i.e., tip is at the free field focal peak. The type-K thermocouple has a diameter of 1.5 mm, the same as that of the electrode in simulation. **(a)** Temperature recording of the first 5 bursts. **(b)** Temperature recording of the entire session.

At the free-field focal peak, a more intensive ultrasound sequence was also tested. A cooling period of 35 minutes was used before starting the new measurements to represent the time needed for the temperature to return to the initial value before ultrasound was applied. The total stimulation duration was kept at 9 minutes but was instead formed by 200 trials of 0.3 s T_{ON},

50% duty cycle burst, followed by 2.4 s T_{OFF}. The resulting temperature rise was 0.75 °C, 59.6% higher than the 0.47 °C achieved by the previous pulsing sequence but still within the 1 °C safety limit. This temperature rise can still be estimated by adding 70% to the temperature rise value given by the thermal modelling without the viscous heating at this more intensive ultrasound sequence (0.44 °C).

The temperature was also taken with the thermocouple shifted away from the free field focal peak in three directions: (i) axially in front of and behind the target; (ii) radially moving sideways; and (iii) radially moving upwards as if the electrode is leaving. These three directions of movement are illustrated in Fig. 4.9 (a). The maximum recorded temperature rises along these three directions are shown in Fig. 4.9 (b), (c), and (d), respectively.

In Fig. 4.9 (b), measurements in the axial direction show that the recorded temperature rise reduced once the thermocouple was moved away from the free field focal peak. Between -10 mm and +10 mm, the transducer was moved relative to the thermocouple and phantom in 1 mm steps. Outside this range, measurements were taken by inserting the thermocouple into the phantom at marked locations with the transducer fixed relative to the phantom. The recorded axial temperature rise distribution was not found to be symmetric, forming a plateau between 0 mm and +10 mm. This trend is similar to the modelled target pressure distribution in Fig. 4.3 (a), proving that the ultrasound was the source of heat formation either directly by tissue absorption or indirectly via viscous heating.

In the radial directions shown in Fig. 4.9 (c) and (d), the measured temperature rise dropped monotonically as expected when the thermocouple was moved away from the free field focal peak.

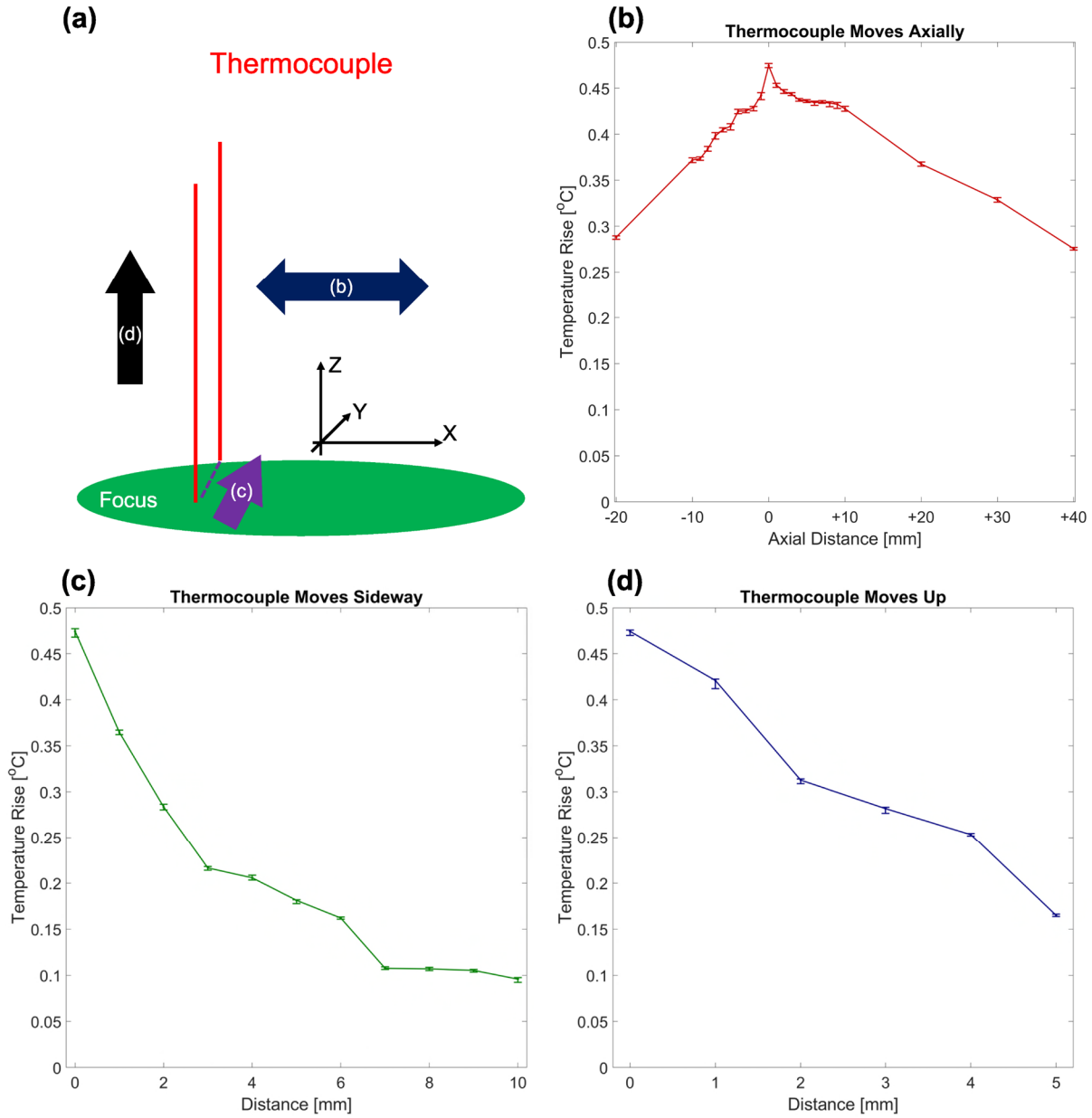

Fig. 4.9 Temperature measurement by thermocouple at positions around the free-field focal peak. (a) Demonstration of the three directions that the thermocouple was moved in. **(b)** The maximum recorded temperature rises along the axial position (X). **(c)** The maximum recorded temperature rises along the sideways radial position (Y). **(d)** The maximum recorded temperature rises along the upward radial position (Z). This Y axis is the direction in which the electrode is placed.

The ultrasound pulsing sequence used here was designed to fulfil FDA intensity safety limits. Using this sequence, the temperature rise measured by the thermocouple was less than the 1 °C temperature rise safety limit in the brain, even at the focal peak. Since the electrode's actual diameter is smaller than the thermocouple, the actual temperature rise caused by the electrode

sitting at the free field acoustic focal peak should be lower than that reported here. CEM43 dosing was also evaluated based on the guidance provided by ISO 14708-3:2017 standards, clause 17.1, showing a CEM43 of 0.003, which is well below the CEM43 dose threshold of 2 in the brain, which corresponds to an average temperature of 41 °C using similar pulsing sequences.

4.7 IMPACT ON ELECTRODE MEASUREMENT IN WATER

So far, the impact on the acoustic field and the resultant temperature distribution due to the electrode's presence in the acoustic field has been studied in the previous sections. From this section on, the acoustic field's impact on the electrode recording is investigated. Although the electrode is designed to detect electrical signals, acoustic waves could induce artefacts not representative of normal brain function.

A Fresnel PDMS lens focusing to 85 mm was used to create a 0.6 MPa free field focal peak as before. The testing was first done in deionised and degassed water, with the electrode placed at the free field focal peak. Firstly, a PRF of 1 kHz was used with bursts of 0.3 s T_{ON}, a 50% duty cycle burst followed by 2.4 s T_{OFF} and the ultrasound pulsing sequence was recorded by the electrode as shown in Fig. 4.10. Three bursts were recorded by the electrode in the shown time window with an amplitude of about 0.055 mV. This is in the same order of magnitude as meaningful brain signals (1 ~ 10 µV) that can be recorded by the electrode, indicating that an ultrasound-induced artefact was generated.

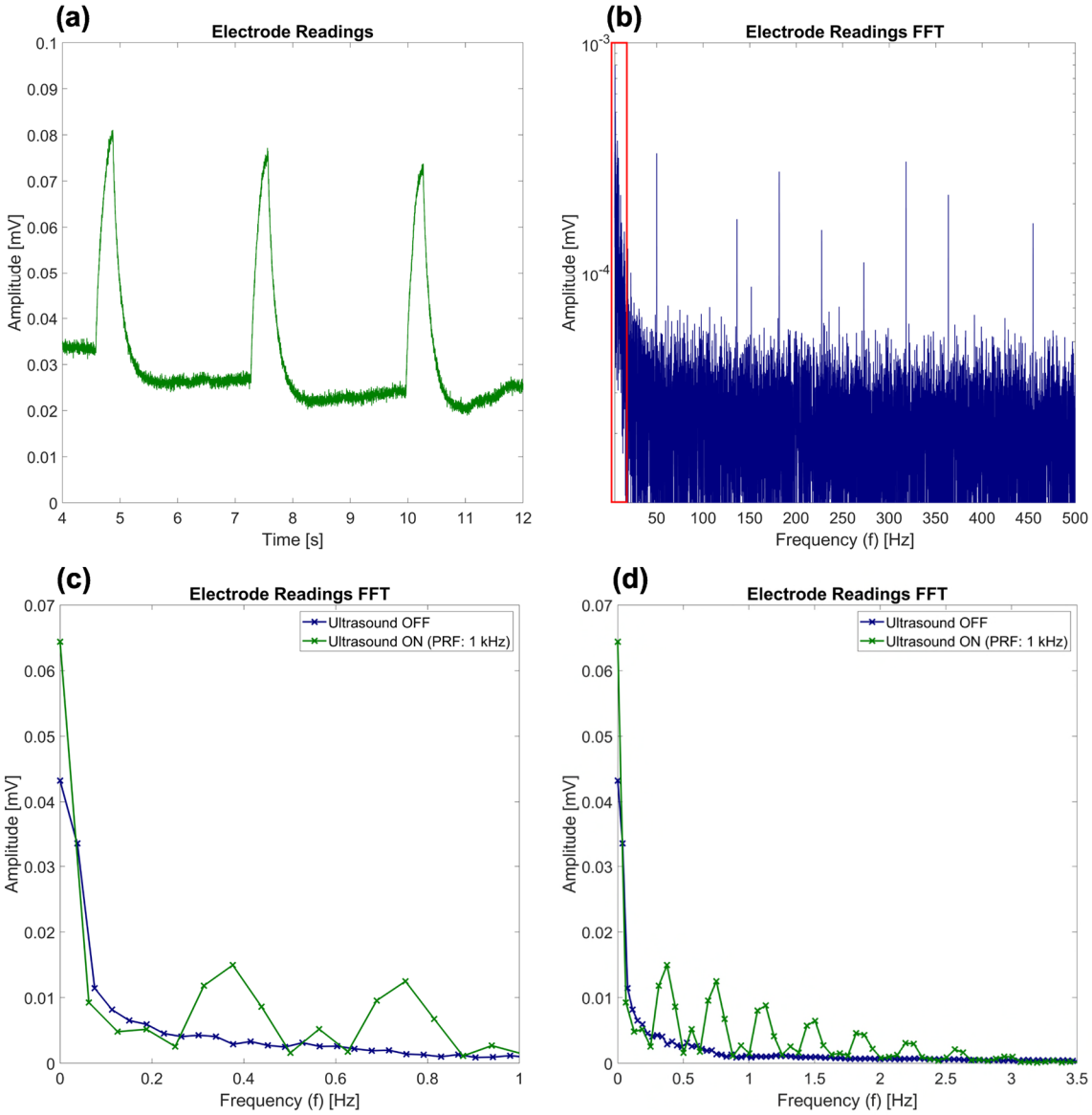

Fig. 4.10 Examples of ultrasound signals captured by the electrode. A PRF of 1 kHz pulsing was used here. **(a)** Electrode recording data in time. 3 trials of 0.3 s bursts were captured by the electrode. **(b)** Full-range FFT of the recorded signal. The red rectangle highlights the low frequency range in (c) and (d). **(c)** Comparison of the FFT of the recorded signal with and without ultrasound from 0 to 1 Hz. **(d)** Comparison of the FFT of the recorded signal with and without ultrasound from 0 to 3.5 Hz.

To evaluate the electrode output signal further, a FFT was generated based on the final electrode output sampling rate of 1 kHz (physical sampling rate of 8 kHz with a built-in 1.5 kHz low pass filter plus after down sampling). As the sampling rate of the electrode output signal is 1 kHz, corresponding to a Nyquist frequency of 500 Hz, ultrasound-induced artefacts should be captured at a frequency of 0.37 Hz based on its 2.7 s burst repetition. The FFT

zoomed in on the lower end of the frequency range and compared to that when no ultrasound was sent in Fig. 4.10 (c) and (d). There is a noticeable signal peak at 0.37 Hz only when there is ultrasound sending towards the electrode, and there are signals at integer harmonics that decay away by 3.5 Hz as shown in Fig. 4.10 (d), further confirming artefact generation.

As the ultrasound signal was detectable by the electrode, lower PRF values were also tested at 5 Hz, 10 Hz, 20 Hz, 50 Hz, 100 Hz, and 200 Hz. The electrode recordings in time and the corresponding FFTs are shown in Fig. 4.11. In these lower PRF cases, the pulsing within the 0.3 s burst could also be recorded by the electrode.

The PRF can be seen in both the recording in time and the FFT. Peak signals can be observed at the corresponding PRF values in the electrode FFT, as highlighted by arrows in Fig. 4.11 (d) ~ (f) and (j) ~ (l). Other signal spikes in the FFTs, such as those at 50 Hz in Fig. 4.11 (d) ~ (f) and those in Fig. 4.11 (k) and (l), were also detectable in the background even when ultrasound was off. For a PRF of 5 Hz, two spikes can be observed in Fig. 4.11 (a). This is because 5 Hz gives a pulse period of 0.2 s. The 0.3 s burst included only the ON period of the second pulse. With a higher PRF, more oscillations in a burst showed the trend towards the peak amplitude. An example is shown in Fig. 4.11 (j) by two red arrows.

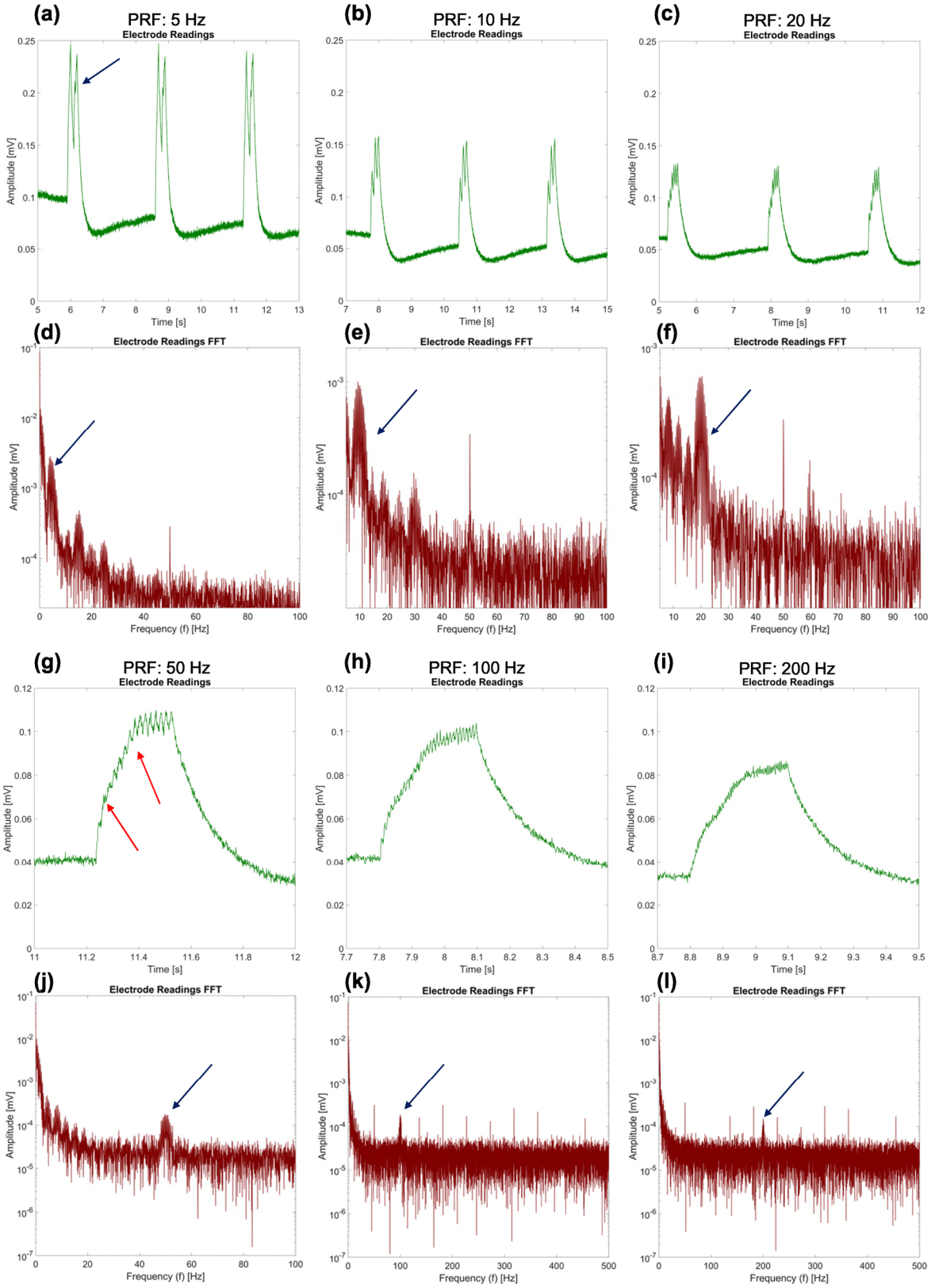

Fig. 4.11 Electrode recording at various PRF. (a), (b), (c) Recording in time for PRF of 5 Hz, 10 Hz and 20 Hz. **(d), (e), (f)** Recording FFT for PRF of 5 Hz, 10 Hz, and 20 Hz. Arrows highlight the peak signal at the corresponding PRF. **(g), (h), (i)** Recording in time for PRF of 50 Hz, 100 Hz, and 200 Hz. **(j), (k), (l)** Recording FFT for PRF of 50 Hz, 100 Hz, and 200 Hz. Arrows highlight the peak signal at the corresponding PRF.

PRF values from 200 Hz to 1400 Hz were also tested and presented in Fig. 4.12. It can be seen that for a PRF of 200 Hz and 400 Hz (in red), an artefact signal is present at the corresponding frequency in the FFT. For higher frequencies, a signal at an aliasing frequency is present, i.e., at 400 Hz for PRF of 600 Hz and PRF of 1400 Hz, and at 200 Hz for PRF of 800 Hz and 1200 Hz. At PRFs of 600 Hz and 1400 Hz, a peak at 400 Hz was recorded in the FFT, although lower in amplitude compared to identical peaks for a PRF 400 Hz. At a PRF of 1200 Hz, a signal peak at 200 Hz was recorded, although it was again lower in amplitude compared to identical peaks for PRFs of 200 Hz and 800 Hz. Due to the built-in 1.5 kHz low-pass filter, the PRF of 1200 Hz had a lower amplitude peak in the electrode signal than lower frequencies, and the PRF of 1400 Hz gave a signal just above the noise level. Comparatively, signals for 600 Hz and 800 Hz were of similar amplitude to those for 400 Hz and 200 Hz, respectively.

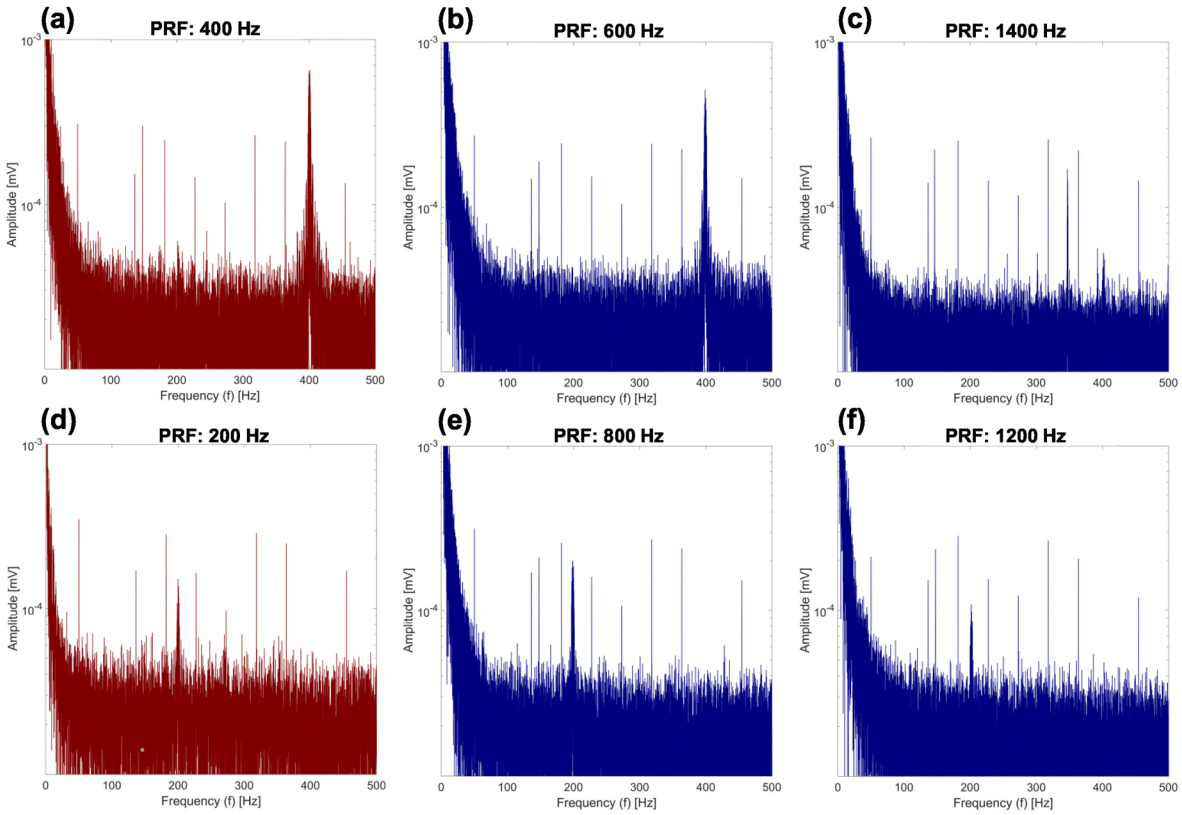

Fig. 4.12 Aliasing effect in electrode recording at PRFs above 200 Hz. **(a)** Recording FFT for PRF of 400 Hz. **(b), (c)** Recording FFT for PRF of 600 Hz and 1400 Hz. **(d)** Recording FFT for PRF of 200 Hz. **(e), (f)** Recording FFT for PRF of 800 Hz and 1200 Hz.

In electrode recordings so far shown in Fig. 4.11 and Fig. 4.12, all signals caused by 0.6 MPa ultrasound had an amplitude lower than 0.20 mV in deionised and degassed water. This is an order of magnitude higher than the meaningful brain signals that can be recorded by the electrode (amplitude range: 1 ~ 10 μV). It can also be seen that the amplitude reduces with increasing PRF in Fig. 4.11. Attempts to mitigate the ultrasound-induced signal are presented in Fig. 4.13.

While keeping the electrode at the acoustic free field focal peak, the effect of varying acoustic pressure on the ultrasound-induced artefact recording was investigated at 0.1 MPa to 0.6 MPa at five PRF values: 5 Hz, 15 Hz, 65 Hz, 130 Hz, and 800 Hz. Among these PRF values, 15 Hz and 65 Hz represent the middle of the beta band (10 Hz ~ 20 Hz) and gamma band (55 Hz ~ 75 Hz) of brain signals most associated with Parkinson's symptoms. As before, a PRF of 130 Hz was also tested as the typical frequency used in DBS. A quadratic relationship between the recorded amplitude and the acoustic pressure can be observed, suggesting that the artefact signal is related to the acoustic radiation force, which is dependent on the square of the envelope of the pressure wave (Fig. 4.13 (a)).

While a higher PRF was seen to lower the recorded ultrasound-induced artefact on the electrode, the tested variations in PRF and acoustic pressure were insufficient to reduce the recorded amplitude to values not otherwise interfering with recorded brain signals. Indeed, acoustic pressures must be as low as 0.1 MPa to give a recorded amplitude comparable to or slightly lower than brain signals with a magnitude of 10 μV. At such low pressures, the reliability of the ultrasound stimulation effect induced is questionable.

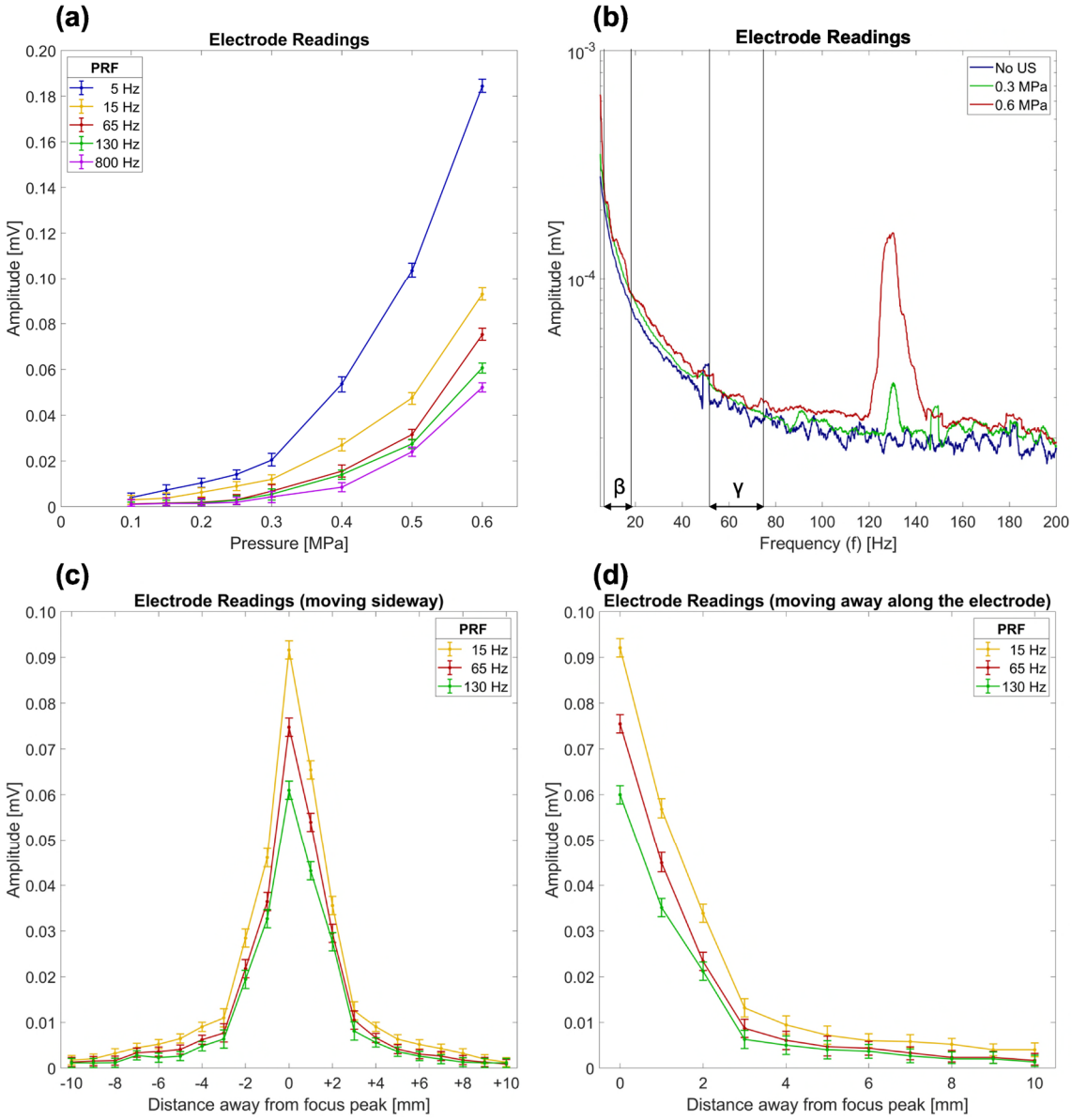

Fig. 4.13 Variation of artefact signal amplitude in the electrode recording due to changes in the acoustic field. The amplitude range of meaningful brain signals associated with Parkinson's symptoms is 1 ~ 10 μV. **(a)** Recorded electrode amplitude against acoustic pressure at different PRFs of 5 Hz, 15 Hz, 65 Hz, 130 Hz, and 800 Hz. **(b)** Using a PRF of 130 Hz, the FFT comparison of no ultrasound, ultrasound of 0.3 MPa, and ultrasound of 0.6 MPa. The beta and gamma bands of brain signals are marked as β and γ in the frequency spectrum, respectively. **(c)** At 0.6 MPa at the free field focal peak, the electrode recording profile when moving radially in the sideways direction (Y) as defined in Fig. 4.9 (a). **(d)** At 0.6 MPa at the free field focal peak, the electrode recording profile when moving radially upwards (Z) as defined in Fig. 4.9 (a).

One option to mitigate interference is to have the ultrasound stimulation operate at a frequency different from that of brain signal measurements (5 Hz ~ 100 Hz). Fig. 4.13 (b) shows the

spectra of the electrode recording for an ultrasound sequence with a PRF of 130 Hz. It can be seen that the ultrasound stimulation does not impact the recorded signals in either the relevant beta or gamma bands, suggesting that it may be possible to focus the ultrasound directly onto the DBS electrode without disrupting the brain signal recording. Three FFTs are plotted here: (i) blue: no ultrasound; (ii) green: ultrasound of 0.3 MPa at the free field focal peak is sent to the electrode; and (iii) red: ultrasound of 0.6 MPa at the free field focal peak is sent to the electrode. Only the signal around 130 Hz increases with increasing acoustic pressure.

An alternative approach to decreasing the artefact is to move the electrode away from the acoustic focal peak. Two radial directions were tested as before, one moving sideways and another moving upwards, as defined in Fig. 4.9 (a). Three PRF values were tested: 15 Hz, 65 Hz, and 130 Hz, as shown in Fig. 4.13 (c) and (d). In both radial directions, it can be seen that the recorded amplitude by electrode dropped to below 10 μV (0.01 mV) once the electrode was beyond ± 3 mm away from the focus, corresponding to the -6 dB focal volume boundary in free field for the 85 mm Fresnel PDMS lens used. Therefore, as long as the electrode is outside the -6 dB focal volume, the recorded amplitude should be comparable to or lower than the meaningful brain signals. It is also shown here that higher PRF cases produced lower recorded signals in the two tested radial directions.

Experimental testing has shown that ultrasound can induce artefacts in the electrode recordings that are over an order of magnitude larger than the meaningful brain signals for Parkinson's symptoms. While the acoustic pressure could be reduced to below 0.1 MPa to give an amplitude lower than the brain signals, this is not practical for reliable ultrasound brain stimulation. Selecting a PRF away from the meaningful frequency range has been shown to be effective in mitigating the impact of the induced artefact signals in the brain signal range of 5 Hz to

100 Hz. In addition, by moving the electrode outside the -6 dB focal volume, the ultrasound-induced signal's amplitude can also be reduced to a lower level than the meaningful brain signals. In reality, the human trial should use a combined approach where a PRF higher than 100 Hz should be used and the ultrasound should avoid forming a focus near the electrode such that the electrode is outside the -6 dB focal volume. Due to the aliasing effect of the electrode device, in order to avoid interactions in the frequency range lower than 100 Hz, a PRF between 900 Hz and 1100 Hz should also be avoided when designing the ultrasound pulsing sequence.

4.8 Impact on Electrode Measurement in Saline

The testing in the previous section was conducted in deionised and degassed water. Ultrasound has been shown to be able to change local salt solution conductivity (Fox et al., 1946), which could also give an artefact signal in the electrode recording. The change in medium conductivity was hypothesised to be the main contributor to the ultrasound induced signal in the electrode. Therefore, further tests were carried out in 0.9% NaCl saline.

The electrolytic conductivity in 0.9% saline was measured (HI 8733, Hanna, RI, USA) to be 12.77 mS/cm, representing a 105-fold increase compared to the deionised water tested previously (121.8 µS/cm). While 12% lower than literature-reported values (14.5 mS/cm at 22 °C; Sauerheber and Heinz, 2015), this still represents a 4.9 (2.6 mS/cm for grey matter; Koessler et al., 2016) to 7.5 times (1.7 mS/cm for white matter; Koessler et al., 2016) higher conductivity than the brain tissues of clinical interest.

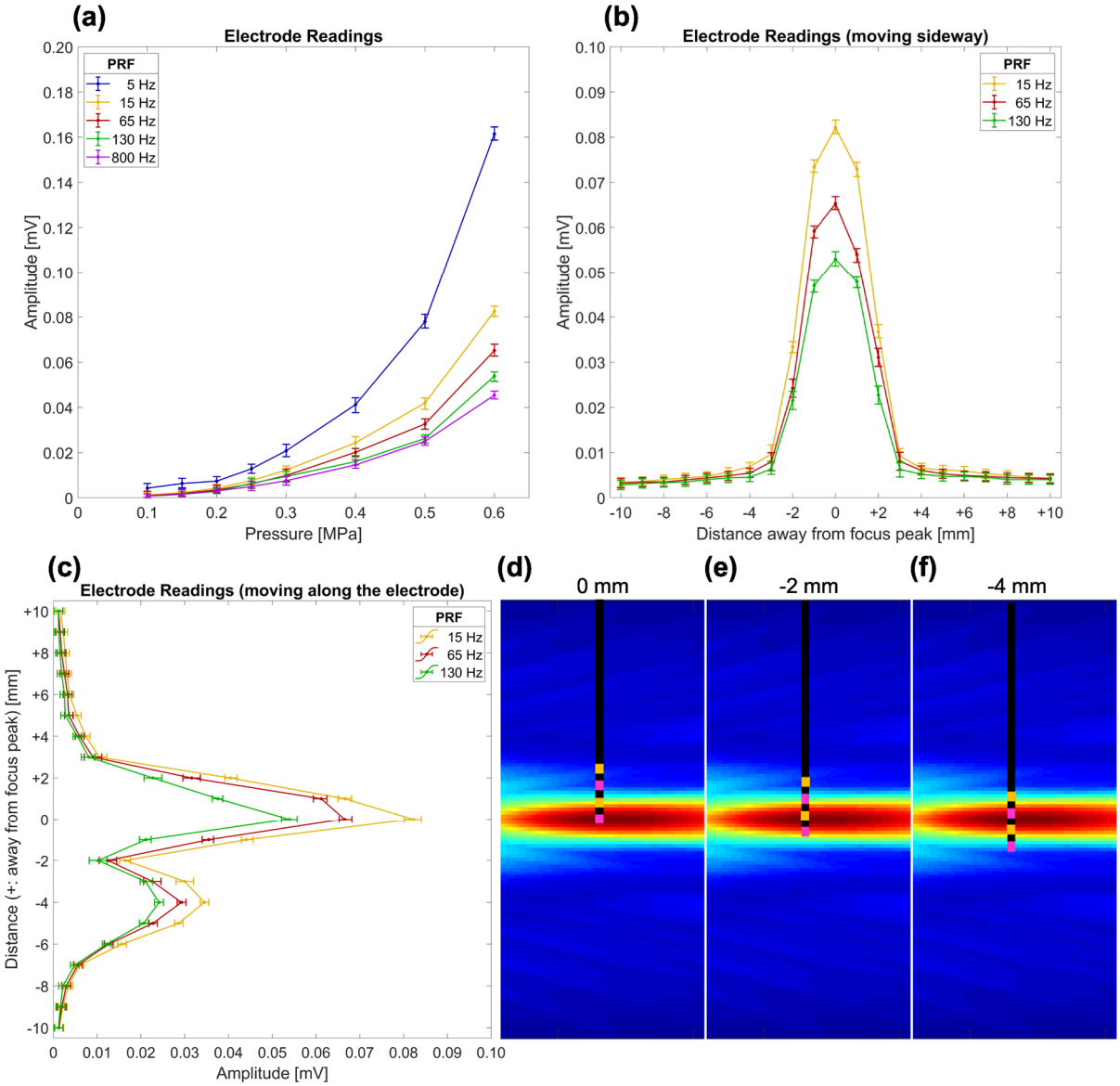

Fig. 4.14 Ultrasound-induced electrode recording in saline. (a) Recorded electrode amplitude against acoustic pressure in saline at different PRFs of 5 Hz, 15 Hz, 65 Hz, 130 Hz, and 800 Hz. **(b)** At 0.6 MPa at the free field focal peak in saline, the electrode recording profile when moving radially in the sideways direction (Y) as defined in Fig. 4.9 (a). **(c)** At 0.6 MPa at the free field focal peak in saline, the electrode recording profile when moving radially along the electrode (Z) as defined in Fig. 4.9 (a). **(d), (e), (f)** Schematics of the electrode overlaid on the free field focusing pressure field formed by the 85 mm Fresnel DPMS lens for 0 mm, -2 mm, and -4 mm along the electrode as in (c). Electrode contact nodes in use are shown in pink.

Fig. 4.14 (a) shows the measured artefact electrode signal amplitude in saline as pressure increases from 0.1 MPa to 0.6 MPa when positioned at the free field acoustic focal peak as before. The measured behaviour was similar to tests performed in deionised water, showing a

quadratic relationship between the recorded amplitude and the acoustic pressure and lower recorded amplitudes with higher PRF values. Despite the two orders of magnitude increase in conductivity, the amplitude of electrode recording was only increased by 11 to 13% for the five PRF values tested. Therefore, the change in conductivity is not the dominant factor in the ultrasound-induced electrode signal.

Movement of the electrode away from the free field focal peak in the two radial directions was also done in saline. When moving in the radial direction Y (Fig. 4.14 (b)), the amplitude of artefact recordings dropped below 10 µV (0.01 mV) when moved ±3 mm away from the free field pressure peak, consistent with findings in deionised water. Therefore, moving the electrode out of the -6 dB focal volume can still reduce the recorded amplitude significantly in saline. However, it can be seen that the recording amplitude's distribution in the focal region (within ±3 mm) does change from similar tests in deionised water (Fig. 4.13 (c)). This change in artefact amplitude distribution could be caused by the change of medium conductivity from deionised water to saline and variations in electrode positioning across the two experiments.

Movement of the electrode in the second radial direction X, i.e., along the electrode, is shown in Fig. 4.14 (c). This time, both the electrode leaving (positive direction) and the electrode inserting deeper than the focus (negative direction) were tested. The amplitude of artefact recordings dropped below 10 µV (0.01 mV) when moved ±3 mm away from the free field pressure peak, consistent with findings in deionised water and movement in the Y radial direction. However, in the negative direction, a distinct secondary peak at -4 mm could be observed before the recorded amplitude decays away. The reason for this asymmetric side lobe is demonstrated in Fig. 4.14 (d) to (f), where the electrode placement relative to the free field focal volume at 0 mm, -2 mm, and -4 mm in this particular radial direction are shown.

When the electrode tip was at the focal peak, as shown in Fig. 4.14 (d), the pressure difference between the two contacts was around 0.5 MPa. At this location, the bottom pink node was at the focal peak, whereas the top pink node was just outside the -6 dB focal region. When the electrode was at -2 mm, as shown in Fig. 4.14 (e), such that both nodes were just inside the -6 dB focal region but outside the focal peak, the pressure difference between the two contacts dropped to about 0.15 MPa. When the electrode was at -4 mm, as shown in Fig. 4.14 (f), such that one node was within the focal peak and the other was beyond the -6 dB focal region, the pressure difference between the two contacts returned to about 0.38 MPa. The pressure difference at these three positions likely explains the asymmetric secondary peak at -4 mm. After passing this secondary peak in signal magnitude, the measured amplitude by electrode continuously dropped until -7 mm, beyond which the amplitude was below 10 μV (0.01 mV). This shows that the acoustic radiation force only caused local deformation at a particular point on the electrode.

By increasing the medium conductivity 105 times to saline, ultrasound-induced artefact signals were reduced by less than 13%, suggesting that about 90% of the ultrasound-induced signal is caused by acoustic radiation force rather than changes in local salt solution conductivity. This was further verified in agar phantoms.

4.9 Impact on Electrode Measurement in Phantoms

Based on the results in the previous two sections, acoustic radiation force was hypothesised to be the dominant factor in the ultrasound-induced electrode recording. Acoustic radiation force can affect the readings of electrodes in two ways: (i) deflection of the entire electrode tip; and (ii) local deformation of the electrode elements.

The electrode was fixed rigidly by a holder in the experiments, as shown in Fig. 4.15 (a), positioned at least 50 mm away from the electrode tip. In the first case, acoustic radiation force can deflect the entire electrode tip, inducing signals from the bulk motion. This could be tested by swinging the electrode with reasonably fast frequencies and amplitudes to assess its impact on electrode recordings. In the second case, the electrode contact nodes in the form of metallic side walls of a hollow cylinder (due to the central lumen) are compressed and locally deformed by the acoustic radiation force. Again, this could be tested by pressing the tip of the electrode against a surface to assess its impact on electrode readings. These effects were evaluated by using agar phantoms at two different concentrations to provide different stiffnesses and shear moduli to elucidate the impact on the first effect.

An agar concentration of 0.3% w/v representing the softest gel-form medium that transforms from liquid to solid (Le Goff et al., 2015; Mcllvain et al., 2019; Normand et al., 2000) and an agar phantom of 3% representing tissue (Collin, 2009) were made. The 0.3% agar phantom was soft enough that the electrode could be easily inserted. The phantom also had sufficient transparency to observe the electrode's position. However, for the 3% agar phantom, it is too stiff to insert the electrode on its own. The stainless-steel mandrel that was in the central lumen of a new electrode was used to make a cavity in the phantom that had a smaller diameter than the electrode beforehand. The electrode could then be inserted into the 3% agar phantom in this cavity. As the 3% agar phantom was not transparent enough, the inserting location was marked prior to inserting the mandrel. The inserting depth was also controlled by markings on the electrode.

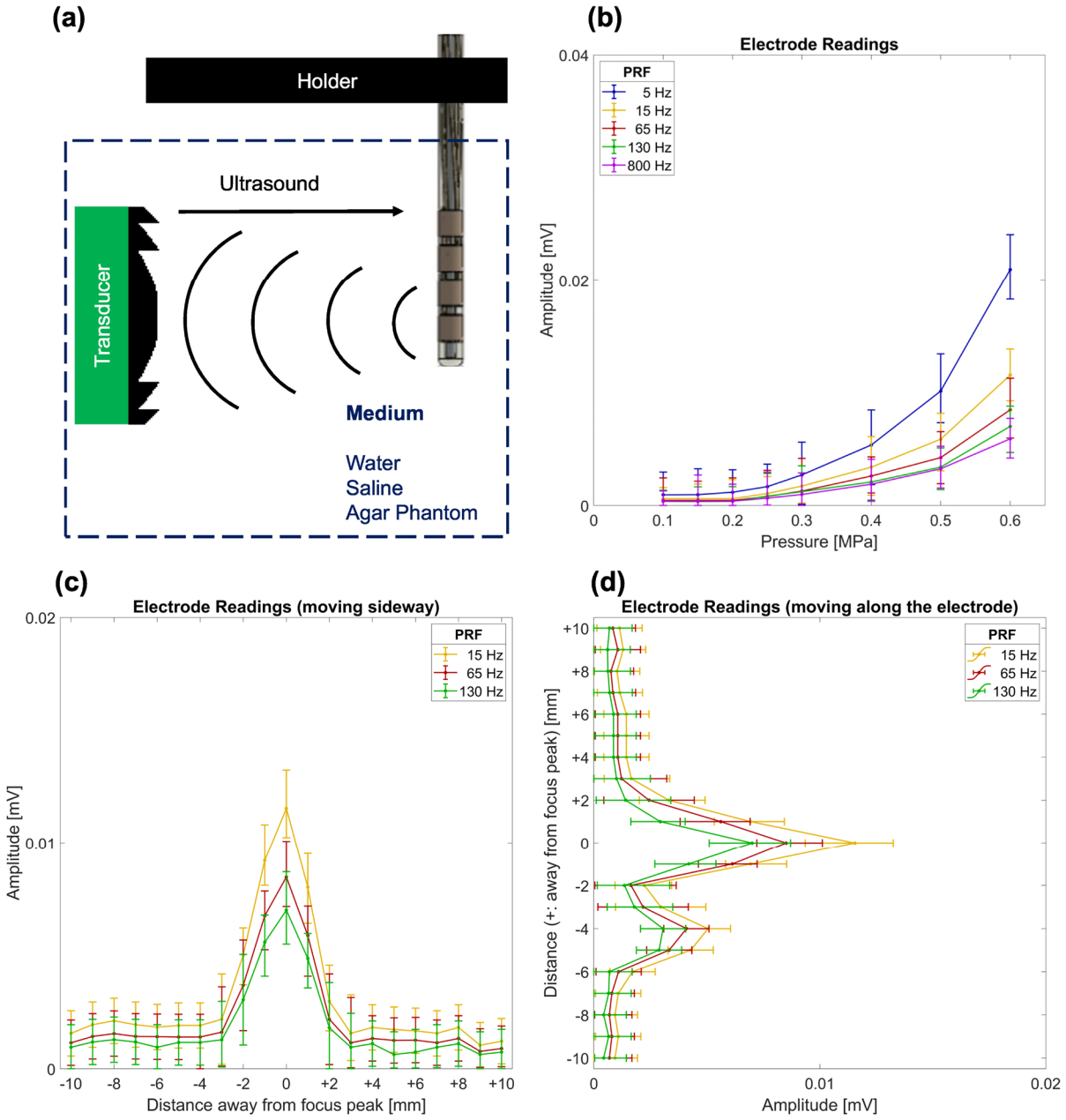

Fig. 4.15 Ultrasound-induced electrode recording in a 0.3% agar phantom. (a) Schematic of the setup. The dashed box represents the medium surrounding the electrode tip. **(b)** Recorded electrode amplitude against acoustic pressure in a 0.3% agar phantom at different PRFs of 5 Hz, 15 Hz, 65 Hz, 130 Hz, and 800 Hz. **(b)** At 0.6 MPa at the free field focal peak in a 0.3% agar phantom, the electrode recording profile when moving radially in the sideways direction (Y) as defined in Fig. 4.9 (a). **(c)** At 0.6 MPa at the free field focal peak in a 0.3% agar phantom, the electrode recording profile when moving radially upwards (Z) as defined in Fig. 4.9 (a).

When the electrode was inserted in the 0.3% agar phantom, the ultrasound-induced electrode recording had a similar response as in the fluid mediums, but the magnitude of the recorded signal was significantly reduced by 87% to 89% (Fig. 4.15 (b)). As before in deionised water

and saline, the quadratic relation between electrode recording amplitude and acoustic pressure was observed with a lower magnitude. Two radial directions were also tested at PRFs of 15 Hz, 65 Hz, and 130 Hz as before, one moving sideways (Y) and one moving upwards (Z) as defined in Fig. 4.9 (a). The recordings are shown in Fig. 4.15 (c) and (d). In Fig. 4.15 (d), the asymmetric side peak at -4 mm in the negative upward direction again appeared, confirming its existence.

When the electrode was inserted into the 3% agar phantom, no ultrasound-induced artefact signal could be distinguished from the noise floor, suggesting that the bulk motion induced by acoustic radiation forces on the electrode accounts for about 90% of the artefact amplitude. The transducer was moved in the axial and two radial directions while creating 0.6 MPa at the free field focal peak to confirm that no signal above noise level existed in the formed focus field.

The 0.3% agar phantom has a shear modulus of 1.5 kPa, and the shear modulus of the 3% agar phantom is 516 kPa (Normand et al., 2000). The 3% agar phantom had too high a shear modulus for the acoustic radiation force to cause electrode motion, which in turn failed to give an artefact signal above noise level.

As the human brain has a shear modulus higher than that of 0.3% agar phantom (3.5 kPa compared to 1.5 kPa; Hamhaber et al., 2007; Morin et al., 2017; Normand et al., 2000), the ultrasound-induced signal amplitude in the worst case, i.e., electrode right at the focal peak of 0.6 MPa and PRF of 5 Hz, should be lower than 0.021 mV (see Fig. 4.15 (b)). While an order of magnitude smaller than in deionised water and saline, this magnitude is still similar to that of a meaningful brain signal. Therefore, a PRF within the frequency band of a meaningful brain

signal should be avoided. In addition, the formation of the ultrasound focus directly on the electrode tip should also be avoided when possible.

4.10 Impact on Electrode Measurement by Angling

So far, all the experiments taking electrode measurements have been done with the electrode orthogonal to the acoustic propagation direction. The electrode measurement when the electrode was angled in the acoustic propagation direction is presented in this section.

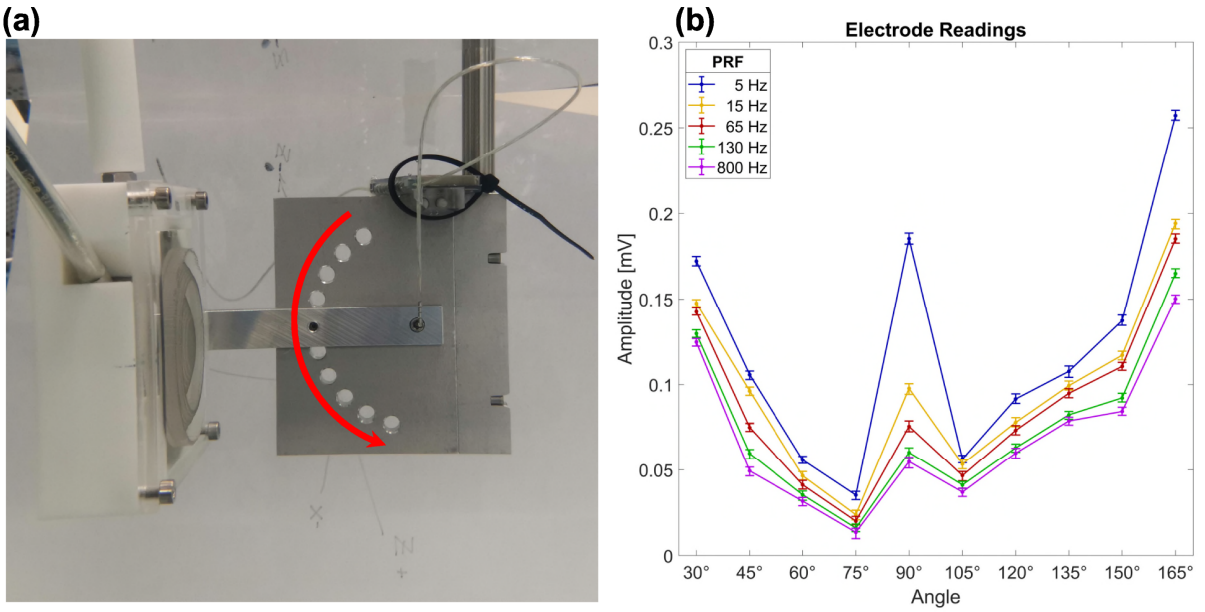

Fig. 4.16 Ultrasound-induced electrode recording at different angles in deionised water. Ten angles were tested from 30° to 165° at 15° steps. **(a)** Photo of the setup at 90°. The electrode was pointed downward by gravity throughout the experiment, with the transducer changing angles relative to the electrode. The red arrow indicates the direction of increasing angle. **(b)** The electrode recording against angles for five PRF values.

As before, the experiment was conducted in deionised water, with the tip of the electrode placed at the 0.6 MPa focal peak. A customised rig was used to fix the angle between the electrode and the transducer from an angling range of 30° to 165° in 15° steps, as shown in Fig. 4.16 (a). This angling range was considered the limit of feasibility for a human subject. The electrode was fixed to hang downward by gravity, while the arm holding the transducer was responsible

for the angling by using different holes on the rig. The holder ensured that the electrode tip was at the focal peak at all angles.

Fig. 4.16 (b) shows the measured artefact signal amplitude as a function of angle for PRFs of 5 Hz, 15 Hz, 65 Hz, 130 Hz, and 800 Hz. It can be seen that signals reduced between 75° and 105° once they moved a small amount away from 90° but increased beyond 75° and 105°. At 165°, the recorded amplitudes for all five PRFs were higher than those at 90°. However, for the anticipated clinical angles (30° ~ 150°), the artefact is highest at 90°, suggesting that the previous cases with the electrode orthogonal to the ultrasound propagation direction remained the worst-case scenario. As before, this result shows that a higher PRF resulted in a lower amplitude in electrode recording at all angles.

The measurement also suggests that despite 45° causing the most significant acoustic field disruption in simulations (see Section 4.4), its measured electrode recording was not the highest. Although the magnitude of acoustic radiation force increases with pressure from 90° to 45°, the angling was seen to reduce its effect on generated artefacts in electrode recording.

The electrode recording between 45 ~ 75° and 105 ~ 120° was lower than or equal to that at 90° for all PRF tested, suggesting possible angles that could be used to minimise disruptions to the electrode recording caused by ultrasound.

4.11 SUMMARY & DISCUSSION

The impact of the DBS electrode on the acoustic and thermal fields and the impact of the ultrasound on the DBS electrode recording have been considered with a mixture of simulations and experiments.

After the acoustic simulation, where the electrode's interaction with the ultrasound was validated by experimental measurement, the impact of the electrode on the acoustic field was studied at various relative positions between the electrode and the formed ultrasound focus. It was found that the electrode influences the acoustic field the most when it is placed at the free field focal peak. The pressure at the target, i.e., the free field focal peak, returns to the designed pressure if the electrode is moved outside the -6 dB focal volume. This finding is true in simulations for both the axial and the two radial directions.

In the axial direction, once the electrode is 5 mm or more away from the free field focal peak, the variation between the created pressure and the designed pressure at the target is less than 10%. In the two radial directions, the -6 dB focal width is 6 mm. This is 3 mm on each side of the focal peak. Therefore, as long as the distance between the electrode and the created ultrasound focal peak is equal to or greater than 3 mm laterally or 5 mm axially, the electrode effect on the target pressure can be neglected. Furthermore, the accuracy of electrode implantation in the brain should also be considered by creating the ultrasound focus at least 5 mm away, factoring in electrode implantation accuracy.

By placing the electrode at the free field focal peak, the impact on the acoustic field of different electrode angling positions was also investigated by acoustic simulation. The tip of the electrode was controlled to be at the free field focal peak, with only the angling of the electrode relative to the ultrasound propagation direction altered. Simulations found that angling slightly larger than orthogonal (90° to 135°) is preferred for lower impact on both the target pressure and the -6 dB focal volume. This is the case where the electrode enters from the side slightly opposite the transducer. Despite the variations in the angling range tested, the angling effect is weak compared to the placement of the electrode in the -6 dB focal volume. If this is not

possible, attempts should be made to arrange the electrode at 90° to 135° relative to the ultrasound propagation direction. However, it is also desired for the angling to be within 45° to 120° in order to limit the amplitude of the artefact signal in the DBS electrode recording. The combined effect would prefer an angle just over orthogonal (90° ~ 120°).

With the electrode presence changing the acoustic field, the resultant change in temperature rise was also investigated and found to be within the safety limit. Using the ultrasound pulsing sequence designed to fulfil the FDA intensity safety limit, the maximum temperature rise measured was within 1 °C, even in the worst-case scenario where the thermocouple was at the ultrasound free field focal peak orthogonal to the ultrasound propagation. Based on the experimental measurement, the thermal simulation only considering the temperature rise due to acoustic pressure was found to underestimate the temperature rise. In contrast, updated thermal modelling considering the electrode-tissue boundary viscous heating effect significantly overestimated the temperature rise (> 7 °C). However, based on the experiments, the initial model not factoring in the viscous heating effect was chosen moving forward after correcting its value by adding 70% to the final simulated temperature rise. The highest temperature rise was found to occur at the focal peak and decay when moving away, as expected from the electrode impact on the acoustic field simulation study. The thermocouple temperature recording in time also captured the ultrasound bursting sequence as rising and cooling periods in temperature.

With the electrode placed at the free field focal peak in deionised water and saline, ultrasound-induced artefact signals were detected in the DBS electrode in a quadratic relationship to the acoustic pressure. This suggests that the acoustic radiation force, which is related to pressure squared, is the main cause of the artefact signal in the electrode recording. It was also found

that with a higher ultrasound PRF, artefact amplitude could be lowered. PRF values outside the frequency band of meaningful brain signals should therefore be used to avoid ultrasound artefacts. It is also worth noticing that due to the geometry of the two electrode nodes used in recording mode, there was a secondary peak of induced signal in 1 of the 4 radial directions, i.e., the negative upward direction where the electrode was inserting deeper and passing through the focus. The pressure difference at the two electrode nodes in use follows a trend to create this secondary side peak.

By moving the electrode outside the -6 dB focal volume radially in deionised water and saline, the induced artefact amplitude drops significantly to a similar magnitude as the brain signal. However, by changing the medium conductivity by two orders of magnitude from deionised water to saline, the reduction in amplitude of the ultrasound induced signal was only found to be 10%, suggesting that the ultrasound-induced artefact signal amplitude is not sensitive to changes in conductivity.

0.3% and 3% agar phantoms were further tested to mimic brain tissue surrounding the electrode tip. The recorded signals against different acoustic pressures in different mediums using a PRF of 130 Hz are compared in Fig. 4.17. In the 0.3% agar phantom, where the shear modulus was 1.5 kPa, the ultrasound-induced signal was only 11 to 13% of that in deionised water. In the 3% agar phantom, where the shear modulus was 516 kPa, no ultrasound-induced signal could be measured above the noise level. Therefore, the acoustic radiation force deflecting the electrode tip is likely the dominant cause of the induced signal.

In the human brain, the shear modulus is 3.5 kPa, which is close but higher than that of 0.3% agar phantom. Therefore, for an electrode inserted in the human brain, the ultrasound-induced

artefact should still be measurable but with an even lower amplitude than that measured in a 0.3% agar phantom. A PRF higher than 100 Hz should be used in the ultrasound pulsing sequence to avoid interfering with meaningful brain signals. However, the data in Fig. 4.17 are with the electrode at the focal peak, which is the worst-case scenario. In reality, the ultrasound focus should first be avoided by forming directly on the electrode (5 mm away or more). The recorded ultrasound artefact signal is then further reduced.

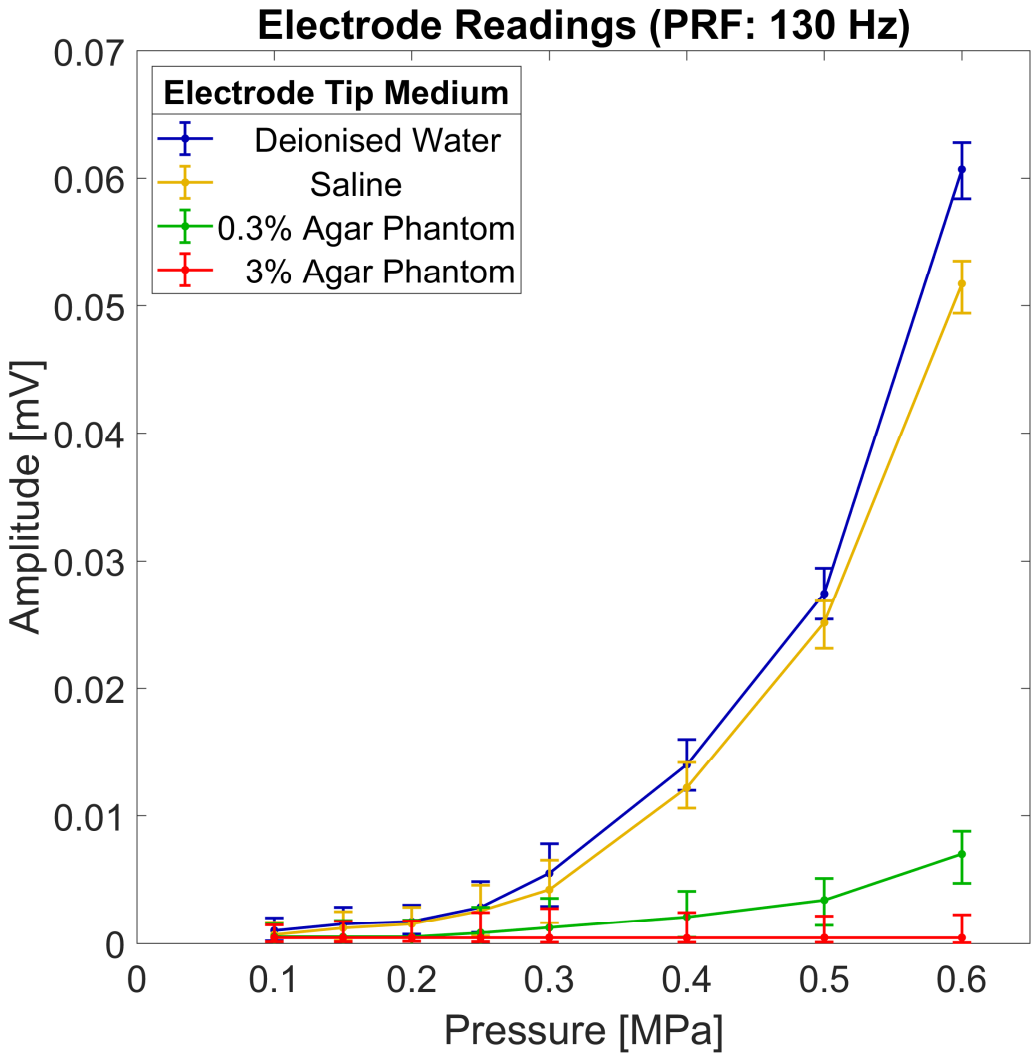

Fig. 4.17 Electrode recording for PRF of 130 Hz at various acoustic pressures in deionised water, 0.9% NaCl saline, 0.3% agar phantom, and 3% agar phantom. In the 3% agar phantom, no ultrasound signal stands out from the noise floor. The shear modulus of deionsied water is on the order of 10^{-6} Pa. The shear modulus of 0.3% agar phantom is 1.5 kPa. The shear modulus of 3% agar phantom is 516 kPa. The shear modulus of the human brain is 3.5 kPa.

The most effective way of avoiding electrodes' impact on the acoustic field and ultrasound's impact on electrode recording is by a combination of forming the ultrasound focus away from the electrode tip and using an ultrasound PRF not in the brain signal's frequency band, i.e., higher than 100 Hz.

5

CONCLUSIONS & FUTURE WORK

This chapter summarises and discusses the work presented in this thesis and the research contributions to the field. Future directions are also outlined.

5.1 SUMMARY & DISCUSSION

This thesis developed and validated a lens method using flat transducers and the temporal bone window on the human skull to stimulate deep brain targets with improved precision, non-invasively, and cost-effectively. The modelling pipeline was shown in experiments to be a feasible stimulation planning method, along with providing the information needed for making the target-specific lenses. The feasibility of applying ultrasound stimulation by lens to Parkinson's disease patients with implanted DBS electrodes was investigated, and methods to mitigate unwanted interactions were also discovered and validated.

5.1.1 FEASIBILITY STUDY OF ACOUSTIC LENS IN HUMAN BRAIN STIMULATION

The simulation study in Chapter 2 has shown that target-specific PDMS lenses can be used to correct transmission aberrations through the skull and generate spatially specific targeting of ultrasound to various deep regions of the brain via the temporal bone window.

The lens concept was tested using full-wave simulations with human MRI data in Chapter 2. By employing phase conjugation simulations for each target in each subject, acoustic simulation results were used to create the lens structure and help determine the optimal source location. Forward simulations were then used to confirm the focusing of the lens at the target site with sufficient pressure gain.

For practical implementation, the back propagation simulation could be done before the stimulation session to acquire phase information. For real-time simulation based on live transducer-head relative position, only the forward simulation step needs to be improved in speed to balance modelling accuracy and computational cost.

By using the phase information on the source grids instead of creating a lens structure in the simulation space, the piston source effectively becomes an array with elements of 0.5 mm by 0.5 mm. The pressure field gives a substantially higher focal gain than that of the lens due to the removal of two acoustic impedance mismatch boundaries on entry and exit of the lens. For optimal performance, array systems similar to those used for brain surgery (Exablate Neuro, Insightec, Tirat Carmel, Israel) are the most versatile and resilient long-term options despite the upfront cost. The forward simulation can use the phase information at the transducer's live position.

Simulation studies were carried out for various source diameters and frequencies. The most appropriate diameter was found to be 65 mm, corresponding to the largest size that can fit the temporal bone window without covering the ear canal. Compared to smaller sizes, this transducer size provides better target pressure gain, a smaller focal volume, and can potentially reduce side effects by preventing the generation of high-pressure spots inside the skull on the ultrasound path. The desired frequency of the source was also found to be 500 kHz to maximise focal gain and reduce focal volume. Based on the simulated target pressure gain, transducers that normally have a maximum surface pressure of over 0.5 MPa can provide sufficient amplitude at the target location to induce neuromodulation.

Simulations using the whole head space were then conducted to evaluate overall field pressure distributions. Standing waves and pressure spots off target due to multiple reflections were observed in whole head simulations.

5.1.2 VALIDATION OF PDMS LENS METHOD ON SKULL SAMPLES

Validation of the simulations was done on two cadaver skull samples and presented in Chapter 3. In total, 9 lenses were tested for 6 target sites. The lenses showed comparable performance in free field to simulated results, which demonstrates that the target-specific PDMS lenses were manufactured to an acceptable standard. Evaluation of the discrepancies between the measurements and simulations showed possible lens structural errors introduced in the manufacturing process as well as aspects of the measured acoustics that were not represented in the linear, fluid-based acoustic simulation.

Among the three types of tested simulations on CT-mapped skulls, simulations using binary skull segmentation were shown to provide better agreement with the measured peak focal gain than segmentation by porous skull segmentation. Using porous skull segmentation, the peak focal gain was found to be significantly overestimated by the simulation, likely due to the more complicated acoustic propagation occurring through the skull structure than in the simple fluid-based simulation based on only local skull porosity imaging information. Additionally, simulations assume that the pores in the skull are filled with water, i.e., the skull is a bone-water mixture. However, the *ex vivo* skull samples have been outside the body for a long time. It is reasonable to say that a lot of the pores are filled with air and are impractical to be fully filled with water again, i.e., the skull is more likely to be a bone-air mixture. This mismatch between simulation and experiment may also help to explain the poor performance of simulations using porous skull segmentation. It was also found that skull acoustic attenuation can decrease with increasing HU in CT scans (Webb et al., 2021), breaching the mixture rule employed for attenuation.

In testing different lens types, binary voxel (BV) lenses for all three perirhinal cortex target sites were found to generate foci significantly larger than predicted in simulations. This suggests that the perirhinal cortex, despite being shallower to the head surface than the anterior hippocampus, is more difficult to target by ultrasound. One possible explanation is that ultrasound focusing of the perirhinal cortex requires the source to be angled so it is further away from normal incidence at the boundary entering the skull, generating shear waves beyond the negligible amounts expected for the anterior hippocampus. In addition, the ultrasound path to the perirhinal cortex is closer to the edge of the temporal bone, an area known for having more complicated skull geometry that may otherwise not be factored into simulations.

To expand clinical application to bilateral brain targets, simultaneous paired source stimulation interference was also examined. Measurements confirmed that the presence of standing waves starts to change the pressure distribution in the main focal lobe in both hemispheres. In cases using a single source, the focus on each side is already larger in measurements than predictions. As a result, the standing waves on the midline acquired a larger magnitude than those in simulations. When using two sources for transcranial focused ultrasound neuromodulation, the standing wave effect must be carefully examined and mitigated when possible, including potentially sending offset bursts from each transducer. Further investigations are generally needed for safety through studies on improved standing wave modelling and its effects on the human brain.

5.1.3 TUS FEASIBILITY ON PD PATIENTS WITH IMPLANTED DBS ELECTRODES

In Chapter 4, to evaluate the utilisation of the designed acoustic lens in Parkinson's disease patients with embedded electrodes, the electrode-ultrasound interaction was studied at various relative positions between the electrode and the ultrasound focus. In simulations and

experiments, the electrode has maximal influence over the acoustic field when it is at the free field focal peak. If the distance between the electrode and the created ultrasound focal peak is equal to or greater than 5 mm, the increase in target pressure was found to be less than 10%. The accuracy of electrode implantation in the brain should also be considered by creating the ultrasound focus at least 5 mm away plus the implantation accuracy. However, even with the electrode right at the free field focal peak perpendicular to ultrasound propagation, the thermocouple temperature measurement was less than the 1 °C temperature rise safety limit.

With the tip of the electrode at the free field focal peak, simulations found that the electrode entering from the same side as the ultrasound source (< 90°) caused higher target pressure and focal volume compared to the electrode entering from the side slightly opposite to the transducer (90° to 135°). However, this improvement in acoustics was found to be marginal. When factoring the angling impact on the electrode recording itself, an angling within 45° to 120° was found to limit ultrasound-induced artefacts. To match both the ultrasound and electrode angling requirements, the electrode must avoid being placed in the -6 dB focal volume. If further angling of the electrode is insufficient to limit ultrasound-induced artefacts, one option would be to cloak the electrode with a biocompatible material that would absorb acoustic waves and replace the metal alloy wire with a carbon-based conductive material.

The insonification of the electrode by ultrasound resulted in an ultrasound-induced electrode artefact at the envelope of the ultrasound waveform. It was found that the amplitude of the recorded signal is quadratically related to the acoustic pressure, suggesting that acoustic radiation force is the main cause of the induced signal. Beyond ensuring that the electrode is at least 5 mm away from the created ultrasound focal peak, the PRF can also be modulated to

ensure its frequency band is outside that of any meaningful brain signals (i.e., > 100 Hz) to prevent any meaningful electrode interference.

The impact of ultrasound-induced artefacts on the electrode in an elastic fluid medium was tested by placing it in agar phantoms of varying shear moduli (1.5 kPa and 516 kPa) to better represent brain tissue (~3.5 kPa). At 1.5 kPa, the artefact was reduced by about 12%, and no artefact could be detected at 516 kPa. For an electrode inserted within the brain, it is anticipated that the signal artefact will still be detectable but reduced by over 12%, even with the electrode at the ultrasound focal peak. The most effective way to avoid electrode-ultrasound interaction is therefore a combination of forming the ultrasound focus away from the electrode tip and using an ultrasound PRF not in the brain signal's frequency band, i.e., higher than 100 Hz.

5.2 FUTURE WORK

Using the acoustic lens techniques presented in this thesis, a human trial is scheduled to be conducted on Parkinson's disease patients with embedded electrodes. They must have a measurable beta peak on the device and be on stable medication therapy with no drug changes for 6 weeks prior to intervention. Baseline testing will be done on the first visit. On the second visit, their DBS modulation will be safely reduced to zero, and TUS application and LFP recording will be carried out. Motor assessment and patient-reported outcome measures will be performed. The hippocampus will be the control site. Measurements will be taken at the STN when TUS targets the GPi and vice versa to mitigate electrode-ultrasound interaction.

As the GPi is potentially large enough to avoid placing the electrode inside the acoustic focus, it may be possible to stimulate and record in the GPi. By using measurements of the LFP in this human trial, the goal is to demonstrate that TUS can non-invasively stimulate brain

networks. This would provide direct evidence for the long-term development of TUS into a tool helping to decide electrode implantation location and upgrading certain therapies that currently require surgery to non-invasive replacement.

k-Wave toolbox has been upgraded from version 1.3 to version 1.4 at the end of 2022. It has additional features such as `kWaveArray` to provide off-grid sources free from staircasing artefacts in modelling discretisation space (Wise et al., 2019). The most recent version of the toolbox should be utilised in future simulations, including angled sources or sources with curved surfaces. The staircasing artefact on the electrode geometry also affects the modelling results in this thesis. Further studies can also apply the techniques in the new toolbox to represent the electrode in a modelling space free from staircasing artefacts.

Viscous heating modelling representation should also be further investigated so that thermal simulations and measurements of the electrode in an acoustic field can agree with smaller discrepancies in temperature rise. Furthermore, a high speed camera can be used when ultrasound is hitting the electrode tip in different mediums, as in Chapter 4. By processing the imaging data, the electrode deformation and movement, as well as the associated artefact signal, can be better understood in different mediums.

Porous skull segmentation and mapping of corresponding material properties require further investigation to make better use of the skull porosity information and produce more accurate modelling results than binary skull segmentation. For example, instead of mapping attenuation based on porosity, as in this thesis, a constant attenuation can be applied across the skull thickness. Furthermore, the porous skull segmentation should still maintain the sharp transition

from medium to cortical skull bone at the skull surfaces despite the diffusive artefact in imaging.

The acoustic properties of fresh skull samples should also be collected, evaluated, and compared to those when they are completely dried in several weeks. The reliability of validation studies employing dried skull samples, such as those in this thesis, should be carefully considered if the results are considerably different.

An organoid model of the brain neuron network could be created to examine the mechanism of ultrasound brain stimulation and also be used for safety investigations. Building, validating, and obtaining relevant findings from the model can offer important knowledge and understanding of the mechanism of ultrasonic brain stimulation. To determine whether ARF is the cause of ultrasonic brain stimulation, a simpler neuron network can be utilised to test in both situations − with and without the standing waves produced by the two transducers − as part of the process leading up to the final organoid model. If stimulation still persists in a complete standing wave state, other auditory phenomena must also be involved since ARF is only present for progressive waves.

Considering the current expensive and complex neuronavigation system currently used for targeting, it would be helpful to have simpler systems to align the ultrasound with the target. After an initial session of optical tracking to align the ultrasound, the ultrasound transducer can send a short imaging pulse and record the reflections generated within the skull. This recorded signal, representing the aligned transducer position and orientation, can then be used as a baseline from which subsequent sessions could be replicated using ultrasound alone, without the need for optical tracking. This signal could further be confirmed using acoustic simulation

modelling to verify positioning. Alternatively, a custom-made patient-specific 3D printed helmet could be developed, physically ensuring consistent ultrasound placement each time. In both cases, initial testing on skull samples would be needed to assess feasibility.

Application of the designed acoustic lens could further be extended to TUS temporal interference (TUS-TI; Liu et al., 2022; Rampersad et al., 2019; Sun et al., 2017). An analogy of electrical brain stimulation, TUS-TI employs frequency modulation from two transducers to generate acoustic radiation forces from the frequency difference at the mutual beam crossing focus (Fatemi and Greenleaf, 1999; Urban et al., 2011). As this frequency difference could range up to 10 kHz, depending on the transducers employed, the full range of brain signal frequencies could be modulated through TUS-TI. Additionally, the use of frequency interference means each transducer does not need to be pulsed, removing the auditory confound caused by conduction in the skull. While an exciting prospect, the optimal angling between the two sources in different acoustic windows will require a careful balance between axial and radial focal sizes (Chen et al., 2004), a procedure likely necessitating further simulations to investigate its feasibility. To start, two acoustic pathways orthogonal to one another should first be explored (Gray et al., 2020; Paverd et al., 2019).

APPENDIX

A. DUAL ARRAY DEVICE

As an alternative stimulation source, the feasibility of a dual array device (Neurosonx System, Cerevast NeuroRehab, Bothell, WA, USA) was studied. The hardware and the array arrangement are shown in Fig. A1.

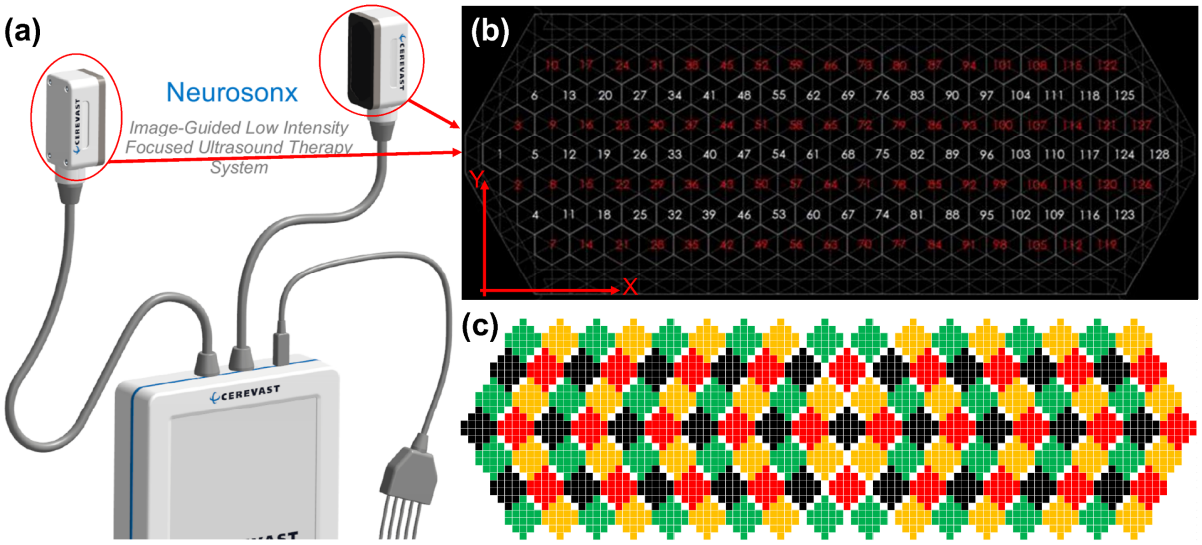

Fig. A1: The dual array device and its array layout. (a) The device schematic. **(b)** The element arrangement of the array. Direction X is along the longer side of the array. Direction Y is along the shorter side of array. **(c)** Reconstructed array onto a space of 0.5 mm grid in simulation. Grids representing the same hexagons are grouped by colour.

The array has 128 hexagonal elements indexed as shown in Fig. A1 (b), each with an edge length of 1.3 mm and an element surface area of 4.39 mm^2. To replicate the array in a computational space, element geometry was represented by grids of 0.5 mm by 0.5 mm. To match the surface area and characteristics of each element, 17.56 (rounded to 18) grids were used and driven by the same signal as one element. Within Fig. A1 (c), each group of 18 grids of the same colour represents one of the hexagonal elements.

As the reconstructed simulated array is slightly smaller than the array tested (X × Y: 51 mm × 16 mm compared to 50 mm × 15 mm), the simulation results could slightly underestimate the

array's focusing and steering capabilities. Although most of the array geometry is successfully reproduced in the simulation space, it can be seen from Fig. A1 (c) that the centre symmetry for the long side of the array (X) is no longer preserved. Before running simulations using this 0.5 mm representation of the array, the analytical representation of the array field was studied first.

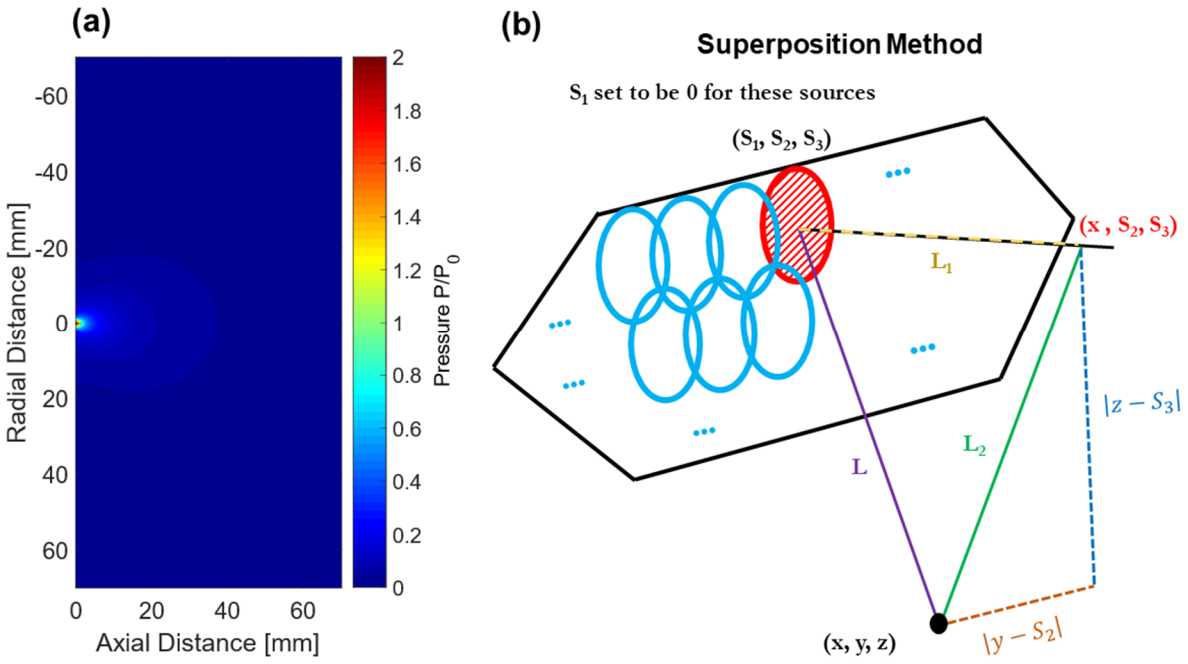

Fig. A2: Analytical solutions to represent the array device. A circular piston of the same area as the hexagonal elements was used to build the analytical results for the whole array. **(a)** Analytical pressure distribution of one piston element. **(b)** Schematic to superimpose the analytical results for the elemental piston to construct the array from the analytical results.

Analytical solutions of pressure fields for a single circular piston are available in the free field (Hutchins et al., 1986; Liauh and Lin, 1999). As there is no built-in curvature in the array device shown in Fig. A1, each array element can be considered a tiny piston. However, an approximation is needed as the array element has the shape of a hexagon instead of a circle. Each hexagonal element was therefore approximated to a circular piston with matching surface area, yielding a circular piston of radius 1.18 mm. At 500 kHz, such a small elemental piston has a calculated Rayleigh distance of 1.46 mm. However, as the Rayleigh distance is smaller than the wavelength (≈ 3 mm), there is no near-field pattern with a drop in pressure away from

the source. This can be demonstrated in the pressure magnitude distribution in Fig. A2 (a). For later comparison to the simulation results, this analytical pressure map is calculated with a matched spatial step size of 0.5 mm.

To analytically represent the array device, each element's pressure distribution was superimposed, as outlined in Fig. A2 (b). A reference centre for the overall array was selected as the geometric centre (that is, the midpoint between element number 61 and 68 in Fig. A1 (c)). The position to be focused by the array device is (x, y, z). The distance of this target to the centre of each element was calculated as **L**. Each element's centre coordinate was determined relative to this origin as (S_1, S_2, S_3). For convenience, the geometry was set to propagate ultrasound in the x direction, and S_1 is set to be 0 for all elements, placing the array source at x = 0. The differences in distance from the focus to the reference array origin and to the element centres are used to calculate the phase needed for each element to achieve constructive interference at the target. This phase is used to modify the analytical complex pressure results such that each element now has its own analytical pressure field with a slightly modified phase based on the focusing target location.

The aforementioned analytical solution assumes axial symmetry for the circular piston. Hence, the 2D map in Fig. A2 (a) can create a 3D pressure field by rotating it around the centre axis of the piston. Each elemental piston's contribution to a particular point can then be calculated by extracting the corresponding complex pressure at the correct position on the analytical pressure map. The correct position is extracted as shown in Fig. A2 (b). L_1 is the component on the element's symmetry axis of the vector **L** from the element centre to the point of interest. L_1 gives the axial position on the analytical pressure map to take the reading. Similarly, L_2 is the other component of vector **L** that is orthogonal to L_1 and effectively parallel to the array

source plane. L_2 gives the radial position on the analytical pressure map to take the reading. L_1, L_2, and **L** are in the same plane where the analytical results are used for calculating the particular element's contribution to the point (x, y, z). L_1 is numerically simplified to be the same as x when the source is placed in the plane x = 0. L_2 is the length of the slope of a right angle triangle parallel to the array source plane, where the other two sides are $|y - S_2|$ and $|z - S_3|$. In this way, each of the 128 elements' contributions can be calculated. As the complex pressure is used for the analytical solution, a summation of the 128 elements' contribution at a point can give the overall array pressure magnitude and phase information. The analytical pressure fields of the array can thus be generated.

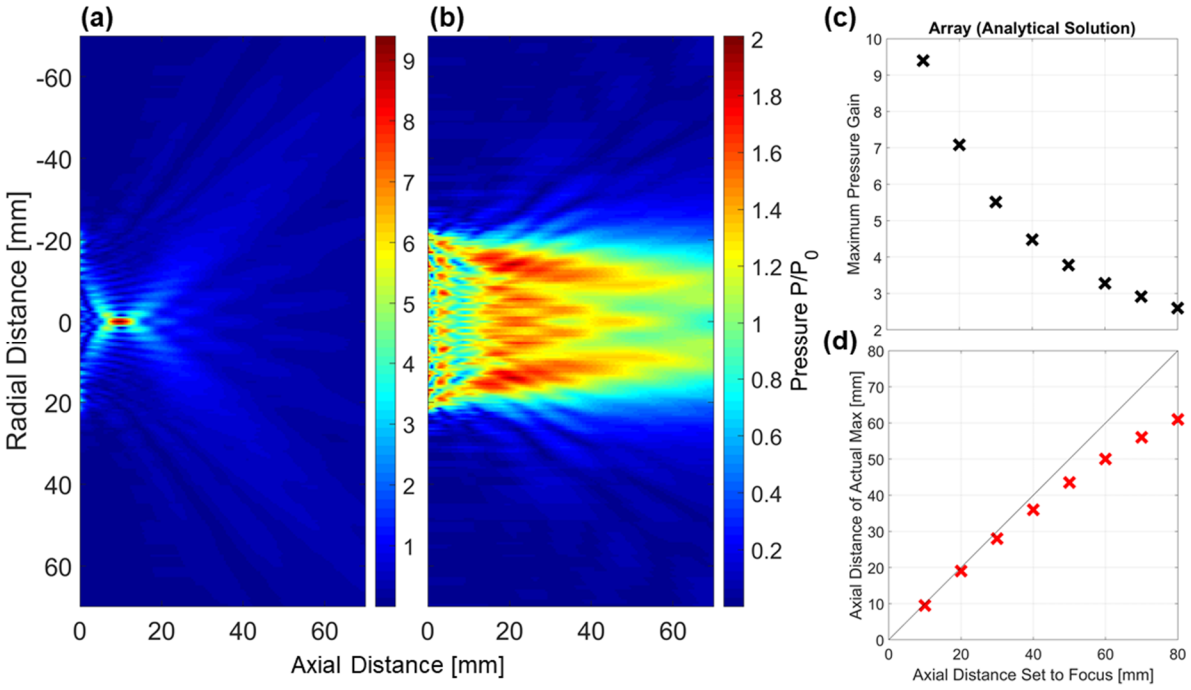

Fig. A3: Array model built with analytical solutions. (a) Focusing 10 mm away from the source plane. **(b)** Focusing 10^9 mm away from the source plane, representing a non-circular piston. **(c)** Maximum pressure gains against set positions to focus. The pressure gain decreases asymptotically as it focuses further away from the array. **(d)** Actual pressure maximums occurred at locations against set positions to focus. The difference is bigger when targeting further away from the array surface.

By approximating each element as a circular piston with identical placement, overlay can be observed, as in Fig. A2 (b). However, this does not affect the superposition described above,

as this is not a simulation where actual propagation happens. While the near-field pressure close to the array surface will vary with this approximation, the calculated analytical result is based on the Fresnel approximation for computation speed, which itself is not accurate for the regions near the source or far off the axis.

The analytical results were generated and tested at a focal point close to the array surface (10 mm) in Fig. A3 (a) and a focal point infinitely far away (10^9 mm) in Fig. A3 (b). In the latter case, the array represents a non-circular piston with a peak pressure in the field twice the source pressure P_0 as expected. As shown in Fig. A3 (c), the maximum pressure drops asymptotically towards $2P_0$ as the focus is set further away from the array on the symmetry axis. It is also noticed that the position difference between the set geometric focus (the set array focal point) and the position of the pressure maximum increases when focusing further away on the axis from the array, as shown in Fig. A3 (d).

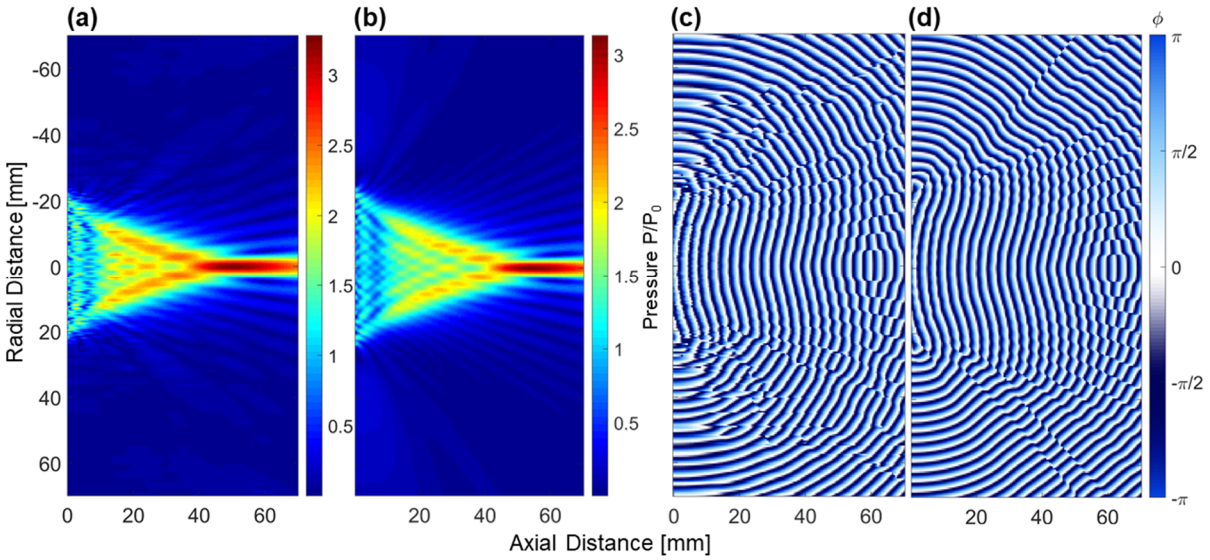

Fig. A4: Array on axis focusing ability. Views show the field of the array along X. The geometric focus is set to 60 mm on axis. **(a)** Pressure magnitude distribution, analytical result. **(b)** Pressure magnitude distribution, k-Wave simulation. **(c)** Phase distribution, analytical result. **(d)** Phase distribution, k-Wave simulation.

Comparing the analytical and simulated array fields at a position on the axis 60 mm away from the array (Fig. A4), the pressure magnitude distribution can be seen to match. However, when comparing phase maps, a distortion to the phase can be observed at angles beyond ±45° (Fig. A4 (c)). For both phase and magnitude, results near the array surface (axial distance close to 0) are noisier than those of the simulated results. It is possible that as the analytical results utilise the Fresnel approximation, the inferior accuracy in field regions far away from the axis may contribute to this discontinuity. Similarly, the summation of rounding errors induced by the 0.5 mm resolution of analysis of each element can cause phase distortions by giving outlying values, as shown by horizontal stripes of phases in the large angle regions. However, when evaluating the absolute pressure and variations of magnitude in these phase distortions, it becomes apparent that the low-pressure magnitude is unlikely to contribute to the observed effects.

Evaluating the phase maps in Fig. A4, a flat wave front is formed at 60 mm on axis in both the simulated and analytical results, suggesting that the array has its geometric focus at 60 mm on axis. However, in the magnitude maps, both the absolute value ($0.2P_0$ higher in analytical) and position (55 mm in simulated and 50 mm in analytical) varied between the analytical and simulated results, with neither matching the 60 mm geometric focus. Interestingly, the pressure maxima occur at different locations despite identical targets and flat wave fronts in both simulated and analytical distributions.

To observe the more subtle differences between the analytical and simulated magnitude distributions, -6 dB contours were used (Fig. A5). In the array's view in direction Y, the analytical results show isolated contours near the source surface, whereas for the simulated results, contours only exist beyond 10 mm from the array. For the simulated view contours

along X, slight signs of asymmetry about the axis can be observed between 15 and 30 mm away from the array axially. As the simulation was created based on a reconstructed array of 0.5 mm grids (Fig. A1 (c)), the strict X direction symmetry was sacrificed to maintain the overall size and geometry of the array, eliciting the asymmetry.

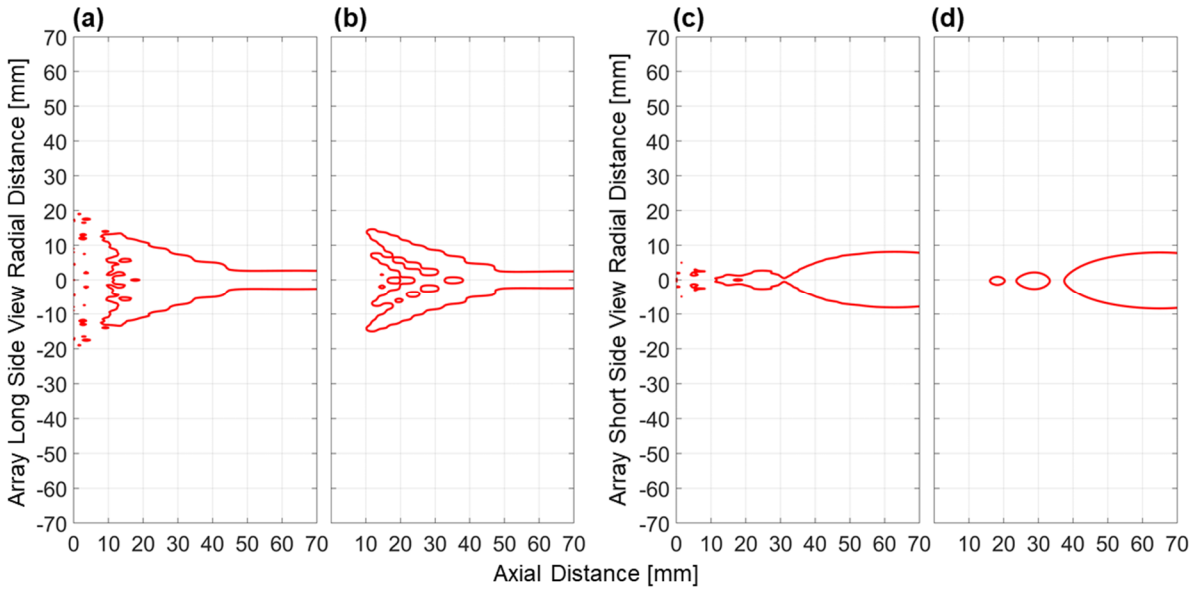

Fig. A5: Pressure magnitude –6 dB contour comparison. The array is targeting 60 mm on the axis. **(a**) Array view along X analytical result. Notice the isolated contours near the source (axial distance = 0). **(b)** Array view along X of the simulation. Notice the slight asymmetry radially in the contour in the axial range of 15 ~ 30 mm. **(c)** Array view along Y analytical result. Notice the isolated contours near the source (axial distance = 0). **(d)** Array view along Y of the simulation. The contour is smaller than that of the analytical result in this view.

The impact of this digitisation artefact was studied by steering radially to a focal point off-axis on both sides (60 mm from the array (L_1 = 60 mm), ±10 mm off the axis; Fig. A6). As before, the phase maps show a flat wave front at 60 mm on axis in both cases, suggesting a 60 mm geometric focus. Similarly, the pressure maximum occurs 5 mm before the geometric focus in both cases at the exact symmetric locations about the axis, suggesting no position differences from artificial asymmetry. However, the +10 mm off-axis target case shows a 3% higher pressure magnitude compared to its reflection, likely due to the larger number of active grids on that side of the array. When steering further off-axis, this difference in pressure magnitude

is amplified. At ±25 mm off axis (L_1 = 60 mm), a 7% difference is observed, whereas at ±40 mm off axis (L_1 = 60 mm), a 9% difference is observed.

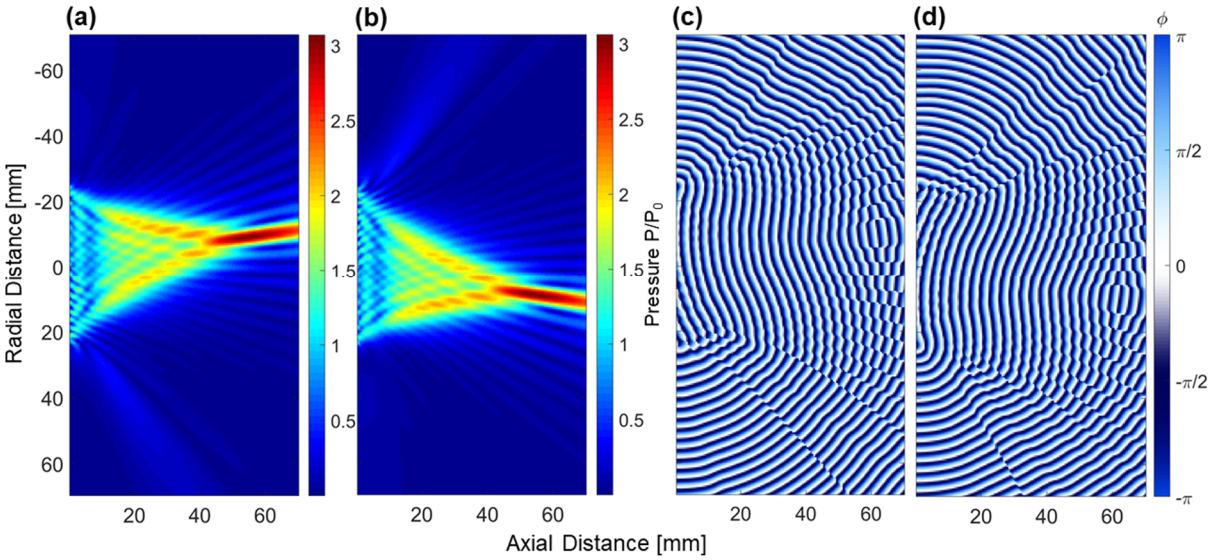

Fig. A6: Array steering k-Wave simulations. The target points are 60 mm away from the source and –10 mm and +10 mm off axis, respectively. All results shown are from k-Wave simulations. **(a), (b)** Magnitude maps for targeting –10 mm off axis and +10 mm off axis, respectively. **(c), (d)** Phase maps for targeting –10 mm off axis and +10 mm off axis, respectively.

In evaluating the overall steering capability across both radial axes of the array, a 2D field was populated with pressure magnitudes corresponding to the pressure when the point was selected as the focal point using the analytical method (Fig. A7 (a)). The maximal pressure achievable by steered focusing of the array is restricted by the contour of value $2P_0$, representing the maximum pressure a piston ultrasound transducer can achieve in free field. The highest focal pressure gain of about $3P_0$ occurs around the region with little or no steering. In outer positions with pressure gain at target below $2P_0$, the steering off-focus became too large to justify the insufficient focal gain, with the lowest pressure gain at $1.5P_0$. The phase plane (Fig. A7 (b)) similarly shows a large region of slow phase variation around the array centre with minimal steering. Taken together, focus steering should be avoided unless necessary.

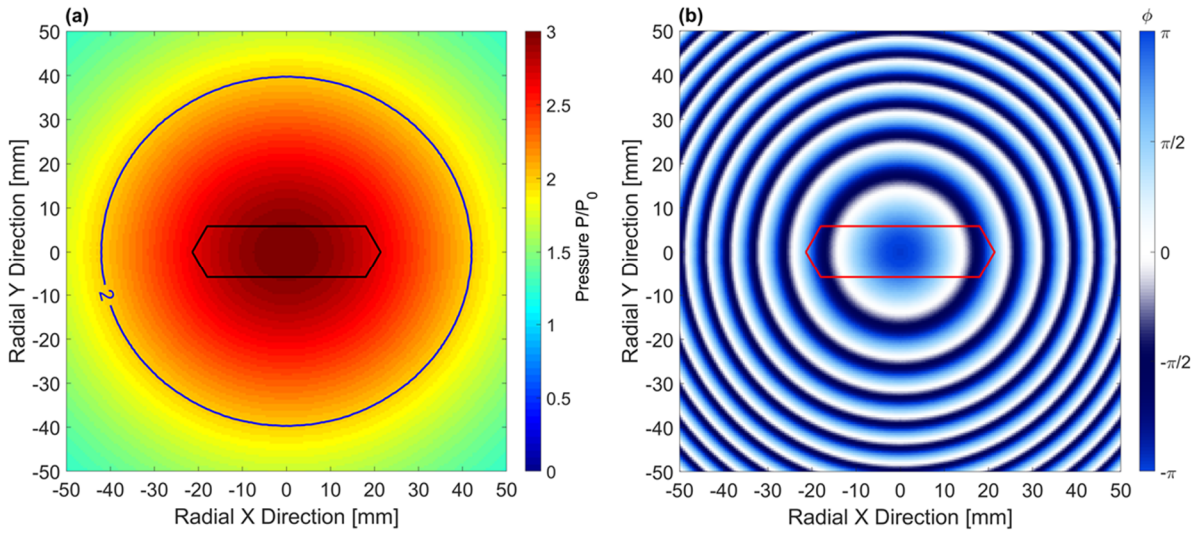

Fig. A7: Array focus steering capability. The analytical method populates a 2D plane 60 mm away from the source, with each point in the plane possessing the pressure magnitude and phase when this point is the target of focusing by the array. The radial X direction is the longer side of the array. The radial Y direction is the shorter side of the array. **(a)** Map of pressure gain. The black hexagon shows the outline of the array and its placement relative to the plane 60 mm into the page. The blue contour shows the $2P_0$ boundary. Pressure lower than that demonstrates the array's focusing ability is weaker than what a piston can achieve. This contour is an ellipse that is wider in the radial X direction. **(b)** Map of phase. The red hexagon shows the outline of the array and its placement relative to the plane 60 mm into the page.

Although this particular array has a total ultrasound driving area too small to be effective for targeting deep brain targets in humans, the analytical array modelling tool (Hutchins et al., 1986; Liauh and Lin, 1999) and array simulation tool (Treeby and Cox, 2011; Treeby et al., 2012) developed for this array arrangement could be converted to examine multi-element ultrasound devices for their effectiveness.

B. AUDITORY FINDINGS

This is a brief investigation of the auditory findings in the previous human trial (Blackmore, 2018; Braun et al., 2020). The setup is replicated from the previous trials and is shown in Fig. B1. The test was done using a 500 kHz, 64 mm diameter transducer (H-107, Sonic Concepts Inc., Bothell, WA, USA) and a flexible polyurethane membrane from a shock wave source (MINILITH SL1, Storz Medical, Tägerwilen, Switzerland). This coupling membrane was fixed to the transducer edges using a custom mount with an O-ring seal, creating a coupling cone that was filled with deionised and degassed water.

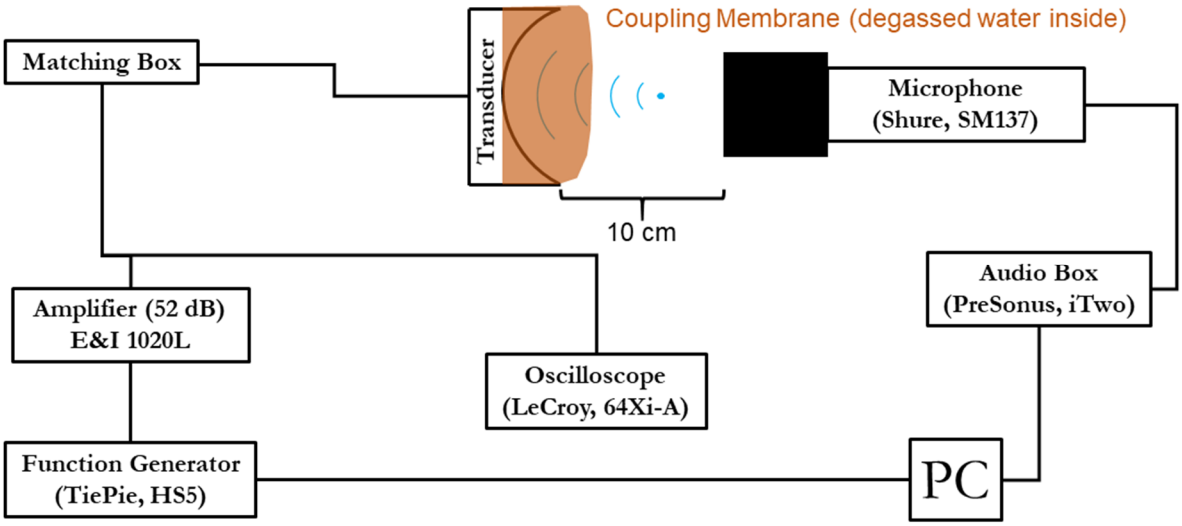

Fig. B1: Experiment setup. The transducer was placed in a polyurethane membrane filled with deionised and degassed water. A matching box for the transducer was in place after the amplifier was monitored by the oscilloscope. The function generator provides the ultrasound pulsing sequence. A microphone and an audio box were used to take the measurements. The recordings were saved on the computer.

A USB function generator (HS5, TiePie, WL Sneck, The Netherlands) was used to send out the pulsing sequences, which were amplified by a 52 dB amplifier (1020L, E&I, Rochester, NY, USA) and then applied to a matching box that was connected to the transducer. An oscilloscope (64Xi-A, Teledyne LeCroy, Chestnut Ridge, NY, USA) was used to monitor the signal being sent towards the transducer. The transducer and its coupling cone were filled with

deionised and degassed water. A microphone (SM-137, Shure, Chicago, IL, USA) was placed in front of the transducer 10 cm away, taking the audio signal. The transducer (with the coupling) and the microphone were both placed in the air. The signal was saved on the computer via an audio box (iTwo, PreSonus, Baton Rouge, LA, USA). The computer controls the start and end of both the function generator and the audio recording loop.

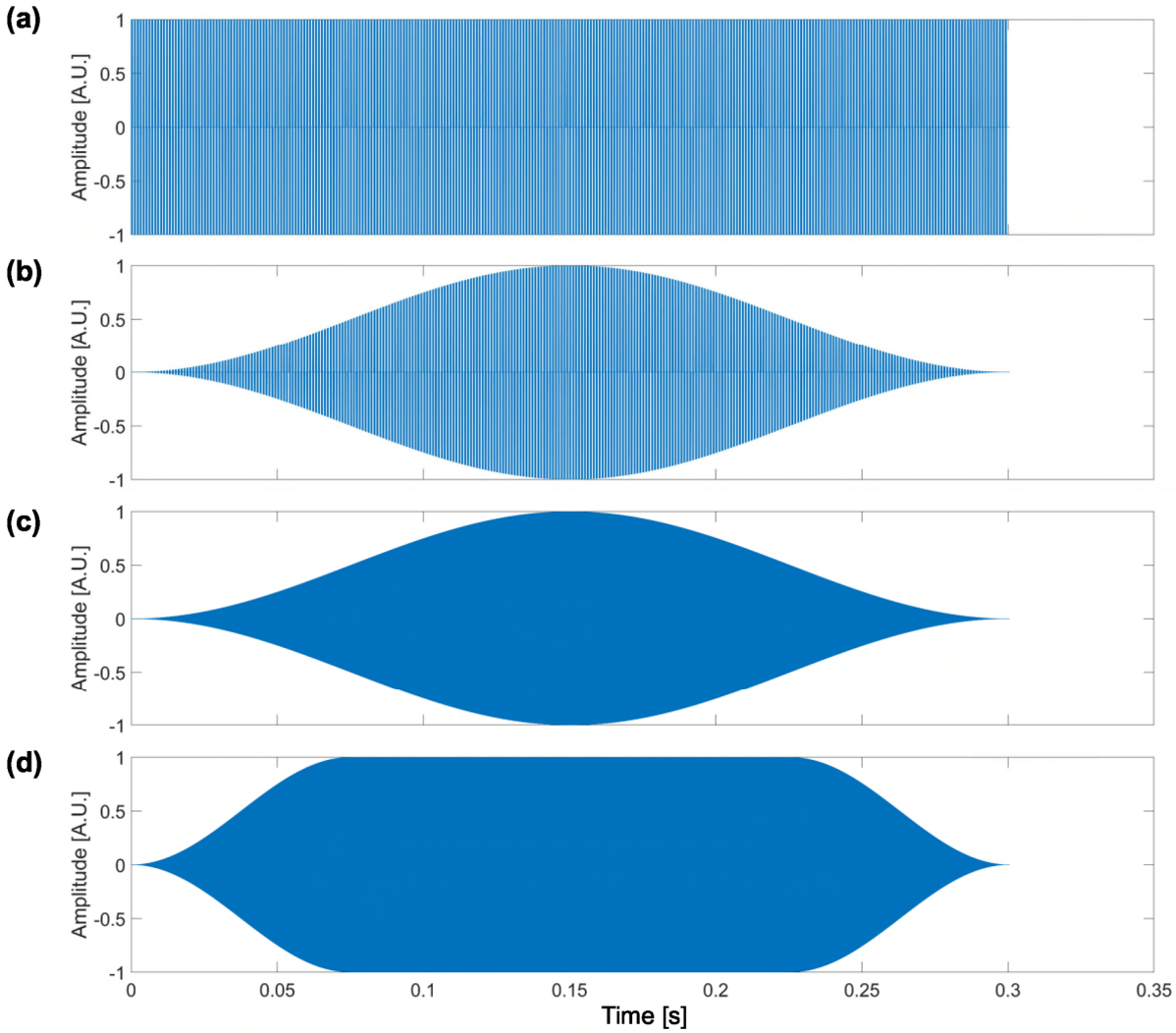

Fig. B2: Burst Examples. Four types of bursts are shown here. **(a)** Pulsed wave Boxcar windowed (R = 0) burst. **(b)** Pulsed wave Hann windowed (R = 1) burst. **(c)** Continuous wave Hann windowed (R = 1) burst. (d) Continuous wave Tukey windowed (R = 0.5) burst.

It was found that the PRF of 1 kHz used in each burst in the previous human trial was audible by the subjects in the trial. The voltage delivered to the transducer was 197.4 V_{pp}. In addition, the burst repetition frequency used (0.37 Hz) was below the 20 Hz lower bound of the human

hearing range. Therefore, this brief test focused on different pulsing settings inside each burst. Fig. B2 is an illustration of several forms of burst used in this test. Boxcar (R = 0) and Hann (R = 1) windows were applied to pulsed waves of various PRFs. Hann and Tukey windows of R = 0.5 were applied to the continuous wave cases. Different voltages were tested for these pulsing sequences. For all cases of continuous waves, no signal was detected in the audible frequency range compared to the background control, where no ultrasound was sent out by the transducer. The signal is cut off above 20 kHz, which is the upper bound of the human hearing range.

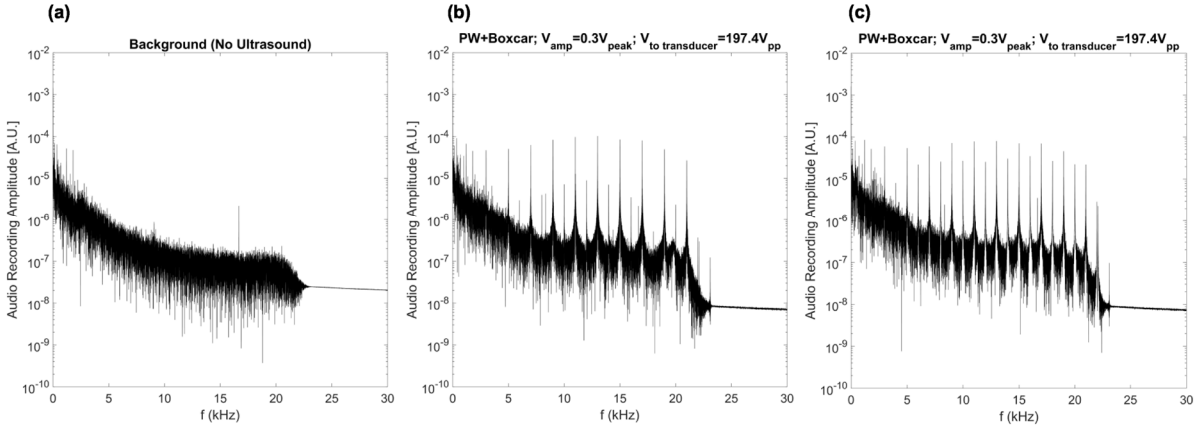

Fig. B3: Audio recording comparison. Examples of the frequency spectrum of the audio signal recorded. **(a)** Frequency spectrum of the background when ultrasound is off. **(b)** Frequency spectrum of pulsed wave (PW) with Boxcar window when the coupling is filled with degassed water. **(c)** Frequency spectrum of pulsed wave (PW) with Boxcar window when the coupling is filled with not degassed water.

All cases using continuous waves resulted in the same signal as this background, regardless of the settings of windowing types and transducer voltages. The frequency spectrum in Fig. B3 (a) is the background noise when the ultrasound is off. This shows some spikes in the audible frequency range in the background. Fig. B3 (b) shows an example where the transducer was sending out a pulsed wave with a Boxcar window (PW + Boxcar) at a PRF of 1 kHz. Peaks were clearly visible at odd harmonics of 1 kHz at 5 kHz, 7 kHz, etc. Peaks at 1 kHz and 3 kHz

were also observed as expected when zoomed in on the 0 to 5 kHz range, despite the higher magnitude of background noise.

Fig. B3 (b) shows the recorded audio signal when the coupling cone was filled with degassed water. With the other conditions kept the same, changing the water from degassed water (Fig. B3 (b)) to not degassed water (Fig. B3 (c)) resulted in an increase in the magnitude of the even harmonics of PRF of 1 kHz. The magnitude of odd harmonics in both cases was comparable. The change in magnitude indicates that bubbles inside the water were likely the source of the even harmonic signals.

At the same voltage to the transducer, the Hann windowed pulse wave generated a lower magnitude of harmonic peaks in the audible range compared to the Boxcar windowed pulse wave. In both cases, lowering the voltage to the transducer reduces the magnitude of the harmonics. When the voltage to the transducer is lower than 20 V_{pp}, the harmonic peaks can no longer be distinguished from the background. This is equivalent to a pressure of less than 0.15 MPa generated at the focus in the free field of water.

Finally, in addition to bursts using a PRF of 1 kHz, bursts using other PRF values were also tested. Fig. B4 shows the cases using pulsed waves with the Boxcar window. The induced harmonics are observed in the audible frequency range, and they clearly follow the set PRF values for all four PRF cases. This confirms that the main source of the audible signal in transcranial ultrasound neuromodulation is the pulsing sequence. The ultrasound signal conducts through the skull's bone structure and reaches the ear. If the frequency of the pulsing sequence is within the audible range, the stimulation is highly likely to be picked up by the subject's hearing system.

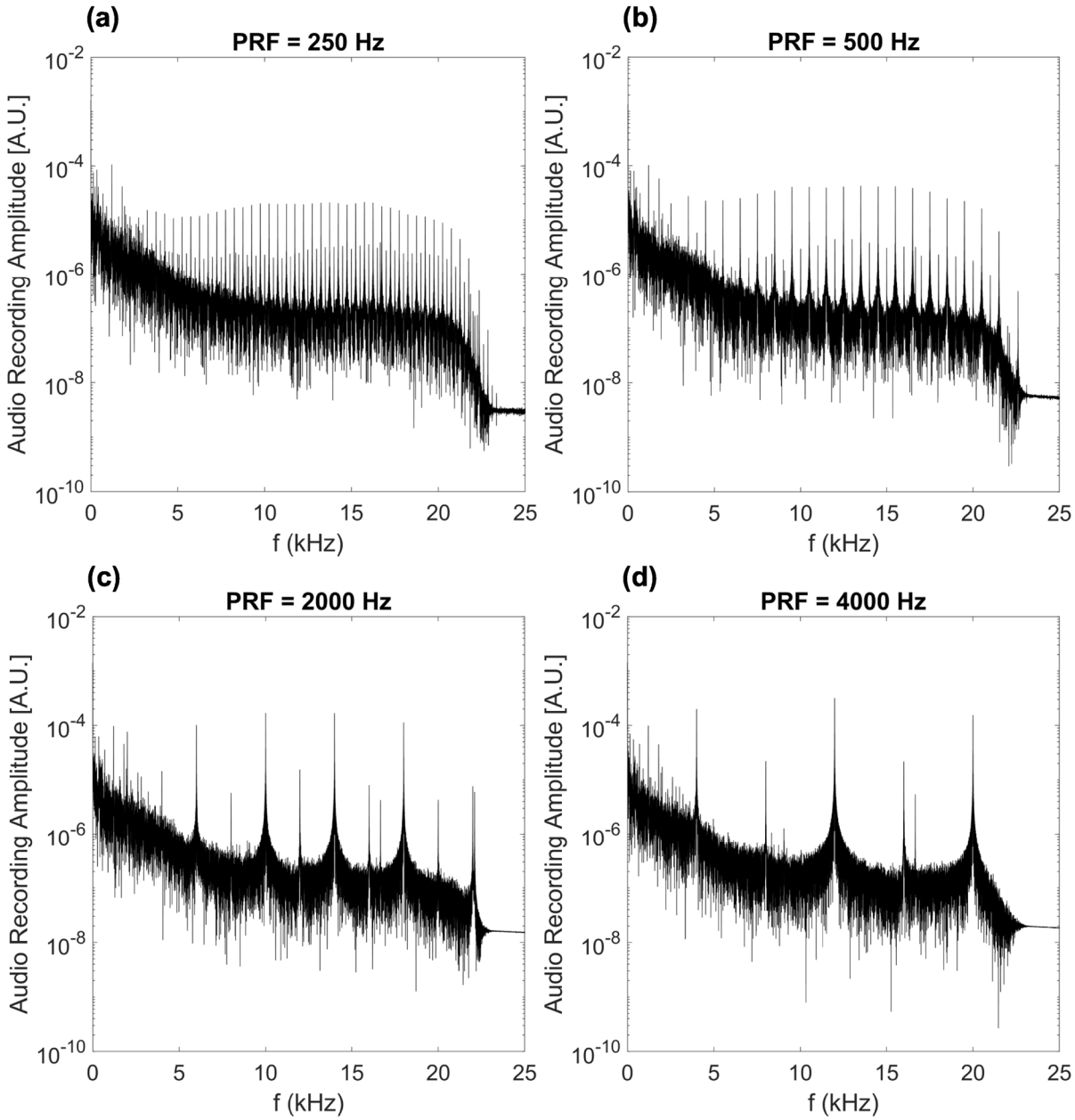

Fig. B4: Testing different PRF values. 4 additional PRF values were used in the pulsed wave Boxcar windowed bursts. **(a)** Audio signal of a burst with a PRF of 250 Hz. **(b)** Audio signal of a burst with a PRF of 500 Hz. **(c)** Audio signal of a burst with a PRF of 2000 Hz. **(d)** Audio signal of a burst with a PRF of 4000 Hz.

This investigation used a microphone to show that the audible signal is a result of a specific ultrasound pulsing sequence. When frequencies within the hearing range are used, audio masks must be applied to the trial subject to conceal the ultrasound bursts for reliable behavioural outcomes.

C. TRANSDUCER COUPLING IN HUMAN TRIAL

In the simulations, the participant's head was submerged in water. To ensure continuous water coupling from the transducer to the surface of the head in human trials, a coupling cone is developed and tested as shown in Fig. C1.

The coupling cone is made watertight and deformable using polyurethane rubber. Polyurethane rubber has a speed of sound of 1397.9 m/s, a density of 1016 kg/m^3, and an acoustic attenuation of 1.42 dB/cm at 500 kHz (Cafarelli et al., 2016; Mott et al., 2002). It has a similar acoustic impedance to water.

This coupling cone has a diameter of 160 mm, which is approximately twice the size of the transducer's outer diameter. This size is picked to fit the parts for fixing the lens to the flat transducer surface inside the water chamber. A circular design allows for the creation of a watertight chamber using O-rings. The coupling cone is filled with degassed water by syringe injection, and air is allowed to escape from the outlet. At the end of the filling process, there is a small amount of residual air trapped in the cone. As the cone is larger, the trapped air is moved to regions not on the ultrasound pathway through gravity and agitation. This mitigates any unwanted artefacts from the air. The large cone also provides a large contact area with the subject, helping with ultrasound transmission.

A Fresnel PDMS lens focusing at 85 mm was used to test the coupling cone. Firstly, the hydrophone was moved relative to the coupling cone mounted with the lens and transducer. The focal peak at 85 mm was located, and then the hydrophone was fixed to the coupling cone

setup at this location. In this arrangement, the hydrophone was always measuring the focal peak.

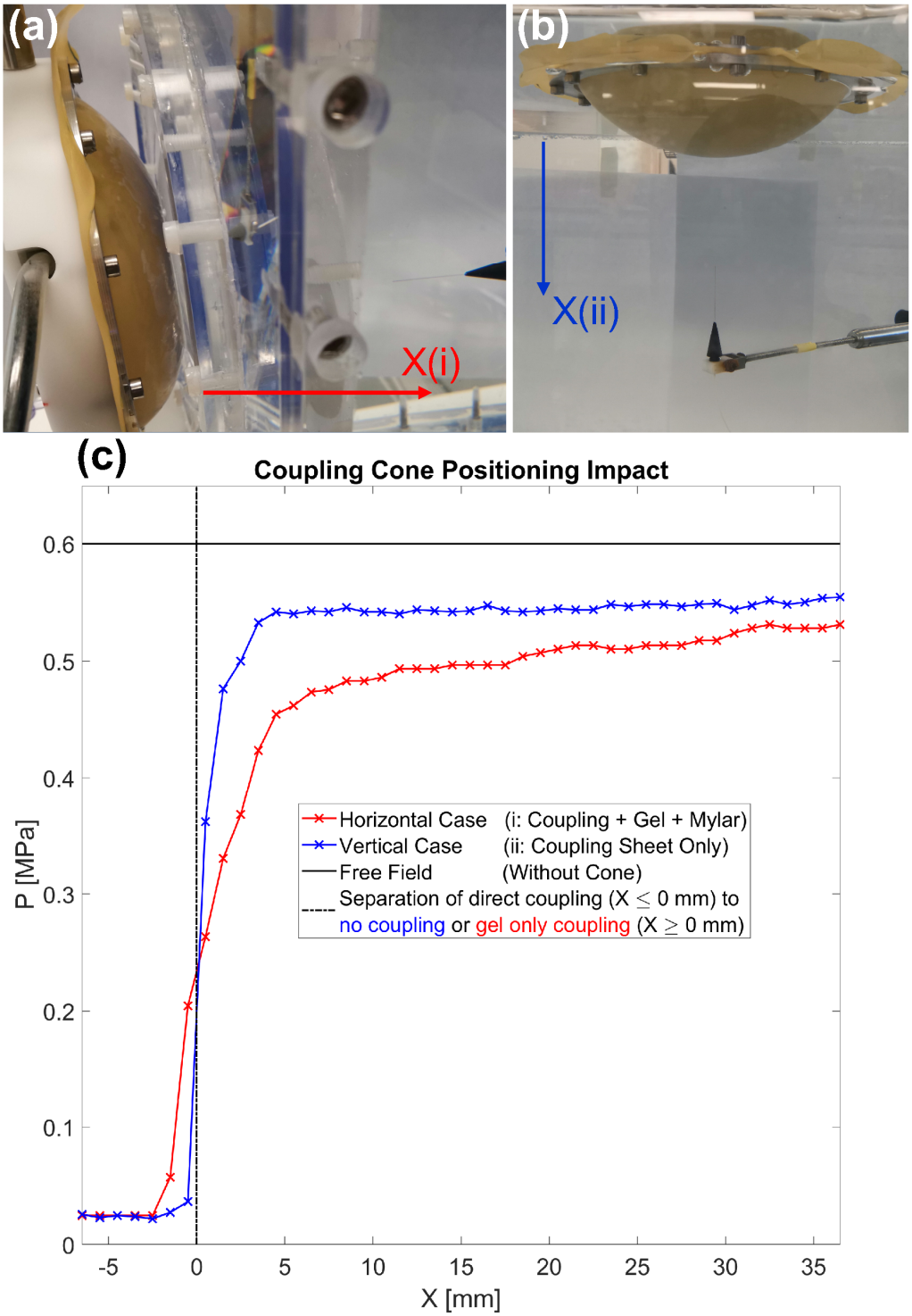

Fig. C1. Testing coupling cone designed for human trial. (a) Arrangement firing ultrasound through the side polyester of the water tank. **(b)** Arrangement firing ultrasound through the top of the water surface. **(c)** Focal peak pressure measured at different coupling depths for the two arrangements. The vertical black dashed line indicates no direct coupling on the negative side (left). The 0.6 MPa was created at the focal peak in the free field.

Two arrangements were tested: (i) the coupling cone can move horizontally and fire into the water tank through a polyester film (Mylar, UKI, Lancashire, UK) as shown in Fig. C1 (a); and (ii) the coupling cone can move vertically and fire into the water above the water surface as shown in Fig. C1 (b).

The arrangement (i) on the side of the water tank mimics the situation in human trials where the transducer targets the brain through the temporal bones on the side of the head. However, to test this arrangement, a polyester sheet had to be used to contain the water inside the tank. In addition, ultrasound gel was used to exclude air from the contact area. To test the case without the polyester film, a water surface was used with the transducer moving vertically (arrangement (ii)). The coupling cone was in direct contact with water in this arrangement.

The measured focal peak pressure at different coupling depths is shown in Fig. C1 (c) for both arrangements. The horizontal axis (X) represents the distance between the transducer and the medium surface (the Mylar sheet on the tank wall in (i) and the water in (ii)). A correction equal to the height of the cone was applied so that X = 0 represents the decoupling of the cone from the surface. A positive X shows that the cone is in direct contact with the surface, and a negative X shows that the cone is not in contact with the surface. An increasing X represents that the transducer is closer to the medium surface, and a larger surface area of the cone is in contact with the surface.

The transducer and the lens created 0.6 MPa at the focal peak in free field. At the largest possible contact area at X = 36.5 mm, the measured focal peak pressure is 0.53 MPa (-11.5%) for the arrangement (i) and 0.55 MPa (-7.6%) for the arrangement (ii). The coupling membrane

was completely immersed, as shown in Fig. C1 (b). The added polyester sheet and ultrasound gel in (i) caused a 4% decrease in pressure compared to (ii).

With the coupling cone moving away (X decreasing), the contact area between the cone and the surface was reduced, reducing the measured focal peak pressure. The difference in loss in pressure for $X > 5$ mm between (i) and (ii) was more likely due to bubbles in ultrasound gel than the polyester sheet. For $X \leq 5$ mm and in (i), the pressure loss starts earlier due to imperfect coupling between the transducer, Mylar sheet, ultrasound gel, and the tank wall. For arrangement (ii), the pressure is maintained until closer to the limit of direct coupling.

In (i), at $X = 0$ mm, even though the cone was not in contact with the wall surface, ultrasound pressure is measured at the peak due to the existing ultrasound gel keeping the last bit of contact. For $X \leq -2$ mm, the measured pressure was negligible for both arrangements. In (ii), at $X = 0$ mm, the pressure changes to negligible, as expected.

This analysis has tested the designed coupling cone, which is necessary in the human trial. By mimicking the human trial, the position of the transducer and the additional polyurethane rubber further reduce the ultrasound pressure by about 10% compared to the free field. This acts as additional safety insurance for the human participants.

References

V. F. Antonov, E. V. Shevchenko, E. T. Kozhomkulov, A. A. Mol'nar and E. Y. Smirnova, "Capacitive and ionic currents in BLM from phosphatidic acid in Ca2+-induced phase transition," *Biochem. Biophys. Res. Coms.*, vol. 133, no. 3, pp. 1098-1103, 1985.

D. Armani, C. Liu and N. Aluru, "Re-configurable fluid circuits by PDMS elastomer micromachining," in *Proc. IEEE 12th Annu. Int. Conf. Microelectromech. Syst.*, Jan. 1999, pp. 222-227.

J. F. Aubry, M. Tanter, M. Pernot, J. L. Thomas and M. Fink, "Experimental demonstration of noninvasive transskull adaptive focusing based on prior computed tomography scans," *J. Acoust. Soc. Am.*, vol. 113, no. 1, pp. 84-93, 2003.

J. F. Aubry, O. Bates, C. Boehm, K. B. Pauly, D. Christensen, C. Cueto, P. Gélat, L. Guasch, J. Jaros, Y. Jing, R. Jones, N. Li, P. Marty, H. Montanaro, E. Neufeld, S. Pichardo, G. Pinton, A. Pulkkinen, A. Stanziola, A. Thielscher, B. Treeby and E. van't Wout, "Benchmark problems for transcranial ultrasound simulation: Intercomparison of compressional wave models," *J. Acoust. Soc. Am.*, vol. 152, no. 2, 2022, Art. no. 1003. doi: 10.1121/10.0013426.

M. R. Bachtold, P. C. Rinaldi, J. P. Jones, F. Reines and L. R. Price, "Focused ultrasound modifications of neural circuit activity in a mammalian brain," *Ultrasound Med. Biol.*, vol. 24, no. 4, pp. 557-565, 1998.

B. W. Badran, K. A. Caulfield, S. Stomberg-Firestei, P. M. Summers, L. T. Dowdle, M. Savoca, X. Li, C. W. Austelle, E. B. Short, J. J. Borckardt, N. Spivak, A. Bystritsky and M. S. George, "Sonication of the anterior thalamus with MRI-Guided transcranial focused ultrasound (tFUS) alters pain thresholds in healthy adults: A double-blind, sham-controlled study," *Brain Stimul.*, vol. 13, no. 6, pp. 1805-1812, 2020.

R. Bailey, "Hippocampus and memory," 2019. [Online]. Available: http://www.thoughtco.com/hippocampus-anatomy-373221, Accessed on: Oct. 13, 2019.

T. W. Barber, J. A. Brockway and L. S. Higgins, "The density of tissues in and about the head," *Acta. Neurol. Scand.*, vol. 46, no. 1, pp. 85-92, 1970.

J. Blackmore, "Focused ultrasound: A non-invasive brain stimulation modality," PhD thesis, University of Oxford, 2018. Accessed on: Oct. 10, 2019. [Online]. Available: https://ora.ox.ac.uk/objects/uuid:c68151a2-335d-45ca-be88-7e34c6a5a6f8

J. Blackmore, S. Shrivastava, J. Sallet, C. R. Butler and R. O. Cleveland, "Ultrasound neuromodulation: A review of results, mechanisms and safety," *Ultrasound in Med. & Biol.*, vol. 45, no. 7, pp. 1509-1536, 2019.

D. T. Blackstock, *Fundamentals of Physical Acoustics*. Hoboken, NJ, USA: Wiley, 2000.

P. E. Bloomfield, W. J. Lo and P. A. Lewin, "Experimental study of the acoustical properties of polymers utilized to construct PVDF ultrasonic transducers and the acousto-electric properties of PVDF and P(VDF/TrFE) films," *IEEE Trans. Ultrason. Ferroelectr. Freq. Control*, vol. 47, no. 6, pp. 1397-1405, 2000.

A. Bongioanni, D. Folloni, L. Verhagen, J. Sallet, M. C. Klein-Flügge and M. F. S. Rushworth, "Activation and disruption of a neural mechanism for novel choice in monkeys," *Nature*, vol. 591, no. 1, pp. 270-274, 2021.

V. Braun, J. Blackmore, R. O. Cleveland and C. R. Butler, "Transcranial ultrasound stimulation in humans is associated with an auditory confound that can be effectively masked," *Brain Stimul.*, vol. 13, no. 6, pp. 1526-1534, 2020.

S. T. Brinker, F. Preiswerk, N. J. McDannold, K. L. Parker and T. Y. Mariano, "Virtual brain projection for evaluating trans-skull beam behavior of transcranial ultrasound devices," *Ultrasound Med. Biol.*, vol. 45, no. 7, pp. 1850-1856, 2019.

S. T. Brinker, F. Preiswerk, P. J. White, T. Y. Mariano, N. J. McDannold and E. J. Bubrick, "Focused ultrasound platform for investigating therapeutic neuromodulation across the human hippocampus," *Ultrasound in Med. & Biol.*, vol. 46, no. 5, pp. 1270-1274, 2020.

S. G. Brohawn, "How ion channels sense mechanical force: Insights from mechanosensitive K2P channels TRAAK, TREK1, and TREK2," *Ann. N. Y. Acad. Sci.*, vol. 1352, no. 1, pp. 20-32, 2015.

M. M. Burlew, E. L. Madsen, J. A. Zagzebski, R. A. Banjavic, and S. W. Sum, ''A new ultrasound tissue-equivalent material,'' *Rad. Phys*., vol. 134, no. 2, pp. 517-520, 1980.

C. R. Butler, E. Rhodes, J. Blackmore, X. Cheng, R. L. Peach, M. Veldsman, F. Sheerin and R. O. Cleveland, "Transcranial ultrasound stimulation to human middle temporal complex improves visual motion detection and modulates electrophysiological responses," *Brain Stimul.*, vol. 15, no. 5, pp. 1236-1245, 2022.

A. Cafarelli, P. Miloro, A. Verbeni, M. Carbone and A. Menciassi, "Speed of sound in rubber based materials for ultrasonic phantoms," *J. Ultrasound*, vol. 19, no. 4, pp. 251-256, 2016.

A. Cafarelli, A. Verbeni, A. Poliziani, P. Dario, A. Menciassi and L. Ricotti, “Tuning acoustic and mechanical properties of materials for ultrasound phantoms and smart substrates for cell cultures,” *Acta. Biomater.*, vol. 49, no. 1, pp. 368-378, 2017.

S. C. Chan, M. Mina, S. S. Udpa, W. Lord, L. Udpa and T. Xue, *Finite element modeling of binary acoustic fresnel lenses*. In: Thompson D.O., Chimenti D.E. (eds) *Review of progress in quantitative nondestructive evaluation*. Boston, MA, USA: Springer, 1995.

D. Chauvet, L. Marsac, M. Pernot, A. L. Boch, R. Guillevin, N. Salameh, L. Souris, L. Darrasse, M. Fink, M. Tanter and J. F. Aubry, “Targeting accuracy of transcranial magnetic resonance-guided high-intensity focused ultrasound brain therapy: A fresh cadaver model,” *J. Neurosurg.*, vol. 118, no. 5, pp. 1046-1052, 2013.

K. S. Chen and R. Chen, “Invasive and noninvasive brain stimulation in Parkinson's disease: Clinical effects and future perspectives,” *Clin. Pharmacol. Ther.*, vol. 106, no. 4, pp. 763-775, 2019.

M. Chen, C. Peng, H. Wu, C.-C. Huang, T. Kim, Z. Traylor, M. Muller, P. Y. Chhatbar, C. S. Nam, W. Feng and X. Jiang, “Numerical and experimental evaluation of low-intensity transcranial focused ultrasound wave propagation using human skulls for brain neuromodulation,” *Med. Phys.*, vol. 50, no. 1, pp. 38-39, 2023.

X. Chen, K. Q. Schwarz and K. J. Parker, “Radiation pattern of a focused transducer: A numerically convergent solution,” *J. Acoust. Soc. Am.*, vol. 94, no. 5, pp. 2979-2991, 1993.

S. Chen, M. Fatemi, R. Kinnick and J. F. Greenleaf, “Comparison of stress field forming methods for vibro-acoustography,” *IEEE Trans. Ultrason. Ferroelectr. Freq. Control.*, vol. 51, no. 3, pp. 313-321, 2004.

H. Choi, J. J. Jeong and J. Kim, “Development of an estimation instrument of acoustic lens properties for medical ultrasound transducers,” *J. Healthc. Eng.*, vol. 2017, no. 1, 2017, Art. no. 6580217.

J. B. Choi, S. H. Lim, K. W. Cho, D. H. Kim, D. P. Jang and I. Y. Kim, “The effect of focused ultrasonic stimulation on the activity of hippocampal neurons in multi-channel electrode,” in *Proc. IEEE/EMBS 6th Int. Conf. on Neural Eng. (NER)*, Nov. 2013, pp. 731-734.

C. C. Church, C. Labuda and K. Nightingale, “A theoretical study of inertial cavitation from acoustic radiation force impulse (ARFI) imaging and implications for the mechanical index,” *Ultrasound Med. Biol.*, vol. 41, no. 2, pp. 472-485, 2015.

J. R. T. Collin, “Detection and interpretation of thermally relevant cavitation during HIFU exposure,” PhD thesis, University of Oxford, 2009. Accessed on: Jul. 28, 2021. [Online]. Available: https://ethos.bl.uk/OrderDetails.do?uin=uk.bl.ethos.526574

C. Constans, T. Deffieux, P. Pouget, M. Tanter and J. F. Aubry, “A 200-1380-kHz quadrifrequency focused ultrasound transducer for neurostimulation in rodents and primates: Transcranial *in vitro* calibration and numerical study of the influence of skull cavity,*” IEEE Trans. Ultrason. Ferroelectr. Freq. Control*, vol. 64, no. 4, pp. 717-724, 2017.

C. Constans, P. Mateo, M. Tanter and J. F. Aubry, “Potential impact of thermal effects during ultrasonic neurostimulation: Retrospective numerical estimation of temperature elevation in seven rodent setups,” *Phys. Med. Biol.*, vol. 63, no. 2, pp. 25003-25014, 2018.

B. T. Cox, S. Kara, S. R. Arridge and P. C. Beard, “K-space propagation models for acoustically heterogeneous media: Application to biomedical photoacoustics,” *J. Acoust. Soc. Am.*, vol. 121, no. 6, pp. 3453-3464, 2007.

R. F. Dallapiazza, K. F. Timbie, S. Holmsberg, J. Gatesman, M. B. Lopes, R. J. Price, G. W. Miller and W. J. Elias, “Noninvasive neuromodulation and thalamic mapping with low-intensity focused ultrasound,” *J. Neurosurg.*, vol.128, no. 3, pp. 875-884, 2018.

G. Darmani, T. O. Bergmann, K. B. Pauly, C. F. Caskey, L. de Lecea, A. Fomenko, E. Fouragnan, W. Legon, K. R. Murphy, T. Nandi, M. A. Phipps, G. Pinton, H. Ramezanpour, J. Sallet, S. N. Yaakub, S. S. Yoo and R. Chen, “Non-invasive transcranial ultrasound stimulation for neuromodulation,” *Clin. Neurophysiol.*, vol. 135, no. 1, pp. 51-73, 2022.

F. Darvas, E. Mehić, C. J. Caler, J. G. Ojemann and P. D. Mourad, “Toward deep brain monitoring with superficial EEG sensors plus neuromodulatory focused ultrasound,” *Ultrasound Med. Biol.*, vol. 42, no. 8, pp. 1834-1847, 2016.

T. Deffieux, Y. Younan, N. Wattiez, M. Tanter, P. Pouget and J.-F. Aubry, “Low-intensity focused ultrasound modulates monkey visuomotor behaviour,” *Curr. Biol.*, vol. 23, no. 23, pp. 2430-2433, 2013.

Z. D. Deng, S. H. Lisanby and A. V. Peterchev, “Electric field depth–focality tradeoff in transcranial magnetic stimulation: Simulation comparison of 50 coil designs,” *Brain Stimul.*, vol. 6, no. 1, pp. 1-13, 2013.

C. Destrieux, D. Bourry and S. Velut, “Surgical anatomy of the hippocampus,” *Neurochirurgie.*, vol. 59, no. 5, pp. 149-158, 2013.

A. Dhar, K. Girdhar, D. Singh, H. Gelman, S. Ebbinghaus and M. Gruebele, “Protein stability and folding kinetics in the nucleus and endoplasmic reticulum of eucaryotic cells,” *Biophys. J.*, vol. 101. No. 2, pp. 421-430, 2011.

M. E. Downs, S. A. Lee, G. Yang, S. Kim, Q. Wang and E. E. Konofagou, “Noninvasive peripheral nerve stimulation via focused ultrasound *in vivo*,” *Phys. Med. Biol.*, vol. 63, no. 3, pp. 50-60, 2018.

F. A. Duck, *Physical Properties of Tissue: A Comprehensive Reference Book*. London, England, UK: Academic, 1990.

F. A. Duck, “Medical and non-medical protection standards for ultrasound and infrasound,” *Prog. Biophys. Mol. Biol.*, vol. 93, no. 3, pp. 176-191, 2007.

F. A. Duck, “Hazards, risks and safety of diagnostic ultrasound,” *Med. Eng. Phys.*, vol. 30, no. 10, pp. 1338-1348, 2008.

H. M. Duvernoy, *The human hippocampus: Functional anatomy, vascularization and serial sections with MRI*. Berlin, Germany: Springer-Verlag, 2005.

M. D. Eames, A. Hananel, J. W. Snell, N. F. Kassell and J. F. Aubry, “Trans-cranial focused ultrasound without hair shaving: Feasibility study in an *ex vivo* cadaver model,” *J. Ther. Ultrasound*, vol. 1, no. 24, pp. 1-6, 2014.

M. S. Fanselow and H. W. Dong, “Are the dorsal and ventral hippocampus functionally distinct structures?,” *Neuron*, vol. 65, no. 1, pp. 7-19, 2010.

P. Faria, M. Hallett and P. C. Miranda, “A finite element analysis of the effect of electrode area and inter-electrode distance on the spatial distribution of the current density in tDCS,” *J. Neural. Eng.*, vol. 8, no. 6, pp. 1-24, 2012.

M. Fatemi and J. F. Greenleaf, “Vibro-acoustography: An imaging modality based on ultrasound-stimulated acoustic emission,” *Proc. Natl. Acad. Sci. U. S. A.*, vol. 96, no. 12, pp. 6603-6608, 1999.

M. Ferri, J. M. Bravo, J. Redondo, S. Jiménez-Gambín, N. Jiménez, F. Camarena and J. V. Sánchez-Pérez, “On the evaluation of the suitability of the materials used to 3D print holographic acoustic lenses to correct transcranial focused ultrasound aberrations,” *Polymers (Basel)*, vol. 11, no. 9, pp. 1521-1545, 2019.

M. Fini and W. J. Tyler, “Transcranial focused ultrasound alters conflict and emotional processing, physiology, and performance I: Dorsal anterior cingulate cortex targeting,” *medRxiv*, 2020a. doi: 10.1101/2020.11.25.20234401

M. Fini and W. J. Tyler, “Transcranial focused ultrasound alters conflict and emotional processing, physiology, and performance II: Right anterior insula/frontal operculum targeting,” *PsyArXiv*, 2020b. doi: 10.31234/osf.io/qgx5d

M. Fink, G. Montaldo and M. Tanter, “Time-reversal acoustics in biomedical engineering,” *Annu. Rev. Biomed. Eng.*, vol. 5, no. 1, pp. 465-497, 2003.

D. Folloni, L. Verhagen, R. B. Mars, E. Fouragnan, C. Constans, J.-F. Aubry, M. F. S. Rushworth and J. Sallet, “Manipulation of subcortical and deep cortical activity in the primate brain using transcranial focused ultrasound stimulation,” *Neuron*, vol. 101, no. 6, pp. 1109-1116, 2019.

E. F. Fouragnan, B. K. H. Chau, D. Folloni, N. Kolling, L. Verhagen, M. C. Klein-Flügge, L. Tankelevitch, G. K. Papageorgiou, J.-F. Aubry, J. Sallet and M. F. S. Rushworth, “The macaque anterior cingulate cortex translates counterfactual choice value into actual behavioral change,” *Nat. Neurosci.*, vol. 22, no. 5, pp. 797-808, 2019.

F. E. Fox, K. F. Herzfeld and G. D. Rock, “The effect of ultrasonic waves on the conductivity of salt solutions,” *Phys. Rev.*, vol. 70, no. 5-6, pp. 329-330, 1946.

F. J. Fry and J. E. Barger, “Acoustical properties of the human skull,” *J. Acoust. Soc. Am.*, vol. 63, no. 5, pp. 1576-1590, 1978.

W. J. Fry and R. B. Fry, “Determination of absolute sound levels and acoustic absorption coefficients by thermocouple probes – Theory,” *J. Acoust. Soc. Am.*, vol. 26, no. 3, pp. 294-310, 1954a.

W. J. Fry and R. B. Fry, “Determination of absolute sound levels and acoustic absorption coefficients by thermocouple probes – Experiment,” *J. Acoust. Soc. Am.*, vol. 26, no. 3, pp. 311-317, 1954b.

H. Fujii, C. Nakaya, H. Takeuchi, T. Kondo and Yasuo Ishikawa, “Acoustic properties of lens materials for ultrasonic probes,” *Jpn. J. Appl. Phys.*, vol. 34, no. 1, pp. 312-315, 1995.

J. Gateau, J. F. Aubry, D. Chauvet, A. L. Boch, M. Fink and M. Tanter, “*In vivo* bubble nucleation probability in sheep brain tissue,” *Phys. Med. Biol.*, vol. 56, no. 22, pp. 7001-7015, 2011.

K. J. Le Goff, C. Gaillard, W. Helbert, C. Garnier and T. Aubry, “Rheological study of reinforcement of agarose hydrogels by cellulose nanowhiskers,” *Carbohydr. Ploym.*, vol. 116, no. 1, pp. 117-123, 2015.

S. A. Goss, R. L. Johnston, and F. Dunn, “Comprehensive compilation of empirical ultrasonic properties of mammalian tissues,” *J. Acoust. Soc. Am.*, vol. 64, no. 2, pp. 423-457, 1978.

M. D. Gray, D. Elbes, C. Paverd, E. Lyka, C. M. Coviello, R. O. Cleveland and C. C. Coussios, "Dual array passive acoustic mapping for cavitation imaging with enhanced 2-D resolution," *IEEE Trans. Ultrason. Ferroelectr. Freq. Control*, vol. 68, no. 3, pp. 647-663, 2020.

R. M. Guillermic, M. Lanoy, A. Strybulevych and J. H.Page, "A PDMS-based broadband acoustic impedance matched material for underwater applications," *Ultrasonics*, vol. 94, no. 1, pp. 152-157, 2019.

H. Guo, M. Hamilton II, S. J. Offutt, C. D. Gloeckner, T. Li, Y. Kim, W. Legon, J. K. Alford and H. H. Lim, "Ultrasound produces extensive brain activation via a cochlear pathway," *Neuron*, vol. 98, no. 5, pp. 1020-1030, 2018.

M. Guo, Y. Xu and M. Gruebele, "Temperature dependence of protein folding kinetics in living cells," *Proc. Natl. Acad. Sci. U. S. A.*, vol. 109, no. 44, pp. 17863-17867, 2012.

B. Hadimioglu, E. G. Rawson, R. Lujan, M. Lim, J. C. Zesch, B. T. Khuri-Yakub and C. F. Quate, "High-efficiency Fresnel acoustic lenses," in *Proc. IEEE Ultrason. Symp.*, Oct. 1993, pp. 579-582.

U. Hamhaber, I. Sack, S. Papazoglou, J. Rump, D. Klatt and J. Braun, "Three-dimensional analysis of shear wave propagation observed by *in vivo* magnetic resonance elastography of the brain," *Acta Biomaterialia*, vol. 3, no. 1, pp. 127-137, 2007.

G. R. Harris, "Review of transient field theory for a baffled planar piston," *J. Acoust. Soc. Am.*, vol. 70, no. 1, pp. 10-20, 1981a.

G. R. Harris, "Transient field of a baffled planar piston having an arbitrary vibration amplitude distribution," *J. Acoust. Soc. Am.*, vol. 70, no. 1, pp. 186-204, 1981b.

P. A. Hasgall, F. Di Gennaro, C. Baumgartner, E. Neufeld, B. Lloyd, M. C. Gosselin, D. Payne, A. Klingenböck and N. Kuster, "Itis database for thermal and electromagnetic parameters of biological tissues," Version 4.0, May. 2018. doi: 10.13099/VIP21000-04-0.itis.swiss/database

T. Heimburg, "The capacitance and electromechanical coupling of lipid membranes close to transitions: The effect of electrostriction," *Biophys. J.*, vol. 103, no. 5, pp. 918-929, 2012.

C. R. Hill, J. C. Bamber and G. R. ter Haar, *Physical Principles of Medical Ultrasonics*. Hoboken, NJ, USA: Wiley, 2004.

A. L. Hodgkin and A. F. Huxley, “A quantitative description of membrane current and its application to conduction and excitation in nerve,” *J. Physiol.*, vol. 117, no. 4, pp. 500-544, 1952.

J. J. Hoffman, A. M. Nelson, M. R. Holland and J. G. Miller, “Cancellous bone fast and slow waves obtained with Bayesian probability theory correlate with porosity from computed tomography,” *J. Acoust. Soc. Am.*, vol. 132, no. 3, pp. 1830-1837, 2012.

A. Hosokawa and T. Otani, “Acoustic anisotropy in bovine cancellous bone,” *J. Acoust. Soc. Am.*, vol. 103, no. 5, pp. 2718-2722, 1998.

J. Huang, R. G. Holt, R. O. Cleveland and R. A. Roy, “Experimental validation of a tractable numerical model for focused ultrasound heating in flow-through tissue phantoms,” *J. Acoust. Soc. Am.*, vol. 116, no. 4, pp. 2451-2458, 2004.

X. Huang, Z. Lin, L. Meng, K. Wang, X. Liu, W. Zhou, H. Zheng and L. Niu, “Non-invasive low-intensity pulsed ultrasound modulates primary cilia of rat hippocampal neurons,” *Ultrasound Med. Biol.*, vol. 45, no. 5, pp. 1274-1283, 2019.

Y. Huang and L. C. Parra, “Fully automated whole-head segmentation with improved smoothness and continuity, with theory reviewed,” *PLoS ONE*, vol. 10, no. 5, pp. 1-34, 2015.

D. A. Hutchins, H. D. Mair, P. A. Puhach and A. J. Osei, “Continuous-wave pressure fields of ultrasonic transducers,” *J. Acoust. Soc. Am.*, vol. 80, no. 1, pp. 1-12, 1986.

J. Jang and J. H. Chang, “Design and fabrication of double-focused ultrasound transducers to achieve tight focusing,” *Sensors*, vol. 16, no. 8, pp. 1248-1261, 2016.

S. Jiménez-Gambín, N. Jiménez, J. M. Benlloch and F. Camarena, “Holograms to focus arbitrary ultrasonic fields through the skull,” *Phys. Rev. Applied*, vol. 12, no. 1, 2019, Art. no. 014016.

Y. Jing, F. C. Meral and G. T. Clement, “Time-reversal transcranial ultrasound beam focusing using a k-space method,” *Phys. Med. Biol.*, vol. 57, no. 4, pp. 901-917, 2012.

A. Johnstone, T. Nandi, E. Martin, S. Bestmann, C. Stagg and B. E. Treeby, “A range of pulses commonly used for human transcranial ultrasound stimulation are clearly audible,” *Brain Stimul.*, vol. 14, no. 5, pp. 1353-1355, 2021.

H. A. S. Kamimura, C. Aurup, E. V. Bendau, N. Saharkhiz, M. G. Kim and E. E. Konofagou, “Iterative curve fitting of the bioheat transfer equation for thermocouple-based temperature estimation *in vitro* and *in vivo*,” *IEEE Trans. Ultrason. Ferroelectr. Freq. Control*, vol. 67, no. 1, pp. 70-80, 2020.

J. J. Kaufman, G. Luo and R. S. Siffert, "Ultrasound simulation in bone," *IEEE Trans. Ultrason. Ferroelectr. Freq. Control.*, vol. 55, no. 6, pp. 1205-1218, 2008.

E. A. Kaye and K. B. Pauly, "Adapting MRI acoustic radiation force imaging for *in vivo* human brain focused ultrasound applications," *Magn. Reson. Med.*, vol. 69, no. 3, pp. 724-733, 2013.

A. Kharine, S. Manohar, R. Seeton, R. G. Kolkman, R. A. Bolt, W. Steenbergen and F. F. de Mul, "Poly(vinyl alcohol) gels for use as tissue phantoms in photoacoustic mammography," *Phys. Med. Biol.*, vol. 48, no. 3, pp. 357-370, 2003.

M. L. Khraiche, W. B. Phillips, N. Jackson and J. Muthuswamy, "Ultrasound induced increase in excitability of single neurons," in *Proc. IEEE 30th Annu. Int. Conf. Eng. Med. Biol. Soc.*, Aug. 2008, pp. 4246-4249.

R. L. King, J. R. Brown, W. T. Newsome and K. B. Pauly, "Effective parameters for ultrasound-induced *in vivo* neurostimulation," *Ultrasound in Med. & Biol.*, vol. 39, no. 2, pp. 312-331, 2013.

J. J. Knierim, "The hippocampus," *Curr Biol.*, vol. 25, no. 1, pp. 1116-1121, 2015.

L. Koessler, S. Colnat-Coulbois, T. Cecchin, J. Hofmanis, J. P. Dmochowski, A. M. Norcia and L. G. Maillard, "*In-vivo* measurements of human brain tissue conductivity using focal electrical current injection through intracerebral multicontact electrodes," *Hum. Brain. Mapp.*, vol. 38, no. 2, pp. 974-986, 2016.

M. A. Kreher, S. A. Johnson, J. M. Mizell, D. K. Chetram, D. T. Guenther, S. D. Lovett, B. Setlow, J. L. Bizon, S. N. Burke and A. P. Maurer, "The perirhinal cortex supports spatial intertemporal choice stability," *Neurobiol. Learn. Mem.*, vol. 162, no. 1, pp. 36-46, 2019.

J. Kubanek, P. Shukla, A. Das, S. A. Baccus and M. B. Goodman, "Ultrasound elicits behavioral responses through mechanical effects on neurons and ion channels in a simple nervous system," *J. Neurosci.*, vol. 38, no.12, pp. 3081-3091, 2018.

A. Kyriakou, E. Neufeld, B. Werner, G. Székely and N. Kuster, "Full-wave acoustic and thermal modelling of transcranial ultrasound propagation and investigation of skull-induced aberration correction techniques: A feasibility study," *J. Ther. Ultrasound.*, vol. 3, no. 11, pp. 1-18, 2015.

C. N. LaFratta, T. Baldacchini, R. A. Farrer, J.T. Fourkas, M. C. Teich, B. E. A. Saleh and M. J. Naughton, "Replication of two-photon-polymerized structures with extremely high aspect ratios and large overhangs," *J. Phys. Chem. B*, vol. 108, no. 31, pp. 11256-11258, 2004.

J. C. F. Lee, J. C. Callaway and R. C. Foehring, “Effects of temperature on calcium transients and Ca2+-dependent afterhyperpolarizaions in neocortical pyramidal neurons,” *J. Neurophysiol.*, vol. 93, no. 4, pp. 2012-2020, 2005.

W. Lee, H. C. Kim, Y. Jung, Y. A. Chung, I. U. Song, J. H. Lee and S. S. Yoo, “Transcranial focused ultrasound stimulation of human primary visual cortex,” *Sci. Rep.*, vol. 6, no. 1, pp. 1-12, 2016a.

W. Lee, S. D. Lee, M. Y. Park, L. Foley, E. Purcell-Estabrook, H. Kim, K. Fischer, L. S. Maeng and S. S. Yoo, “Image-guided focused ultrasound-mediated regional brain stimulation in sheep,” *Ultrasound Med. Biol.*, vol. 42, no. 2, pp. 459-470, 2016b.

W. Legon, S. Adams, P. Bansal, P. D. Patel, L. Hobbs, L. Ai, J. K. Mueller, G. Meekins and B. T. Gillick, “A retrospective qualitative report of symptoms and safety from transcranial focused ultrasound for neuromodulation in humans,” *Sci. Rep.*, vol. 10, no.1, pp. 1-10, 2020.

W. Legon, L. Ai, P. Bansal and J. K. Mueller, “Neuromodulation with single element transcranial focused ultrasound in human thalamus,” *Hum. Brain Mapp.*, vol. 39, no. 5, pp. 1995-2006, 2018a.

W. Legon, P. Bansal, R. Tyshynsky, L. Ai, and J. K. Mueller, “Transcranial focused ultrasound neuromodulation of the human primary motor cortex,” *Sci. Rep.*, vol. 8, no. 1, pp. 7-21, 2018b.

W. Legon, T. F. Sato, A. Opitz, J. Mueller, A. Barbour, A. Williams and W. J. Tyler, “Transcranial focused ultrasound modulates the activity of primary somatosensory cortex in humans,” *Nat. Neurosci.*, vol. 17, no. 2, pp. 322–329, 2014.

D. Liao, M. Hsiao, G. Xiang and P. Zhong, “Optimal pulse length of insonification for Piezo1 activation and intracellular calcium response,” *Sci. Rep.*, vol. 11, no. 1, 2021, Art. no. 709.

C. T. Liauh and W. L. Lin, “Fast numerical scheme of computing acoustic pressure fields for planar circular ultrasound transducers,” *J. Acoust. Soc. Am.*, vol. 105, no. 4, pp. 2243-2247, 1999.

N. N. Liu, Y. D. Cui, B. C. Khoo and A. M. Zhang, “Damage characteristics of elastic material through a thin membrane using high-intensity focused ultrasound (HIFU),” *AIP Adv.*, vol. 8, no. 11, pp. 1-14, 2018.

R. Liu, R. Ma, X. Liu, X. Zhou, X. Wang, T. Yin and Z. Liu, “A noninvasive deep brain stimulation method via temporal-spatial interference magneto-acoustic effect: Simulation and experimental validation,” *IEEE Trans. Ultrason. Ferroelectr. Freq. Control*, vol. 69, no. 8, pp. 2474-2483, 2022.

C. Livermore and J. Voldman, “6.777J/2.751J material properties database,” 2016. Accessed on: Mar. 22, 2021. [Online]. Available: http://www.mit.edu/~6.777/matprops/matprops.htm

M. K. Lovmo, P. T. Yemane, A. Bjorkoy, R. Hansen, R. O. Cleveland, B. A. Angelsen and C. de Lange Davies, “Effect of acoustic radiation force on displacement of nanoparticles in collagen gels,” *IEEE Trans. Ultrason. Ferroelectr. Freq. Control*, vol. 68, no. 3, pp. 416-431, 2021.

E. Macé, G. Montaldo, I. Cohen, M. Baulac, M. Fink and M. Tanter, “Functional ultrasound imaging of the brain,” *Nat. Methods*, vol. 8, no. 8, pp. 662-666, 2011.

G. Maimbourg, A. Houdouin, T. Deffieux, M. Tanter and J. F. Aubry, “3D-printed adaptive acoustic lens as a disruptive technology for transcranial ultrasound therapy using single-element transducers,” *Phys. Med. Biol.*, vol. 63, no. 2, 2018, Art. no. 025026.

G. Maimbourg, J. Guilbert, T. Bancel , A. Houdouin, G. Raybaud, M. Tanter and J.-F. Aubry, “Computationally efficient transcranial ultrasonic focusing: Taking advantage of the high correlation length of the human skull,” *IEEE Trans. Ultrason. Ferroelectr. Freq. Control*, vol. 67, no. 10, pp. 1993-2002, 2020a.

G. Maimbourg, A. Houdouin, T. Deffieux, M. Tanter, and J.-F. Aubry, “Steering capabilities of an acoustic lens for transcranial therapy: Numerical and experimental studies,” *IEEE Trans. Biomed. Eng.*, vol. 67, no. 1, pp. 27-37, 2020b.

J. E. Mark, *Polymer Data Handbook*. New York, NY, USA: Oxford University Press, 1999.

F. Marquet, M. Pernot, J. F. Aubry, G. Montaldo, L. Marsac, M. Tanter and M. Fink, “Non-invasive transcranial ultrasound therapy based on a 3D CT scan: Protocol validation and *in vitro* results,” *Phys. Med. Biol.*, vol. 54, no. 9, pp. 2597-2613, 2009.

L. Marsac, D. Chauvet, R. La Greca, A.-L. Boch, K. Chaumoitre, M. Tanter and J.-F. Aubry, “*Ex vivo* optimisation of a heterogeneous speed of sound model of the human skull for non-invasive transcranial focused ultrasound at 1 MHz,” *Int. J. Hyperthermia*, vol. 33, no. 6, pp. 635-645, 2017.

E. Martin, Y. T. Ling and B. E. Treeby, “Simulating focused ultrasound transducers using discrete sources on regular cartesian grids,” ,” *IEEE Trans. Ultrason. Ferroelectr. Freq. Control.*, vol. 63, no. 10, pp. 1535-1542, 2016.

J. D. Maynard, E. G. Williams and Y. Lee, “Nearfield acoustic holography: I. Theory of generalized holography and the development of NAH,” *J. Acoust. Soc. Am.*, vol. 78, no. 4, pp. 1395-1413, 1985.

G. Mcllvain, E. Ganji, C. Cooper, M. L. Killian, B. A. Ogunnaike and C. L. Johnson, “Reliable preparation of agarose phantoms for use in quantitative magnetic resonance elastography,” *J. Mech. Behav. Biomed. Mater.*, vol. 97, no. 1, pp. 65-73, 2019.

A. Merola, M. Zibetti, C. A. Artusi, L. Rizzi, S. Angrisano, M. Lanotte, L. Lopiano and M. G. Rizzone, “80 Hz versus 130 Hz subthalamic nucleus deep brain stimulation: Effects on involuntary movements,” *Parkinsonism Relat. Disord.*, vol. 19, no. 4, pp. 453-456, 2013.

R. T. Mihran, F. S. Barnes and H. Wachtel, “Temporally-specific modification of myelinated axon excitability *in vitro* following a single ultrasound pulse,” *Ultrasound Med. Biol.*, vol. 16, no. 3, pp. 291-309, 1990.

A. S. Mikhail, A. H. Negussie, C. Graham, M. Mathew and B. J. Wood, “Evaluation of a tissue mimicking thermochromic phantom for radiofrequency ablation,” *Med. Phys.*, vol. 43, no. 7, pp. 4304-4311, 2016.

B. K. Min, A. Bystritsky, K. I. Jung, K. Fischer, Y. Zhang, L. S. Maeng, S. I. Park, Y. A. Chung, F. A. Jolesz and S. S. Yoo, “Focused ultrasound-mediated suppression of chemically-induced acute epileptic EEG activity,” *BMC Neurosci.*, vol. 12, no. 1, pp. 2301-2312, 2011.

M. M. Monti, C. Schnakers, A. S. Korb, A. Bystritsky and P. M. Vespa, “Non-invasive ultrasonic thalamic stimulation in disorders of consciousness after severe brain injury: A first-in-man report,” *Brain Stimul.*, vol. 9, no. 6, pp. 940-941, 2016.

F. Morin, M. Chabanas, H. Courtecuisse and Y. Payan, “Biomechanical modeling of brain soft tissues for medical applications,” *Biomechanics of Living Organs*. vol. 1, no. 6, pp. 127-146, 2017.

C. E. Morris, *Why are so many ion channels mechanosensitive?. Cell Physiology Source Book 4th Ed*. London, England, UK: Academic, 2012.

H. Morris, I. Rivens, A. Shaw and G. R. ter Haar, “Investigation of the viscous heating artefact arising from the use of thermocouples in a focused ultrasound field,” *Phys. Med. Biol.*, vol. 53, no. 17, pp. 4759-4776, 2008.

P. H. Mott, C. M. Roland and R. D. Corsaro, “Acoustic and dynamic mechanical properties of a polyurethane rubber,” *J. Acoust. Soc. Am.*, vol. 111, no. 4, pp. 1782-1790, 2002.

J. K. Mueller and W. J. Tyler, “A quantitative overview of biophysical forces impinging on neural function,” *Phys. Biol.*, vol. 11, no. 5, pp. 1001-1015, 2014.

J. K. Mueller, L. Ai, P. Bansal and W. Legon, “Numerical evaluation of the skull for human neuromodulation with transcranial focused ultrasound,” *J. Neural. Eng.*, vol. 14, no. 6, pp. 1-19, 2017.

F. Munoz, A. Meaney, A. Gross, K. Liu, A. N. Pouliopoulos, D. Liu, E. E. Konofagou and V. P. Ferrera, “Long term study of motivational and cognitive effects of low-intensity focused ultrasound neuromodulation in the dorsal striatum of nonhuman primates,” *Brain Stimul.*, vol. 15, no. 2, pp. 360-372, 2022.

Y. Nie, X. Guo, X. Li, X. Geng, Y. Li , Z. Quan, G. Zhu, Z. Yin, J. Zhang and S. Wang, “Real-time removal of stimulation artifacts in closed-loop deep brain stimulation,” *J. Neural Eng.*, vol. 18, no. 6, 2021, Art. no. 066031.

K. Nightingale, M. S. Soo, R. Nightingale and G. Trahey, “Acoustic radiation force impulse imaging: *In vivo* demonstration of clinical feasibility,” *Ultrasound Med. Biol.*, vol. 28, no. 2, pp. 227-235, 2002.

M. A. Nitsche, L. G. Cohen, E. M. Wassermann, A. Priori, N. Lang, A. Antal, W. Paulus, F. Hummel, P. S. Boggio, F. Fregni and A. Pascual-Leone, “Transcranial direct current stimulation: State of the art 2008,” *Brain Stimul.*, vol. 1, no. 3, pp. 206-223, 2008.

V. Normand, D. L. Lootens, E. Amici, K. P. Plucknett and P. A. Aymard, “New insight into agarose gel mechanical properties,” *Biomacromolecules*, vol. 1, no. 4, pp. 730-738, 2000.

W. L. Nyborg, *Physical Acoustics*. New York, NY, USA: Academic, 1965.

W. L. Nyborg, “Heat generation by ultrasound in a relaxing medium,” *J. Acoust. Soc. Am.*, vol. 70, no. 2, pp. 310-312, 1981.

H. T. O'Neil, “Theory of focusing radiators,” *J. Acoust. Soc. Am.*, vol. 21, no. 5, pp. 516-526, 1949.

R. Ortega, A. Téllez, L. Leija and A. Vera, “Measurement of ultrasonic properties of muscle and blood biological phantoms,” *Phys. Procedia*, vol. 3, no. 1, pp. 627-634, 2010.

V. Ozenne, C. Constans, P. Bour, M. D. Santin, R. Valabrègue, H. Ahnine, P. Pouget, S. Lehéricy, J.-F. Aubry and B. Quesson, “MRI monitoring of temperature and displacement for transcranial focus ultrasound applications,” *Neuroimage*, vol. 204, no. 1, 2020, Art. no. 116236.

C. Paverd, E. Lyka, D. Elbes and C. Coussios, “Passive acoustic mapping of extravasation following ultrasound-enhanced drug delivery,” *Phys. Med. Biol.*, vol. 64, no. 4, 2019, Art. no. 045006.

H. H. Pennes, “Analysis of tissue and arterial blood temperature in the resting human forearm,” *J. Appl. Physiol.*, vol. 1, no. 2, pp. 93-122, 1948.

M. Pernot, J. F. Aubry, M. Tanter, J. L. Thomas and M. Fink, “High power transcranial beam steering for ultrasonic brain therapy,” *Phys. Med. Biol.*, vol. 48, no. 16, pp. 2577-2589, 2003.

A. G. Petrov, “Flexoelectricity of model and living membranes,” *Biochim. Biophys. Acta. - Biomembranes*, vol. 1561, no. 1, pp. 1-25, 2002.

A. D. Pierce, *Acoustics: An Introduction to Its Physical Principles and Applications*. Boston, MA, USA: Springer, 1990.

G. F. Pinton, J. Aubry, M. Fink and M. Tanter, “Numerical prediction of frequency dependent 3D maps of mechanical index thresholds in ultrasonic brain therapy,” in *Proc. IEEE Ultrason. Symp.*, Oct. 2010, pp. 2258-2261.

R. Polanía, M. A. Nitsche and C. C. Ruff, “Studying and modifying brain function with non-invasive brain stimulation,” *Nat. Neurosci.*, vol. 21, no. 2, pp. 174-187, 2018.

A. N. Pouliopoulos, S. Y. Wu, M. T. Burgess, M. E. Karakatsani, H. A. S. Kamimura and E. E. Konofagou, “A clinical system for non-invasive blood-brain barrier opening using a neuronavigation-guided single-element focused ultrasound transducer,” *Ultrasound in Med. & Biol.*, vol. 46, no. 1, pp. 73-89, 2020.

M. L. Prieto, K. Firouzi, B. T. Khuri-Yakub and M. Maduke, “Mechanical activation of Piezo1 but not Nav1.2 channels by ultrasound,” *Ultrasound Med. Biol.*, vol. 44, no. 6, pp. 1217-1232, 2018.

A. F. Prokop, S. Vaezy, M. L. Noble, P. J. Kaczkowski, R. W. Martin and L. A. Crum, “Polyacrylamide gel as an acoustic coupling medium for focused ultrasound therapy,” *Ultrasound in Med. & Biol.*, vol. 29, no. 9, pp. 1351-1358, 2003.

Z. Qiu, S. Kala, J. Guo, Q. Xian, J. Zhu, T. Zhu, X. Hou, K. F. Wong, M. Yang, H. Wang and L. Sun, “Targeted neurostimulation in mouse brains with non-invasive ultrasound,” *Cell Rep.*, vol. 32, no. 7, 2020, Art. no. 108033.

K. V. Ramnarine, T. Anderson and P. R. Hoskins, “Construction and geometric stability of physiological flow rate wall-less stenosis phantoms,” *Ultrasound in Med. & Biol.*, vol. 27, no. 2, pp. 245-250, 2001.

S. Rampersad, B. Roig-Solvas, M. Yarossi, P. P. Kulkarni, E. Santarnecchi, A. D. Dorval and D. H. Brooks, "Prospects for transcranial temporal interference stimulation in humans: A computational study," *Neuroimage*, vol. 202, no. 1, 2019, Art. no. 116124.

J. Y. Rho, M. C. Hobatho and R. B. Ashman, "Relations of mechanical properties to density and CT numbers in human bone," *Med. Eng. Phys.*, vol. 17, no. 5, pp. 347-355. 1995.

V. Rieke and K. B. Pauly, "MR thermometry," *J. Magn. Reson. Imaging*, vol. 27, no. 2, pp. 376-390, 2008.

P. C. Rinaldi, J. P. Jones, F. Reines and L. R. Price, "Modification by focused ultrasound pulses of electrically evoked responses from an *in vitro* hippocampal preparation," *Brain Res.*, vol. 558, no. 1, pp. 36-42, 1991.

J. Robertson, E Martin, B. Cox and B. E. Treeby, "Sensitivity of simulated transcranial ultrasound fields to acoustic medium property maps," *Phys. Med. Biol.*, vol. 62, no. 7, pp. 2559-2580, 2017.

M. A. Rocca, F. Barkhof, J. De Luca, J. Frisén, J. J. G. Geurts, H. E. Hulst, J. Sastre-Garriga and M. Filippi, "The hippocampus in multiple sclerosis," *Lancet Neurol.*, vol. 17, no. 10, pp. 918-926, 2018.

A. Romagnolo, M. Zibetti, M. Lenzi, S. Vighetti, C. Pongmala, C. A. Artusi, E. Montanaro, G. Imbalzano, M. G. Rizzone and L. Lopiano, "Low frequency subthalamic stimulation and event-related potentials in Parkinson disease," *Parkinsonism Relat. Disord.*, vol. 82, no. 1, pp. 123-127, 2021.

P. B. Rosnitskiy, P. V. Yuldashev, O. A. Sapozhnikov, L. R. Gavrilov and V. A. Khokhlova, "Simulation of nonlinear trans-skull focusing and formation of shocks in brain using a fully populated ultrasound array with aberration correction," *J. Acoust. Soc. Am.*, vol. 146, no. 3, pp. 1786-1798, 2019.

Safety Group of the British Medical Ultrasound Society, "Guidelines for the safe use of diagnostic ultrasound equipment," *Ultrasound*, vol.18, no.1, pp. 52-59, 2010.

J. L. Sanguinetti, S. Hameroff, E. E. Smith, T. Sato, C. M. W. Daft, W. J. Tyler and J. J. B. Allen, "Transcranial focused ultrasound to the right prefrontal cortex improves mood and alters functional connectivity in humans," *Front. Hum. Neurosci.*, vol. 14, no. 1, 2020, Art. no. 52.

O. A. Sapozhnikov, Y. A. Pishchal'nikov and A. V. Morozov, "Reconstruction of the normal velocity distribution on the surface of an ultrasonic transducer from the acoustic pressure measured on a reference surface," *Acoust. Phys.*, vol. 49, no. 3, pp. 354-360, 2003.

O. A. Sapozhnikov, A. E. Ponomarev and M. A. Smagin, “Transient acoustic holography for reconstructing the particle velocity of the surface of an acoustic transducer,” *Acoust. Phys.*, vol. 52, no. 3, pp. 324-330, 2006.

O. A. Sapozhnikov, S. A. Tsysar, V. A. Khokhlova and W. Kreider, “Acoustic holography as a metrological tool for characterizing medical ultrasound sources and fields,” *J. Acoust. Soc. Am.*, vol. 138, no. 3, pp. 1515-1532, 2015.

T. Sato, M. G. Shapiro and D. Y. Tsao, “Ultrasonic neuromodulation causes widespread corticalactivation via an indirect auditory mechanism,” *Neuron*, vol. 98, no. 5, pp. 1031-1041, 2018.

R. Sauerheber and B. Heinz, “Temperature effects on conductivity of seawater and physiologic saline, mechanism and significance,” *Chem. Sci. J.*, vol. 6, no. 4, 2015, Art. no. 1000109. doi: 10.4172/2150-3494.1000109.

U. Schneider, E. Pedroni and A. Lomax, “The calibration of CT Hounsfield units for radiotherapy planning,” *Phys. Med. Biol.*, vol. 41, no. 1, pp. 111-124, 1996.

P. H. Seidenberg and A. I. Beutler, *The Sports Medicine Resource Manual*. Philadelphia, PA, USA: W.B. Saunders, 2008.

A. R. Selfridge, “Approximate material properties in isotropic materials,” *IEEE Trans. Sonics Ultrason.*, vol. SU-32, no. 3, pp. 381-394, 1985.

D. E. Soulioti, D. Espindola, P. A. Dayton and G. F. Pinton, “Super-resolution imaging through the human skull,” *IEEE Trans. Ultrason. Ferroelectr. Freq. Control.*, vol. 67, no. 1, pp. 25-36, 2020.

J. M. Stern, N. M. Spivak, S. A. Becerra, T. P. Kuhn, A. S. Korb, D. Kronemyer, N. Khanlou, S. D. Reyes, M. M. Monti, C. Schnakers, P. Walshaw, I. Keselman, M. S. Cohen, W. Yong, I. Fried, S. E. Jordan, M. E. Schafer, J. Engel Jr and A. Bystritsky, “Safety of focused ultrasound neuromodulation in humans with temporal lobe epilepsy,” *Brain Stimul.*, vol. 14, no. 4, pp. 1022-1031, 2021.

C. Sugino, M. Ruzzene and A. Erturk, “Experimental and computational investigation of guided waves in a human skull,” *Ultrasound Med. Biol.*, vol. 47, no. 3, pp. 787-798, 2021.

T. Sun, J. T. Sutton, C. Power, Y. Zhang, E. L. Miller and N. J. McDannold, “Transcranial cavitation-mediated ultrasound therapy at sub-MHz frequency via temporal interference modulation,” *Appl. Phys. Lett.*, vol. 111, no. 16, 2017, Art. no. 163701.

T. L. Szabo, *Diagnostic Ultrasound Imaging: Inside Out*. New York, NY, USA: Academic, 2004.

M. Tabei, T. D. Mast and R. C. Waag, "A k-space method for coupled first-order acoustic propagation equations," *J. Acoust. Soc. Am.*, vol. 111, no. 1, pp. 53–63, 2002.

A. Taflove and S. C. Hagness, *Computational electrodynamics: The finite-difference time-domain method*. Boston, MA, US: Artech House, 2005.

M. Tanter, J. I. Thomas and M. Fink, "Focusing and steering through absorbing and aberrating layers: Application to ultrasonic propagation through the skull," *J. Acoust. Soc. Am.*, vol. 103, no. 5, pp. 2403-2410, 1998.

G. J. Taylor, F. A. Heberle, J. S. Seinfeld, J. Katsaras, C. P. Collier and S. A. Sarles, "Capacitive detection of low-enthalpy, higher-order phase transitions in synthetic and natural composition lipid membranes," *Langmuir*, vol. 33, no.1, pp. 10016-10026, 2017.

G. ter Haar, "Ultrasound bioeffects and safety," *Proc. Inst. Mech. Eng. H*, vol. 224, no. 2, pp. 363-373, 2010.

J. L. Thomas and M. A. Fink, "Ultrasonic beam focusing through tissue inhomogeneities with a time reversal mirror: Application to transskull therapy," *IEEE Trans. Ultrason. Ferroelectr. Freq. Control*, vol. 43, no. 6, pp. 1122-1129, 1996.

S. M. Thompson, L. M. Masukawa and D. A. Prince, "Temperature dependence of intrinsic membrane properties and synaptic potentials in hippocampal CA1 neurons *in vitro*," *J. Neurosci.*, vol. 5, no. 3, pp. 817-824, 1985.

T. Tiennot, H. A. S. Kamimura, S. A. Lee, C. Aurup and E. E. Konofagou, "Numerical modeling of ultrasound heating for the correction of viscous heating artifacts in soft tissue temperature measurements," *Appl. Phys. Lett.*, vol. 114, no. 20, 2019, Art. no. 203702. doi: 10.1063/1.5091108.

C. B. Top, P. J. White and N. J. McDannold, "Nonthermal ablation of deep brain targets: A simulation study on a large animal model," *Am. Assoc. Phys. Med.*, vol. 43, no. 2, pp. 870-882, 2016.

T. Trantidou, Y. Elani, E. Parsons and O. Ces, "Hydrophilic surface modification of PDMS for droplet microfluidics using a simple, quick, and robust method via PVA deposition," *Microsyst. Nanoeng.*, vol. 3, no. 1, 2017, Art. no. 16091.

B. E. Treeby, J. Budisky, E. S. Wise, J. Jaros and B. T. Cox, "Rapid calculation of acoustic fields from arbitrary continuous-wave sources," *J. Acoust. Soc. Am.*, vol. 143, no. 1, pp. 529-537, 2018.

B. E. Treeby and B. T. Cox, “k-Wave: MATLAB toolbox for the simulation and reconstruction of photoacoustic wave fields,” *J. Biomed. Opt.*, vol. 15, no. 2, pp. 1-12, 2010.

B. E. Treeby and B. T. Cox, “A k-space Green's function solution for acoustic initial value problems in homogeneous media with power law absorption,” *J. Acoust. Soc. Am.*, vol. 129, no. 6, pp. 3652-3660, 2011.

B. E. Treeby and B. T. Cox, “Modeling power law absorption and dispersion in viscoelastic solids using a split-field and the fractional Laplacian,” *J. Acoust. Soc. Am.*, vol. 136, no. 4, pp. 1499-1510, 2014.

B. E. Treeby, J. Jaros, A. P. Rendell and B. T. Cox, “Modeling nonlinear ultrasound propagation in heterogeneous media with power law absorption using a k-space pseudospectral method,” *J. Acoust. Soc. Am.*, vol. 131, no. 6, pp. 4324-4336, 2012.

B. E. Treeby, F. Lucka, E. Martin and B. T. Cox, “Equivalent-source acoustic holography for projecting measured ultrasound fields through complex media,” *IEEE Trans. Ultrason. Ferroelectr. Freq. Control.*, vol. 65, no. 10, pp. 1857-1864, 2018.

S. J. Tsai, “Transcranial focused ultrasound as a possible treatment for major depression,” *Med. Hypotheses*, vol. 84, no. 4, pp. 381-383, 2015.

Y. Tufail, A. Matyushov, N. Baldwin, M. L. Tauchmann, J. Georges, A. Yoshihiro, S. I. H. Tillery and W. J. Tyler, “Transcranial pulsed ultrasound stimulates intact brain circuits,” *Neuron*, vol. 66, no. 5, pp. 681-694, 2010.

P. Turner, C. Banahan, M. Alharbi, J. Ince, S. Venturini, S. Berger, I. Bnini, J. Campbell, K. W. Beach, M. Horsfield, M. Oura, A. Lecchini-Visintini and E. M. L. Chung, “Brain tissue pulsation in healthy volunteers,” *Ultrasound Med. Biol.*, vol. 46, no. 12, pp. 3268 3278, 2020.

W. J. Tyler, Y. Tufail, M. Finsterwald, M. L. Tauchmann, E. J. Olson and C. Majestic, “Remote excitation of neuronal circuits using low-intensity, low-frequency ultrasound,” *PLoS ONE*, vol. 3, no. 10, pp. 3511-3521, 2008.

W. J. Tyler, “The mechanobiology of brain function,” *Nat. Rev. Neurosci.*, vol. 13, no. 1, pp. 867-878, 2012.

M. W. Urban, A. Alizad, W. Aquino, J. F. Greenleaf and M. Fatemi, “A review of vibro acoustography and its applications in medicine,” *Curr. Med. Imaging Rev.*, vol. 7, no. 4, pp. 350-359, 2011.

L. Verhagen, C. Gallea, D. Folloni, C. Constan, D. E. Jensen, H. Ahnine, L. Roumazeilles, M. Santin, B. Ahmed, S. Lehericy, M. C. Klein-Flügge, K. Krug, R. B. Mars, M. F. Rushworth, P. Pouget, J.-F. Aubry and J. Sallet, "Offline impact of transcranial focused ultrasound on cortical activation in primates," *eLife*, vol. 8, no. 1, 2019, Art. no. e40541.

V. Walsh and A. Cowey, "Transcranial magnetic stimulation and cognitive neuroscience," *Nat. Rev. Neurosci.*, vol. 1, no. 1, pp. 73-79, 2000.

J. H. Wang and B. P. Thampatty, "An introductory review of cell mechanobiology," *Biomech. Model. Mechanobiol.*, vol. 5, no. 1, pp. 1-16, 2006.

K. Wang, E. Teoh, J. Jaros and B. E. Treeby, "Modelling nonlinear ultrasound propagation in absorbing media using the k-Wave toolbox: Experimental validation," in *Proc. IEEE Ultrason. Symp.*, Oct. 2012, pp. 523-526.

X. Wang, J. Yan, Z. Wang, X. Li and Y. Yuan, "Neuromodulation effects of ultrasound stimulation under different parameters on mouse motor cortex," *IEEE Trans. Biomed. Eng.*, vol. 67, no. 1, pp. 291-297, 2020.

T. D. Webb, S. A. Leung, P. Ghanouni, J. J. Dahl, N. J. Pelc and K. B. Pauly, "Acoustic attenuation: Multifrequency measurement and relationship to CT and MR imaging," *IEEE Trans. Ultrason. Ferroelectr. Freq. Control*, vol. 68, no. 5, pp. 1532-1545, 2021.

D. N. White, G. R. Curry and R. J. Stevenson, "The acoustic characteristics of the skull," *Ultrasound Med. Biol.*, vol. 4, no. 3, pp. 225-252, 1978.

P. J. White, K. Hynynen and G. T. Clement, "Longitudinal and shear mode ultrasound propagation in human skull bone," *Ultrasound Med. Biol.*, vol. 32, no. 7, pp. 1085-1096, 2006.

E. S. Wise, B. T. Cox, J. Jaros and B. E. Treeby, "Representing arbitrary acoustic source and sensor distributions in Fourier collocation methods," *J. Acoust. Soc. Am.*, vol. 146, no. 1, pp. 278-288, 2019.

B. Wu, Y. Chen and J. D. Müller, "Fluorescence fluctuation spectroscopy of mCherry in living cells ," *Biophys. J.*, vol. 96. No. 6, pp. 2391-2404, 2009.

W. Xia, D. Piras, J. C. G. van Hespen, W. Steenbergen and S. Manohar, "A new acoustic lens material for large area detectors in photoacoustic breast tomography," *Photoacoustics*, vol. 1, no. 2, pp. 9-18, 2013.

L. Yang and J. T. Kindt, "Simulation study of the permeability of a model lipid membrane at the fluid solid phase transition," *Langmuir*, vol. 31, no. 7, pp. 2187-2195, 2015.

H. Yang, Y. Yuan, X. Wang and X. Li, “Closed-loop transcranial ultrasound stimulation for real-time non-invasive neuromodulation *in vivo*,” *Front. Neurosci.*, vol. 14, no. 445, pp. 1-9, 2020.

P. P. Ye, J. R. Brown and K. B. Pauly, “Frequency dependence of ultrasound neurostimulation in the mouse brain,” *Ultrasound in Med. & Biol.*, vol. 42, no. 7, pp. 1512-1530, 2015.

S. S. Yoo, A. Bystritsky, J. H. Lee, Y. Zhang, K. Fischer, B. K. Min, N. J. McDannold, A. Pascual-Leone, F. A. Jolesz, “Focused ultrasound modulates region-specific brain activity,” *Neuroimage*, vol. 56, no. 3, pp. 1267-1275, 2011.

K. Yoon, W. Lee, P. Croce, A. Cammalleri and S. S. Yoo, “Multi-resolution simulation of focused ultrasound propagation through ovine skull from a single-element transducer,” *Phys. Med. Biol.*, vol. 63, no. 10, pp. 1-18, 2018.

K. Yoon, W. Lee, J. E. Lee, L. Xu, P. Croce, L. Foley and S. S. Yoo, “Effects of sonication parameters on transcranial focused ultrasound brain stimulation in an ovine model,” *PLoS ONE*, vol. 14, no. 10, pp. 1-31, 2019.

P. Zeidman, A. Lutti and E. A. Maguire, “Investigating the functions of subregions within anterior hippocampus,” *Cortex*, vol. 73, no. 1, pp.240-256, 2015.

P. Zeidman and E. A. Maguire, “Anterior hippocampus: The anatomy of perception, imagination and episodic memory,” *Nat. Rev. Neurosci.*, vol. 17, no. 3, pp. 173-182, 2016.

K. Zell, J. I. Sperl, M. W. Vogel, R. Niessner and C. Haisch, “Acoustical properties of selected tissue phantom materials for ultrasound imaging,” *Phys. Med. Biol.*, vol. 52, no. 20, pp. 475-484, 2007.

X. Zeng and R. J. McGough, “Evaluation of the angular spectrum approach for simulations of near field pressures,” *J. Acoust. Soc. Am.*, vol. 123, no. 1, pp. 68-76, 2008.

T. I. Zohdi and R. Krone, “Estimates for the acoustical stimulation and heating of multiphase biotissue,” *Biomech. Model. Mechanobiol.*, vol. 17, no. 3, pp. 717-725, 2018.